Experimental results and theoretical investigation of adsorption of gases in crystalline hydrophobic dipeptides

Rui Vieira Afonso

Dissertation presented to obtain the degree of

Doctor in Chemical and Biological Engineering

by the

University of Porto

Supervisors:

Luís Miguel Gales Pereira Pinto, Associate Professor

Adélio Miguel Magalhães Mendes, Cathedratic Professor

Ana Margarida Moreira Leitão de Barros Martins Damas, Cathedratic Professor

University of Porto, Porto 2016

UNIÃO EUROPEIA
Fundo Europeu
de Desenvolvimento Regional

GOVERNO DE PORTUGAL

FCT
Fundação para a Ciência e a Tecnologia

Acknowledgements

I would like to acknowledge the Portuguese Foundation for Science and Technology (FCT) for my Ph.D. grant (ref SFRH/BD/43821/2008).

My gratitude goes to my supervisors Professors Luís Gales, Adélio Mendes and Ana Margarida Damas.

I would like to express my gratitude to all the colleagues with which I was lucky to share this long and arduous path. In particular, thanks to Roberto Magalhães and Daniel Ferreira for all the support.

My thankful words are also directed to IBMC, LEPABE, DEQ and FEUP for providing the necessary conditions to carry out my work.

Special thanks to my close friends, Emanuele, Öznur, Barney and Nira, for their unconditional support.

Finally, special gratitude goes to my mother, Dulcínea, grandmother, Setélia, and girlfriend, Gina, who, loyally by my side, have, more than anyone else, made this thesis possible.

Preface

The present work was developed in cooperation between IBMC (Institute for Molecular and Cell Biology) and FEUP (Faculty of Engineering of University of Porto) and was carried out at IBMC and Laboratory for Process Engineering, Environmental, Biotechnology and Energy (LEPABE). All work was accomplished under FCT PhD scholarship SFRH/BD/43821/2008.

This work emerged from the recognition that hydrophobic dipeptides form crystalline arrays of unidimensional ultramicropores. The work that followed sought to determine the usefulness of this class of materials in the context of existing and potential applications of microporous materials currently known.

This thesis comprises three scientific articles published during the PhD period, and two currently under submission.

Abstract

This work had the objecting of testing the host-guest properties and potential applications of crystalline hydrophobic dipeptides. This kind of peptide-based microporous solid has unidimensional ultramicropores that show remarkable framework flexibility and adsorption properties. The pores of crystals of hydrophobic dipeptides can be either hydrophilic or hydrophobic, with the latter being naturally more interesting than the former. Permeation and adsorption experiments with some such dipeptides were performed, after which models were developed to describe adsorption.

Single-crystal permeation of He, N_2, O_2 and Ar in hydrophobic dipeptides LS, VI and AA showed these dipeptides can indeed act as guests for small gases. Millimetre-sized crystals showed a strong tendency for pore blockage, influencing different crystals and species in a different manner. Ar permeation in VI crystals seems to have been all but eliminated, while N_2, O_2 and He permeated easily. As Ar adsorbs in crystals tens of micrometres-long, this effect is construed to be due to pore blockage, with framework flexibility possibly playing a role in letting other species permeate. In the case of AA, framework flexibility led to a formally non-porous solid allowing the penetration of gas molecules into the isolated cavities of the crystalline framework.

Adsorption isotherms of atmospheric gases Ar, N_2 and O_2 were determined in the hydrophobic dipeptides VI, IA, IV and VV. These four dipeptides have pore sizes of, respectively, 0.37 nm, 0.37 nm, 0.39 nm and 0.44 nm. In all dipeptides, the preferential adsorption sequence observed was $Ar>O_2>N_2$, a highly unusual result. Similarly, the sequence of preferential adsorption observed for each gas was VI<IA<IV<VV. Total adsorption concentration thus increases monotonically with pore size. High Ar/O_2 selectivites were observed, especially for VI, a highly prised property in adsorption-based air separation systems. The 1.30 value determined, for VI, at 5 ºC, is the highest ever reported for Ag-free porous materials.

Simple thermodynamic models were developed to better interpret the results obtained and gain insight into guest species behaviour inside the pores. By adapting the Gibbs Adsorption Isotherm to 1D adsorption systems, it was possible to derive simple equations that are traditionally only used to describe monolayer surface (2D) adsorption. A 3D adsorption model was also created for implementation in supermicroporous systems, which is not

entirely a new approach. Considering localised adsorption leads to the derivation of the Langmuir equation, considering distributed adsorption leads to the Volmer equations. Taking into account adsorbate-adsorbate interactions, the Fowler-Guggenheim (localised adsorption) and Hill-de Boer (distributed adsorption) equations are also easily derived. The derivations obtained through this thermodynamic approach decisively show that equations such as Langmuir need not work only as mathematical correlations when applied to microporous systems. The developed models were tested with Xe and CO_2 adsorption in VI, IA, IV and VV. Through fitting of adsorption data, it was possible to determine that Xe adsorbs in a more distributed way, while CO_2 adsorbs in a more localised way.

In order to better visualise the adsorption process in ultramicropores, kinetic derivations were made of all the equations previously derived thermodynamically. The same approach originally used by Langmuir was applied, so the validity of the analogous 1D and 3D equations can be easily inferred. A previously inexistent kinetic derivation of the Volmer equation for 2D systems is also presented. Isolating the adsorbate-adsorbate contribution of the heat of adsorption allows the derivation of the Fowler-Guggenheim and Hill-de Boer equations from the Langmuir and Volmer equations, respectively.

Sumário

O presente trabalho teve como objectivo testar as propriedades de adsorção e aplicações potenciais de dipéptidos hidrofóbicos cristalinos. Este tipo de sólido microporoso peptídico tem ultramicroporos unidimensionais que mostram assinaláveis flexibilidade da rede e propriedades de adsorção. Os poros de cristais de dipéptidos hidrofóbicos podem ser hidrofílicos ou hidrofóbicos, com os últimos sendo naturalmente mais interessantes do que os primeiros. Foram efectuadas experiências de permeação e adsorção com alguns destes dipéptidos, após as quais modelos foram desenvolvidos para descrever a adsorção.

Experiências de permeação por cristal-único de He, N_2, O_2 e Ar, nos dipéptidos hidrofóbicos LS, VI e AA, mostraram que estes dipéptidos podem, efectivamente, ser usados na adsorção de gases com moléculas pequenas. Os cristais milimétricos mostraram uma forte tendência para bloqueio dos poros, influenciando cristais e espécies diferentes de forma diferente. A permeação de Ar em cristais de VI foi completamente eliminada, enquanto o N_2, o O_2 e o He permearam facilmente. Uma vez que o Ar adsorve em cristais com dezenas de micrómetros de comprimento, este efeito é interpretado como sendo devido ao bloqueio de poros, com a flexibilidade de rede possivelmente a permitir que as outras espécies permeiem. No caso da AA, a flexibilidade de rede levou a que sólidos formalmente não-porosos permitissem a penetração de moléculas de gás em cavidades isoladas na rede cristalina.

Foram determinadas isotérmicas de adsorção dos gases atmosféricos Ar, N_2 e O_2 nos dipéptidos hidrofóbicos VI, IA, IV e VV. Estes quatro dipéptidos têm tamanhos de poro, respectivamente, de 0,37 nm, 0,37 nm, 0,39 nm e 0,44 nm. Em todos os dipéptidos, a sequência de adsorção preferencial observada para cada gás foi VI < IA < IV < VV. A concentração de adsorção aumenta portanto com o tamanho de poro. Foram observadas altas selectividades Ar/O_2, especialmente em VI, uma propriedade altamente valorizada em sistemas de separação de ar por adsorção. O valor 1,30, determinado para adsorção em VI, a 5 ºC, é o mais alto algumas vez reportado em materiais porosos não contendo Ag.

Foram desenvolvidos modelos termodinâmicos simples para melhor interpretar os resultados obtidos e visualizar o comportamento das moléculas e átomos adsorvidos dentro dos poros. Adaptando a Isotérmica de Adsorção de Gibbs a sistemas de adsorção 1D, foi possível derivar equações simples que são tradicionalmente usadas apenas para descrever adsorção em monocamada (2D). Foi criado um modelo 3D também para implementação em sistemas

supermicroporosos, uma estratégia não completamente nova. Considerando adsorção localizada resulta na derivação da equação de Langmuir, enquanto considerando adsorção distribuída resulta na equação de Volmer. Tendo em conta interacções adsorvido-adsorvido, as equações de Fowler-Guggenheim (adsorção localizada) e Hill-de Boer (adsorção distribuída) também são facilmente deriváveis. As derivações obtidas desta forma mostram que equações tal como Langmuir não precisam de funcionar apenas como correlações matemáticas quando aplicadas a sistemas microporosos. Os modelos desenvolvidos foram testados na adsorção de Xe e CO_2 em VI, IA, IV e VV. Através do ajuste dos dados de adsorção, foi possível determinar que o Xe adsorve de uma forma distribuída, enquanto o CO_2 adsorve de uma forma mais localizada.

De forma a melhor visualizar o processo de adsorção em ultramicroporos, foram efectuadas derivações cinéticas de todas as equações previamente derivadas termodinamicamente. A mesma estratégia originalmente usada por Langmuir foi aplicada, de forma a que a validade das equações análogas em 1D e 3D possa ser facilmente inferida. Uma derivação cinética da equação de Volmer, previamente inexistente, para sistemas 2D também foi apresentada. A isolamento da contribuição adsorvido-adsorvido do calor de adsorção permite a derivação das equações de Fowler-Guggenheim e Hill-de Boer a partir, respectivamente, das equações de Langmuir e Volmer.

Table of Contents

Nomenclature

Acronyms and abbreviations

Latin letters

1D	One-dimensional
2D	Two-dimensional
3D	Three-dimensional
A	One-letter abbreviation of alanine
Ala	Three-letter abbreviation of alanine
BCP	Block co-polymer
CMS	Carbon molecular sieve
CMSM	Carbon molecular sieve membrane
CNT	Carbon nanotube
CP	Cyclic peptide
CPN	Cyclic peptide nanotube
D	Dextrorotatory
DA	Dubinin-Astakhov
DR	Dubinin-Radushkevich
EoS	Equation of state
F	One-letter abbreviation of phenylalanine
FTIR	Fourier-transform infrared
G	One-letter abbreviation of glycine
GCMC	Grand canonical Monte Carlo
Gln	Three-letter abbreviation of glycine
GNF	Graphite nanofiber

I	One-letter abbreviation of isoleucine
Ile	Three-letter abbreviation of isoleucine
L	One-letter abbreviation of leucine
L	Levorotatory
Leu	Three-letter abbreviation of leucine
MAP	Multiple antigene peptide
MOF	Metal-organic framework
NMR	Nuclear magnetic resonance
OSMS	Organic supramolecular microporous solids
Phe	Three-letter abbreviation of phenylalanine
PSA	Pressure-swing adsorption
PTA	Potential theory of adsorption
S	One-letter abbreviation of serine
Ser	Three-letter abbreviation of serine
SC-XRD	Single-crystal X-ray difraction
T	One-letter abbreviation of threonine
Thr	Three-letter abbreviation of threonine
V	One-letter abbreviation of valine
Val	Three-letter abbreviation of valine
TVFM	Theory of volume-filling of micropores

Greek letters

α	Prefix referring to an amino acid (or its residue) with a single carbon linking the amino and carboxylic groups.
ß	Prefix referring to an amino acid (or its residue) with two carbons linking the amino and carboxylic groups.

ß[3]	Prefix referring to an amino acid (or its residue) with two carbons linking the amino and carboxylic groups, with the side-chain linked to the carbon next to the amine group.
γ	Prefix referring to an amino acid (or its residue) with three carbons linking the amino and carboxylic groups.

Variables

Latin letters

A	Specific surface area, $m^2 \cdot kg^{-1}$
A_0	Area of an adsorbed molecule, $m^2 \cdot molecule^{-1}$
$A_{molecule}$	Average area occupied by a molecule, $m^2 \cdot molecule^{-1}$
A_{mouth}	Average pore mouth area, $m^2 \cdot mouth^{-1}$
a	Molar surface area, $m^2 \cdot mol^{-1}$
a_0	Minimum molar surface area, $m^2 \cdot mol^{-1}$
$a_{molecule}$	Molar area of a single adsorbed molecule, $m^2 \cdot mol^{-1}$
a_{pore}	Interfacial molar area of a given pore, $m^2 \cdot kg^{-1}$
a_s	Molar area of the circle centred on the centre of the impact site, and touching the nearest adsorbed molecule, whether in a surface of 2D adsorption systems or at the pore mouth interface of 3D adsorption systems, $m^2 \cdot mol^{-1}$
$\langle a_s \rangle$	Average of a_s, $m^2 \cdot mol^{-1}$
b	Affinity constant, bar^{-1}
c	Interaction parameter in the Hill-de Boer and Fowler-Guggenheim equations
d	Distance between the pore mouth and the adsorbed molecule closest to it (1D adsorption systems), $m \cdot mol^{-1}$

d^*	Critical distance that allows adsorption of incoming molecules in surface adsorption, m
d_{ads}	Critical distance allowing adsorption (1D adsorption systems), m·mol^{-1}
d_{inter}	Intermolecular distance between two adsorbed molecules, m
E_a	Activation energy of desorption, J·mol^{-1}
$(-\Delta H)_{ads}$	Heat of adsorption, J·mol^{-1}
$(-\Delta H_{inter})$	Term of the isosteric heat of adsorption due to lateral interactions, J·mol^{-1}
K_H	Henry's constant, mol·kg^{-1}·bar^{-1}
K_H^{∞}	Pre-exponential factor in van't Hoff's equation, mol·kg^{-1}·bar^{-1}
k_0	Minimum frequency of adsorption, s^{-1}
k_d	Frequency of desorption, s^{-1}
k_{hit}	Frequency with which the molecule closest to the exit "hits" the pore mouth (1D adsorption systems), s^{-1}
L	Specific micropore length, m·kg^{-1}
l	Molar pore length, m·mol^{-1}
l_0	Minimum molar pore length, m·mol^{-1}
M	Molar mass, kg·mol^{-1}
N_{mouth}	Average number of mouths per pore, mouth·pore^{-1}
N_{pore}	Total specific number of pores, pore·kg^{-1}
n	Adsorbed concentration, mol·kg^{-1}
n_{max}	Maximum adsorbed concentration, mol·kg^{-1}
$n_{interface}$	Amount of adsorbed molecules located at the pore mouth interface, mol·mouth^{-1}
P	Three-dimensional pressure, bar
Q_{ads}	Term of the isosteric heat of adsorption due to adsorbate-adsorbent interactions, J·mol^{-1}

q_{st}	Isosteric heat of adsorption, $J \cdot mol^{-1}$
R	Ideal gas constant, $J \cdot mol^{-1} \cdot K^{-1}$
r_a	Rate of adsorption, $mol \cdot kg^{-1} \cdot s^{-1}$
r_d	Rate of desorption, $mol \cdot kg^{-1} \cdot s^{-1}$
T	Absolute temperature, K
V	Specific pore volume, $m^3 \cdot kg^{-1}$
v	Molar pore volume, $m^3 \cdot mol^{-1}$
v_0	Minimum molar pore volume, $m^3 \cdot mol^{-1}$
$\bar{v}$	Mean speed of adsorbed molecules (1D adsorption systems), $m \cdot s^{-1}$
w	Energy of the interaction between two adsorbed molecules, $J \cdot mol^{-1}$
z	Number of positions, adjacent to each adsorbed molecule, that other molecules can occupy

Greek letters

α	Fraction of successful impacts on adsorption sites in a surface
α	Fraction of impacts with an angle that allows a molecule to enter a pore
α	Interaction constant in the two-dimensional van der Waals equation of state, $mol^2 \cdot m^{-4}$
$\alpha_{i/j}$	Adsorbent selectivity
γ	Surface tension, $N \cdot m^{-1}$
γ_0	Surface tension of the free surface, $N \cdot m^{-1}$
Γ	Excess concentration at the imaginary interface of the 2D Gibbs adsorption isotherm, $mol \cdot m^{-2}$
θ	Amount adsorbed relative to the maximum that can be adsorbed
λ	Distribution parameter of the exponential probability distributions, $mol \cdot m^{-2}$ (2D) and $mol \cdot m^{-1}$ (1D)
μ	Chemical potential, $J \cdot mol^{-1}$

Π	Spreading pressure, $N \cdot m^{-1}$
Φ	3D spreading pressure, $N \cdot m^{-2}$
Ω	1D spreading pressure, N

Chapter 1. Introduction*

1.1. Microporous Solids

1.1.1. Classical Materials and Their Applications

Microporous solids are one of the most successful examples of materials engineering. The two most widely used porous solids, activated carbons and zeolites, are both microporous [1]. The next two, silica gel and activated alumina, can also be microporous, to a varying extent [1]. Adsorption and catalysis constitute the two main applications of microporous solids [1], with separation and reaction processes based on microporous solids being central to the chemical industry. Recent advances have also made the industrial use of microporous solids as membrane material a real possibility [2].

Activated carbon can be described as a network of cross-linked defective carbon graphitic planes. It has been used as a purification agent since antiquity and was the first porous material to be used in adsorption experiments, in 1773. It was also, the first to be used in a modern industrial process, in 1794, in sugar syrup decolouration [1]. It remains, to this day, the most industrially significant microporous solid [1]. Produced initially from coal and charcoal, it was eventually realized that it could be derived from nearly any carbon-rich raw material, through adequate anaerobic thermal processing [3].

The term "zeolite" was originally used for naturally occurring aluminosilicates, having later been extended to synthetic aluminosilicates. A natural zeolite was first identified in 1756, and zeolites were used in adsorption experiments throughout the 19th century [4]. However, it was only after the determination of their crystal structures in the 1920's and 1930's [4] that it was possible to create an accurate picture of adsorption in zeolites, with the development and wide acceptance of the "zeolitic solid solution" theory [5-7]. Their potential as selective adsorbents of gases was soon recognised [6, 7] and studies on their use as adsorbents [4, 8] and catalysts [4, 9] paved the way to industrial use [1, 4, 10].

---

* Sub-chapters 1.1 and 1.2 are adapted from parts of Afonso et al., J. Mater. Chem. 22 (2012), 1709-1723.

Many other microporous materials have been developed in the post-WWII period. Interestingly, most are either purely carbonaceous, as activated carbon, or mineral, as zeolites. The several allotropic forms of carbon resulted in the development of many carbon-based microporous solids, with different structures and morphologies. The simplest case is that of carbon molecular sieves (CMSs), activated carbons with pores small enough to exclude certain species, and a narrow pore size distribution [11]. This is an important class of materials given their use in the separation of nitrogen from air by pressure swing adsorption (PSA) [12]. Other, more recent but less important (as adsorbents or catalysts) carbon-based microporous solids include carbon nanotubes (CNTs), pillared graphite, graphite nanofibers (GNFs) and graphene (see Table 1.1).

Numerous families of mineral crystalline microporous solids were discovered, building on the success of zeolites. Aluminophosphates were the first of such materials to be discovered, followed by other metallophosphates, metallosilicates and many others (see Table 1.1).

There are essentially two main types of microporous frameworks: random three-dimensional frameworks (such as CMSs), with wider pore size distributions, and crystal structures with well-defined pore networks (such as zeolites). Among the latter, a distinction can be made between those having isolated unidimensional pores and those with more complex pore networks and morphologies. The interconnected “cages” constituting most zeolite structures are a good example of a relatively complex three-dimensional framework. Structures with unidimensional pores are relatively rare, although zeolites possessing unidimensional pores have been known for some time [13]. Unidimensional pores offer some significant advantages over multidimensional pore networks. When entering the pores, non-spherical molecules face steric constraints, which reduces their diffusivity [14, 15]. The smaller the pore and the greater the anisotropy of the diffusing molecule, the more important this effect is [16]. For complex pore networks, either crystalline or amorphous, frequent molecular “hopping” between larger “cages” or pore intersections, through smaller “windows”, multiplies this effect, creating an entropic resistance that should be minimised [17]. Unidimensional, uniform and single-sized pores create a system with only two transitions between cavities of different size, pore entrance and pore exit. Unidimensional pores have the disadvantage of being more easily blocked than two- and three-dimensional frameworks, either by contaminants or crystal framework irregularities.

Table 1.1 – Known classes of microporous solids, classified according to their chemical properties. Adapted from [18]. For references for each class, refer to the original publication.

Inorganic	Carbon	Activated Carbon	
		Carbon Molecular Sieves	
		Carbon Nanotubes	
		Graphene	
		Graphite Nanofibers	
		Pillared Graphite	
	Crystalline Minerals	Metallosilicates	
		Alumina	
		Metallophosphates	
		Metallogermanates	
		Others	
	Silica Gel		
Organic	Covalent Organic Frameworks (COFs)		
	Polymers of Intrinsic Microporosity (PIMs)		
	Supramolecular	Dianin's Compound, Hidroquinone and Alicyclic Diols	
		Hydrogen and Halogen-bonded “Tectons”	
		Calixarenes	
		Cyclodextrins	
		Arylene-ethynylene Macrocycles (AEMs)	
		Other Macrocycles	
		Others	
		Peptide-based	Macrocycles
			Dendrimeric
			Hydrophobic dipeptides
Hybrid			Metal-Peptide Frameworks (MPFs)
		Metal-Organic frameworks (MOFs)	
		Zeolitic Imidazole Frameworks (ZIFs)	
	Metal Phosphonates		
	Others		

The crystal framework of mineral and carbonaceous solids, made-up of covalent bonds, creates a robust pore network, capable of withstanding the extreme thermal, pressure and chemical environments of industrial processes, being a fundamental factor behind their success. All the previously enumerated inorganic materials share this characteristic with zeolites, allowing a fast and easy transition to industrial applications. Although this constitutes one of their main strengths, it is also their main limiting factor.

Table 1.1 summarizes the known classes of microporous solids and classifies them according to chemical composition.

1.1.2. Present Trends and Potential Developments

In 2008, the synthetic zeolite market involved a total of 1.8 Mt [19]. 72 % (per volume) of the synthetic zeolite market was used in the manufacture of detergents [19]. Adsorption and catalysis constituted 10 % and 17 %, respectively. However, per market value, the biggest market was that of catalysis, with 55 % of the total. Over 95 % of the catalyst market was due to fluid catalytic cracking (FCC). Synthetic zeolites typically cost 3-4 $/kg for FCC, and no more than 20 $/kg for specialty catalysis applications. For adsorbents, the normal price range is 5-9 $/kg, with some exceptional cases of tens of dollars per kilogram. For use in detergents, prices of ~2 $/kg are typical [19]. Also in 2008, the total market of natural zeolites was of 3.0 Mt [19]. They are mainly used in cement manufacture, with prices of 0.04-0.25 $/kg. It was not possible to uncover equivalent numbers for activated carbon and silica-gel, the other two materials used on a large-scale.

One of the most promising areas of development in zeolite research is in the construction of zeolite membranes. They have the potential to greatly reduce the cost of many separations currently achieved by distillation [20], both through kinetic and equilibrium mechanisms. The cost of zeolite membranes is one order of magnitude higher than that of polymeric membranes, due to their complex fabrication procedure. Thus, they will probably only be useful in separations that involve temperatures and solvents incompatible with polymeric membranes. The main challenge in the production of zeolite membranes is creating thin active layers with no holes, creating good compromises between permeance and selectivity [21]. Microporous solids can still be used as membrane material in mixed-matrix membranes, to improve the performance of polymeric membranes. Mixed-matrix membranes are relatively easy to build, but have far less potential than dense zeolite membranes [20].

Carbon molecular sieve membranes (CMSMs) are also thermally and chemically inert, and have been the subject of research for similar reasons as zeolite membranes. The porous framework of CMS is much more heterogeneous than that of zeolites, with only a few pores having molecular sieving properties. Thus, unlike with zeolite membranes, the selection performance is due to the combined effect of molecular sieving and surface diffusion [22]. CMSMs can be produced more easily than zeolite membranes, and have a pore size that can be regulated by manipulation of production parameters, such as temperature or processing time. Furthermore, different functional groups can be present at the surface of the pores, depending on the precursor used in their production. However, unlike zeolite membranes, CMSMs are extremely brittle, and must be handled carefully [23].

Microporous materials are one of the oldest examples of nanotechnology, as atomic structure is fundamental to their properties, and its understanding and manipulation is the central aspect of the science and engineering of microporous materials. Thus, any technology that uses microporous materials is, in a certain sense, “nanotechnology”. Contemporarily, micropores appear in nanotechnological applications mainly as discrete unidimensional nanotubes, not bulk materials. Bulk microporous solids can, nonetheless, be used in a range of nanotechnological applications where the typical functions of microporous solids as catalyst, adsorbent and molecular sieve fill specific needs in a larger process. In an example of stereoselectivity, microporous solids have recently been proposed as frameworks for confined polymerisation [24, 25], as matrices for the formation of arrays of noble metal nanowires/nanorods [26] and even as drug delivery agents [21, 27]. Given the many current and potential future uses of microporous materials, it is expected that they will continue to be used in increasing amounts, into the foreseeable future.

New microporous materials, both amorphous and crystalline, can find use in traditional as well as in new applications. In traditional applications, it is usually desired that new materials present better performance properties, such as faster catalysis or greater adsorption. For new applications, new materials may be desired to present also different properties than traditional materials. For example, microporous thin-films can be used to functionalise surfaces, and are thus envisioned as tools for micro-scale process intensification. Such applications include micro-reactors, permselective barriers for gas sensors and Lab-on-a-chip devices [21].

Engineering of important characteristics such as pore size and shape, pore wall chemistry, tortuosity and chirality, among others, require control at the molecular level, which is difficult to accomplish with hard and inflexible inorganic solids. Several alternatives have been

proposed to deal with these problems. CMSs, amorphous in nature, can have their sieving properties fine-tuned through manipulation of the synthesis parameters [28], a "top-down" approach. Another approach, used in crystalline solids, is to control pore properties by manipulating molecular composition, a "bottom-up" approach. Soft crystalline organic materials, with greater structural possibilities, are particularly appealing for this task. Metal-Organic Frameworks (MOFs) are probably the best-known example of such materials (see Table 1.1). Organic Supramolecular Microporous Solids (OSMSs) are increasingly seen as a viable alternative to other microporous materials, offering great advantages in biocompatibility, molecular and architectural fine-tuning and framework flexibility [29-31], besides being more soluble in most solvents than inorganic and hybrid materials [29].

1.1.3. Organic Supramolecular Microporous Solids

There is a plethora of fully organic compounds (unlike MOFs, which are hybrid), self-assembling to form microporous molecular crystals, which can be used as OSMSs. In some cases, the individual components of an OSMS can be designed to achieve a specific structure. It is thus possible to have greater control over network properties, although at the expense of network robustness. The "molecular tectonics" approach [32], is a good example of this concept. However, it is the case that many OSMSs have a far less clear connection between molecular structure and porous network configuration. In fact, most OSMSs are discovered purely by chance [29]. Microporosity in OSMSs is frequently unidimensional, to a much greater extent than in inorganic materials [30].

OSMSs are usually synthesised in solution as crystalline inclusion compounds, in a host-guest configuration, in which the guest is usually the solvent. In most inclusion compounds, the host network does not withstand guest removal, collapsing immediately [30]. However, in a few cases, the intermolecular forces between host molecules are strong enough to stabilize the host structure, even after guest removal [29, 30]. The resulting structure is typically not thermodynamically stable, and will eventually collapse. However, this may take a long time to occur, and many of such structures can, for all practical purposes, be considered stable. If this happens, the host's new phase can be used as an OSMS.

The first fully organic inclusion compound to be experimentally shown to act as an adsorbent was Dianin's compound, by Barrer, in 1976. The crystalline form of the material reversibly adsorbed CO_2, noble gases and light hydrocarbons [33]. As can be seen in Figure 1.1(a), its

crystal structure consists of uniaxially connected hourglass-shaped cavities, held together by cyclic hexameric $(OH)_6$ synthons. This is not an awkward situation; the strength and directionality of hydrogen bonds make them one of the most common structuring elements in supramolecular chemistry [34], as would later be observed on several other guest-free stable organic inclusion compounds. Among these, hydroquinone (or quinol) and alicyclic alcohols [35] display stable guest-free structures similar to that of Dianin's compound, having sometimes been classified in a common family of compounds [36].

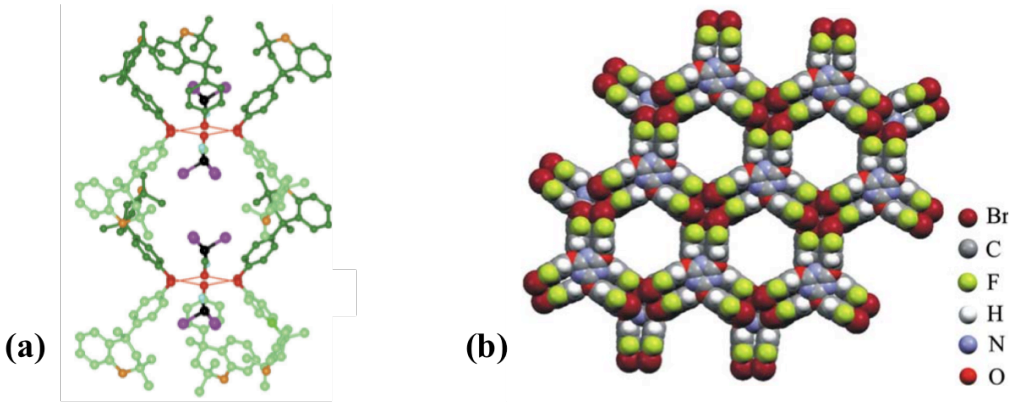

Figure 1.1. (a) Open cages formed by Dianin's compound, with chloroform as a host (reproduced from ref. [36]). (b) Crystal structure of 2,4,6-tris(4-bromo-3,5-difluorphenoxy)-1,3,5-triazin, viewed along the c-crystallographic axis, with the 10.5 Å-wide pores clearly visible (reproduced from [37]).

Following Barrer's original work, it was only in 1991, with the work of Ung et al. on polyalicyclic diols, that another organic inclusion compound was found to possess guest-free stable porosity, in a way that "may be compared to those of inorganic zeolite lattices" [38]. Interestingly, these also possess an identical crystal structure and porous network to that of Dianin's compound.

It was not until the theoretical work of Lee and Venkataraman, in 1996, that the topic of "organic zeolites" was fully revived [39]. Since then, a plethora of crystalline organic inclusion compounds were found to have meta-stable, guest-free inclusion lattices and exhibiting adsorption properties. Most of them (but not all [40, 41]) display one-dimensional pores, frequently called nanochannels, originating in the one-molecule-wide [42] cavities typical of inclusion compounds. The field has been successively reviewed [29, 30, 39, 43, 44], with increasing thoroughness and complexity, sometimes grouping the discussion of

MOFs and fully organic compounds [31, 45]. The most important families of OSMSs are listed in Table 1.1.

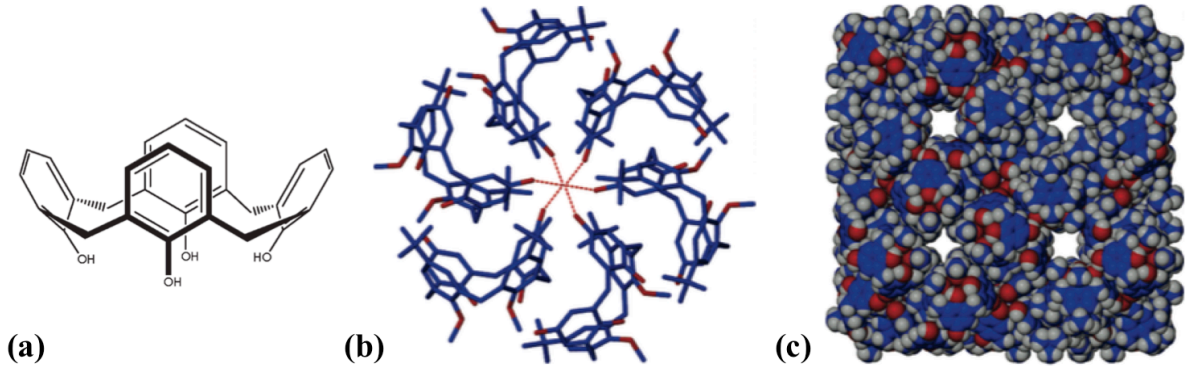

Figure 1.2. (a) Calixarene molecule with 'lower rim' OH functionality. Upper rim functionality may also occur (reproduced from [42]). (b) Calixarenes packed and forming a central cavity (reproduced from [46]). (c) Porous structure created by a calixarene, with two types of pores clearly visible (reproduced from [46]).

One of the oldest and most successful examples of OSMSs is that of calixarenes [42]. These are polycyclicbenzylethers (or esthers or alcohols), typically adopting a cone formation with upper and lower rims that can be functionalised (as shown in Figure 1.2). They have been studied both in solid and solution phases. The crystal structures formed by calixarenes typically give rise to unidimensional pores of nanometric size, whether meso- or microporous. Despite being macrocycles, with the exception of the larger calixarenes [47], the pores formed by most calixarenes do not run across the central void of each molecule, but rather are formed by a perimeter of aromatically-stacked [46, 48] and hydrogen-bonded [49] molecules. Functionalisation of the aromatic ring and the phenolic oxygen allows control over the chemistry of the pores' walls in any geometry.

Many other types of OSMSs have been prepared and studied, although they are not as easily grouped into classes as calixarenes [50-52]. Many of the guest-free host structures were successfully tested as adsorbents, typically displaying high adsorption capacities [33, 53-58]. It has been proposed that many well-known inclusion compounds, that have never been tested as gas adsorbents, could be used as such [43]. Aromatic π-π stacking and hydrogen bonds are the most common structuring forces stabilizing the guest-free meta-stable structures, sometimes occurring together [34, 59]. Also very frequent are π-halogen [58] and full-halogen synthons [37, 50], such as the ones present on the structure shown in Figure 1.1(b).

Also, aliphatic London interactions are present in virtually every single supramolecular compound, being often overlooked.

Cocrystallisation of different but compatible molecular motifs ("mix-and-match") can create multifunctional porous networks, in a way analogous to the poly-specificity of many biological systems. It may be thus possible to rationally design and easily synthesise molecularly tuned porous materials, highly specific to certain guests. The weak interactions creating the framework of supramolecular crystals make the porous networks more flexible and adaptable to guest molecules, thus generating lower activation energies for movement inside the pore, increasing pore mobility [29].

Part of the driving force in developing soft supramolecular materials resides in the hope of replicating the diverse range of functions and high molecular specificity of biological systems. For porous materials, the highly selective and fast mass transfer capacity of biological nanotubes is particularly important as a reference. Use of peptides as building blocks of microporous materials is a direct way of trying to recreate some of the desired functionalities.

1.2. Crystalline Dipeptides

Some dipeptides (Figure 1.3), the simplest of peptides, crystallise in a way as to form unidimensional micropores. These structures are created mainly by dipeptides with two hydrophobic side-chains (so-called "hydrophobic dipeptides"), having recently received considerable attention due to a number of interesting characteristics [60-64].

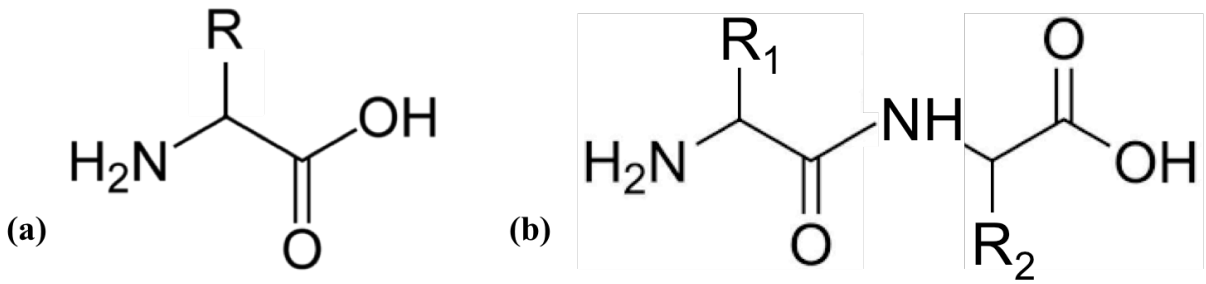

Figure 1.3. (a) Scheme of a generic amino acid. (b) Scheme of a generic dipeptide. R, R1 and R2 represent the substituents constituting the side-chains. The rest of the dipeptide molecule is the "main-chain".

Their structures, shown in Figure 1.4, display single-sized, unidirectional micropores, tunable through residue substitution [60]. The micropores have helical geometry, albeit having low tortuosity [51]. The crystal matrixes are stable, and have been experimentally shown to resist exchange of pore guest molecules [60, 65, 66]. Microporous dipeptide crystals characteristically have high pore density (10^{13}-10^{14} pores/cm^2) but low porosity (down to 5 %). This is due to the very small pore sizes, from non-porous to 10 Å-wide. Since a few Ångstroms are necessary to fit the atoms that make up the pore wall, the small dimension of the resulting pore reduces porosity. Hydrophobic dipeptides are intrinsically non-toxic and bio-compatible. Their thermodynamic stability has been questioned [67, 68], but they have (so far) proven to be exceedingly stable [25, 61, 63-66, 69].

Peptides are named by the sequence of amino-acids polymerised from the amine to the carboxylic termini. The molecular motif remaining from the amino acid upon polymerisation is designated "residue". Usually, the one-letter or three-letter abbreviations are used to designate peptides, such that, for example, valylalanine can be abbreviated as Val-Ala and VA. The prefixes "L" (levorotatory) and "D" (dextrorotatory) can also be used, to indicate residue chirality; L-valyl-L-alanine can be abbreviated as L-Val-L-Ala. When chirality is not indicated, levorotatory residues must be assumed.

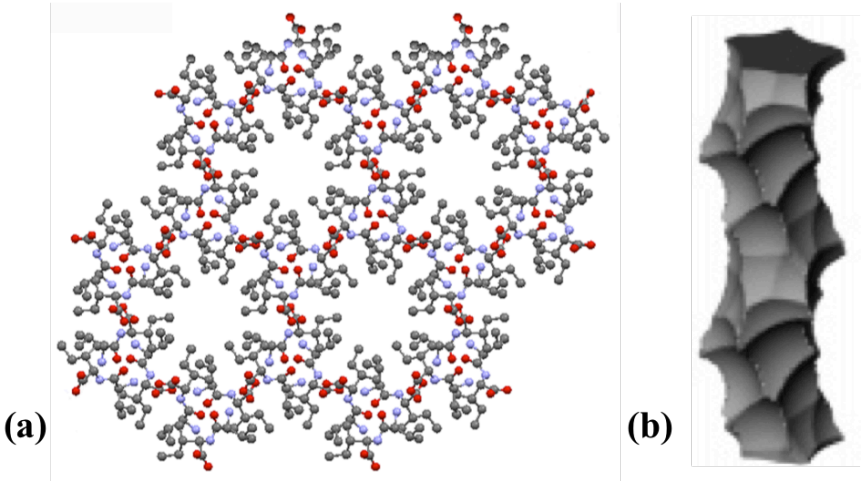

Figure 1.4. a.) Crystal structure of L-Valyl-L-Isoleucine (VI), as seen from the c-crystallographic axis, with the openings in the structure that create the unidimensional pores clearly visible. b.) A lateral view of the morphology of the formed pores. Reproduced from [51].

Dipeptides crystallise in their zwitterionic state, resulting in structures largely determined by the most favourable hydrogen-bond configurations. Based on crystal structure, it is possible to identify two main classes of hydrophobic dipeptides [61]; the VA-class and the FF-class, named after the first dipeptide discovered in each class. The structure of the VA-class is made from a three-dimensional network of hydrogen-bonded main-chains, with dipeptide side-chains pointing inwards to the centre of the pore, thus forming hydrophobic pores. All VA-class dipeptides have two aliphatic side-chains, with varying number of carbons. The crystal structure is the same for all members of the class, and pore size varies mainly according to the size of the side-chains, with bulkier side-chains leading to smaller pores. The other consequence of bulkier side-chains is the decrease in porosity, as can be seen in the systematic increase of porosity with pore size shown in Table 1.2.

FF-class dipeptides display considerably more structural heterogeneity than those of the VA-class, with nearly every dipeptide in the class having a different crystal structure. FF-class dipeptides form two-dimensional networks of hydrogen-bonded main-chains, curled-up on themselves, thus forming pores. The side-chains point outward and aggregate the different pores by the action of London forces between them. The pores thus formed are the hollow interior of the curled-up network of main-chains, being therefore hydrophilic. Only dipeptides with heavy side-chains are able to form these structures, whether aromatic or aliphatic.

Table 1.2 –Pore size and porosity in VA-class dipetides. Data taken from [51].

Dipeptide	Pore size / Å	Porosity / %
VI	3.702	5.69
IA	3.736	6.04
IV	3.904	6.25
VV	4.390	8.23
VA	4.724	9.68
AI	4.740	10.02
AV	5.014	10.90

The hydrophobic nature of the pores in VA-class dipeptides makes them more appealing for traditional adsorption applications than FF-class dipeptides, given their easier regeneration. VA-class dipeptides have repeatedly been tested as adsorbents [25, 51, 63, 64, 67-74] and as catalysts [62]. They display interesting equilibrium separation properties [25, 64] and have been proposed as an ideal template for the study of single-file diffusion [63].

LS is a dipeptide forming hydrophobic pores, which does not share the crystal structure of the VA-class [75]. It is not an hydrophobic dipeptide, since serine is charged, and seems to be an exception to the rule that only dipeptides with two hydrophobic side-chains form porous structures [61]. VS crystals also have hydrophobic pores, but removal of co-crystallised solvent is significantly more difficult than with the other peptides [76].

FF-class crystals are, in fact, co-crystals, as the pores formed are completely filled with water [77]. It is not clear if the water can be completely removed, which may explain why they have attracted very little attention as potential gas adsorbents.

Being the central focus of the work here reported, a more extensive introduction to these materials is given in the next section, in the broader context of peptide-based microporous solids.

1.3. Modelling Adsorption in Micropores

Understanding of guest interaction with the host network of microporous solids naturally requires the adoption of phenomenologically correct and mathematically coherent models. At present, this is almost entirely missing for micropore adsorption. Neither surface models nor the filling models based on the Dubinin equations are able to describe in a phenomenologically meaningful way the process of adsorption in micropores. Thus, the need emerged to develop appropriate, yet simple, models for adsorption in the micropores of dipeptide crystals. In turn, these make excellent templates to test the simple models developed, being chemically and morphologically homogeneous.

In micropores (especially ultramicropores, < 0.7 nm), the adsorption potentials start to coalesce, forming an adsorption environment where it is more accurate to talk of filling of the pores than layered deposition of molecules. In supermicropores (0.7 – 2.0 nm) a combined mechanism of layering and filling takes place, to different extents depending on pore size and

the species under consideration [78]. In both cases, adsorption equilibrium typically follows a Type I isotherm (Figure 1.5).

The micropore filling concept first emerged in the context of studying microporous activated carbon [79]. Amorphous materials are hard to study, since observational determination of pore size distribution is quite troublesome and using the pore size distribution in calculations is also rather complicated. Thus, the overwhelming majority of authors opt for one of the several Dubinin equations/models. The Dubinin-Radushkevich equation, first proposed in 1947 [80], has the form,

$$\theta = \exp[-(A/E)^2] \tag{1-1}$$

where

$$A \equiv -\Delta G_{liq-ads} = RT \ln\left(\frac{P_0}{P}\right) \tag{1-2}$$

and θ is the ratio of adsorbed concentration and the maximum adsorbed concentration, A is the so-called potential of adsorption, defined as the negative of the variation of Gibbs energy from liquid to the adsorbed state, $\Delta G_{liq-ads}$, E is the characteristic energy of the adsorbent, R is the universal gas constant, T is absolute temperature, P is the absolute pressure of the gas phase and P_0 is the saturation pressure of the vapour in the gas phase at T.

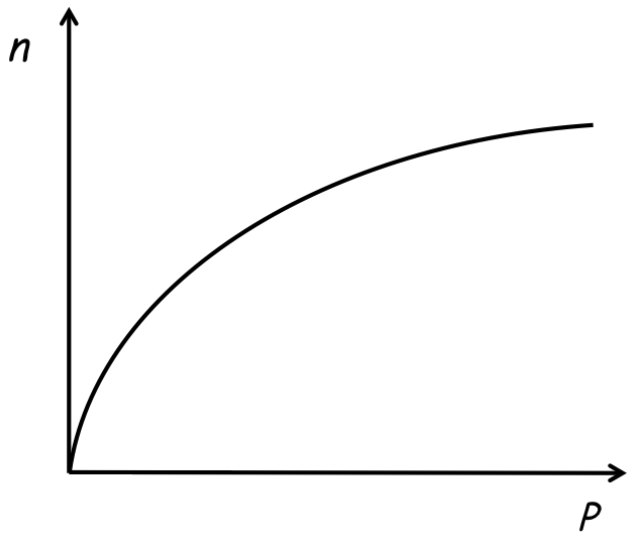

Figure 1.5. Type I adsorption isotherm. For adsorption from liquid solutions, pressure is replaced by concentration.

The Dubinin-Radushkevich equation emerged from an effort to apply the Potential Theory of Adsorption [81] to microporous activated carbon. It started as a fully empirical correlation between the potential of adsorption, A, and the relative amount adsorbed, θ, for some microporous activated carbons. The fact that the equation is reminiscent of a Gaussian probability distribution function, led the authors to postulate that this reflected a Gaussian pore size distribution. Adsorption would thus proceed as the potential of adsorption of the gas/vapour equalled that of a given pore size, with step adsorption for each pore size. The authors referred to this phenomenon as "micropore filling", imagining it as analogous to capillary condensation. They called this the Theory of Volume Filling of Micropores (TVFM). That the step-wise adsorption model is incorrect was soon recognised [82], but many attempts to reformulate it and its simplicity managed to not only maintain its popularity but also make it a reference model to understand micropore adsorption. The term "micropore filling" thus came to mean something slightly different than what it had meant originally, and is used to this day.

The Dubinin-Asthakov equation was introduced [82] to extend applicability of the TVFM to zeolites. It replaced the exponent of the Dubinin-Radushkevich equation with a variable "*n*", called the heterogeneity parameter. Introducing an extra fitting parameter allowed the equation to fit a greater number of adsorption isotherms. The new equation was interpreted as a form of the cumulative expression of the Weibull distribution (making the Dubinin-Radushkevich equation a form of the cumulative expression of a Rayleigh distribution), now expressing a distribution of adsorption energies inside the pores, instead of a pore size distribution.

Working with a global variable such as the "adsorption potential" and simple equations such as the Dubinin-Radushkevich and Dubinin-Asthakov equations is an easy and expedient route to modelling and characterising the adsorption system. Which explains, together with the difficulty of working with pore size distributions, why they have been, and are, so successful. Nonetheless, there is a growing consensus [83, 84], even from authors that have been associated with Dubinin [85], that the Dubinin equations should be considered fully empirical.

Micropore adsorption modelling is highly dependent on the type of adsorbent being considered. Crystalline materials, contrarily to amorphous materials, whose pore sizes and types are known, are usually modelled using thermodynamics-derived expressions, such as Langmuir, Volmer, Fowler-Guggenheim or Hill-de Boer [86]. These equations were

originally derived and used to describe surface adsorption, but were shown by Barrer [87] to be valid also for the porous frameworks of zeolites. The most commonly used equation is, by far, the Langmuir equation [25, 67],

$$\theta = \frac{bP}{1 + bP} \Leftrightarrow bP = \frac{\theta}{1 - \theta} \tag{1-3}$$

where b is the so-called "affinity constant".

The Langmuir equation is still sometimes considered (wrongly) to be valid only for surface adsorption [86], due to it having been originally derived using kinetic arguments, better understood in the context of free surfaces.

Independently of the configuration and morphology of the porous framework (see Section 5), the Langmuir equation applies for cases of localised adsorption with no significant interactions between adsorbed molecules. For distributed adsorption, the Volmer equation should be applied. The Volmer equation [86] is expressed as,

$$bP = \frac{\theta}{1 - \theta} \cdot \exp\left(\frac{\theta}{1 - \theta}\right) \tag{1-4}$$

During the work here reported, adsorption in the micropores of dipeptide crystals was understood to be well represented by both the Langmuir and Volmer equations, depending on the dipeptide and adsorbate used.

1.4. Motivation and Outline

This thesis is primarily the result of a study of adsorption and mass transport properties of microporous crystals of hydrophobic dipeptides. During this study, the need emerged to systematise some of the theoretical models used to analyse the adsorption data, and the result of this investigation is also reported.

Chapter 2 describes hydrophobic dipeptides with other peptide-based microporous solids, namely, cyclic peptides, dendritic peptides and metal-peptide frameworks. The evolution of research on these materials is outlined, with particular emphasis on their properties as molecular hosts. The structure of hydrophobic dipeptide crystals is discussed detailedly.

Chapter 3 presents the experimental results of mass transport and adsorption with atmospheric gases (N_2, O_2 and Ar). Mass transport experiments were performed by single-crystal permeation of dipeptide crystals AA(non-porous) and LS (0.49 nm), with high permeabilities being observed. Adsorption experiments were performed in the four dipeptide crystals with the smallest pores, VI, IA, IV and VV. The results are analysed from practical and theoretical perspectives. The unusual selectivity[†], $\alpha_{Ar/O2} > 1$, is very interesting for oxygen production from air by pressure swing adsorption. Although the materials are unlikely to be used in this application, they provide guidelines for the design of other adsorbents. This unusual selectivity is apparently connected to the extremely small pore size, 0.37-0.44 nm, although the way it influences adsorption is extremely complex.

Chapter 4 formulates a new way of understanding adsorption in micropores, in agreement with the concept of pore filling and using precise thermodynamic arguments. The approach implemented is basically the same that has been applied for two-dimensional adsorbed phases for many decades, only extrapolated to three- and one-dimensional adsorbed phases, typical of adsorption in micropores. The isotherm equations derived for three- and one-dimensional spaces are the same already derived for two-dimensional space, with the exception of those requiring localised adsorption, not applicable to three-dimensional adsorption spaces.

A lot of resistance still exists regarding the approach taken in Chapter 5, although it is based in simple and well-established principles of classical thermodynamics. Thus, to improve the ease of visualisation of the dynamics of adsorption, a simple kinetic derivation of the adsorption isotherm equations previously presented is given in Chapter 5. The kinetic derivation is based on kinetic gas theory and assuming the adsorbed phases behave like fluids, so the phenomenological accuracy of the derivation is not perfect. This derivation aims only at providing an easily intelligible kinetic derivation of equations whose validity has already been established through the thermodynamic derivations.

[†] In the context of mono-component adsorption isotherms, the term “selectivity” is used to designate the ratio between the adsorbed concentration of two pure-compounds, at a given pressure.

1.5. References

1. R. T. Yang, in *Adsorbents: Fundamentals and Applications*, Ch. 1., pp. 1-7 (John Wiley & Sons, 2003).
2. J. Caro and M. Noack, Zeolite membranes – Recent developments and progress, Micropor. Mesopor. Mater. 115 (2008), 215–233.
3. E. Berl, Formation and Properties of Activated Carbon, Trans. Faraday Soc. 34 (1938), 1040-1052.
4. D. W. Breck, Crystalline Molecular Sieves, J. Chem. Educ. 41 (1964), 678-689.
5. M. H. Hey, Studies on the Zeolites. Part I. General review., Mineralog. Mag. 22 (1930), 422-436.
6. R. M. Barrer, The sorption of polar and non-polar gases by zeolites, Proc. R. Soc. Lond. A 167 (1938), 392-420.
7. R. M. Barrer and D. A. Ibbitson, Occlusion of hydrocarbons by chabazite and analcite, Trans. Faraday Soc. 40 (1944), 195-206.
8. R. M. Barrer, Separations Using Zeolitic Materials, Disc. Faraday Soc. 7 (1949), 135-141.
9. C. J. Plank, E. J. Rosinski, and W. P. Hawthorne, Acidic Crystalline Aluminosilicates, Ind. Eng. Chem. Prod. RD 3 (1964), 165-169.
10. A. Corma, State of the art and future challenges of zeolites as catalysts, J. Cat. 216 (2003), 298-312.
11. R. E. Franklin, A Study of the Fine Structure of Carbonaceous Solids by Measurements of True and Apparent Densities — Part II.-Carbonized Coals, Trans. Faraday Soc. 45 (1949), 668-682.
12. H. Jüntgen, New Applications For Carbonaceous Adsorbents, Carbon 15 (1977), 273-283.
13. M. E. Davis, C. Saldarriaga, C. Montes, J. Garces, and C. Crowdert, A molecular sieve with eighteen-membered rings, Nature 331 (1988), 698-699.
14. C. Nguyen and D. D. Do, Dual Langmuir Kinetic Model for Adsorption in Carbon Molecular Sieve Materials, Langmuir 16 (2000), 1868-1873.
15. S. Farooq, H. Qinglin, and I. A. Karimi, Identification of Transport Mechanism in Adsorbent Micropores from Column Dynamics, Ind. Eng. Chem. Res. 41 (2002), 1098-1106.
16. J. V. d. Mynsbrugge, J. D. Ridder, K. Hemelsoet, M. Waroquier, and V. V. Speybroeck, Enthalpy and Entropy Barriers Explain the Effects of Topology on the Kinetics of Zeolite-Catalyzed Reactions, Chem. Eur. J. 19 (2013), 11568–11576.
17. S. W. Rutherford and J. E. Coons, Adsorption equilibrium and transport kinetics for a range of probe gases in Takeda 3A carbon molecular sieve, J. Colloid Interface Sci. 284 (2005), 432–439.
18. R. Afonso, A. Mendes, and L. Gales, Peptide-based solids: porosity and zeolitic behavior, J. Mater. Chem. 22 (2012), 1709-1723.
19. E. M. Flanigen, R. W. Broach, and S. T. Wilson, in *Zeolites in Industrial Separation and Catalysis*, (ed. S. Kulprathipanja), Ch. 1, pp. 1-26 (Wiley-VCH Verlag GmbH & Co. KGaA, 2010).
20. J. Caro, Diffusion in porous functional materials: Zeolite gas separation membranes, proton exchange membrane fuel cells, dye sensitized solar cells, Micropor. Mesopor. Mater. 125 (2009), 79–84.

21. M. P. Pina, R. Mallada, M. Arruebo, M. Urbiztondo, N. Navascués, O. d. l. Iglesia, and J. Santamaria, Zeolite films and membranes. Emerging applications, Micropor. Mesopor. Mater. 144 (2011), 19–27.
22. A. F. Ismail and L. I. B. David, A review on the latest development of carbon membranes for gas separation, J. Memb. Sci. 193 (2001), 1-18.
23. A. F. Ismail, D. Rana, T. Matsuura, and H. C. Foley, in *Carbon-based Membranes for Separation Processes*, Ch. 11., pp. 299-317 (Springer, 2011).
24. T. Uemura, N. Yanaia, and S. Kitagawa, Polymerization reactions in porous coordination polymers, Chem. Soc. Rev. 38 (2009), 1228–1236.
25. A. Comotti, A. Fraccarollo, S. Bracco, M. Beretta, G. Distefano, M. Cossi, L. Marchese, C. Riccardi, and P. Sozzani, Porous dipeptide crystals as selective CO2 adsorbents: experimental isotherms vs. grand canonical Monte Carlo simulations and MAS NMR spectroscopy, Cryst. Eng. Commun. 15 (2013), 1503–1507.
26. O. Carny, D. E. Shalev, and E. Gazit, Fabrication of Coaxial Metal Nanocables Using a Self-Assembled Peptide Nanotube Scaffold, Nano Lett. 6 (2006), 1594-1597.
27. H. Lülf, A. Bertucci, D. Septiadi, R. Corradini, and L. D. Cola, Multifunctional Inorganic Nanocontainers for DNA and Drug Delivery into Living Cells, Chem. Eur. J. 20 (2014), 10900–10904.
28. R. T. Yang, in *Adsorbents: Fundamentals and Applications*, Ch. 1., pp. 109-122 (John Wiley & Sons, 2003).
29. J. R. Holst, A. Trewin, and A. I. Cooper, Porous organic molecules, Nat. Chem. 2 (2010), 915-920.
30. N. B. McKeown, Nanoporous molecular crystals, J. Mater. Chem. 20 (2010), 10588–10597.
31. D. V. Soldatov and J. A. Ripmeester, Organic Zeolites, Stud. Sur. Sci. Cat. 156 (2005), 37-54.
32. J. D. Wuest, Engineering crystals by the strategy of molecular tectonics, Chem. Commun. 41 (2005), 5830–5837.
33. R. M. Barrer, Dianin's Compound as a Zeolitic Sorbent, J. Chem. Soc., Chem. Comm. 5 (1976), 333-334.
34. J. W. Steed and J. L. Atwood, in *Supramolecular Chemistry*, 2nd ed., Ch. 8., pp. 441-536 (John Wiley & Sons, Ltd., 2009).
35. V. T. Nguyen, R. Bishop, D. C. Craig, and M. L. Scudder, Alternative crystal forms produced by a dialcohol inclusion host, Cryst. Eng. Comm. 11 (2009), 1275–1280.
36. V. T. Nguyen, R. Bishop, I. Y. H. Chan, D. C. Craig, and M. L. Scudder, Nodal equivalence of (O–H)6 and aromatic rings: a supramolecular cousin of Dianin's compound and ß-hydroquinone, Cryst. Eng. Comm. 10 (2008), 1810–1815.
37. K. Reichenbächer, G. Couderc, A. Neels, K. Krämer, E. Weber, and J. Hulliger, Improved thermal stability of an organic zeolite by fluorination, J. Incl. Phenom. Macrocycl. Chem. 61 (2008), 127–130.
38. A. T. Ung, R. Bishop, D. C. Craig, I. G. Dance, and M. L. Scudder, Stability of the Helical Tubuland Inclusion Lattice, J. Chem. Soc., Chem. Comm. 19 (1991), 1012-1014.
39. S. Lee and D. Venkataraman, Organic Zeolites?, Stud. Sur. Sci. Cat. 102 (1996), 75-95.
40. X. Wang, M. Simard, and J. D. Wuest, Molecular Tectonics. Three-Dimensional Organic Networks with Zeolitic Properties, J. Am. Chem. Soc. 116 (1994), 12119-12120.

41. E. Demers, T. Maris, and J. D. Wuest, Molecular Tectonics. Porous Hydrogen-Bonded Networks Built from Derivatives of 2,2′ ,7,7′ -Tetraphenyl-9,9′ -spirobi[9H-fluorene], Cryst. Growth Des. 5 (2005), 1227-1235.
42. S. J. Dalgarno, P. K. Thallapally, L. J. Barbour, and J. L. Atwood, Engineering void space in organic van der Waals crystals: calixarenes lead the way, Chem. Soc. Rev. 36 (2007), 236–245.
43. E. Zass, D. A. Plattner, A. K. Beck, and M. Neuburger, In Search of Organic Zeolites: Does Modern Information Retrieval Inevitably Become a 'Sieving-the-Desert' Exercise?, Helv. Chim. Acta 85 (2002), 4012-4045.
44. J. Tian, P. K. Thallapally, and B. P. McGrail, Porous organic molecular materials, Cryst. Eng. Comm. 14 (2012), 1909-1919.
45. A. Sopková, T. Wadsten, J. Bubanec, and M. Reháková, Inclusion Compounds: Desorption and Sorption of the Guest, J. Therm. Analys. Calorim. 56 (1999), 1359-1366.
46. P. K. Thallapally, B. P. McGrail, J. L. Atwood, C. Gaeta, C. Tedesco, and P. Neri, Carbon Dioxide Capture in a Self-Assembled Organic Nanochannels, Chem. Mater. 19 (2007), 3355-3357.
47. M. Perrin, N. Ehlinger, L. Viola-Motta, S. Lecocq, I. Dumazet, S. Bouoit-Montesinos, and R. Lamartine, Crystal Structures of Two Calix[10]arenes Complexed with Neutral Molecules, J. Incl. Phenom. Macrocycl. Chem. 39 (2001), 273-276.
48. C. Tedesco, I. Immediata, L. Gregoli, L. Vitagliano, A. Immirzia, and P. Neri, Interconnected water channels and isolated hydrophobic cavities in a calixarene-based, nanoporous supramolecular architecture, Cryst. Eng. Comm. 7 (2005), 449–453.
49. K. S. Kim, S. B. Suh, J. C. Kim, B. H. Hong, E. C. Lee, S. Yun, P. Tarakeshwar, J. Y. Lee, Y. Kim, H. Ihm, H. G. Kim, J. W. Lee, J. K. Kim, H. M. Lee, D. Kim, C. Cui, S. J. Youn, H. Y. Chung, H. S. Choi, C.-W. Lee, S. J. Cho, S. Jeong, and J.-H. Cho, Assembling Phenomena of Calix[4]hydroquinone Nanotube Bundles by One-Dimensional Short Hydrogen Bonding and Displaced π-π Stacking, J. Am. Chem. Soc. 124 (2002), 14268-14279.
50. H. I. Süss and J. Hulliger, Organic channel inclusion compound featuring an open pore size of 12 Å, Micropor. Mesopor. Mater. 78 (2005), 23-27.
51. D. V. Soldatov, I. L. Moudrakovski, E. V. Grachev, and J. A. Ripmeester, Micropores in Crystalline Dipeptides as Seen from the Crystal Structure, He Pycnometry, and 129Xe NMR Spectroscopy, J. Am. Chem. Soc. 128 (2006), 6737-6744.
52. J. L. Flippen, J. Karle, and I. L. Karle, The Crystal Structure of a Versatile Organic Clathrate. 4-p-Hydroxyphenyl-2,2,4-trimethylchroman (Dianin's Compound), J. Am. Chem. Soc. 92 (1970), 3749-3755.
53. S. A. Talipov, A. Manakov, B. T. Ibragimov, J. Lipkowski, and Z. G. Tiljakov, Sorption of Ammonia, Methylamine and Methanol by the *P*3 Polymorph of Gossypol. Synthesis of Unsymmetrical Monoamine Derivatives of Gossypol by a Solid-state Reaction., J. Incl. Phenom. Mol. Recog. Chem. 29 (1997), 33–39.
54. D. Sun, J. Chen, W. Lu, and X. Zheng, Heats of adsorption of some organic compounds on ß-cyclodextrin determined by gas – solid chromatography, J. Chromatogr. A 864 (1999), 293–298.
55. P. Sozzani, S. Bracco, A. Comotti, L. Ferretti, and R. Simonutti, Methane and Carbon Dioxide Storage in a Porous van der Waals Crystal Angew. Chem. Int. Ed. 44 (2005), 1816 –1820.

56. G. Couderc, T. Hertzsch, N.-R. Behrnd, K. Krämer, and J. Hulliger, Reversible sorption of nitrogen and xenon gas by the guest-free zeolite tris(o-phenylenedioxy)cyclotriphosphazene (TPP), Micropor. Mesopor. Mater. 88 (2006), 170–175.
57. S. Lim, H. Kim, N. Selvapalam, K.-J. Kim, S. J. Cho, G. Seo, and K. Kim, Cucurbit[6]uril : Organic Molecular Porous Material with Permanent Porosity, Exceptional Stability, and Acetylene Sorption Properties, Angew. Chem. Int. Ed. 47 (2008), 3352 –3355.
58. K. J. Msayib, D. Book, P. M. Budd, N. Chaukura, K. D. M. Harris, M. Helliwell, S. Tedds, A. Walton, J. E. Warren, M. Xu, and N. B. McKeown, Nitrogen and Hydrogen Adsorption by an Organic Microporous Crystal, Angew. Chem. Int. Ed. 48 (2009), 3273–3277.
59. J. W. Steed and J. L. Atwood, in *Supramolecular Chemistry*, 2nd ed., Ch. 1., pp. 1-48 (John Wiley & Sons, Ltd., 2009).
60. C. H. Görbitz, Nanotubes from hydrophobic dipeptides: pore size regulation through side chain substitution, New J. Chem. 27 (2003), 1789-1793.
61. C. H. Görbitz, Microporous Organic Materials from Hydrophobic Dipeptides, Chem. Eur. J. 13 (2007), 1022–1031.
62. G. Distefano, A. Comotti, S. Bracco, M. Beretta, and P. Sozzani, Porous Dipeptide Crystals as Polymerization Nanoreactors, Angew. Chem. Int. Ed. 51 (2012), 9258–9262.
63. M. Dvoyashkin, H. Bhase, N. Mirnazari, S. Vasenkov, and C. R. Bowers, Single-File Nanochannel Persistence Lengths from NMR, Anal. Chem. 86 (2014), 2200-2204.
64. R. Afonso, A. Mendes, and L. Gales, Hydrophobic dipeptide crystals: a promising Ag-free class of ultramicroporous materials showing argon/oxygen adsorption selectivity, Phys. Chem. Chem. Phys. 16 (2014), 19386-19393.
65. C. H. Görbitz, An exceptionally stable peptide nanotube system with flexible pores, Acta Crystallogr. B58 (2002), 849-854.
66. C. H. Görbitz, M. Nilsen, K. Szeto, and L. W. Tangen, Microporous organic crystals: an unusual case for L-leucyl–L-serine, Chem. Commun. 41 (2005), 4288–4290.
67. D. V. Soldatov, I. L. Moudrakovski, and J. A. Ripmeester, Dipeptides as Microporous Materials, Angew. Chem. Int. Ed. 43 (2004), 6308-6311.
68. R. Anedda, D. V. Soldatov, I. L. Moudrakovski, M. Casu, and J. A. Ripmeester, A New Approach to Characterizing Sorption in Materials with Flexible Micropores, Chem. Mater. 20 (2008), 2908-2920.
69. A. Comotti, S. Bracco, G. Distefano, and P. Sozzani, Methane, carbon dioxide and hydrogen storage in nanoporous dipeptide-based materials, Chem. Commun. 45 (2009), 284–286.
70. I. Moudrakovski, D. V. Soldatov, J. A. Ripmeester, D. N. Sears, and C. J. Jameson, Xe NMR lineshapes in channels of peptide molecular crystals, Proc. Nat. Acad. Sci. 101 (2004), 17924-17929.
71. C.-Y. Cheng and C. R. Bowers, Observation of Single-File Diffusion in Dipeptide Nanotubes by Continuous-Flow Hyperpolarized Xenon-129 NMR Spectroscopy, Chem. Phys. Chem. 8 (2007), 2077-2081.
72. K. M. Siegrist, C. Pfefferkorn, A. Schwarzkopf, V. B. Podobedov, and D. F. Plusquellic, Experimental and computational investigations of the THz spectra of dipeptide nanotubes, Proc. SPIE 6853 (2008), 685302.

73. H. Zhang, K. Siegrist, D. F. Plusquellic, and S. K. Gregurick, Terahertz Spectra and Normal Mode Analysis of the Crystalline VA Class Dipeptide Nanotubes, J. Am. Chem. Soc. 130 (2008), 17846–17857.
74. M. Dvoyashkin, A. Wang, S. Vasenkov, and C. R. Bowers, Xenon in l--alanyl--l--valine nanochannels: A highly ideal molecular single--file system, J. Phys. Chem. Lett. 4 (2013), 3263-3267.
75. C. H. Görbitz, M. Nilsen, K. Szeto, and L. W. Tangen, Microporous organic crystals: an unusual case for L-leucyl–L-serine, Chem. Commun. (2005), 4288–4290.
76. C. H. Görbitz, Monoclinic nanoporous crystal structures for L-valyl–L-alanine acetonitrile solvate hydrate and L-valyl–L-serine trifluoroethanol solvate, Cryst. Eng. Commun. 7 (2005), 670-673.
77. C. H. Görbitz, Nanotube Formation by Hydrophobic Dipeptides, Chem. Eur. J. 7 (2001), 5153-5159.
78. C. Nguyen and D. D. Do, Adsorption of Supercritical Gases in Porous Media: Determination of Micropore Size Distribution, J. Phys. Chem. B 103 (1999), 6900-6908.
79. M. M. Dubinin, The Potential Theory of Adsorption of Gases and Vapors for Adsorbents with Energetically Nonuniform Surfaces, Chem. Rev. 60 (1960), 235–241.
80. M. M. Dubinin and L. V. Radushkevich, Equation of the characteristic curve of activated charcoal, Chem. Zentr. 1 (1947), 875-890.
81. M. Polányi, Section III.-Theories of the Adsorption of Gases. A General Survey and Some Additional Remarks., Trans. Faraday Soc. 28 (1932), 316-333.
82. M. M. Dubinin and V. A. Astakhov, in *Molecular Sieve Zeolites - II*, (eds. E.M. Flanigen and L.B. Sand), Ch. 44, pp. 69-85 (American Chemical Society, 1971).
83. A. P. Terzyk, S. Furmaniak, P. A. Gauden, P. J. F. Harris, and J. Włoch, Testing isotherm models and recovering empirical relationships for adsorption in microporous carbons using virtual carbon models and grand canonical Monte Carlo simulations, J. Phys.: Condens. Matter 20 (2008),
84. D. D. Do, D. Nicholson, and H. D. Do, Adsorption in micropores (nanopores): a computer appraisal of the Dubinin equations, Molec. Sim. 35 (2009), 122–137.
85. F. Stoeckli, Dubinin´s Theory and its Contribution to Adsorption Science, Russ. Chem. Bulletin Int. Ed. 50 (2001), 2265-2272.
86. D. D. Do, in *Adsorption Analysis: Equilibria and Kinetics*, Ch. 2, pp. 11-48 (Imperial College Press, 1998).
87. R. M. Barrer, in *Zeolites and Clay Minerals as Sorbents and Molecular Sieves*, Ch. 3, pp. 104-161 (Academic Press Inc., 1978).

Chapter 2. Peptide-Based Microporous Solids*

The emergence of soft supramolecular materials offers the opportunity of bringing some of the properties and functionalities typical of biological pores into classical microporous materials applications. Peptide-based microporous solids, based on the same building blocks and using the same molecular motifs as proteins, are obvious materials to be used in this experimental approach.

The idea of synthesising peptide nanotubes was first explored [1, 2] due to the realisation of their similarity to naturally occurring antibiotic and metal ion transporting pores. Transmembrane channels in living cells are macromolecular pores that have long been known for their combined high selectivities and permeabilities [3, 4]. They are built from proteins with highly complex structures and a range of functionalities inexistent in most microporous materials, such as "gate-keeping" and stimuli-activated pore opening/closing. Although selectivity is partly related to molecular sieving, they are still capable of extremely fast ion transport, ~10^7 ions·s^{-1}·$channel^{-1}$, for concentration differences of just ~ 100 mM. This result is confirmed by theoretical calculations as well as experimental results using Gramicidin A [3, 4]. It was the attempt to create artificial biological membrane protein pores that drove most of the initial research effort on the field, although many other applications have since been studied.

Selectivity in artificial nanotubes ("micropores" according to IUPAC nomenclature, i.e. pores smaller than 2 nm) is created by differences in adsorption affinity, diffusion rate or size selection (molecular sieving) [5]. All three strategies require a compromise between permeation speed ("permeability") and selectivity. This relation is well illustrated in the well-known Robeson Upper Bound [6], valid for polymer membranes.

There are well-known stability and robustness issues associated with using all types of soft materials, constituting one of the main hindrances to their widespread use in industrial processes and products. Peptide-based materials are no exception. There are, however, solutions to this problem, which have been tried with different degrees of success. The most fundamental approach, known as "covalent capture", involves stabilizing a supramolecular

* Adapted and updated from parts of Afonso et al., J. Mater. Chem. 22 (2012), 1709-1723.

entity by creating covalent bonds between its molecules, in a way that does not change its structure [7, 8]. This strategy not only allows the material to be "locked" in the desired solid phase, but also increases the material's chemical, baric and thermal robustness and long-term stability. This probably comes at the expense of some framework flexibility, which, as will be discussed later, should diminish the speed and selectivity of molecular permeation.

There are other hypothetical strategies to increase overall material stability. A very easily accomplished one is encapsulation in a more stable material, which does not interfere with permeation of the desired species, but prevents contact with harmful compounds. Although built with a different purpose, MOF-based mixed matrix membranes illustrate this approach well [9]. Not so easy, but farther-reaching in stabilizing the material, is the possibility of creating carbon molecular sieves from the original peptide framework, as it is done with some polymers [10]. This, however, could be technically challenging to achieve and would transform the soft material into a hard one, therefore losing all the advantages of the former. Still, the possibility of easily designing the porous network architecture of a very robust solid is very interesting and should not be overlooked.

In the last 20 years, many peptide-based crystalline materials have been proposed as an interesting kind of organic supramolecular microporous solids. Although protein and peptide crystals have been long known to form solvent-filled pores, these usually collapse upon solvent removal. The first stable peptide nanotubes were discovered by Ghadiri et al., in 1993, by using rationally designed cyclopeptides [11]. The field was further expanded by the discovery, in 1994, of pore-forming dendritic peptides [12], in 1996, of dipeptides with hydrophobic side-chains [13] and, more recently, in 2008, peptide-based MOFs [14]. A detailed assessment of each of these four kinds will follow.

2.1. Cyclic Peptides

Cyclic Peptides (CPs) are macrocyclic polyaminoacids. Nanotube formation through stacking of CPs was first proposed by Hassall, in 1972 [15]. He predicted CPs consisting of alternating α,ß-residues would self-assemble in a columnar manner via main-chain to main-chain hydrogen bonds. Preliminary and inconclusive experimental results on this hypothesis were obtained in 1975, by Karle et al. [2].

However, it would be with alternating L,D-α-CPs that the main developments on the field of peptide macrocycles would be made. In 1974, De Santis et al. published a theoretical work [1] seeking to explore the conformational differences between poly(L-α-amino acid) chains and those containing alternating L, D residues. It was shown that a macrocycle of the latter type would form interannular hydrogen bonds, in a beta-sheet-like conformation, as shown in Figure 2.1. Following this theoretical work, several attempts were made at creating self-assembling cyclic L,D-α-peptides. Early trials were hindered by the peptides' tendency to co-crystallize with water [16, 17]. The first successful attempt came in 1993, by Ghadiri et al. [11], when cyclo[-(D-Ala-Glu-D-Ala-Gln)$_2$-] was crystallised by acidification of an alkaline solution of the peptide. The formation mechanism of this type of CPs is shown in Figure 2.2. Posterior works by the same authors proved CP polymerization can also occur through self-assembly in solution, and is not only a consequence of the crystallisation process [18, 19]. These experiments also showed the potential of the CPs to act as cellular-membrane hydrophilic channels [18] and that pore-size control can be achieved by manipulating the number of residues [19].

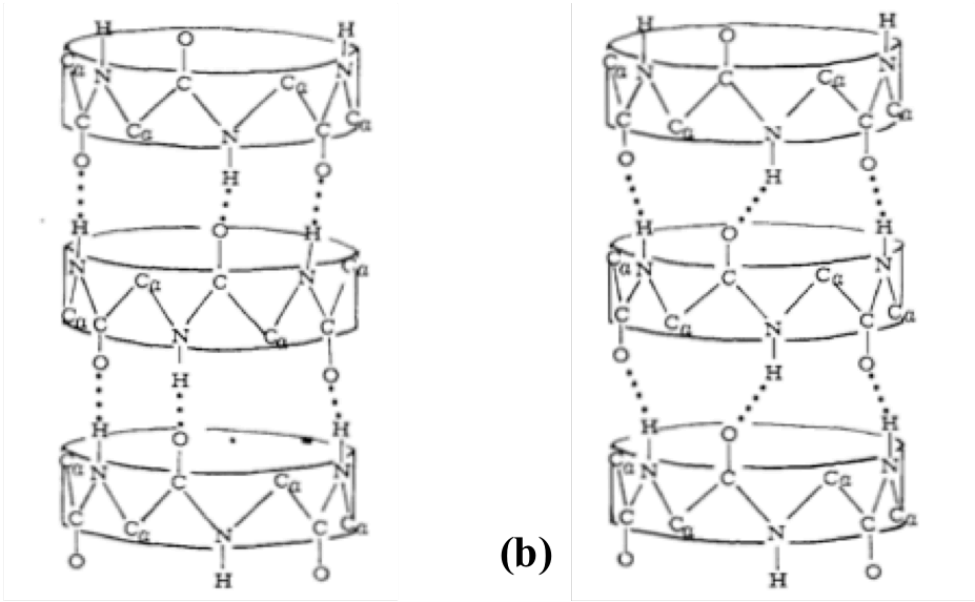

Figure 2.1. Possible interannular pore-forming hydrogen-bonds, as predicted by De Santis in 1974. (a) parallel conformation. (b) antiparallel conformation. Adapted from [1].

A few different types of peptide macrocycles have been studied since then, primarily as drug and metal ion transport agents. Most tests were performed on alternating L,D-α-peptides, due to the early and successful trials by Ghadiri et al. [11, 18], which have pores 2-13 Å-wide [20]. Other intensely studied classes of macrocyclic peptides are ß-peptides [21, 22]

(analogous to the α,ß-peptides studied by Hassal et al. [15]and Karle et al. [2]), α,γ-peptides [23, 24], depsipeptides [25, 26], cystines [26, 27] and pyrrolinones [28, 29]. ß-peptides have the capacity to resist enzymatic degradation, which made them very appealing for solution phase medical applications [30, 31]. α,γ-peptides have the unique characteristic of the C2 methylene group pointing to the pore interior, thus constituting the bulk of the pore inner wall [32]. Wall composition control and functionalisation can therefore be achieved by simple substitution of the methylene group during the molecular synthesis stage.

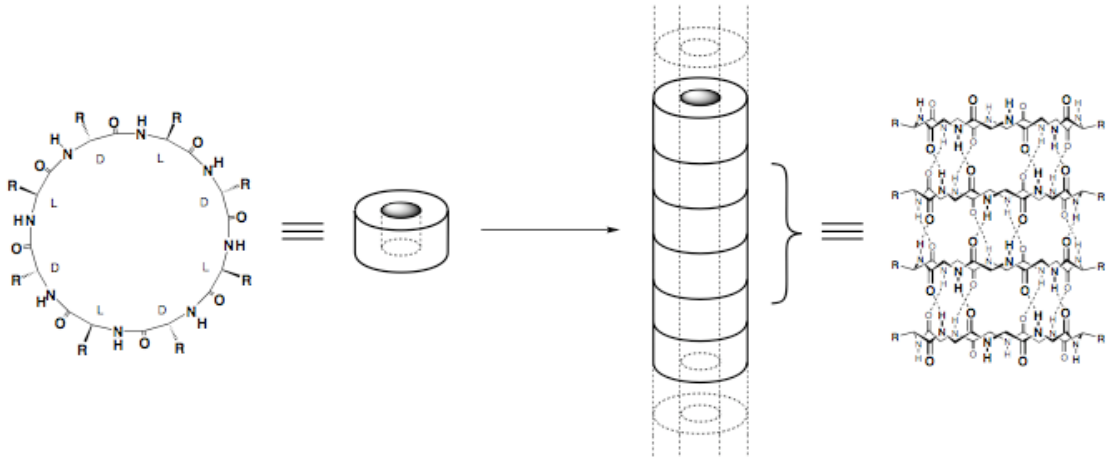

Figure 2.2. Schematic diagram of nanotube assembly from cyclic D,L-peptides (adapted from [33]).

The first study on mass-transport on cyclic peptide nanotubes (CPNs) [18], in 1994, using cyclo[-(Trp-D-Leu)$_3$-Gln-D-Leu-] proved their capacity to spontaneously self-assemble and integrate, with a site-adjusted length, into cell-like lipid bilayers. Hydrophobic functional groups, from the leucine and tryptophan side-chains, promoted CPNs' incorporation into the lipidic bilayer. Proton transport activity across the 9 Å pore was tested by preparing lipidic vesicles with an internal pH of 6.5, and inserting them in a solution with pH of 5.5. Very fast ion-transport rates, ~10^7 ions·s^{-1}·$channel^{-1}$, were observed, similar to those of well known natural ion channels, such as Gramicidin A and Amphotericin B [3].

Still in 1994, the Ghadiri group presented another study, showing that not only monoatomic ions but also molecules could be transported across CPs [34]. The authors created a 10-residue cyclopeptide that, just like the previous one, was constituted essentially of leucine and tryptophane residues, and therefore had similar self-assembling properties. It had, however, a

slightly larger (10 Å) diameter, so that glucose could pass through it. The cyclopeptide was shown, through FTIR spectroscopy, to self-assemble and integrate into transmembrane tubular channels and glucose concentrations in solution were monitored spectrophotometrically. Upon introduction of solubilised CPs into the vesicle suspension, concentration inside and outside the vesicles tended to equalisation. Equalisation rates were directly proportional to peptide concentration, indicating peptide aggregation into the membrane was the limiting step.

In 1998, tetra-ß^3-CPs were successfully used as ion carriers, in lipidic vesicle-based proton and K^+ transport assays and in single channel conductance experiments [21]. Nanotube self-assembling into the vesicle membrane was assessed through FTIR spectroscopy. Two tryptophan-containing tetra-ß^3-CPs proved capable of self-assembling into the vesicular membrane and performing proton transport, with one having a performance very close to that of Gramicidin D. Based on van der Waals surface calculations, the authors argued that a flat-ring conformation with a central hole of 2.6-2.7 Å is expected upon self-assembly as transmembrane channels. Previous results [35] suggested that a different flat-ring structure, with a collapsed core, is also stable for some tetra-ß^3-CPs. It is nonetheless unclear whether CPs shown to perform mass transport possess a permanent open structure or if guest inclusion is necessary to promote it.

Another study on transmembrane solution-phase mass transport further indicates a fast, highly selective permeation through CPNs, this time with glutamic acid [36]. The octa and decapeptide previously shown to be able to work as transmembrane channels were used, together with Gramicidin A, in liposome-based mass-transport assays and single-channel conductance experiments. Once again, the space-filling analysis proved to accurately predict the sieving behaviour of the channels. Glutamate ion efflux out of the liposomes remained unaffected upon octapeptide and Gramicidin A addition to a liposome solution. On the other hand, addition of decapeptides caused a significant increase in ion efflux rate. These results were confirmed by single-channel conductance experiments in planar lipid bilayers. The fact that the glutamate ion had a similar size to that of the octapeptide pore, and, still, was sieved-off, indicates that CPs have very little radial framework flexibility, probably stemming from the all-covalent rings that create the channels, as the one shown in Figure 2.2. Indeed, a recent computational study on the transport properties of α,γ-CPNs [37] showed that they are very stable and rigid entities, with only some axial flexibility, depending on the permeating species' capacity to compete with inter-annular hydrogen bonds.

This same study showed that framework dynamics is as important as structure in determining CPNs' mass transport properties. The use of α,γ-CPs creates nanotubes with mixed hydrophilic/ hydrophobic inner cavities, allowing for strong bonding both with polar and apolar molecules. However, the hydrophilic rim of the tube's exterior has dramatic consequences on the behaviour of the permeating molecules. Small polar molecules, such as water, can easily enter the 5.4 Å nanotube, although hydrogen bonds between the molecules and the nanotube slowdown their diffusion through it. Slightly larger methanol molecules are completely unable to enter or, if "placed" inside, exit the nanotubes. Even more awkward, polar chloroform molecules can enter, but not leave, the tube, probably due to the hydrophilic outer rim of the tubes. These results are partly confirmed by the experimental work of Amorín et al. [23, 32], and open very interesting perspectives on storage and capture of small hydrophobic molecules, such as hydrogen or methane.

A series of molecular dynamics studies have also shown that CP nanotubes possess remarkable water transport properties [38-42], in-line with results observed in other nanotubes [43, 44]. Strong flux dependence has been observed with pore size [39] and the chemical nature of inner pore walls [42]. Theoretical considerations support these results [41].

As the aforementioned examples show, most of the work so far done with CPs is related to solution-phase applications, where the nanotubes are used discretely to create nanochannels on specific locations of a vaster ensemble. Several peptides have been shown to incorporate into hydrophobic membranes [18, 34, 36], with some even showing anti-bacterial activity [45]. The mode of membrane permeation depends mainly on amino-acid sequence [45, 46]. Successful transport of monoatomic ions [18, 21], glucose [34] and glutamate ion [36] across CPs has been observed repeatedly in solution-phase trials. These materials also have a proven ability to create microcrystalline powders with an intact tubular structure [47]. Therefore, their utilisation as crystalline molecular sieves and gas adsorbents is only limited by their unknown stability after removal of co-crystallised solvent.

There has been one instance of CPs being used as nanotubes in a microporous solid. An eight residue L,D–α–CP was used as the self-assembling nanotube-forming motif within a block copolymer (BCP) matrix, in order to create a microporous composite membrane [48]. The material synthesis starts with a pre-templated block copolymer thin-film with monodisperse hollow cylindrical pores (~3 nm). L,D-α-CPs are dissolved into the thin-film, after being conjugated with polymer strands, for improved solubility. Finally, a heating-cooling cycle (up to 180 ºC) of the material leads to self-assembly of the CP-polymer conjugates inside the

block copolymer matrix, forming nanotubes within the original pores, but with the smaller CP inner diameter. This synthesis sequence is represented in Figure 2.3. Pore alignment was confirmed by microscopic and spectroscopic techniques. Pore opening was assessed through successful proton permeation experiments on a supported CP/BCP thin-film. These are very exciting results, that prove that CPs can be used in laboratory scale membrane modules. Nonetheless, further testing is necessary to assess the fraction of open pores and effective tortuosity, and determine single-channel permeability and inter-membrane reproducibility.

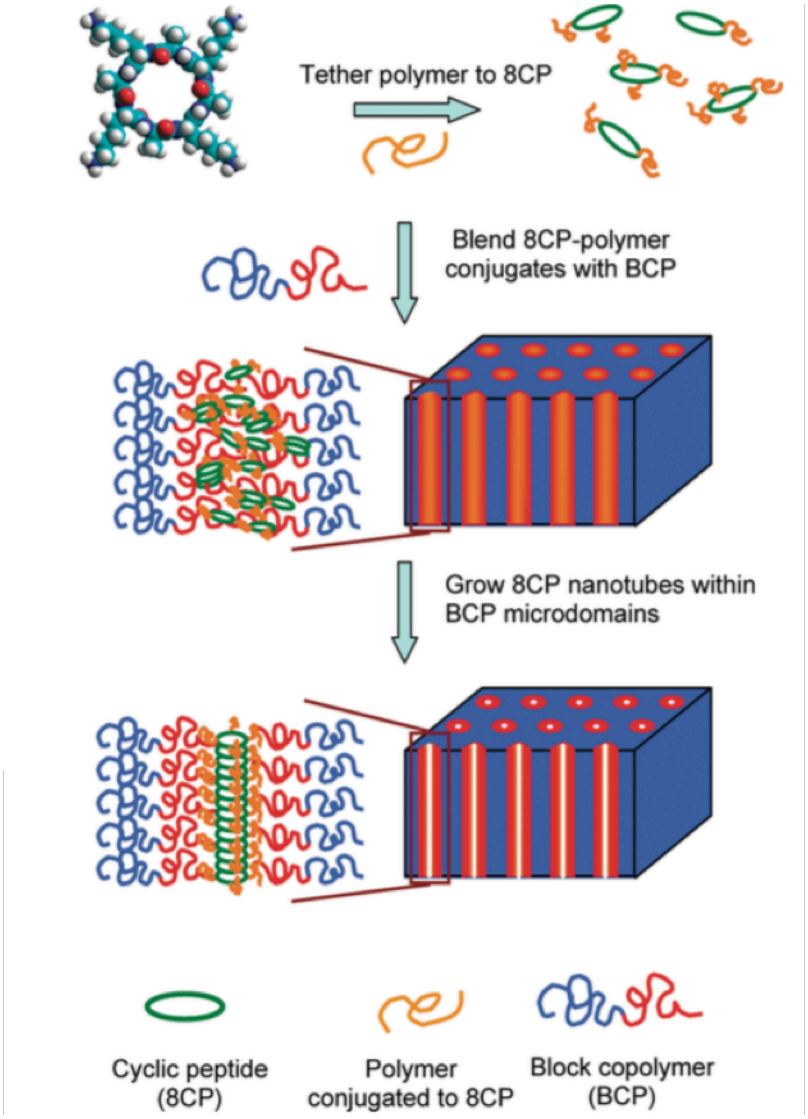

Figure 2.3. Schematic diagram of the sequence of synthetic steps of a CP/BCP composite membrane, as described by Xu et al. [48].

Other intensely tested applications for CPs are related to their electric properties. In a similar way as natural helical peptides, with well known electron transfer properties [49-51], it has been proposed that CPs could be used as "molecular wires", i.e. 1-D electron transfer structures, on nanoelectronic devices [52-57]. CPs are more stable than natural helical peptides, and easily assemble in 1-D structures, but are not electronically conductive enough to be of any use [54]. This was overcome by chemically manipulating the side-chains [55], with CPs thus serving as templating agents for the electronically active functional groups [52, 53]. Good optoelectronic properties have also led to the successful application of CPs in artificial photosynthetic devices [58]. Use of dendritic CPs enabled the synthesis of porous liquid crystals [59].

Macrocycles are a relatively common micropore-forming molecular architecture, and a few other macrocyclic microporous solids have been identified [60-63]. Xu et al. have used diacetylene macrocycles, self-assembled into columns via amide hydrogen bonds, as a CO_2 adsorbent [63]. The material retained crystallinity after solvent removal and displayed Type I adsorption isotherms, consistent with micropore adsorption. Together with the previously mentioned mass transport properties, this indicates CPs should be able to be used as bulk microporous solids. It would also be interesting to assess the influence the gating effect previously tested [18, 34, 36, 47, 64] in solution, could have on gas desorption hysteresis and separation selectivity.

2.2. Dendritic Peptides

Dendrimers, or cascade molecules, are three-dimensional polymeric macromolecules, with tree-like branches extending outwards from a multifunctional core [65-68]. Typically, their structure is interpreted as a sequence of layers (or generations) [69], with three components being distinguished in an n-generations dendrimer: the core (or root, generation 0), branching units (branched branches, generations 1 to n-1) and functional units (the last layer of branches, generation n). In solution, dendrimers usually take a globular structure, with functional units constituting a polyvalent outer surface. Dendrimers can be synthesised by: a) an iterative sequential multi-step reaction, where successive generations of branches are added to the original core molecule [70] (the divergent approach), or b) independent synthesis of each branch, sequentially merged from the nth to 0th generations, until all are linked to the core molecule (the convergent approach).

When a core molecule, chemically distinct from the branching units, is absent, the resulting branched molecule is called a "dendron". A dendrimer can be seen as a collection of dendrons linked through a core molecule. When several types of dendrons are present in the same molecule, the dendrimer is called "cascadane" [68].

The first materials combining peptides and dendrimers were peptide bond-containing dendrimers ("peptide dendrimers"). They have been extensively studied as drug and DNA delivery agents, in a wide range of biomedical applications, work that has been thoroughly reviewed before [70-73]. They were designed seeking to merge the water-solubility, biocompatibility and biodegradability of peptides (peptide bonds, in particular) with the stability and protein-like ligand selectivity and drug-delivery properties of dendrimers [70]. They are often used as "artificial proteins", due to the globular structure adopted in solution and the polyvalence shown by the peptidyl functional units. In particular, lysine-based dendrimers, since their discovery in 1988, by Tam [74], have been extensively used as multiple antigene peptide (MAPs) systems [75-78]. The molecular structure of two such dendrimers is shown in Figure 2.4. The amino group on the side-chain can form amide bonds, just like the main-chain terminal amino group, allowing the construction of branched structures using well-known peptide-forming synthetic paths [74, 79].

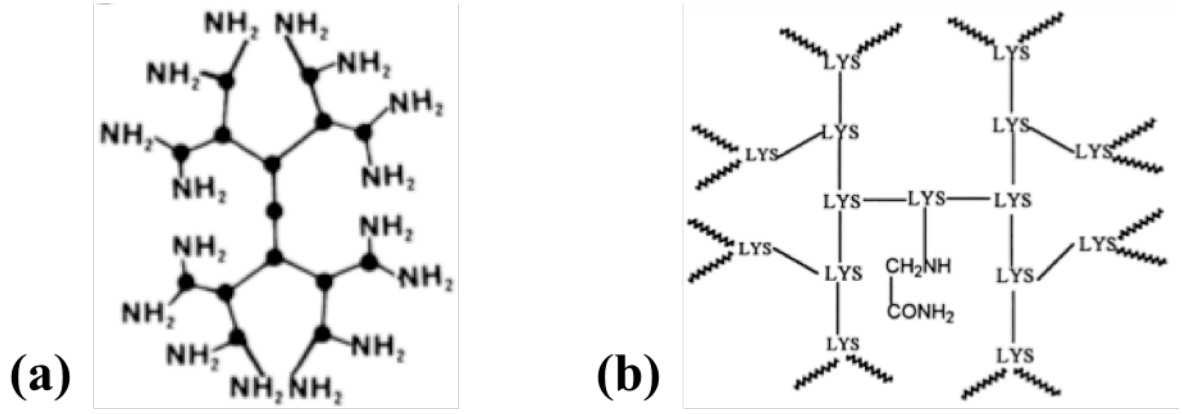

Figure 2.4. Peptide dendrimers. (a) Diagram of the original lysine dendrimer used by Tam (adapted from [74]). (b) Diagram of a lipid functionalised lysine dendrimer (adapted from [80]).

Dendryl-substituted dipeptides constitute another, more recent, type of material that synergistically combines the peptide bond and dendrimeric structures. These porous materials, stable in solution and solid phase, were first reported in 2004, by Percec et al. [81],

following on their research on column-forming dendrons [82]. A representation of a pore formed by dendritic peptides can be seen in Figure 2.5. Several enantiomers of Boc-Tyr-Ala-OMe were used, with a two-generation, benzyl ether-based dendron linked to the oxygen atom of the Tyr residue. They readily self-assemble in bulk and in solution [83], through thermal treatment. The resulting supramolecular polymer is structured by intermolecular hydrogen bonds and hydrophobic interactions between different dendrons. Heating causes two- and three-dimensional organization of the columnar assemblies, in the solid state, while, reversely, in solution, cooling is necessary to promote self-assembly. Careful annealing of solid samples allows formation of a crystalline (as the one shown in Figure 2.5) or fibrillar arrangement of the columnar supramolecular polymer [83]. X-ray diffraction analyses of these samples allowed the determination of crystal structure and, therefore, internal pore size and external diameter of the columnar assemblies. Internal pore diameters are usually within the 6-16 Å range [84, 85], but extension of the lower limit down to 2-3 Å seems easily viable. It has been observed that residue chirality can significantly influence pore size [86, 87].

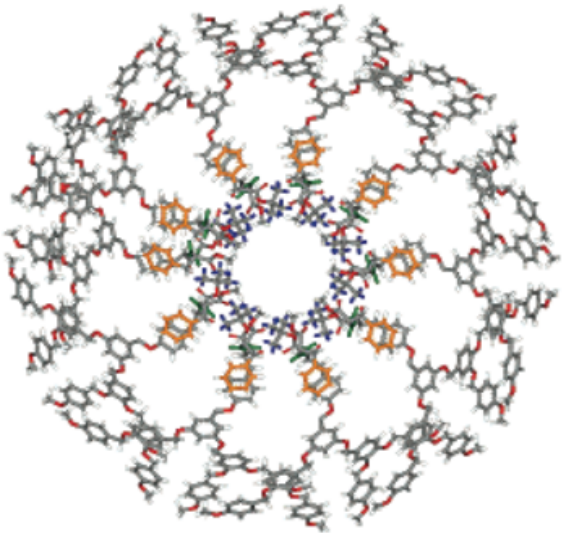

Figure 2.5. Pore, 9.6 Å-wide, observed in the crystal structure of the dendritic peptide (4-3,4-3,5)12G2-CH2-Boc-L-Tyr-L-Phe-OMe (adapted from [88]).

As represented in Figure 2.6, pores are formed by dendritic dipeptides as individual molecules pack consecutively in a helical fashion, with hydrogen bonds between dipeptide main-chains holding together the pore. Nonetheless, contributions from hydrophobic forces are also essential in stabilising the structure. The interior wall is constituted by the protective groups stemming from the dipeptide molecules' termini. The formed pore can be seen as a

supramolecular quasi-macrocycle, but displays few of the most interesting properties of covalent macrocycles, such as intrinsic microporosity. On the other hand, pore chirality [85] and, probably, radial framework flexibility are interesting characteristics of the material that are practically absent in covalent macrocycles. Pore-size control can be easily achieved by changing the protective groups of the dipeptide chain supporting the dendrons [84]. Unlike what would be intuitively expected, the bigger the protective group, the bigger the pore. This results from the greater difficulty of packing all the molecules, increasing the average distances between molecules and, thus, increasing pore size. However, this also increases the average distance of inter-chain hydrogen bonds making the structure less stable.

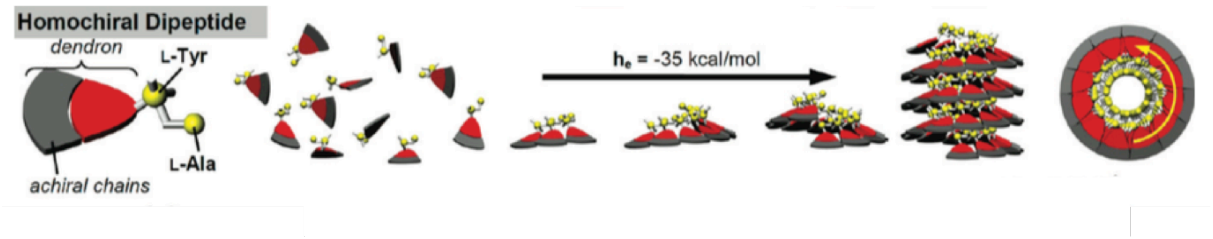

Figure 2.6. Schematic representation of pore-forming aggregation mechanism of dendritic peptides (adapted from [86]).

Results from solution phase proton permeation tests were presented by Percec et al. in the same article where the material was introduced [81]. The dendritic dipeptide nanotubes were allowed to self-assemble onto phospholipidic vesicles, serving as proton conductors in a pH-monitoring assay. Gramicidin was also used in a parallel assay, yielding comparable results. In similar experiments, Kaucher et al. have used nanotubes built from slightly modified dendritic dipeptides, with the benzyl group replaced by a naphthyl group [89]. Once again, protons were successfully transferred across the nanotubes, but assays with Li^+, Na^+ and Cl^- yielded negative results. The tube's internal diameter is (14.5 ± 1.5) Å, more than enough to allow the permeation of the hydrated form of these ions [90], being hard to understand what causes this ion selectivity. Furthermore, water transport across the nanotubes was also measured in independent osmotic pressure-driven experiments, based on measuring the volume of a unilamellar vesicle. Therefore, the rejection mechanism for the ions cannot involve water rejection. Further study on this issue could shed light on the rejection mechanism, which would be very interesting, as it could unfold a new "gate-keeping" strategy.

Solid phase adsorption or permeation experiments have not, to the best of our knowledge, been performed with these materials although this seems perfectly viable. Important properties such as pore size and inner wall chemistry can also be controlled through substitution of the non-dendron residue. [88] As with CPs, the issue of stability after co-crystallised solvent removal (when present) could be the main unknown to hinder their use as microporous solids.

2.3. Dipeptides

Large peptides and proteins form crystals with complex molecular structures, having several organisational levels. Amino acids, on the other hand, crystallise in simple, head-to-tail hydrogen-bonded chains. Small peptides form crystal structures sharing some aspects of both, being sometimes more akin to amino acids and others to proteins [91]. The discovery that hydrophobic dipeptides form porous crystalline frameworks resulted from the exploration of the crystal structures of small peptides.

Amino acids crystallise by the creation of parallel infinite head-to-tail hydrogen-bonded chains [91-93], with each of the three amino hydrogen atoms of a given molecule bonding to a carboxylic oxygen atom from three different other molecules. Amino acids with hydrophobic side-chains form segregated layers of hydrophobic and hydrophilic moieties. When the side-chain is able to form hydrogen-bonds, a somewhat more complex network may be created, although segregation of hydrophobic and hydrophilic moieties still occurs.

A representation of the typical crystal structure of an amino acid (valine, in this case) with an hydrophobic side-chain is shown in Figure 2.7. The layered segregation of the hydrophobic and hydrophilic moieties is clearly visible, both in Figure 2.7b and Figure 2.7c. The crystalline structure is stabilised by London forces between the aliphatic side-chains and hydrogen bonds between the amine and carboxylate groups. Although the focus is usually on the latter, the former can be just as important, or even more. However, as it is hard to quantify, it typically receives much less attention. This fact will become clear when discussing dipeptides.

The hydrophilic layer is formed by head-to-tail hydrogen-bonded chains of carboxylate and amino groups, while the isopropyl side-chains form the hydrophobic layer. Each molecule bonds via six hydrogen bonds to five other molecules, four lateral and one frontal (as shown

in Figure 2.7d through Figure 2.7f). The frontal molecule is bound by two hydrogen bonds, one involving the amino group and another involving the carboxylate group. The four lateral molecules surrounding each molecule are connected each by one hydrogen bond. Two sides are connected by each of the oxygen atoms (left and bottom of Figure 2.7c) and the other two sides are connected via the amine group.

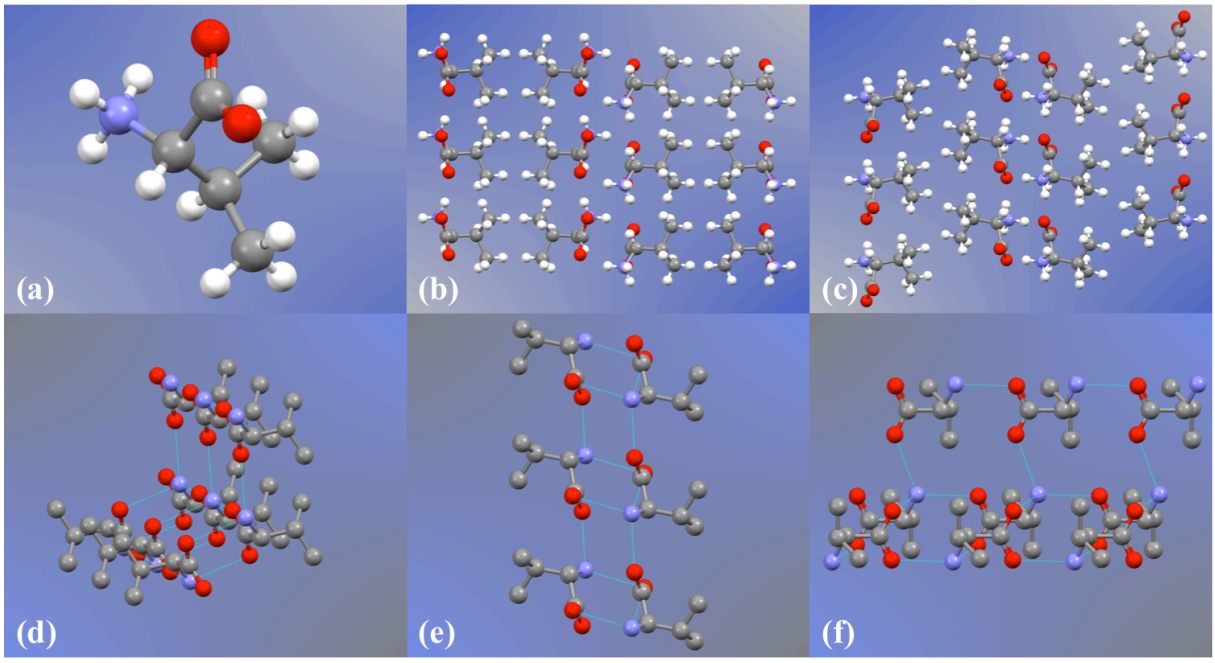

Figure 2.7. (a) Crystalline conformation of a valine molecule. (b) Crystal structure of valine viewed along the c-crystallographic axis. (c) Crystal structure of valine viewed along the a-crystallographic axis (frontal view of (b) is now the bottom view). (d), (e) and (f) are different views of the same representation of the hydrogen bond network in the crystalline structure of valine. Only nine molecules are represented. Hydrogen atoms not shown for clarity. Hydrogen bonds are represented as pale blue lines connecting nitrogen (blue) and oxygen (red) atoms.

Peptides (< 50 residues) and proteins (> 50 residues) are polymers of amino acids, and form far more complex crystal structures than single amino acids [94]. The basic supramolecular structures of both large peptides and proteins (the "secondary" structures) are the alpha-helix and the beta-sheet [94]. Representations of these structures are shown in Figure 2.8. Alpha-helices are peptide chains coiled on themselves, stabilised by amide hydrogen bonds, O···HN, with 3.6 residues per turn. Beta-sheets are parallel peptide chains stabilised by amide hydrogen bonds between the two chains.

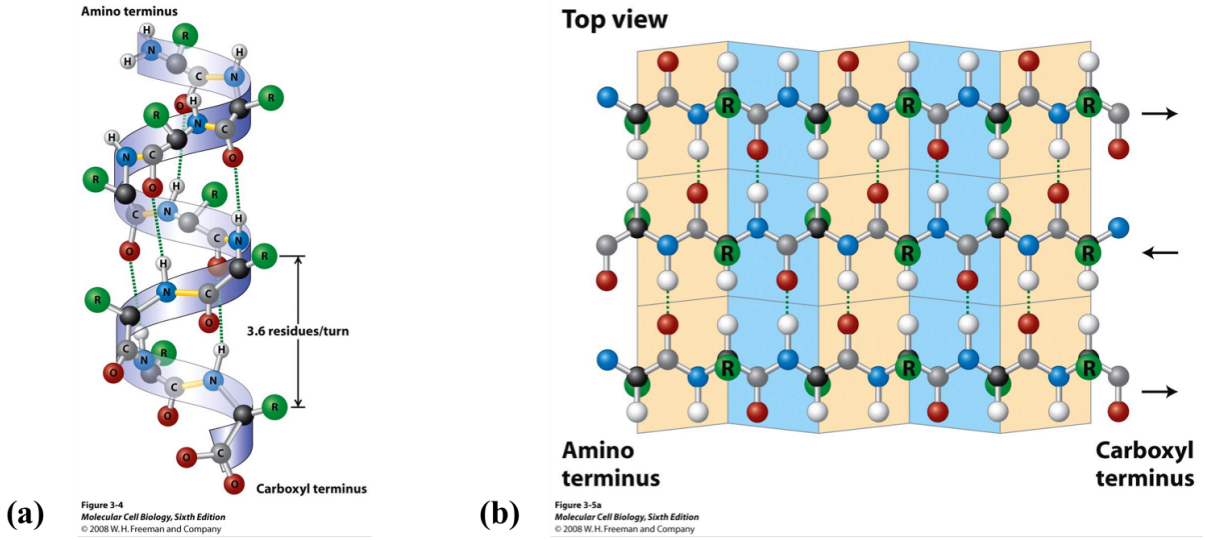

Figure 2.8. Representation of secondary structures of peptides and proteins. (a) Alpha-helix. (b) Beta-sheet. Hydrogen bonds represented as dotted green lines. Adapted from [95].

Unlike large peptides and proteins, in the structure of short peptides, the amino and carboxylate termini are fundamental in determining their crystal structure. The longer the peptide, the smaller the influence of these groups, as the relative importance of the functional groups in the side-chains and the amide groups increases. The structure formed by very small peptides is thus somewhere in between those of larger peptides and those of amino acids [93]. There is no cut-off at which peptides of a given size start forming alpha-helices and beta-sheets. The more hydrogen bonds involving the amide group there are, the more structures will emerge that are more and more like alpha-helices and beta-sheets.

The simplest dipeptide, glycylglycine, can form a crystal structure with a beta-sheet consisting of a single amide hydrogen bond [96]. As described below, and as has been summarised in Chapter 1.2, dipeptides with bulkier side-chains will not form these structures. Dipeptides cannot form alpha-helices, but tripeptides can have alpha-helix-like molecular conformations, and some tetrapeptides form full-fledged alpha-helices. For crystal structures of pentapeptides and above, alpha-helices are relatively common [93]. Tripeptide and tetrapeptide molecules can adopt many different conformations in a crystal structure [93], forming very complex three-dimensional hydrogen-bond networks. These will still exhibit separation between hydrophobic and hydrophilic moieties, in the form of columns or layers [93].

Dipeptides, on the other hand, due to the rigidity of the peptide bond, have basically only two possible molecular conformations. They are either in a parallel (side-chains pointing in the

same direction) or an antiparallel (side-chains pointing in opposite directions) conformation. As shown in Figure 2.9, Glycylglycine, lacking side-chains, adopts a crystal structure very much like that of glycine, only (as already mentioned) with an extra amide hydrogen bond connecting parallel molecules. Dipeptides with side-chains cannot pack with this structure, as the main chains are too separated from each other to form hydrogen bonds. An antiparallel conformation, where the third amino hydrogen atom is accepted by one of the side-chains, is the most common arrangement [97]. Alternatively, the third amino hydrogen atom may be accepted by co-crystallised solvent molecules, if they can function as an hydrogen bond acceptor. Structures such as the one shown in Figure 2.9, for valine, are made possible for dipeptides precisely if the dipeptide molecules have a parallel conformation and the cocrystallised solvent functions as a proton acceptor in hydrogen bonds [97]. Nonetheless, as discussed below, there is a class of pore-forming dipeptides displaying such a structure, although with columns, not layers (see Figure 2.12).

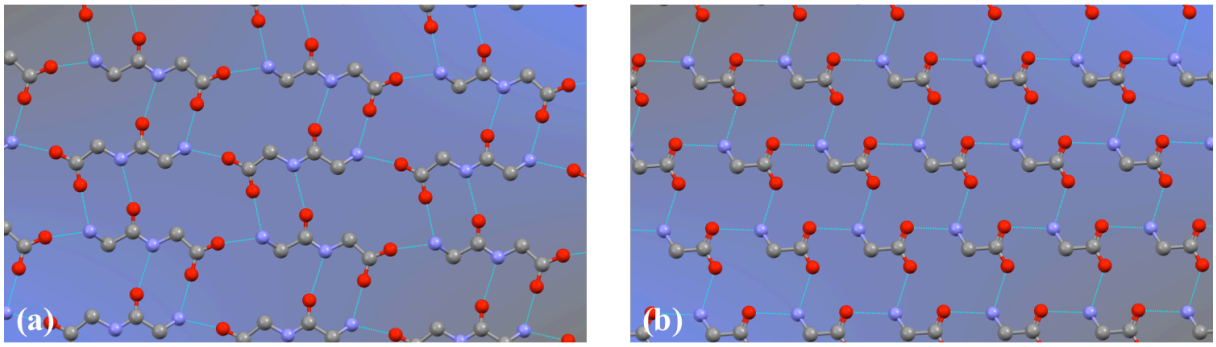

Figure 2.9. Hydrogen bond network in a sheet of the crystal structure of (a) Glycylglycine and (b) Glycine. In both cases, the crystal structure is made by parallel sheets such as those represented, bound by hydrogen bonds between the amine and carboxylic groups.

It was curiosity regarding which crystal structure would be favoured if neither the side-chain or solvent hydrogen bond acceptor was available that led C. H. Görbitz to investigate hydrophobic dipeptides [13]. The first report on microporous dipeptide crystals was presented by Görbitz, in 1996 [13], in an article on the crystal structure of Valylalanine (VA). In the crystal structure of this dipeptide, the packing problem is resolved by the formation of a complex three-dimensional network of hydrogen bonds, that does away with the head-to-tail configuration.

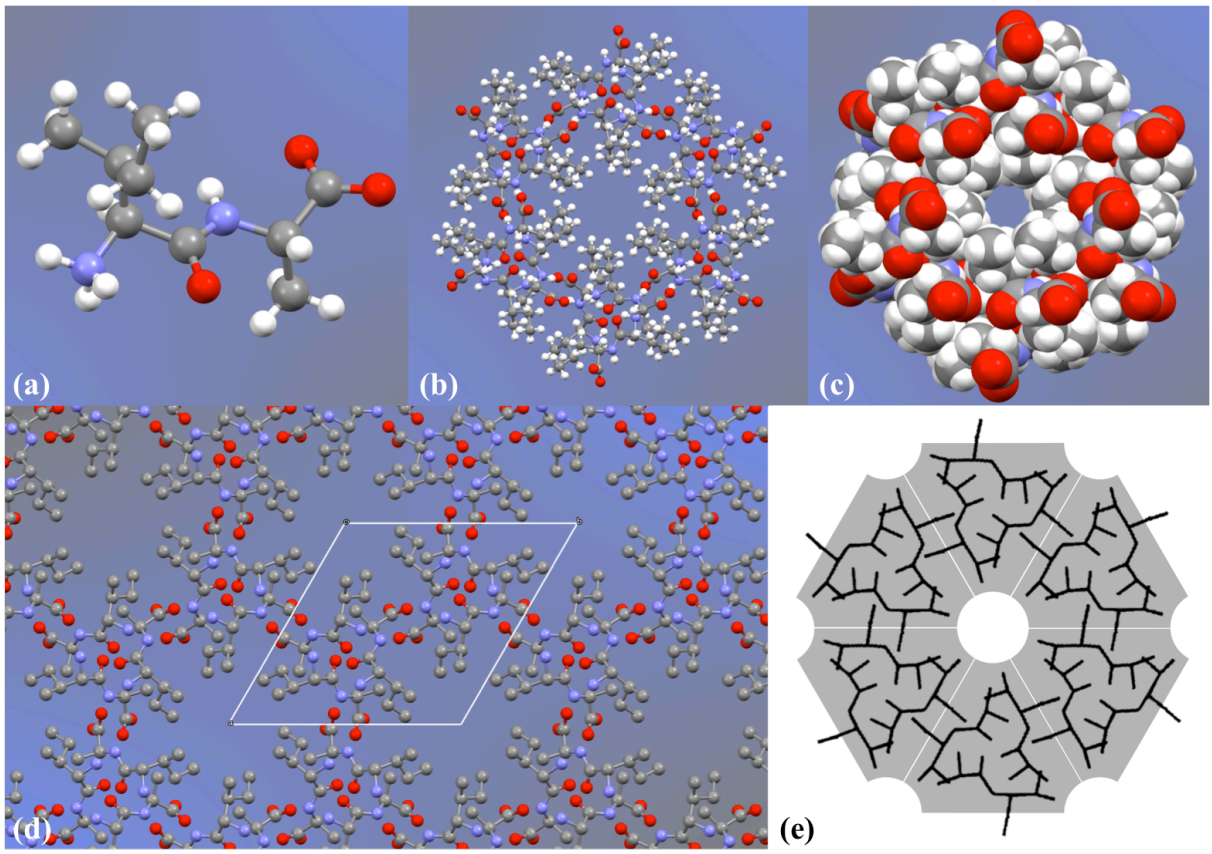

Figure 2.10. (a) Representation of an IA molecule, in its crystalline conformation. (b) Crystal structure of IA, as seen from the c-crystallographic axis. (c) Spacefill representation of (b), with the empty space remaining in the centre clearly visible. (d) Representation of the crystal structure of IA (VA-class) as seen from the c-crystallographic axis, with a unit cell represented. Hydrogen atoms omitted for clarity. (e) Stylised representation of the triangular prisms forming the crystal framework (adapted from [98]). Hydrogen bonds not represented.

Two of the three amino hydrogen atoms still bond with carboxylic oxygen atoms, in this case from two different molecules, as in head-to-tail bonding. However, the third bonds with an amide oxygen from yet another molecule, so it is no longer appropriate to call this arrangement "head-to-tail" bonding. Some secondary hydrogen bonds are also formed between the amide NH and amide oxygen atom (of two different molecules). The resulting hydrogen bond network is depicted in Figure 2.11b. Segregation of the hydrophobic and hydrophilic moieties occurs by the formation of hydrophobic columns surrounded by the three-dimensional hydrogen bond network.

It was later discovered that many hydrophobic dipeptides crystallise in this fashion even if from an aqueous solution, where water is available to co-crystallise [97]. Those that do not crystallise form amorphous aggregates, not other crystal structures, showing the stability of the crystal structure. Although similar columnar structures had been discovered previously

[99, 100], VA was the first where the hydrophobic columns were identified as having "empty central channels" [13]. These emerge due to the side-chains not being big enough to completely fill the cross-sectional area of the hydrophobic column formed.

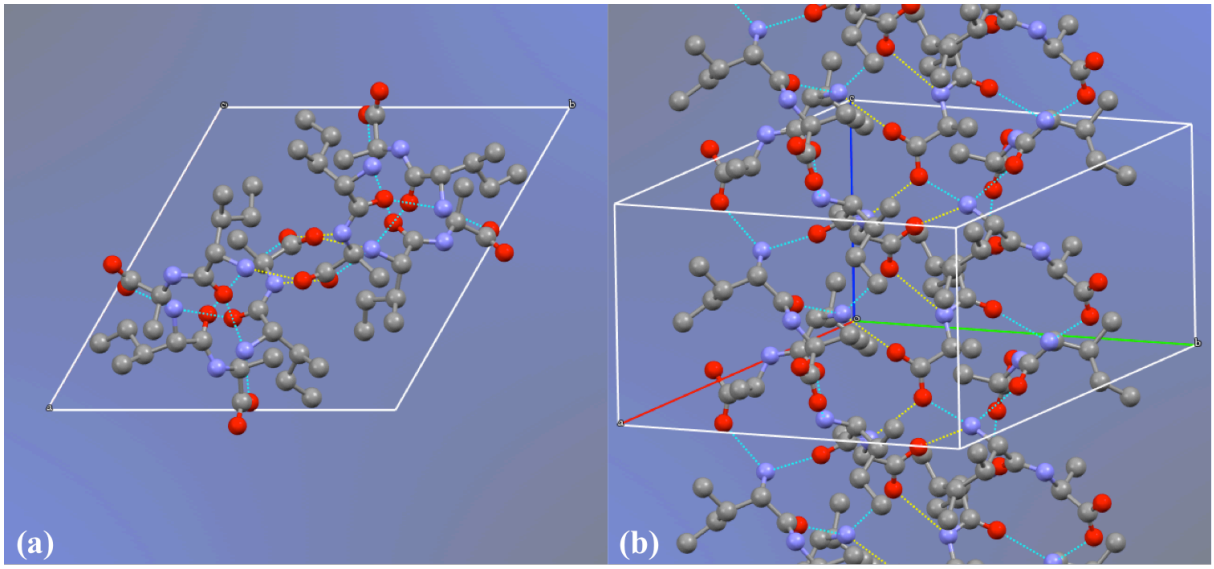

Figure 2.11. Representations of the crystal structure of VA-class dipeptides (IA in this case), with hydrogen bonds shown in light blue and yellow. The figure is one unit cell-wide, one unit cell-long and several unit cells-high. Light blue hydrogen bonds connect molecules in the same triangular column, while yellow hydrogen bonds connect different triangular columns. Hydrogen atoms omitted for clarity.

VA came to be only the first of several channel-forming hydrophobic dipeptides discovered by Görbitz. Initially, crystals big enough to be used in single-crystal X-ray diffraction (SC-XRD) were only produced through slow diffusion of alcohols (especially 2-propanol) into an aqueous solution of the dipeptide, typically resulting in layered alcohol solvates [101-103]. Another six hydrophobic dipeptides with crystal structures similar to that of VA [104] were discovered only in 2003, by using similar techniques. Due to this similarity of the crystal structures and VA's precedence, this was called the VA-class of microporous dipeptides. Peptides from this class share a common crystal structure, such as the one that can be seen in Figure 2.10, with only side-chains and pore sizes varying.

The view along the c-crystallographic axis of the VA-class crystal structure (Figure 2.10b through Figure 2.10d) shows a unit cell composed of two triangular motifs, with amide oxygen atoms at the centre of each. The triangular shape is seen only from the perspective of the c-axis and is created by the existence of three molecules per unit cell sharing the same

conformation (for each of the two prisms), but rotated around a central axis perpendicular to the a-b plan, and translated in the c-axis, forming a spiral.

VA-class structures can thus be seen, as exemplified in the diagram of Figure 2.10e, as a set of spiralling triangular motifs, aggregated to form a framework of equilateral triangular prisms, with pores located at the edges of the prism. The different prisms are connected by hydrogen bonds between the nitrogen and oxygen-containing functional groups in the molecules.

Figure 2.11 shows the hydrogen bond network of the VA-class crystal structure. Hydrogen bonds between molecules in the same prism are shown in blue, while hydrogen bonds between different prisms are shown in yellow. Behind the apparent chaos of the three-dimensional hydrogen bond network, it is possible to observe systematically ordered components. The amide oxygen atoms are all close to the central axis of each prism. Each of them forms a single hydrogen bond, to an amino group in another molecule in the same prism. The amide NH also forms a single hydrogen bond, to a carboxylate oxygen atom in another prism. Thus, the three amide NH in a prism, per unit cell, bond with each of the other three prisms surrounding it. The amino and carboxylate groups in each molecule bond with molecules both from the same prism and from two other prisms. The amino group forms three hydrogen bonds; one with a amide oxygen from the same prism, one with a carboxylate oxygen atom from a different molecule in the same prism (which is also bound to a NH from a different prism) and one with a carboxylate oxygen atom in another prism (different from the one the amide NH from the same molecule is bonding). The two oxygen atoms in the carboxylate group form three bonds, one atom bonds with an amine in the same prism and with an amide NH in a different prism, while the other bonds only with an amine in a different prism. Each molecule thus forms eight hydrogen bonds, three with molecules from the same prism and five with molecules from a different prism. This means there are fifteen hydrogen bonds per unit cell between one prism and the three other prisms around it, five between any two prisms.

In 2001, one of the first articles resulting from Görbitz's systematic study of hydrophobic dipeptide crystal structures reported the discovery of four channel-forming dipeptides with a different pore structure from that of VA [105]. When crystallising the four dipeptides containing Leucine and Phenylalanine, LL, LF, FL and FF, it was discovered that they crystallise in a completely new way, forming hydrophilic columns, instead of the hydrophobic columns of the VA-class. The four dipeptides have rather different structures and space

groups, with the only common feature being the formation of water-filled, unidirectional channels across the crystallographic c-axis, with pore walls being formed by main-chains of dipeptide molecules with parallel conformation. Co-crystallisation of water is possible due to the hydrophilic interior of the pores, which does not occur on the VA-class. Named after its member with the biggest pore, diphenylalanine (FF), this is the so-called FF-class of hydrophobic dipeptides.

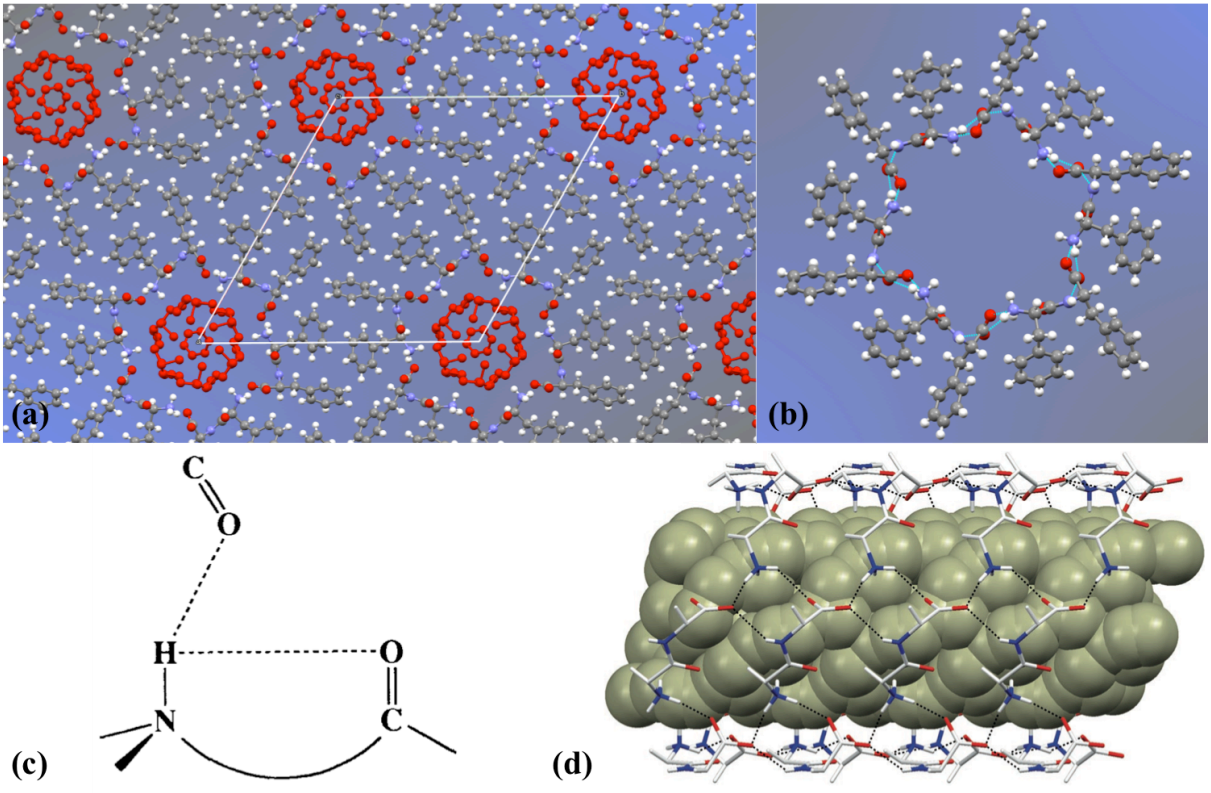

Figure 2.12. (a) Crystal structure of FF, as viewed from the c-crystallographic axis, with co-crystallised water. (b) A single pore, with hydrogen bonds shown in light blue. (c) Example of inter and intramolecular hydrogen bonds involving the amine group of a peptide (adapted from [93]). (d) Perpendicular view of a pore formed by FF, with hydrogen bonds represented as black dotted lines. Side-chains omitted for clarity (adapted from [97]).

Tryptophylglycine (WG), the crystal structure of which was discovered in 2000, by Emge et al. [106], would later also be included in this category. Two dipeptides later studied by Görbitz, IL [107] and FW [108], also crystallise in the same fashion and thus came to be included in the FF-class. The main-chains of the dipeptide molecules form a two-dimensional network of hydrogen bonds, curled-up on itself, forming a tube with a circular/hexagonal cross-section (see Figure 2.12). The side-chains point outward from the tube, separating the

different main-chain hydrogen-bonded networks from each other. Thus, FF-class crystals can be seen as ordered aggregates of individual nanotubes, held together by hydrophobic interactions between the bulky side-chains. These interactions are, in fact, determinant to the creation of FF-class structures, in place of the VA-class structure, since side-chain size is the only difference between the compounds in both classes. The fact that IL and LL form this kind of structure shows that aromatic interactions are not central to the stabilisation of FF-class crystal structures.

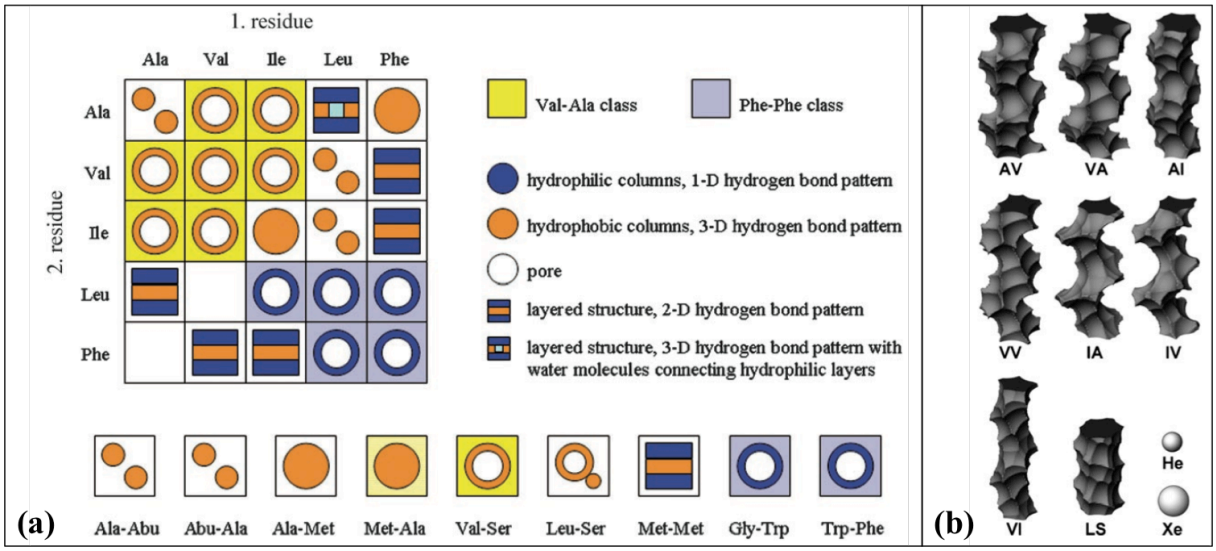

Figure 2.13. (a) Diagram showing the crystal structure of different dipeptides. (adapted from [97]). (b) Pore morphology of VA-class and LS crystals, represented with He and Xe atoms. (adapted from [109]).

The hydrogen bond network of FF is shown in Figure 2.12b and Figure 2.12d. Each molecule forms one hydrogen bond with each of the six molecules surrounding it in the two-dimensional hydrogen bond network. Three bonds involve the carbonate group, one with the amide NH and two with the amine group. Although not shown in Figure 2.12d, the amide oxygen atom is probably forming an hydrogen bond with the methylene group in front of it [13, 93]. It is also possible that the oxygen atom is involved in an intramolecular hydrogen bond with the amino group [93], as shown in Figure 2.12c.

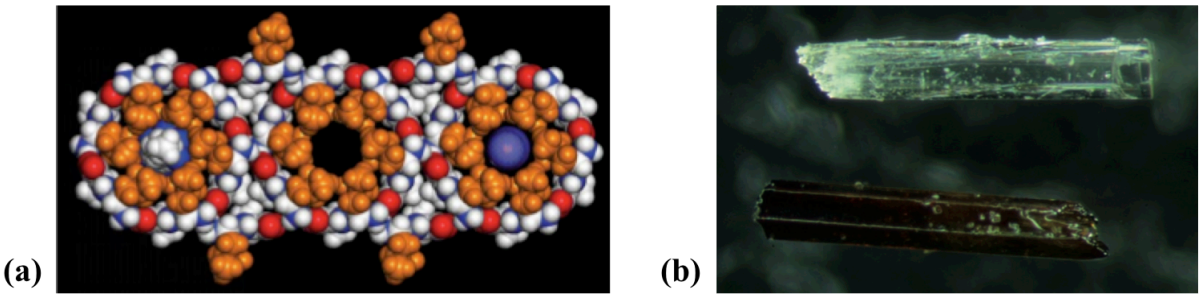

Figure 2.14. (a) Structure of Leu-Ser crystal, pores with acetonitrile (left), empty (center) and iodine (right). (b) Empty and iodine-filled Leu-Ser crystals. Adapted from [110].

There are thus two main classes of porous peptide crystals; the VA-class, having hydrophobic pores in the 0.37-0.50 nm range, and the FF-class, having hydrophilic pores in the 0.32-0.92 nm range [97]. It has been suggested [97, 104] that pore wall chemistry could be modified by chemical functionalization of the side-chains (VA-class) or main-chains (FF-class). It should be noted, however, that this approach includes the danger of changing crystal structure if it involves covalently bonding the desired functional groups to the original molecule. As the differences in VA-class and FF-class crystal structure show, in these materials crystal structure is very sensitive to molecular structure. Figure 2.13a shows that simply moving the location of a single methyl group in a side-chain (between isoleucine and leucine) can changes the crystal structure of dipeptides. If the pores are big enough, pore functionalisation would be far more easily achieved through irreversible adsorption of functional groups after crystallisation (for example, by soaking). This approach would thus apply mainly to FF-class dipeptides, as the pores of VA-class dipeptides are so small that any adsorbed compound effectively blocks them.

In 2005, another dipeptide with hydrophobic pores, but not sharing the crystal structure of the VA-class, LS, was reported [111], widening the range of porous dipeptide crystals. Although possessing a side-chain with an alcohol group, and thus not being a “hydrophobic dipeptide” strictly speaking, a peculiar organisation of the hydrogen bond network leads to the formation of a crystal framework with hydrophobic pores, with the leucine side-chain forming the pore wals. The resulting crystal structure is different from that of the VA-class dipeptides, but forms pores very much like those of VA-class dipeptides. The analysed crystal was able to withstand solvent substitution (Figure 2.14), from the original co-crystallised acetonitrile, through the guest-free structure after drying for two days, to an iodine-complexed structure after soaking.

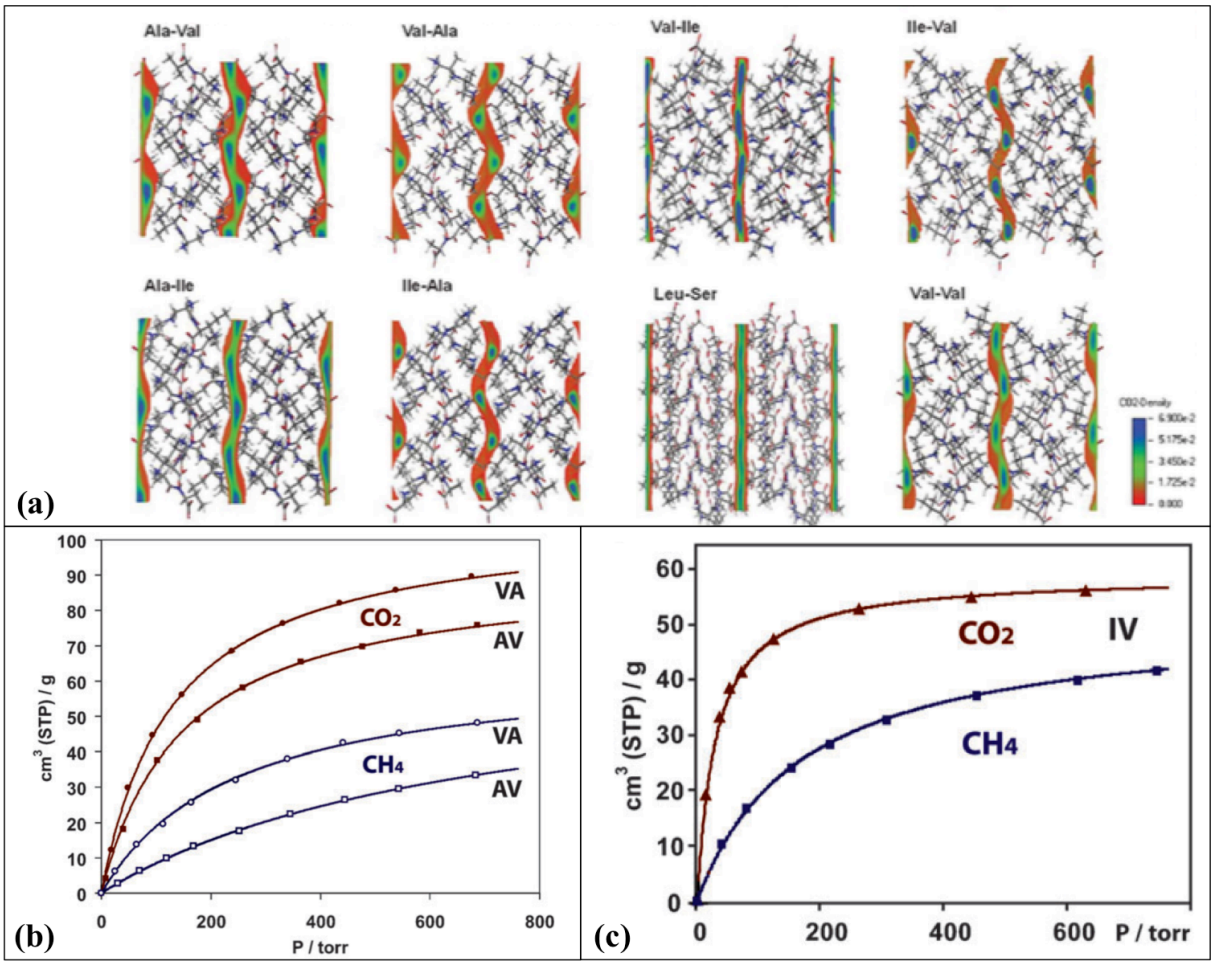

Figure 2.15. (a) Representation of zones of preferential adsorption in VA-class dipeptides and LS, as determined from Grand Canonical Monte Carlo simulations (adapted from [112]). (b) Adsorption isotherms of CO_2 and CH_4 in VA and AV, at 195 K (adapted from [113]). (c) Adsorption isotherms of CO_2 and CH_4 in IV at 195 K (adapted from [113]).

This was not the first time guest substitution was observed in these materials. In 2002, Görbitz reported [98] that an AV crystal, synthesised by acetonitrile diffusion into an aqueous solution of the dipeptide, could undergo successive solvent substitution cycles, with different solvents. With 2-propanol, the pores are greatly deformed, trapping the solvent molecules inside the pores, thus forming a clathrate. In 2004, Soldatov et al. reported successful Xe adsorption on Ala-Val and Val-Ala in an article arguing that dipeptide crystals could be used as microporous materials [114]. These early results were even more significant due to the pore expansion that had to take place to allow adsorption to occur, showing great framework flexibility. This property was further investigated and confirmed in a 2006 article [109], this time for all VA-class dipeptides. By using X-ray crystallography and NMR spectroscopy, it

was also possible to determine pore size and helicity and internal pore morphology. Results from this article were used in Table 1.2, from Chapter 1.2.

Recent experiments confirmed the capacity these materials have to adsorb and transport gases with small molecules [112, 113, 115] proving they can be used as adsorbents. Comotti *et al.* have used AV, VA, IV and VI as adsorbents of CO_2, CH_4 and H_2, observing high and fully reversible adsorption for all gases. Some of these results for CO_2 and CH_4 are shown in Figure 2.15b and Figure 2.15c. The authors obtained sorption selectivities of 3.5-5 for CO_2/CH_4 using IV, Figure 2.15c. It was also found that IV has a particular affinity for hydrogen, adsorbing 0.5 mol / mol of IV at 77 K and atmospheric pressure. In a follow-up study, in 2013 [112], the same authors showed that CO_2 and also N_2 adsorb in all crystalline dipeptides of the VA-class (plus LS) at room temperature. As expected, CO_2 adsorbs much more than N_2. GCMC simulations and NMR experiments showed that, for most dipeptides, CO_2 adsorption is essentially localised (Figure 2.15a). Only in the straight and large pores of LS, is adsorption almost perfectly distributed. Taking advantage of the high CO_2/CH_4 adsorption ratios (selectivities), the authors performed breakthrough experiments with equimolar CH_4/CO_2 mixtures, using VI, IV and AV as adsorbents. Using VI, an exit stream with up to ~ 3:1 CH_4/CO_2 ratios could be obtained.

Another potential use as adsorbent was put forth by Afonso *et al.* [115], by showing that some VA-class dipeptides display Ar/O_2 selectivity. This is a rare characteristic, sought for the production of O_2 from air by adsorption-based separation processes. Testing VI, IA, IV and VV (the four VA-class dipeptides with the smallest pores), the authors discovered that all display Ar/O_2 positive selectivity. It was also observed that selectivities decrease with increasing pore size, indicating this factor is central to the observed effect.

The properties observed in these studies are consistent with those of classical hydrophobic solids, such as pure silica zeolites and activated carbon, with the exception of the anomalous Ar/O_2 selectivity. The low adsorption of N_2 when compared to O_2 and Ar is also observed in MOFs, but completely different from those of zeolites. N_2 probably has much higher affinity to organic chains than to the Si-O-Si chains of zeolites.

FF-class microporous crystals have never been tested as adsorbents, probably because the co-crystallised water is difficult to remove, especially the innermost layer. In dipeptides with very small pores, it is questionable if it will even be possible to remove any of the co-crystallised water. The work of Amdursky et al. [116, 117] suggests the FF crystal structure

undergoes an irreversible phase transition when heated to 150 ºC, creating a cyclic compound with a completely different crystal structure.

Although significant hopes have been placed on peptide-based solids to work as smart materials for a number of applications [114], they have yet to show any of the expected properties, in an analogous way as, for example, MOFs have [118, 119]. It would be interesting to see what could be achieved by bringing together the pore-size-based sieving selectivity of VA-class dipeptides and the "gate-keeper" functionality predicted by García-Fandiño *et al.* [37] for peptide macrocycles, where the functional groups on the rim of the tube entrance determined which species' molecules were able to enter it. This would be a first step in mimicking the successful combination found in biological transmembrane channels, which yield nearly single-species specificity without compromising flux [3].

A 2007 study by Sopher et al. [120] discussed the integration of FF "peptide nanotubes" on micro-fabrication lithographic processes. Some of these structures are probably of crystalline nature [121] and provide good indicators for effective crystal stability during processing. The study confirmed FF crystals do not withstand hydrophobic solvents and are etched using oxygen plasma. They are also unable to retain their structure above 100 ºC, and should not be used above 85 ºC. They do, however, not only resist contact with water, but are also able to permeate aqueous solutions. Although only slightly, FF is hydrosoluble, making this quite a remarkable result. Although their slow water solubility kinetics have been observed before [97], it is possible that partial encapsulation in a hydrophobic polymer such as PDMS stabilises the structure even more. This stabilisation effect should be further investigated, since it opens up the possibility of using microporous peptide crystals with all sorts of solvents and reagents previously thought incompatible with them, whether this happens with full or partial encapsulation.

FF is also supposed to be able to form "fibrils", extensively studied by Gazit et al. [120, 122-124]. However, there has never been any direct evidence that "fibrils" with pores tens of nanometers-long, as originally claimed [122], are produced by FF. The best evidence available indicates that FF dipeptides assemble into fully crystalline structures, possessing unidimensional micropores, as those originally reported by Görbitz, [105, 125], and also that these crystals may, sometimes, form pores a few micrometers-wide [117], as shown in Figure 2.16.

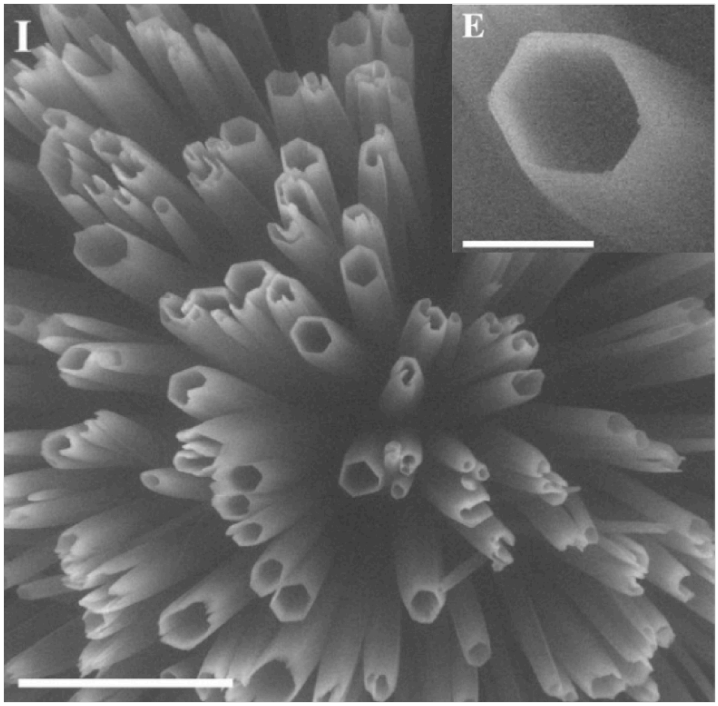

Figure 2.16. Electron Microscopy photographs of FF PNTs grown by rapid water evaporation from an aqueous FF solution. The inset shows a zoomed-in view of an individual PNT. The hollow crystals are clearly visible. The white scale bar is 20 μm long for the main image and 2 μm for the inset (adapted from [117]).

2.4. Peptide-Based MOFs

Although previous work had been done with amino-acids [126], peptide-based metal-organic frameworks (metal-peptide frameworks, MPFs) constitute a relatively recent field, whose uniqueness is still being explored [14, 127-129]. They are not structurally and functionally different from other MOFs, but peptides' high structural diversity, conformational flexibility and intrinsic chirality raised hopes of unwinding properties such as gated-adsorption and chiral recognition [128]. Metal cations are coordinated by oxygen and nitrogen atoms on the peptides, present, at least, on the amino, carboxylic and amide functional groups of the peptide [14, 129]. Initial works on the subject intended to use peptide-metal complexes as models for more complex protein-metal complexes, ubiquitous in the natural world and whose structure is hard to determine [127]. It was not long before these complexes were identified and studied as MOFs [14, 128], resulting in a variety of 2D and 3D-porous architectures.

In 2010, Matthew Rosseinsky and co-workers reported [129] an MPF where tetrahedral zinc ions coordinate GA linkers in $Zn(GA)_2$, resulting in bilobal pores with Ala side-chains

pointing torwards the pore interior, as can be seen in Figure 2.17. Each peptide molecule is linked to two zinc ions, forming a grid-like layer of the coordination polymer. Different layers are connected through hydrogen bonds between the amide groups of each dipeptide. CO_2 adsorption experiments were performed, yielding very promising results. In particular, a pronounced gating effect, resulting from a conformational shift on the C-C bond of the dipeptide main-chain, was observed, a phenomenon typical of pore-forming proteins.

The MPF was synthesised in a liquid mixture, with 90 % methanol and 10 % water. These solvents were co-crystallised with the solid, occupying the pores in the structure shown in Figure 2.17a. Following desolvation, the pores collapse upon changes in the torsional angles of the two residues, bringing the methyl side-chains closer together, and eliminating the solid's porosity. This is not the first time guest-sensitive porosity has been observed for MOFs. The well-known MIL-53 displays a framework with a so-called "breathing" behaviour, contracting and expanding according to the molecular size of the adsorbed species [130]. However, the behaviour of MPF $Zn(GA)_2$ is a bit more complex. Its desolvated structure is uncapable of adsorbing H_2 and N_2, even at temperatures as low as 77 K. With regards to these species, the material is, effectively, non-porous.

On the other hand, CO_2 adsorption and H_2O and CH_3OH resolvation are very easy to accomplish, almost as if the structure opens specifically for these species. CO_2 adsorption is accompanied by gradual pore opening, increasing proportionally to the amount of adsorbed CO_2. This mechanism is controlled by (also gradual) changes in the torsion angles of the dipeptide linkers. Although there is a pore-opening minimum pressure for CO_2 adsorption, the selection mechanism is thought to be associated with the establishment of polar interactions between CO_2 molecules and the amide bonds, thus stabilising the mixture. The inexistence of these bonds in H_2 and N_2 makes the sorbed state thermodynamically unfavourable. The small energy landscape associated with the structure's conformational shift makes such a mechanism possible, allowing small differences in pore wall-molecule interactions to determine pore opening or closing.

The Rosseinsky group has since continued their work on MPFs. Using peptide linkers only slightly different from GA, the group observed drastic changes in the properties of the porous framework [131, 132]. This effect is reminiscent of the dramatic changes a single-point mutation can create in the structure and functional properties of proteins. It is precisely this kind of structure-function relation that was originally hoped for, when deciding to use peptides as linkers in MOFs.

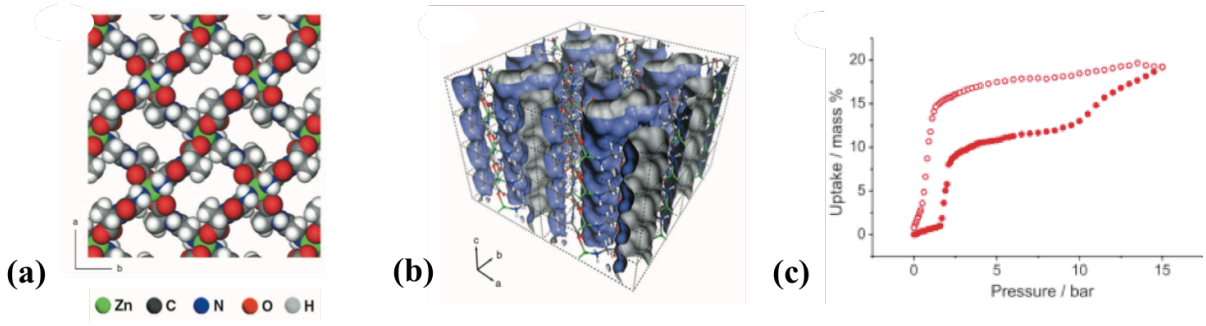

Figure 2.17. (a) Structure of the MPF $[Zn(GA)_2]$ viewed along the c-axis. (b) Three-dimensional perspective view of the pores formed by $[Zn(GA)_2]$. (c) Sorption and desorption CO_2 isotherms (closed and open circles, respectively) at 273 K. Adapted from [129].

Using GT instead of GA, the authors were able to synthesise $Zn(GT)_2$, a compound whose crystal structure displays a rigid framework with permanent porosity [131]. The crystal structure of $Zn(GT)_2$ is significantly different from that of $Zn(GA)_2$. The zinc cation now forms six coordination bonds, instead of four. However, because two peptide linkers per node bond twice to Zn, through the amine and the amide groups, the linker to node ratio remains 2:1. The coordination framework formed is now three-dimensional, instead of two-dimensional, but the pores are still one-dimensional. The side-chains do not point directly inwards, only the methyl substituent from the threonine side-chain does, with the hydroxyl groups forming hydrogen bonds with other N and O containing groups. These extra hydrogen bonds and the higher coordination number of zinc are probably at the root of the increased stability of the framework.

$Zn(GT)_2$ adsorbs CO_2 and CH_4, in a ratio of 14:1 (w/w), at 195 K, a relatively normal result. The authors attribute this to the polar nature of the pores, which potentiates strong interactions with the large quadrupole moment of CO_2. CH_4, having a null quadrupole moment is not as strongly adsorbed. The authors also claim that N_2 is virtually unadsorbed. Although they did not perform an experiment at 195 K, as for the other gases, a 77 K test did, indeed, reveal some N_2 adsorption.

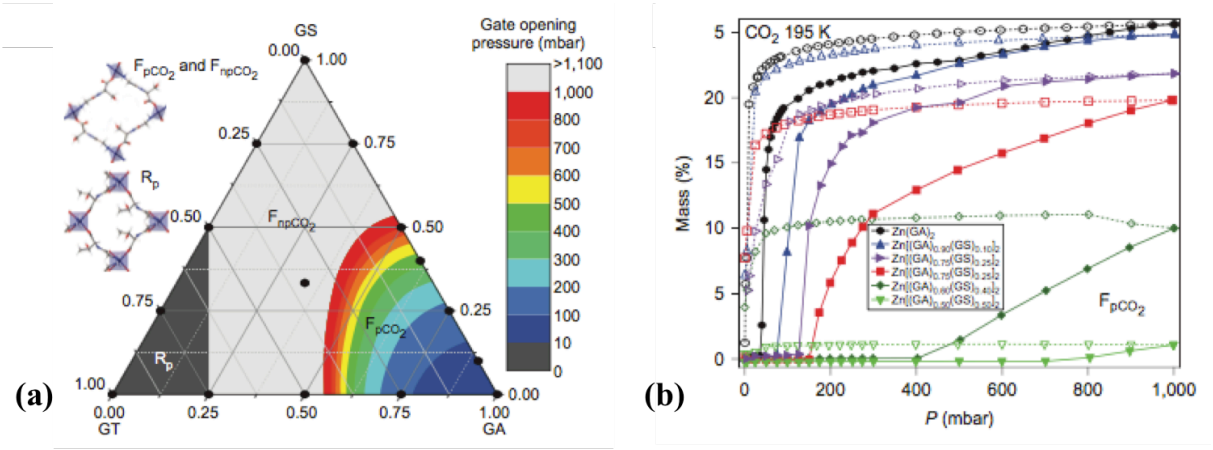

Figure 2.18. (a) Phase diagram for crystalline solid mixtures of the three Zn-containing MPFs tested by the Rosseinsky group. (b) CO_2 adsorption isotherms for solid mixtures with the formula $Zn[(GA)_x(GS)_y]_2$. Adapted from [132].

The authors then tested $Zn(GS)_2$ [132], which is isostructural with $Zn(GA)_2$. The inward directed side-chains now have an hydroxyl group, changing pore chemistry and adsorption properties. As in $Zn(GA)_2$, the framework of $Zn(GS)_2$ opens and closes depending on the presence or absence of adsorbate molecules. However, unlike $Zn(GA)_2$, it only opens to polar molecules, capable of interacting strongly with the hydroxyl group inside the pore. Thus, not only N_2 and H_2 are not adsorbed, as with $Zn(GA)_2$, but also CO_2 cannot enter the pores. However, resolvation with methanol is achieved easily, showing that the structure is not permanently closed, but opens or closes to specific chemical species. Once again, this behaviour is typical of biological systems, but almost never found in synthetic nanomaterials.

In this paper, the authors also reported the study of the properties of solid crystalline mixtures between $Zn(GA)_2$, $Zn(GS)_2$ and $Zn(GT)_2$. Only one tricomponent mixture was tested, with equal parts of the three linkers, having been observed it adopted the $Zn(GA)_2$ conformation, of opening and closing pores. Binary mixtures incorporating threonine may have $Zn(GA)_2$-like or $Zn(GT)_2$-like structure, depending on the relative proportions of the linkers. $Zn((GA)_x(GT)_y)_2$) mixtures are isotructural with $Zn(GA)_2$ for GT proportions inferior to 25 %, showing this is a much more stable conformation. $Zn((GS)_x(GT)_y)_2$) mixtures are isotructural with $Zn(GA)_2$ for GT proportions inferior to ~50 %, as shown in Figure 2.18a. The hydroxyl group in the serine side-chain stabilises the open structure for higher GS proportion than with GA.

For GA- and GS-containing binary mixtures, crystal structure is independent of linker proportion. Conversely, CO_2 adsorption is highly dependent on structure, given the very different behaviour of both pure component adsorbents. As GS proportion increases, the porous solid requires a higher pressure to start adsorbing and exhibits progressively lower affinity to CO_2. For GS proportions above 60 %, the material is essentially closed to CO_2 molecules (Figure 2.18).

Also from the Rosseinsky group, another zinc-based MPF was reported [133], containing imidazole and forming a crystal structure akin to that of a zeolitic imidazole framework (ZIF). The resulting three-dimensional structure of the coordination crystal has unidimensional pores 0.5 nm wide. Both the zinc cation and the peptide form four coordination bonds, all with diferent cations/peptides, resulting in a peptide to metal ratio of 1:1. The peptide, carnosine (ß-alanyl-L-histidin), possesses a beta amino acid residue that confers it extra configurational flexibility. The material is stable in water and organic solvents, but its crystal structure is dependent on the guest. Due to the conformational flexibility conferred by ß-alanyl, adsorbed water is able to form a chain of hydrogen bonds that deforms the pores relatively to adsorption of other species.

Another recent study [134] has reported two MPFs co-crystallised with water, where it is not possible to remove the water molecules from the cavities they occupy in the crystal structure. Thus, these two MPFs, are effectively non-porous. There have also been many other cases where, contrary to the claims of the authors, the porous MOFs discussed do not have peptide linkers [135-137].

2.5. Conclusions

A wide range of applications based on microporous solids constitute today a stalwart foundation of the chemical industry, ranging from adsorption based separation processes to catalysis, and, more recently, membrane processes. Many of the new applications envisioned for porous solids require a tight control over very specific material properties. A “bottom-up” approach to doing this involves controlling the chemical nature of the building blocks of the material, thus controlling its morphology and structure. Supramolecular porous solids are one of the most intensely studied alternatives to the creation of such materials, due to their well-known conformational flexibility and controllable composition and structure. Possessing a unique set of properties, and hoping to replicate the incredibly fast and selective molecular

transport occurring in cellular protein channels, several peptide-based porous materials have emerged in recent years as one of the most interesting and promising kinds of supramolecular porous solids.

Crystals of cyclic peptides, dendritic peptides, hydrophobic dipeptides and metal-dipeptide frameworks possess permanent microporosity, long-term stability and tunable characteristics, such as pore size, inner wall chemistry and porous network geometry. More significantly, framework and conformational flexibility lead to an adaptable porous network, "sensitive" to the chemical species being adsorbed. These characteristics are controllable through residue substitution, similarly to the structure-property relation of proteins in the natural world. Gate-keeping effects have been theoretically predicted on cyclic peptides, with functional groups far simpler than those of naturally occurring transmembrane ion channels.

Dipeptides and metal-dipeptide frameworks have successfully been tested as gas adsorbents, showing their guest-free stability and potential as microporous solids. High gas uptakes were observed in both cases, which are partially explained by the adaptable nature of the porous network. Just as with biological systems, “single-point mutations” can have dramatic effects on both structure and function of these materials.

2.6. References

1. P. D. Santis, S. Morosetti, and R. Rizzo, Conformational Analysis of Regular Enantiomeric Sequences, Macromolecules 7 (1974), 52-58.
2. I. L. Karle, B. K. Handa, and C. H. Hassall, The conformation of the cyclic tetrapeptide L-Ser(O-t-Bu)-[beta]-Ala-Gly-L-[beta]-Asp(OMe) containing a 14-membered ring, Acta Crystallogr. Sect. B 31 (1975), 555-560.
3. B. Hille, *Ionic Channels of Excitable Membranes*, 2nd ed., (Sinauer Associates, 1992).
4. J. Zhao, X. Zhao, Z. Jiang, Z. Li, X. Fan, J. Zhu, H. Wu, Y. Su, D. Yang, F. Pana, and J. Shi, Biomimetic and bioinspired membranes: Preparation and application, Progr. Polymer Sci. 39 (2014), 1668–1720.
5. M. Mulder, *Basic Principles of Membrane Technology*, 2nd ed., (Kluwer Academic Publishers, 1996).
6. L. M. Robeson, The upper bound revisited, J. Memb. Sci. 320 (2008), 390–400.
7. T. D. Clark and M. R. Ghadiri, Supramolecular Design by Covalent Capture. Design of a Peptide Cylinder via Hydrogen-Bond- Promoted Intermolecular Olefin Metathesis, J. Am. Chem. Soc. 117 (1995), 12364-12365
8. L. J. Prins and P. Scrimin, Covalent Capture: Merging Covalent and Noncovalent Synthesis, Angew. Chem. Int. Ed. 48 (2009), 2288–2306.
9. R. Adams, C. Carson, J. Ward, R. Tannenbaum, and W. Korosa, Metal organic framework mixed matrix membranes for gas separations, Micropor. Mesopor. Mat. 131 (2010), 13–20.
10. S. M. Saufi and A. F. Ismail, Fabrication of carbon membranes for gas separation – a review, Carbon 42 (2004), 241–259.
11. M. R. Ghadiri, J. R. Granja, R. A. Milligan, D. E. McRee, and N. Khazanovich, Self-assembling organic nanotubes based on a cyclic peptide architecture, Nature 366 (1993), 324-327.
12. C. Rao and J. P. Tamunder, Synthesis of Peptide Dendrimer, J. Am. Chem. Soc. 116 (1994), 6975-6976.
13. C. H. Görbitz and E. Gundersen, L-Valyl-L-Alanine, Acta Crystallogr. Sect. C 52 (1996), 1764-1767.
14. H.-Y. Lee, J. W. Kampf, K. S. Park, and E. N. G. Marsh, Covalent Metal-Peptide Framework Compounds That Extend in One and Two Dimensions, Cryst. Growth Des. 8 (2008), 296-303.
15. C. H. Hassall, SOME STUDIES RELATING TO THE SYNTHESIS OF CYLINDRICAL PEPTIDES, in *Chem. Bio. Pept., Proc. Third Am. Pept. Symp.*,1972, Ann Arbor, Michigan, Ann Arbor Science Publishers.
16. L. Tomasic and G. P. Lorenzi, Some Cyclic Oligopeptide with S2n Symmetry, Helv. Chim. Acta 70 (1987), 1012-1016.
17. V. Pavone, E. Benedetti, B. D. Blasio, A. Lombardi, C. Pedone, L. Tomasich, and G. P. Lorenzi, Regularly alternating L,D-peptides. III. Hexacyclic peptides from valine or phenylalanine, Biopolymers 28 (1989), 215-223.
18. M. R. Ghadiri, J. R. Granja, and L. K. Buehler, Artificial transmembrane ion channels from self-assembling peptide nanotubes, Nature 369 (1994), 301-304.

19. N. Khazanovich, J. R. Granja, D. E. McRee, R. A. Milligan, and M. R. Ghadiri, Nanoscale Tubular Ensembles with Specified Internal Diameters. Design of a Self-Assembled Nanotube with a 13-Å Pore, J. Am. Chem. Soc. 116 (1994), 6011-6012.
20. R. Chapman, M. Danial, M. L. Koh, K. A. Jolliffe, and S. Perrier, Design and properties of functional nanotubes from the self-assembly of cyclic peptide templates, Chem. Soc. Rev. 41 (2012), 6023–6041.
21. T. D. Clark, L. K. Buehler, and M. R. Ghadiri, Self-Assembling Cyclic ß[3]-Peptide Nanotubes as Artificial Transmembrane Ion Channels, J. Am. Chem. Soc. 120 (1998), 651-656.
22. T. Hirata, F. Fujimura, and S. Kimura, A novel polypseudorotaxane composed of cyclic ß-peptide as bead component, Chem. Commun. (2007), 1023–1025.
23. M. Amorín, L. Castedo, and J. R. Granja, Self-Assembled Peptide Tubelets with 7 Å Pores, Chem. Eur. J. 11 (2005), 6543–6551.
24. R. García-Fandiño, L. Castedo, J. R. Granja, and S. A. Vázquez, Interaction and Dimerization Energies in Methyl-Blocked α,γ-Peptide Nanotube Segments, J. Phys. Chem. B 114 (2010), 4973–4983.
25. D. Ranganathan, V. Haridas, R. Gilardi, and I. L. Karle, Self-Assembling Aromatic-Bridged Serine-Based Cyclodepsipeptides (Serinophanes): A Demonstration of Tubular Structures Formed through Aromatic π-π Interactions, J. Am. Chem. Soc. 120 (1998), 10793-10800.
26. D. Ranganathan, Designer Hybrid Cyclopeptides for Membrane Ion Transport and Tubular Structures, Acc. Chem. Res. 34 (2001), 919-930.
27. D. Ranganathan, C. Lakshmi, and I. L. Karle, Hydrogen-Bonded Self-Assembled Peptide Nanotubes from Cystine-Based Macrocyclic Bisureas, J. Am. Chem. Soc. 121 (1999), 6103-6107.
28. I. Amos B. Smith, W. Wang, A. K. Charnley, P. J. Carroll, C. S. Kenesky, and R. Hirschmann, Design, Synthesis, and Structural Analysis of D,L-Mixed Polypyrrolinones. 1. From Nonpeptide Peptidomimetics to Nanotubes, Org. Lett. 12 (2010), 2990-2993.
29. I. Amos B. Smith, H. Xiong, A. K. Charnley, M. Brenner, E. F. Mesaros, C. S. Kenesky, L. D. Costanzo, D. W. Christianson, and R. Hirschmann, Design, Synthesis, and Structural Analysis of D,L-Mixed Polypyrrolinones. 2. Macrocyclic Hexapyrrolinones, Org. Lett. 12 (2010), 2994-2997.
30. R. J. Brea, C. Reiriz, and J. R. Granja, Towards functional bionanomaterials based on self-assembling cyclic peptide nanotubes, Chem. Soc. Rev. 39 (2010), 1448–1456.
31. R. P. Cheng, S. H. Gellman, and W. F. DeGrado, ß-Peptides: From Structure to Function, Chem. Rev. 101 (2001), 3219–3232.
32. M. Amorín, V. Villaverde, L. Castedo, and J. R. Granja, New α,γ-peptide tubulets, J. Drug Deliv. Sci. Tech. 15 (2005), 87-92.
33. D. T. Bong, T. D. Clark, J. R. Granja, and M. R. Ghadiri, Self-Assembling Organic Nanotubes, Angew. Chem. Int. Ed. 40 (2001), 988-1011.
34. J. R. Granja and M. R. Ghadiri, Channel-Mediated Transport of Glucose Across Lipid Bilayers, J. Am. Chem. Soc. 116 (1994), 10785-10786.
35. D. Seebach, J. L. Matthew, A. Meden, T. Wessels, C. Baerlocher, and L. B. McCusker, Cyclo-ß-peptides: Structure and Tubular Stacking of Cyclic Tetramers of 3-Aminobutanoic Acid as Determined from Powder Diffraction Data, Helv. Chim. Acta 80 (1997), 173-182.

36. J. Sánchez-Quesada, H. S. Kim, and M. R. Ghadiri, A Synthetic Pore-Mediated Transmembrane Transport of Glutamic Acid, Angew. Chem. Int. Ed. 40 (2001), 2503-2506.
37. R. García-Fandiño, J. R. Granja, M. D'Abramo, and M. Orozco, Theoretical Characterization of the Dynamical Behavior and Transport Properties of alfa,γ-Peptide Nanotubes in Solution, J. Am. Chem. Soc. 131 (2009), 15678–15686.
38. M. Engels, D. Bashford, and M. R. Ghadiri, Structure and dynamics of self-assembling peptide nanotubes and the channel-mediated water organization and self-diffusion. A molecular dynamics study., J. Am. Chem. Soc. 117 (1995), 9151-9158.
39. J. Liu, J. Fan, M. Tang, M. Cen, J. Yan, Z. Liu, and W. Zhou, Water Diffusion Behaviors and Transportation Properties in Transmembrane Cyclic Hexa-, Octa- and Decapeptide Nanotubes, J. Phys. Chem. B 114 (2010), 12183–12192.
40. J. Liu, J. Fan, M. Tang, and W. Zhou, Molecular Dynamics Simulation for the Structure of the Water Chain in a Transmembrane Peptide Nanotube, J. Phys. Chem. A 114 (2010), 2376–2383.
41. J. Comer, F. i. Dehez, W. Cai, and C. Chipot, Water Conduction through a Peptide Nanotube, J. Phys. Chem. C 117 (2013), 26797–26803.
42. L. Ruiz, Y. Wub, and S. Keten, Tailoring the water structure and transport in nanotubes with tunable interiors, Nanoscale 7 (2015), 121–132.
43. D. Cohen-Tanugi and J. C. Grossman, Water Desalination across Nanoporous Graphene, Nano Letters 12 (2012), 3602–3608.
44. G. Hummer, J. C. Rasaiah, and J. P. Noworyta, Water conduction through the hydrophobic channel of a carbon nanotube, Nature 414 (2001), 188-190.
45. S. Fernandez-Lopez, H.-S. Kim, E. C. Choi, M. Delgado, J. R. Granja, A. Khasanov, K. Kraehenbuehl, G. Long, D. A. Weinberger, K. M. Wilcoxen, and M. R. Ghadiri, Antibacterial agents based on the cyclic D,L-α-peptide architecture, Nature 412 (2001), 452-455.
46. H. S. Kim, J. D. Hartgerink, and M. R. Ghadiri, Oriented Self-Assembly of Cyclic Peptide Nanotubes in Lipid Membranes, J. Am. Chem. Soc. 120 (1998), 4417-4424.
47. J. Zhu, J. Cheng, Z. Liao, Z. Lai, and B. Liu, Investigation of structures and properties of cyclic peptide nanotubes by experiment and molecular dynamics, J. Comput. Aided. Mol. Des. 22 (2008), 773–781.
48. T. Xu, N. Zhao, F. Ren, R. Hourani, M. T. Lee, J. Y. Shu, S. Mao, and B. A. Helms, Subnanometer Porous Thin Films by the Co-assembly of Nanotube Subunits and Block Copolymers, ACS Nano 5 (2011), 1376–1384.
49. S. S. Isied, M. Y. Ogawa, and J. F. Wishart, Peptide-Mediated Intramolecular Electron Transfer: Long-Range Distance Dependence, Chem. Rev. 92 (1992), 381-394.
50. M. Kai, K. Takeda, T. Morita, and S. Kimura, Distance dependence of long-range electron transfer through helical peptides, J. Pept. Sci. 14 (2008), 192 – 202.
51. S. Sek, A. Misicka, K. Swiatek, and E. Maicka, Conductance of α-Helical Peptides Trapped within Molecular Junctions, J. Phys. Chem. B 110 (2006), 19671-19677.
52. W. S. Horne, N. Ashkenasy, and M. R. Ghadiri, Modulating Charge Transfer through Cyclic D,L-α-Peptide Self-Assembly, Chem. Eur. J. 11 (2005), 1137-1144.
53. N. Ashkenasy, W. S. Horne, and M. R. Ghadiri, Design of Self-Assembling Peptide Nanotubes with Delocalized Electronic States, Small 2 (2006), 99-102.

54. R. Takahashi, H. Wang, and J. P. Lewis, Electronic Structures and Conductivity in Peptide Nanotubes, J. Phys. Chem. B 111 (2007), 9093-9098.
55. F. Fujimura and S. Kimura, Columnar Assembly Formation and Metal Binding of Cyclic Tri-ß-peptides Having Terpyridine Ligands, Org. Lett. 9 (2007), 793-796.
56. H. Okamoto, T. Nakanishi, Y. Nagai, M. Kasahara, and K. Takeda, Variety of the Molecular Conformation in Peptide Nanorings and Nanotubes, J. Am. Chem. Soc. 125 (2003), 2756-2769.
57. G. Praveena, P. Kolandaivel, N. Santhanamoorthi, V. Renugopalakrishnan, and S. Ramakrishna, Looking Beyond Carbon Nanotubes: Polypeptide Nanotubes as Alternatives?, J. Nanosci. Nanotechnol. 7 (2007), 2253-2259.
58. R. J. Brea, L. Castedo, J. R. Granja, M. Á. Herranz, L. Sánchez, N. Martín, W. Seitz, and D. M. Guldi, Electron transfer in Me-blocked heterodimeric α,γ-peptide nanotubular donor–acceptor hybrids, Proc. Nat. Acad. Sci. 104 (2007), 5291–5294.
59. M. Amorín, A. Perez, J. Barber, H. L. Ozores, J. L. Serrano, J. R. Granja, and T. Sierra, Liquid crystal organization of self-assembling cyclic peptides, Chem. Commun. 50 (2014), 688-690.
60. S. Höger, Shape-Persistent Macrocycles: From Molecules to Materials, Chem. Eur. J. 10 (2004), 1320-1329.
61. D. Pasini and M. Ricci, Macrocycles as Precursors for Organic Nanotubes, Cur. Org. Synth. 4 (2007), 59-80.
62. M. Numata, Creation of unique supramolecular nanoarchitectures utilizing natural polysaccharide as a one-dimensional host, J. Incl. Phenom. Macrocycl. Chem. 68 (2010), 25–47.
63. Y. Xu, M. D. Smith, M. F. Geer, P. J. Pellechia, J. C. Brown, A. C. Wibowo, and L. S. Shimizu, Thermal Reaction of a Columnar Assembled Diacetylene Macrocycle, J. Am. Chem. Soc. 132 (2010), 5334-5335.
64. I. Karle and D. Ranganathan, Construction of polar and hydrophobic pores and channels by assembly of peptide molecules, J. Mol. Struct. 647 (2003), 85–96.
65. E. Buhleier, W. Wehner, and F. Vögtle, "Cascade"- and "Nonskid-Chain-like" Syntheses of Molecular Cavity Topologies, Synthesis 1978 (1978), 155-158.
66. D. A. Tomalia, H. Baker, J. Dewald, M. Hall, G. Kallos, S. Martin, J. Roeck, J. Ryder, and P. Smith, A New Class of Polymers: Starburst-Dendritic Macromolecules, Polym. J. 17 (1985), 117-132.
67. J. M. J. Fréchet, Dendrimers and supramolecular chemistry, Proc. Nat. Acad. Sci. 99 (2002), 4782-4787.
68. J. H. Friedhofen and F. Vögtle, Detailed nomenclature for dendritic molecules, New J. Chem. 30 (2006), 32–43.
69. G. R. Newkome, C. N. Moorefield, and F. Vögtle, *Dendrimers and Dendrons: Concepts, Syntheses, Applications*, (WILEY-VCH Verlag GmbH, 2001).
70. L. Crespo, G. Sanclimens, M. Pons, E. Giralt, M. Royo, and F. Albericio, Peptide and Amide Bond-Containing Dendrimers, Chem. Rev. 105 (2005), 1663-1681.
71. P. Veprek and J. Jezek, Peptide and Glycopeptide Dendrimers. Part I, J. Pept. Sci. 5 (1999), 5–23.
72. K. Sadler and J. P. Tam, Peptide dendrimers: applications and synthesis, Rev. Mol. Biotech. 90 (2002), 195-229.
73. J. Sebestik, P. Niederhafner, and J. Jezek, Peptide and glycopeptide dendrimers and analogous dendrimeric structures and their biomedical applications, Amino Acids 40 (2011), 301-370.

74. J. P. Tam, Synthetic peptide vaccine design: Synthesis and properties of a high-density multiple antigenic peptide system, Proc. Nat. Acad. Sci. 85 (1988), 5409-5413.
75. A. T. Florence, T. Sakthivel, and I. Toth, Oral uptake and translocation of a polylysine dendrimer with a lipid surface, J. Control. Release 65 (2000), 253–259.
76. J. Gariépy and K. Kawamura, Vectorial delivery of macromolecules into cells using peptide-based vehicles, Trends Biotech. 19 (2001), 21-28.
77. D. S. Shah, T. Sakthivel, I. Toth, A. T. Florence, and A. F. Wilderspin, DNA transfection and transfected cell viability using amphipathic asymmetric dendrimers, Int. J. Pharma. 208 (2000), 41–48.
78. D. Singh, R. Kiarash, K. Kawamura, E. C. LaCasse, and J. Gariépy, Penetration and Intracellular Routing of Nucleus-Directed Peptide-Based Shuttles (Loligomers) in Eukaryotic Cells, Biochemistry 37 (1998), 5798-5809.
79. R. B. Merrifield, Solid Phase Peptide Synthesis. I. The Synthesis of a Tetrapeptide, J. Am. Chem. Soc. 85 (1963), 2149-2154.
80. A. T. Florence, T. Sakthivel, and I. Toth, Oral uptake and translocation of a polylysine dendrimer with a lipid surface, J. Contr. Release 65 (2000), 253–259.
81. V. Percec, A. E. Dulcey, V. S. K. Balagurusamy, Y. Miura, J. Smidrkal, M. Peterca, S. Nummelin, U. Edlund, S. D. Hudson, P. A. Heiney, H. Duan, S. N. Magonov, and S. A. Vinogradov, Self-assembly of amphiphilic dendritic dipeptides into helical pores, Nature 430 (2004), 764-768.
82. V. Percec, W.-D. Cho, G. Ungar, and D. J. P. Yeardley, Synthesis and Structural Analysis of Two Constitutional Isomeric Libraries of AB2-Based Monodendrons and Supramolecular Dendrimers, J. Am. Chem. Soc. 123 (2001), 1302-1315.
83. V. Percec, A. Dulcey, M. Peterca, M. Ilies, Y. Miura, U. Edlund, and P. A. Heiney, Helical Porous Protein Mimics Self-Assembled from Amphiphilic Dendritic Dipeptides, Aust. J. Chem. 58 (2005), 472-482.
84. V. Percec, A. E. Dulcey, M. Peterca, M. Ilies, J. Ladislaw, B. M. Rosen, U. Edlund, and P. A. Heiney, The Internal Structure of Helical Pores Self-Assembled from Dendritic Dipeptides is Stereochemically Programmed and Allosterically Regulated, Angew. Chem. Int. Ed. 44 (2005), 6516 –6521.
85. V. Percec, A. E. Dulcey, M. Peterca, M. Ilies, S. Nummelin, M. J. Sienkowska, and P. A. Heiney, Principles of self-assembly of helical pores from dendritic dipeptides, Proc. Nat. Acad. Sci. 103 (2006), 2518-2523.
86. B. M. Rosen, M. Peterca, K. Morimitsu, A. e. E. Dulcey, P. Leowanawat, A.-M. Resmerita, M. R. Imam, and V. Percec, Programming the Supramolecular Helical Polymerization of Dendritic Dipeptides via the Stereochemical Information of the Dipeptide, J. Am. Chem. Soc. 133 (2011), 5135-5151.
87. V. Percec and P. Leowanawat, Why Are Biological Systems Homochiral?, Isr. J. Chem. 51 (2011), 1107-1117.
88. V. Percec, A. E. Dulcey, M. Peterca, P. Adelman, R. Samant, V. S. K. Balagurusamy, and P. A. Heiney, Helical Pores Self-Assembled from Homochiral Dendritic Dipeptides Based on L-Tyr and Nonpolar α-Amino Acids, J. Am. Chem. Soc. 129 (2007), 5992-6002.
89. M. S. Kaucher, M. Peterca, A. E. Dulcey, A. J. Kim, S. A. Vinogradov, D. A. Hammer, P. A. Heiney, and V. Percec, Selective Transport of Water Mediated by Porous Dendritic Dipeptides, J. Am. Chem. Soc. 129 (2007), 11698-11699.

90. A. G. Volkov, S. Paula, and D. W. Deamer, Two mechanisms of permeation of small neutral molecules and hydrated ions across phospholipid bilayers, Bioelectrochem. Bioenergetics 42 (1997), 153-160.
91. E. Boldyreva, in *Models, Mysteries and Magic of Molecules*, (eds. J.C.A. Boeyens and J.F. Ogilvie), Ch. 7, pp. 167-192 (Springer, 2008).
92. C. G. Suresh and M. Vijayan, Occurrence and geometrical features of head-to-tail sequences involving amino acids in crystal structures, Int. J. Pept. Protein Res. 22 (1983), 129-143.
93. C. H. Görbitz and M. C. Etter, Hydrogen bond connectivity patterns and hydrophobic interactions in crystal structures of small, acyclic peptides, Int. J. Pept. Protein Res. 39 (1992), 93-110.
94. K. P. C. Vollhardt and N. E. Schore, in *Organic Chemistry*, Ch. Chapter 26, (W. H. Freeman and Company, 2007).
95. H. Lodish, A. Berk, C. A. Kaiser, M. Krieger, A. Bretscher, H. Ploegh, A. Amon, and M. P. Scott, in *Molecular Cell Biology*, 7th ed., Ch. 3, (W. H. Freeman and Company, 2013).
96. Y. Iitaka, The crystal structure of β-glycine, Acta Crystallogr. 13 (1960), 35-45.
97. C. H. Görbitz, Microporous Organic Materials from Hydrophobic Dipeptides, Chem. Eur. J. 13 (2007), 1022–1031.
98. C. H. Görbitz, An exceptionally stable peptide nanotube system with flexible pores, Acta Crystallogr. B58 (2002), 849-854.
99. C. H. Görbitz and E. Gundersen, L-Leu-L-Val.3/4H2O: A Hexagonal Crystal Structure with Z = 24, Acta Chem. Scand. 50 (1996), 537-543.
100. R. J. Fletterick, C.-c. Tsai, and R. E. Hughes, The Crystal and Molecular Structure of L-Alanyl-L-alanine, J. Phys. Chem. 75 (1971), 918-922.
101. C. H. Görbitz, Solvent Site Preferences in the Crystal Structures of L-Leucyl-L-leucine Alcohol (1:1) Complexes), Acta Chem. Scand. 52 (1998), 1343-1349.
102. C. H. Görbitz, L-Alanyl-L-phenylalanine-2-propanol (1/2) (s-form), L-valyl-L-phenylalanine-2-propanol (1/1) and L-leucyl-L-phenyl-alanine-2-propanol (1/1) (/3-form), Acta Crystallogr. Sect. C 55 (1999), 2171-2177.
103. C. H. Görbitz, L-Leucyl-L-leucine 2-methyl-l-propanol solvate, Acta Crystallogr. Sect. C 55 (1999), 670-672.
104. C. H. Görbitz, Nanotubes from hydrophobic dipeptides: pore size regulation through side chain substitution, New J. Chem. 27 (2003), 1789-1793.
105. C. H. Görbitz, Nanotube Formation by Hydrophobic Dipeptides, Chem. Eur. J. 7 (2001), 5153-5159.
106. T. J. Emge, A. Agrawal, J. P. Dalessio, G. Dukovic, J. A. Inghrim, K. Janjua, M. Macaluso, L. L. Robertson, T. J. Stiglic, Y. Volovik, and M. M. Georgiadis, Alaninyltryptophan hydrate, glycyl-tryptophan dihydrate and tryptophyl-glycine hydrate, Acta Crystallogr. Sect. C 56 (2000), e469-e471.
107. C. H. Görbitz, Nanotubes of L-isoleucyl-L-leucine 0.91-hydrate, Acta Crystallogr. E60 (2004), o626-o628.
108. C. H. Görbitz, L-Phenylalanyl-L-tryptophan 0.75-hydrate, Acta Crystallogr. C62 (2006), o328-o330.
109. D. V. Soldatov, I. L. Moudrakovski, E. V. Grachev, and J. A. Ripmeester, Micropores in Crystalline Dipeptides as Seen from the Crystal Structure, He Pycnometry, and 129Xe NMR Spectroscopy, J. Am. Chem. Soc. 128 (2006), 6737-6744.
110. D. V. Soldatov and J. A. Ripmeester, Organic Zeolites, Stud. Sur. Sci. Cat. 156 (2005), 37-54.

111. C. H. Görbitz, M. Nilsen, K. Szeto, and L. W. Tangen, Microporous organic crystals: an unusual case for L-leucyl–L-serine, Chem. Commun. (2005), 4288–4290.
112. A. Comotti, A. Fraccarollo, S. Bracco, M. Beretta, G. Distefano, M. Cossi, L. Marchese, C. Riccardi, and P. Sozzani, Porous dipeptide crystals as selective CO2 adsorbents: experimental isotherms vs. grand canonical Monte Carlo simulations and MAS NMR spectroscopy, Cryst. Eng. Commun. 15 (2013), 1503–1507.
113. A. Comotti, S. Bracco, G. Distefano, and P. Sozzani, Methane, carbon dioxide and hydrogen storage in nanoporous dipeptide-based materials, Chem. Commun. 45 (2009), 284–286.
114. D. V. Soldatov, I. L. Moudrakovski, and J. A. Ripmeester, Dipeptides as Microporous Materials, Angew. Chem. Int. Ed. 43 (2004), 6308-6311.
115. R. Afonso, A. Mendes, and L. Gales, Hydrophobic dipeptide crystals: a promising Ag-free class of ultramicroporous materials showing argon/oxygen adsorption selectivity, Phys. Chem. Chem. Phys. 16 (2014), 19386-19393.
116. N. Amdursky, M. Molotskii, E. Gazit, and G. Rosenman, Elementary Building Blocks of Self-Assembled Peptide Nanotubes, J. Am. Chem. Soc. 132 (2010), 15632–15636.
117. N. Amdursky, P. Beker, I. Koren, B. Bank-Srour, E. Mishina, S. Semin, T. Rasing, Y. Rosenberg, Z. Barkay, E. Gazit, and G. Rosenman, Structural Transition in Peptide Nanotubes, Biomacromolecules 12 (2011), 1349–1354.
118. S. Horike, S. Shimomura, and S. Kitagawa, Soft Porous Crystals, Nat. Chem. 1 (2009), 695-705.
119. D. V. Soldatov, Soft Supramolecular Materials, J. Incl. Phenom. Macrocycl. Chem. 48 (2004), 3-9.
120. N. B. Sopher, Z. R. Abrams, M. Reches, E. Gazit, and Y. Hanein, Integrating peptide nanotubes in micro-fabrication processes, J. Micromech. Microeng. 17 (2007), 2360–2365.
121. C. H. Görbitz, The structure of nanotubes formed by diphenylalanine, the core recognition motif of Alzheimer's ß-amyloid polypeptide, Chem. Commun. (2006), 2332–2334.
122. M. Reches and E. Gazit, Casting Metal Nanowires Within Discrete Self-Assembled Peptide Nanotubes, Science 300 (2003), 625-627.
123. P. Tamamis, L. Adler-Abramovich, M. Reches, K. Marshall, P. Sikorski, L. Serpell, E. Gazit, and G. Archontis, Self-Assembly of Phenylalanine Oligopeptides: Insights from Experiments and Simulations, Biophys. J. 96 (2009), 5020–5029.
124. L. Adler-Abramovich and E. Gazit, The physical properties of supramolecular peptide assemblies: from building block association to technological applications, Chem. Soc. Rev. 43 (2014), 6881-6893.
125. C. H. Görbitz, The structure of nanotubes formed by diphenylalanine, the core recognition motif of Alzheimer's ß-amyloid polypeptide, Chem. Commun. 42 (2006), 2332–2334.
126. J.-B. Weng, M.-C. Hong, R. Cao, Q. Shi, and A. S. C. Chan, The Paramagnetic 2D Chiral-porous Polymer of L-Phenylalanine and Manganese, Chinese J. Struct. Chem. 22 (2003), 195-199.
127. M. Tiliakos, E. Katsoulakou, A. Terzis, C. Raptopoulou, P. Cordopatis, and E. Manessi-Zoupa, The dipeptide H-Aib-L-Ala-OH ligand in copper(II) chemistry: Variation of product identity as a function of pH, Inorg. Chem. Comm. 8 (2005), 1085–1089.

128. A. Mantion, L. Massüger, P. Rabu, C. Palivan, L. B. McCusker, and A. Taubert, Metal-Peptide Frameworks (MPFs): "Bioinspired" Metal Organic Frameworks, J. Am. Chem. Soc. 130 (2008), 2517-2526.
129. J. Rabone, Y.-F. Yue, S. Y. Chong, K. C. Stylianou, J. Bacsa, D. Bradshaw, G. R. Darling, N. G. Berry, Y. Z. Khimyak, A. Y. Ganin, P. Wiper, J. B. Claridge, and M. J. Rosseinskyable, An Adaptable Peptide-Based Porous Material, Science 329 (2010), 1053-1057.
130. F. Millange, C. Serre, N. Guillou, G. Férey, and R. I. Walton, Structural Effects of Solvents on the Breathing of Metal–Organic Frameworks: An In Situ Diffraction Study, Angew. Chem. Int. Ed. 47 (2008), 4100–4105.
131. C. Martí-Gastaldo, J. E. Warren, K. C. Stylianou, N. L. O. Flack, and M. J. Rosseinsky, Enhanced Stability in Rigid Peptide-Based Porous Materials, Angew. Chem. Int. Ed. 51 (2012), 11044–11048.
132. C. Martí-Gastaldo, D. Antypov, J. E. Warren, M. E. Briggs, P. A. Chater, P. V. Wiper, G. J. Miller, Y. Z. Khimyak, G. R. Darling, N. G. Berry, and M. J. Rosseinsky, Side-chain control of porosity closure in single- and multiple-peptide-based porous materials by cooperative folding, Nature Chem. 6 (2014), 343-351.
133. A. P. Katsoulidis, K. S. Park, D. Antypov, C. Martí-Gastaldo, G. J. Miller, J. E. Warren, C. M. Robertson, F. Blanc, G. R. Darling, N. G. Berry, J. A. Purton, D. J. Adams, and M. J. Rosseinsky, Guest-Adaptable and Water-Stable Peptide-Based Porous Materials by Imidazolate Side Chain Control, Angew. Chem. Int. Ed. 53 (2014), 193–198.
134. S. Emami, F. A. A. Paz, A. Mendes, and L. Gales, Toward the Construction of 3D Dipeptide−Metal Frameworks, Cryst. Growth Des. 14 (2014), 4777−4780.
135. B. Lou and X. Huang, A Homochiral Metal-Dipeptide Supramolecular Framework Including a Hydrogen-bonded Guest Network of Water and Uncoordinated 4,4-Bipyridine, Z. Anorg. Allg. Chem. 638 (2012), 1855–1860.
136. R. Miyake, C. Kuwata, and Y. Masumoto, Selective CO2 gas adsorption in the narrow crystalline cavities of flexible peptide metallo-macrocycles, Dalton Trans. 44 (2015), 2993-2996.
137. W.-x. Chen, L. Tan, Q.-p. Liu, Y. Zhou, Y.-x. Fan, G.-r. Qiang, and G.-l. Zhuang, Lanthanide-based metal–peptide frameworks prepared by ionothermal method: Anion direct effect, DFT calculation and luminescence property, Inorg. Chem. Comm. 42 (2014), 29–32.

Chapter 3. Adsorption and Diffusion Inside Porous Crystals*

3.1. Abstract

In the first part of this chapter, permeation results of single dipeptide crystals are shown and discussed. Both high permeabilities and ideal selectivities are reported. These results are then put into perspective with new data obtained afterwards concerning the adsorption isotherms in dipeptide powder samples and additional single crystal permeation experiments.

In the second part of this chapter, the adsorption isotherms of nitrogen, oxygen and argon in four VA-class hydrophobic dipeptides are presented. Isotherms were determined at 5, 20 and 35 ºC, for a pressure range of 0-6 bar. Under these conditions, adsorption is still in the Henry region. For all materials and temperatures, the sequence of preferential adsorption is $Ar>O_2>N_2$, a highly abnormal result. At 5 ºC, the dipeptide with the smallest pores, VI, has Ar/O_2 adsorption equilibrium selectivities up to 1.30, the highest ever measured in Ag-free adsorbents. Gas uptakes, at 1 bar and 20 ºC, are ~0.05 $mol \cdot kg^{-1}$, very low relative values that are partially explained by the low porosity of the solids (< 10 %). The significance of these results for the development of new materials for the process of O_2 generation by pressure swing adsorption (PSA) is discussed. The results hint at some of the structural and chemical properties that prospective Ag-free adsorbents might have in order to exhibit Ar/O_2 selectivity; hydrophobic pores, less than 0.5 nm-wide, and porosity of, at least, 20 %.

3.2. Introduction

Crystalline hydrophobic dipeptides of the VA-class [1, 2] are a type of ultramicroporous solids that has received considerable attention in recent years [3-6]. The structure of these molecular crystals is stabilised by H-bonds and hydrophobic interactions, being essentially the same for all VA-class dipeptides. This crystal structure displays an array of identical,

* Adapted from Afonso et al., Angew. Chem. Int. Ed. 49 (2010), 3034–3036 and Afonso et al., Phys. Chem. Chem. Phys. 16 (2014), 19386-19393.

parallel unidimensional micropores [2, 7]. The pore walls are formed by the aliphatic side-chains of the dipeptides, making the pores highly hydrophobic [1]. Different side-chain combinations create slightly different crystal structures, with different pore sizes [1]. The micropores are helical and have an approximately circular cross-section, somewhat uniform throughout the unit cell [4, 7]. Nominal, average pore sizes of VA-class dipeptide crystals range from 0.37 nm to 0.50 nm [2, 7].

Crystal porosity has been proven several times, by determination of adsorption isotherms [4, 8, 9], and through ^{129}Xe NMR [3, 5-7, 10, 11]. Additionally, when embedded in solvents of different colours, the crystals also become uniformly coloured [12], indicating thorough solvent permeation into the pores. Recent NMR experiments have also shown that the pores in VA and AV dipeptide crystals typically span the entire crystal length [6]. Dipeptide crystals thus have incredibly open pores. Moreover, the supramolecular framework of the dipeptide crystals is very flexible, allowing penetration of guests bigger than the guest-free pore [8, 13, 14]. This observation is supported by vibration spectroscopy [15] and ^{129}Xe NMR [3] studies. For guest molecules smaller than the pore, there has yet to be demonstrated any clear effect resulting from framework flexibility [4].

3.3. Preliminary Studies: Single-Crystal Permeation of Atmospheric Gases

Herein, we report the use of dipeptide crystals as permselective materials. Although this looks like an obvious engineering application for the kind of porous topology present in the crystals, there are issues that call for an experimental support, namely i) potential crystal defects, like twinning or fractures may greatly diminish their actual selectivity and ii) potential lack of rigidity of the crystal structure, allowing the pores to adapt to some extent to the size of the guest molecules.

We envisage the selective permeation of argon, nitrogen and oxygen (main components of air) through dipeptide crystals. This is a highly relevant industrial separation process and also a very ambitious one given the similarity of the molecular sizes of the individual components. The dipeptide crystals that were tested as single-crystal membranes are L-leucyl-L-serine (LS), L-valyl–L-isoleucine (VI) and L-alanyl-L-alanine (AA) crystals.

The peptides were crystallized and their structures determined by X-ray diffraction (Figure 3.1). The structures of all three peptides had been resolved previously [1, 16, 17]. The VI

crystal packing has hexagonal symmetry with molecules forming helices with six dipeptides per turn. LS crystals have a unique crystal packing with the inner walls formed by leucine side chains and with right-handed heliticity. AA packs in the tetragonal space group I4 and the crystal arrangement is characterized by the segregation of the hydrophobic methyl groups into columns.

The calculated void volumes in the three crystal structures that are accessible to He, the molecule with the smallest kinetic diameter (2.6 Å), are shown in Figure 3.1a. LS and VI contain nanochannels while AA should be considered nonporous. The average channel diameters of LS and VI are displayed in Table 3.1.

The LS, VI and AA single crystal permeabilities towards O_2, N_2, Ar and He were determined at room temperature (Table 3.1). The LS crystals are permeable to all the gas molecules and the respective selectivities are low, probably because the channels size is much bigger than the van der Waals diameter of the guest molecules.

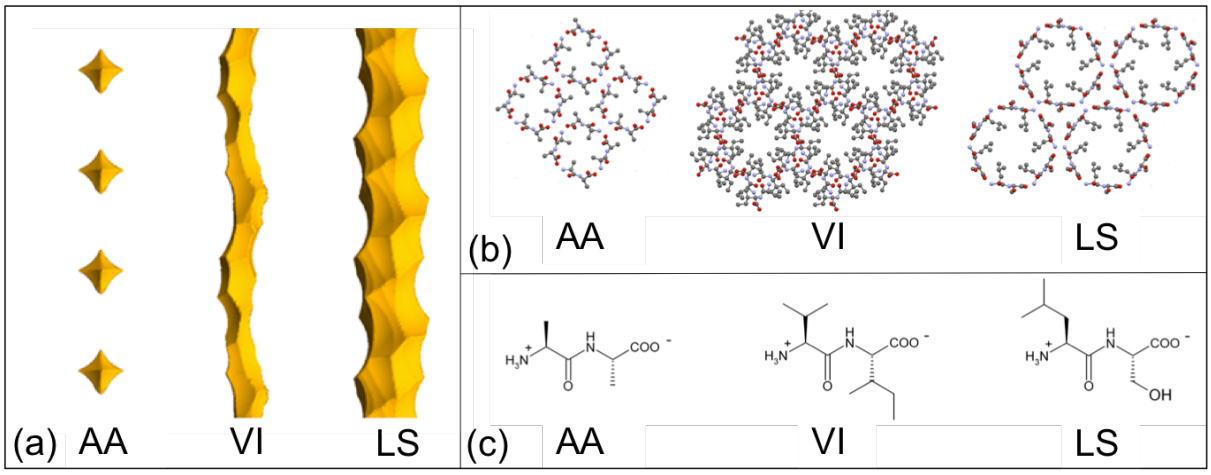

Figure 3.1. (a) Void volumes of the crystals structures of AA, VI and LS that can hold a spherical "probe" with a diameter of 2.6 Å. The calculation and visualisation of the void volumes were carried using the software Mercury 2.2 with 0.1 Å of grid spacing [18]. (b) Crystal structures of the dipeptides viewed along the *c*-crystallographic axis. Hydrogen atoms omitted for clarity. (c) Structural formulae of the three dipeptides.

Thus, we have decided to test VI crystals because they display narrower channels. We observed that VI crystals are permeable to O_2 and N_2 but not to Ar (Table 3.1). However, the selectivity achieved for the O_2/N_2 (1.2) separation is too low to be of any practical significance, which prompted us to search for dipeptides forming smaller pores. We decided

to study the nominally non-porous AA crystals, given that, despite the fact of the pores being too small, the dynamics of the crystal matrix had never been investigated.

Remarkably, it was observed that the AA crystals are permeable to O_2 but not to N_2 or Ar (Table 3.1). The permeability of the AA crystals towards the smaller He molecules is lower than towards O_2, indicating that the host crystal matrix seems to respond individually to each particular guest molecule.

The minimum measurable permeabilities of VI and AA determine the maximum selectivities corresponding to the cases of undetected permeation. For VI, the minimum O_2/Ar selectivity that could generate such a result is 135. For AA, it is 124 for both O_2/N_2 and O_2/Ar.

The unexpected penetration of guest molecules into too narrow pores was already noticed in three other dipeptide crystals and attributed to the flexibility of the crystals framework [7]. Moreover, the experimental determination of the porosity of eight crystal dipeptides (AV, VA, AI, VV, IA IV, VI and LS) showed that two, AV and VA, undergo pore size expansion upon gas sorption [7]. It was suggested that in the VA class, there are backbone vibrational modes that contribute to the pore permeability [15].

Table 3.1. Dipeptide crystals permeabilities and selectivities towards He, O_2, N_2 and Ar. The minimum permeate flow rate that can be accurately measured in the setup is ~0.0005 mm^3/h which corresponds to a permeability of ~0.25 barrer (AA crystals) and of ~20 barrer (VI crystals).

Dipeptide	Channel Diameter / nm	Permeabilities / barrer			
		He	O_2	N_2	Ar
LS	0.49	1.7×10^7	9.5×10^6	1.1×10^7	1.2×10^7
VI	0.37	2.8×10^4	2.7×10^3	2.2×10^3	Not detected
AA	—	19	31	Not detected	Not detected

Despite the fact that irreversible changes were found with AV, VA and AI crystals [3], the flexibility of the AA packing seems to be reversible. The AA crystals remain non-permeable to N_2 after the O_2 experiments and there was a full retention of the crystal structure after 2 months of permeation experiments. Interestingly, traces of oxygen molecules are found in the channels at a pressure of 8.5 bar of pure oxygen (Figure 3.2).

There are four symmetry equivalent positions for oxygen molecules in each vacancy void volume. The transport may be described in terms of hopping diffusion along the vacancy void volumes that are limited by the four methyl groups (Figure 3.2). The total O_2 occupation per void volume (0.018) can be obtained from the adsorption isotherm.

Although it is known that the Knudsen model does not apply to micropores [19], it is interesting to observe that the measured gas flow through the LS channels significantly exceeds Knudsen diffusion predictions (see Appendix A). Very fast air flow rates were already observed through 1.6 nm carbon nanotubes and attributed to the smoothness of the carbon pore walls [20]. Apparently, the weak nature of the interactions produced by the methyl groups that decorate the LS channels walls also allows high gas flow rates.

A breakdown in the mass transport rate arises from the size-matching between the guest molecules and channel diameters as shown by the drastic decline of the VI and AA permeabilities (Table 3.1). The decrease in the gas sorption equilibrium, in particular for AA, and the reduction in the gas diffusivities certainly combine for such a strong drop in the permeabilitites.

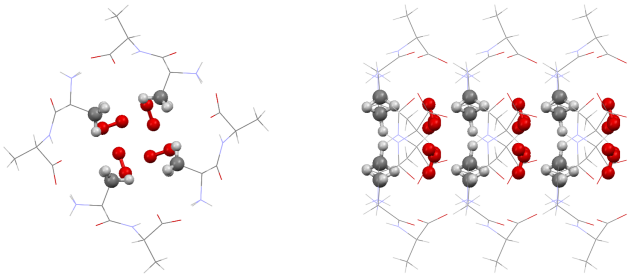

Figure 3.2. Crystal structure of AA with O_2 viewed along the *c*-axis (left) and along the *b*-axis (right). Highlighted are the oxygen molecules trapped inside the pores and the Ala side chains that form the pore constrictions.

The LS permeability values were surprisingly high when compared to the behaviour of the other dipeptide crystals and to the values for other microporous materials reported in the literature. Though the experiments had been repeated with crystals with different dimensions it was noticed that more recent results by our group using the same method, Durão and Gales [21], showed that the LS permeability is in fact of the same order of magnitude of the VI permeability reported here.

Durão and Gales [21] have also shown that there is a propensity for pore blocking in dipeptide crystals which increases drastically with the crystal size (diffusing path length) and with the molecular dimension of the diffusing species. In agreement with that, in the next section it is shown that Ar is readily adsorbed in 1-50 mm powder polycrystalline solids (see Appendix B) but becomes blocked in 1-2 mm single crystals (Table 3.1). Nevertheless, it was concluded that dipeptide crystals can indeed be used as permselective materials but, as it happen with any unidimensional pore material, care must be taken concerning pore blocking.

3.4. Adsorption Studies

The relatively few gas adsorption studies performed with VA-class dipeptides have yielded some notable results, such as high H_2 adsorption capacities [9], high CO_2/CH_4 selectivities [4] and Xe adsorption in pores nominally too small for that to happen [8]. In this article, we report the adsorption isotherms and heats of adsorption of Ar, O_2 and N_2 in four crystalline dipeptides. The four dipeptides used have the smallest pores of the VA-class; VI, IA, IV and VV, having, respectively, 0.370 nm, 0.374 nm, 0.390 nm and 0.439 nm average crystallographic diameters [2], corresponding, respectively, to porosities of 5.7 %, 6.0 %, 6.3 % and 8.3 % (as determined from the crystal structure) [7]. The adsorbents show inverted Ar/O_2 selectivity, a highly abnormal result, extremely interesting in the context of the very important industrial process of O_2 production by PSA.

Industrial O_2 production relies almost exclusively on air-separation processes [22, 23]. One of these, PSA, is a cyclic chromatographic separation process [24], which, in the last four decades, has steadily been displacing cryogenic distillation as the process of choice for O_2 production, in an increasing number of conditions [22, 23]. Presently, improvement of the process of air separation by PSA depends mainly on the development of new adsorbent materials, with greater working capacities [25, 26] and selectivities; this is especially the case for O_2, which is particularly hard to separate from Ar.

PSA production of O_2 with up to 95 % purity is done using zeolites with N_2/O_2 selectivities of 2 to 10 [22, 27, 28]. In these adsorbents, it is very common that the adsorption isotherms of O_2 and Ar are close [29, 30], causing the Ar/O_2 ratio to remain unchanged throughout the column, approximately 1/20 (the same as in air), thus limiting the O_2 purity achievable to 95 %. Separation of O_2 and Ar for high-purity (> 95 %) O_2 generation is usually done using a kinetically selective carbon molecular sieve (CMS) adsorbent, where O_2 has a much higher

diffusivity than Ar and N_2; that is, the adsorbent has O_2/Ar and O_2/N_2 kinetic selectivities. This separation can be performed before [31] or after [32] removing the bulk of N_2 with another PSA unit, using a zeolite adsorbent. For technical reasons [28-30, 33], the optimal situation combines initial N_2 removal followed by Ar/O_2 separation based on an adsorbent with Ar/O_2 selectivity (instead of O_2/Ar). Enormous efforts have been directed at finding materials displaying this property [28, 30].

Adsorbents that preferentially adsorb Ar over O_2 are rare, and the ones that do exist have marginal selectivities. The first Ar-selective adsorbent discovered was silver-exchanged mordenite, Ag-mordenite, with an Ar/O_2 selectivity of 1.13 [34]. The potential for PSA separation of Ar/O_2 mixtures of Ag-mordenite was immediately recognised [29]. In the next two decades, several articles and patents followed, describing adsorbents with greater selectivities and capacities, as well as more efficient O_2-generating PSA processes [26, 28, 30, 33, 35-38].

The highest Ar/O_2 adsorption selectivity value ever measured was 1.65, on a Ag-exchanged zeolite ZSM-5, closely followed by that of a Ag-exchanged zeolite A, 1.63, both at atmospheric pressure [36]. Adsorbents used in PSA or gas chromatography experiments are all also Ag-exchanged zeolites [28-30, 33, 34, 38]. These have the additional advantage of having extremely high N_2/O_2 selectivities (>10) [26]. However, incorporation of silver also makes these materials quite expensive, greatly hindering their usage. Discovery of Ag-free porous materials displaying the desired selectivities is thus of great commercial and technical interest.

The overwhelming majority of porous solids adsorb more O_2 than Ar [26, 28, 39, 40]. Metal-organic frameworks (MOFs) typically have the preferential adsorption sequence O_2>Ar>N_2 [41, 42], zeolites have N_2>O_2>Ar [43, 44] and carbon-based materials display the two situations with similar frequency [45, 46]. We were able to find a single case of an adsorbent having an O_2>N_2>Ar sequence of preferential adsorption [47]. To date, to the best of our knowledge, only six known Ag-free porous materials show Ar/O_2 equilibrium selectivity; MIL-53(Al) (the “breathing” MOF) [48], mordenite (zeolite) [36, 49], a CMS [50], ZSM-5 (zeolite) [36, 51], a polymer of intrinsic microporosity [52] and an activated carbon [53], having equilibrium Ar/O_2 selectivities of, respectively, 1.26, 1.12, 1.11, 1.08, 1.09 and 1.06. Out of the six, the first four adsorb in the sequence N_2>Ar>O_2, the last two Ar>O_2>N_2 and not a single instance of adsorption in the sequence Ar>N_2>O_2. The reason for this exceptional behaviour was not addressed in any case. This limited number and inexistence of appropriate

explanations of the selection mechanism prevent the design of strategies for the development/discovery of new Ag-free Ar/O_2 selective adsorbents.

The dipeptide crystals tested for this work have the order of adsorption $Ar>O_2>N_2$, with a maximum Ar/O_2 selectivity of 1.30, at 5 ºC, for VI. A discussion of the reasons for these abnormal results and their significance in the context of the development of new materials for air separation by PSA is given.

3.4.1. Experimental

Excess adsorption isotherms of N_2, O_2 and Ar were determined for crystalline samples of four dipeptide crystals, VI, IA, IV and VV, at 5 ºC, 20 ºC and 35 ºC. Samples of dipeptides VI, IA, IV and VV were purchased from Bachem. Samples were received as a crystalline white powder [9], which were regenerated overnight, under vacuum (< 1 mbar), at 70 ºC, before being used in the adsorption experiments. The adsorption isotherms were determined using the volumetric method. This method is based on measuring the variation of pressure of the gas after an expansion between two tanks of known volume, one of which contains the adsorbent sample. Using an appropriate equation of state for the gas phase (the Peng-Robinson equation was used in this work) and performing a mass balance, it is possible to determine the total amount adsorbed. The sorbate concentration is determined by dividing this value by the sample mass. The sample tank and feed tank volumes were, respectively, 13.32 mL and 54.37 mL. The masses of VI, IA, IV and VV used were, respectively, 2.4927 g, 1.0144 g, 2.4131 g and 1.0064 g. The pressure transducer used was a WIKA P-30, 0-6 bar (accuracy of 0.1 % FS). The temperature of the system was controlled through immersion in a Huber CCE-K12 thermostatic bath. Swagelok tubing and valves were used to connect the tanks, the gas feed and the exhaust. Pressures below 1 atm were achieved using a Vacuubrand RZ 2.5 vacuum pump. Alphagaz 1 gases, supplied by Air Liquide, were used, with purities of 99.99965 % for O_2 and 99.99945 % for the remaining ones.

3.4.2. Results and Discussion

3.4.2.1. Adsorption Isotherms and Monocomponent Selectivities

The adsorption isotherms of Ar, O_2 and N_2 in the crystalline powder of dipeptides VI, IA, IV and VV, at 20 ºC, are shown, grouped by material, in Figure 3.3. Graphs of isotherms at 5 ºC

and 35 ºC and grouped by gas species are presented in Appendix C. Adsorption takes place, essentially, in the Henry region, with isotherms being only slightly bent. 80 % of adsorption took place, at least, in the first 30 s, and very often in the first 5-10 s. The dipeptide crystals in the powder are 1-50 μm in length. Desorption isotherms were also determined in every case (not shown) and hysteresis was never detected. N_2 adsorption isotherms have been determined before, for 25 ºC [4], and are similar to the ones here reported.

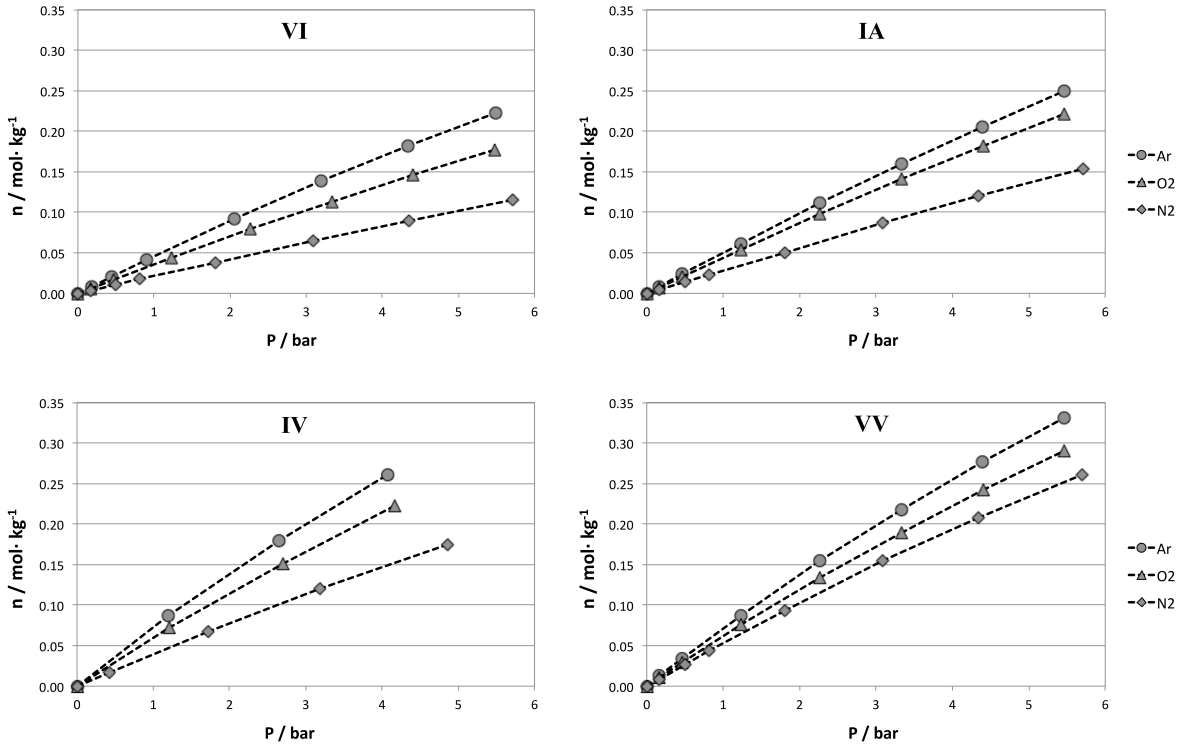

Figure 3.3. Excess adsorption isotherms [54] of Ar, O_2 and N_2 on VI, IA, IV and VV, at 20 ºC, grouped per material.

The adsorption isotherms were numerically fitted with the Volmer equation,

$$bP = \frac{\theta}{1-\theta}\exp\left(\frac{\theta}{1-\theta}\right) \tag{3-1}$$

where

$$b = \frac{K_H}{n_{max}} \tag{3-2}$$

and

$$\theta \equiv \frac{n}{n_{max}} \tag{3-3}$$

b is the affinity constant, P is the pressure, θ is the amount adsorbed relative to the maximum that can be adsorbed, K_H is Henry's constant, n is the adsorbed concentration and n_{max} is the maximum adsorbed concentration. The parameters fitted were n_{max} and b. Both excess and absolute adsorption equilibrium values were determined. Fitting results are shown in Appendix C.

A previous report [4] showed that CO_2 adsorption in VA-class dipeptides has a mixed localised/mobile character. However, the N_2 and O_2 molecules and the Ar atom are much shorter and more electronically homogeneous than the CO_2 molecule. This leads us to think that the N_2, O_2 and Ar adsorbed phases must have a predominantly mobile character, being thus better represented by the Volmer rather than the Langmuir equation. Nonetheless, the Henry constants determined for both equations, through Eq. (3-2), are essentially the same, with only b and n_{max} varying. This was to be expected, since both equations reduce to the Henry equation at low loadings.

Adsorption trends are similar for the four dipeptides. The adsorbed concentration varies according to the sequence $Ar>O_2>N_2$, for all cases. This is a highly unusual sequence, as previously discussed, having been observed only in two other adsorbents [52, 53]. It is noteworthy that both of these cases refer to fully organic microporous materials, like the crystalline dipeptides considered here. For the three gas species, the amount adsorbed increases with pore size/porosity, i.e., VI<IA<IV<VV. This increase is not even, being greater for the least adsorbed species, N_2, and smallest for the most adsorbed species, Ar (see Appendix C). A similar overall trend of increased adsorption with pore size was also observed for CO_2 and CH_4 [4].

Figure 3.4 plots Ar/O_2 and O_2/N_2 monocomponent selectivities (*i.e.*, concentration ratios) as a function of pressure, for VI, at the three temperatures used. Monocomponent adsorption selectivities were determined from the adsorption results, with adsorption isotherms being expressed by data-fitted Volmer equations. The graphs for IA, IV and VV are shown in Appendix C, since they display the exact same trends, with somewhat smaller values. The monocomponent selectivity curves have the typical shape for two gases displaying Type I adsorption isotherms; an asymptotic decline to the ratio of capacities. Since, for the pressure range tested, the isotherms are still close to the Henry region, this decline is moderate. Selectivity variation with temperature is very dependent on pressure, with curves for different

temperatures crossing in the graph. Still, at close to vacuum (Henry) conditions, the selectivity always decreases with temperature, as a consequence of the greater heat of adsorption of the most adsorbed gas. This is not always the case for the other three dipeptides, as will be later discussed, and is apparent in their respective graphs (see Appendix C).

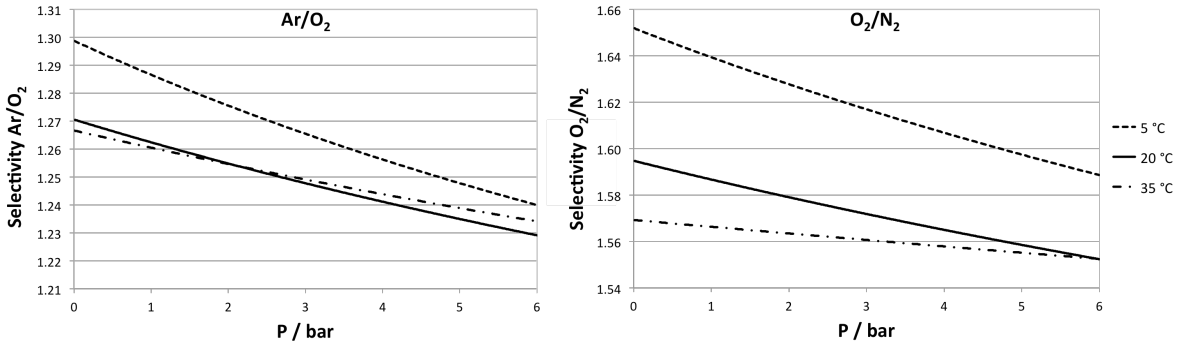

Figure 3.4. Variation of Ar/O_2 and O_2/N_2 selectivities with pressure, for VI, at 5 ºC, 20 ºC and 35 ºC.

The vacuum (Henry) Ar/O_2 and O_2/N_2 selectivities of the four dipeptides, at 20 ºC, are plotted against pore size in Figure 3.5. The selectivities of VI, IV and VV form an approximately linear, descending trend with increasing pore size, reflecting the importance of confinement in determining the unusual sequence of intensity of adsorption. IA is a clear outlier, falling significantly below the trend line, especially for Ar/O_2. The linearity of the trend may be just a coincidence, but it is interesting to notice that, if it was to continue, the Ar/O_2 and O_2/N_2 selectivities would reach 1 at ~0.55 nm and ~0.46 nm, respectively. These are still very small pore sizes, again showing the paramount importance of pore size in determining the unordinary sequence of adsorption.

The well-established and consistent kinetic selectivities of atmospheric gases in CMSs [43, 45, 50, 55, 56] show that the relative size of the three species, in the context of adsorption and diffusion, in atomic-sized pores of hydrophobic materials, is N_2>Ar>O_2. The Lennard-Jones atomic diameter of Ar and minimum molecular widths of N_2 and O_2 have been estimated as 0.32, 0.34 and 0.31 nm, respectively [57], all clearly below the pore sizes of the dipeptide crystals used.

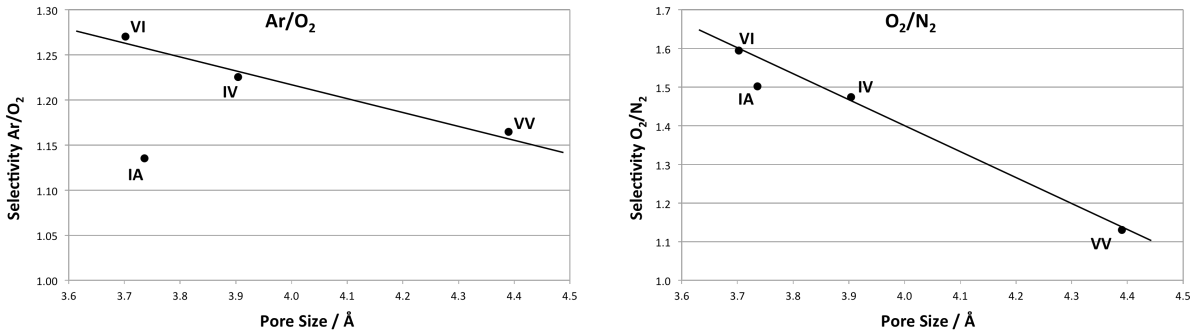

Figure 3.5. Ar/O_2 and N_2/O_2 selectivities of the four dipeptides, at 20 ºC, plotted against nominal pore size. The two straight lines represent the linear decreasing trend apparent for three of the four points, in both graphs.

Studies performed using ^{129}Xe NMR [3, 10] showed that sorbate-sorbent interactions in dipeptide crystal micropores are maximised when pore-size precisely matches sorbate size, decreasing for bigger and smaller pores. This is exactly the same behaviour as that observed for hard materials [57]. We thus think that the size sequence of the three gases established from CMS adsorption experiments is also valid for dipeptide crystals. A lot has also been made of the possibility of using the chiral pores of dipeptide crystals to separate enantiomers [2, 8]. However, in the context of adsorption of symmetrical molecules/atoms smaller than the pores, there is not reason to think that pore helicity and chirality influence adsorption.

The Lennard-Jones minimum width serves as a good indicator of cut-off size for sieving but is not the best measure of the most energetically favourable intermolecular distance. From the Lennard-Jones potential, this distance can be estimated as $2^{1/6}$ times the minimum width, that is, 0.36, 0.38 and 0.34 nm, respectively [57]. It has long been known that molecules even slightly bigger than the pore/constriction experience a significantly lower adsorption potential [57], which is precisely why CMSs are able to have very high kinetic selectivities. The N_2 molecule is slightly bigger than the pore size of VI and IA, being thus tempting to explain the fact that N_2 is the least adsorbed species because of a similar effect. This could explain both why N_2 is the least adsorbed species and the most sensitive to pore size increment. However, for IV and VV, this effect should disappear and N_2 become the most adsorbed species. This is not the case, so there are clearly other factors involved. The range of phenomena determining adsorption becomes much clearer upon analysis of the heats of adsorption.

3.4.2.2. Heats of Adsorption and Influence of Pore Size in Adsorption

Isosteric heats of adsorption were determined using the Clausius-Clapeyron equation. Assuming ideal gas behaviour, it can be written as,

$$q_{st} = -R\left(\frac{\partial \ln(P)}{\partial\,(1/T)}\right)_n \tag{3-4}$$

where q_{st} is the isosteric heat of adsorption, R is the ideal gas constant and T is the absolute temperature. Having adsorption isotherms for 5 ºC, 20 ºC and 35 ºC, heats of adsorption were estimated through linearization of $\ln(P)$ vs $(1/T)$, for a given n (when pressure values corresponding to the desired n were unavailable, they were estimated by linear interpolation). Results are shown in Figure 3.6.

With the exception of N_2, it is clear the heat of adsorption does not show any variation trend with adsorbed concentration, being approximately constant in the tested range. The N_2 trend, however, is also not clear enough, so for it, too, a constant heat of adsorption was considered. Therefore, the heat of adsorption of each gas was obtained by averaging the values of Figure 3.6. These are shown in Figure 3.7. The errors were calculated from this averaging, corresponding to 95 % confidence intervals.

In other materials, excluding those containing silver, the heats of adsorption of N_2, O_2 and Ar are typically in the range of 15-27 kJ/mol, 13-25 kJ/mol and 12-20 kJ/mol, respectively [34, 36, 44, 45, 47-51, 58-60]. The heats of adsorption determined for VI, IA, IV and VV are close to, or below, the lower limit of these ranges. For Ar and O_2, all the values are within the respective ranges. For N_2, three out of four of those values are clearly and significantly below 15 kJ/mol, the lower limit mentioned. We were unable to find a single isosteric heat of adsorption for N_2 below 15 kJ/mol in the literature, showing that the N_2 interaction with the aliphatic side-chains is exceptionally weak.

In the Henry region of a Type I isotherm, the isosteric heat of adsorption can be related to Henry's constant by the van't Hoff equation,

$$K_H = K_H^{\infty} \cdot \exp\left(\frac{q_{st}}{RT}\right) \tag{3-5}$$

where K_H^{∞} is the pre-exponential factor. K_H^{∞} expresses the entropic and capacity contributions to Henry's constant [61]. By using the q_{st} values obtained from the adsorption isotherms at three temperatures and the K_H obtained from the data fitting of individual adsorption

isotherms, it is possible, using Eq. (3-5), to calculate a K_H^{∞} for each isotherm. Results shown in Figure 3.7 are averages for the three temperatures, with the respective errors.

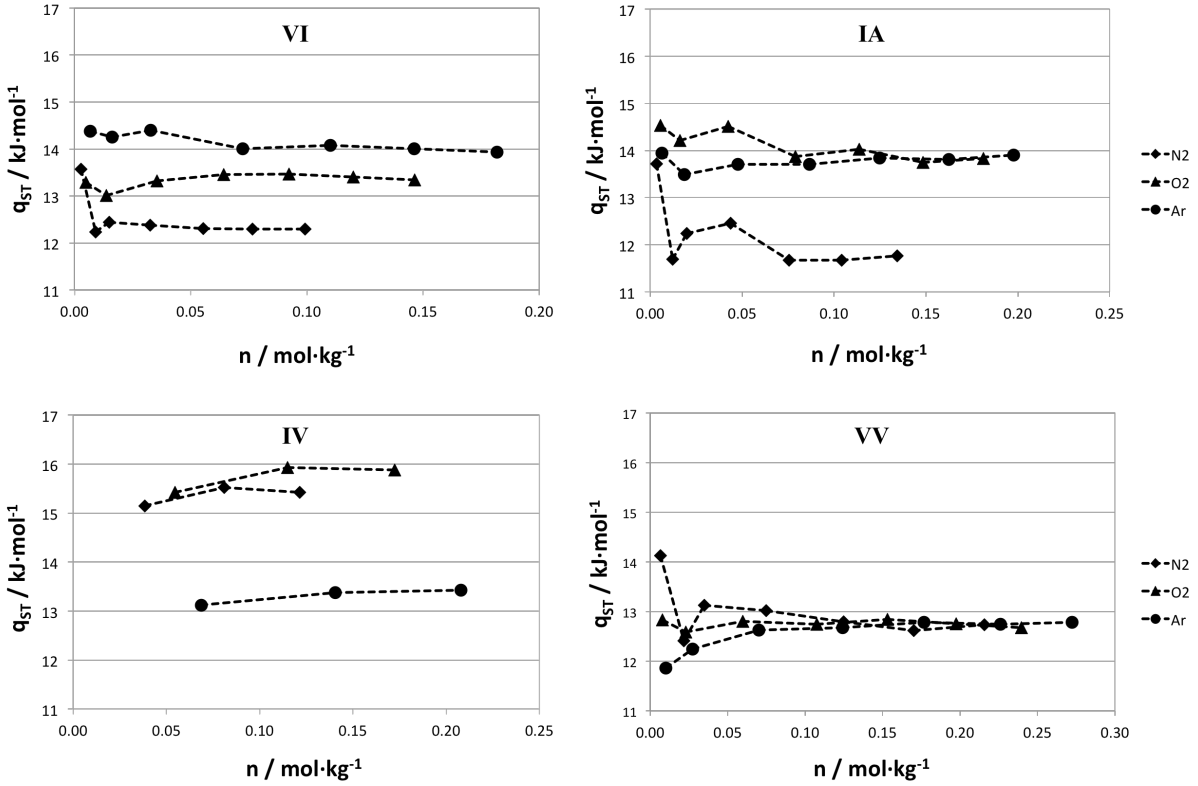

Figure 3.6. Heat of adsorption as a function of the adsorbed concentration, for Ar, O_2 and N_2, in VI, IA, IV and VV, grouped per adsorbent.

The sequences observed for the heats of adsorption in Figure 3.7 are less regular than those observed in the adsorption isotherms. In fact, it could be argued they are highly irregular. VI is the only material having an Ar>O_2>N_2 trend for heats of adsorption, equivalent to that existing in the adsorption isotherm. No other material shows it, or even any other trend. Regarding variation with pore size, only for Ar there seems to be a trend, VV<IV<IA<VI, precisely the opposite of that observed for the adsorption isotherms. This indicates that Ar-framework interactions diminish with increasing pore size. For N_2 and O_2, variation of adsorbent-adsorbate interaction intensity with pore size is not monotonic. The complex profiles obtained for O_2 and N_2 are very similar to each other, which could indicate that pore size increase has a similar physical effect on the two species, different from the one it has on Ar.

The polarisabilities of Ar and O_2 are, respectively, 1.6411 and 1.5812 $Å^3$ [62]. Both species do not have a dipole moment, but only Ar does not have a quadrupole moment. Thus, since adsorbate-adsorbent interactions can rarely be considered exclusively dispersive, O_2 typically adsorbs more than Ar, due to the effect of its non-negligible quadrupole moment [26, 36, 39, 44]. However, in the confined environment of a micropore, the polarisability of atoms and molecules may be influenced by the limited ways in which they are able to interact with the framework [63], making such analyses more complicated.

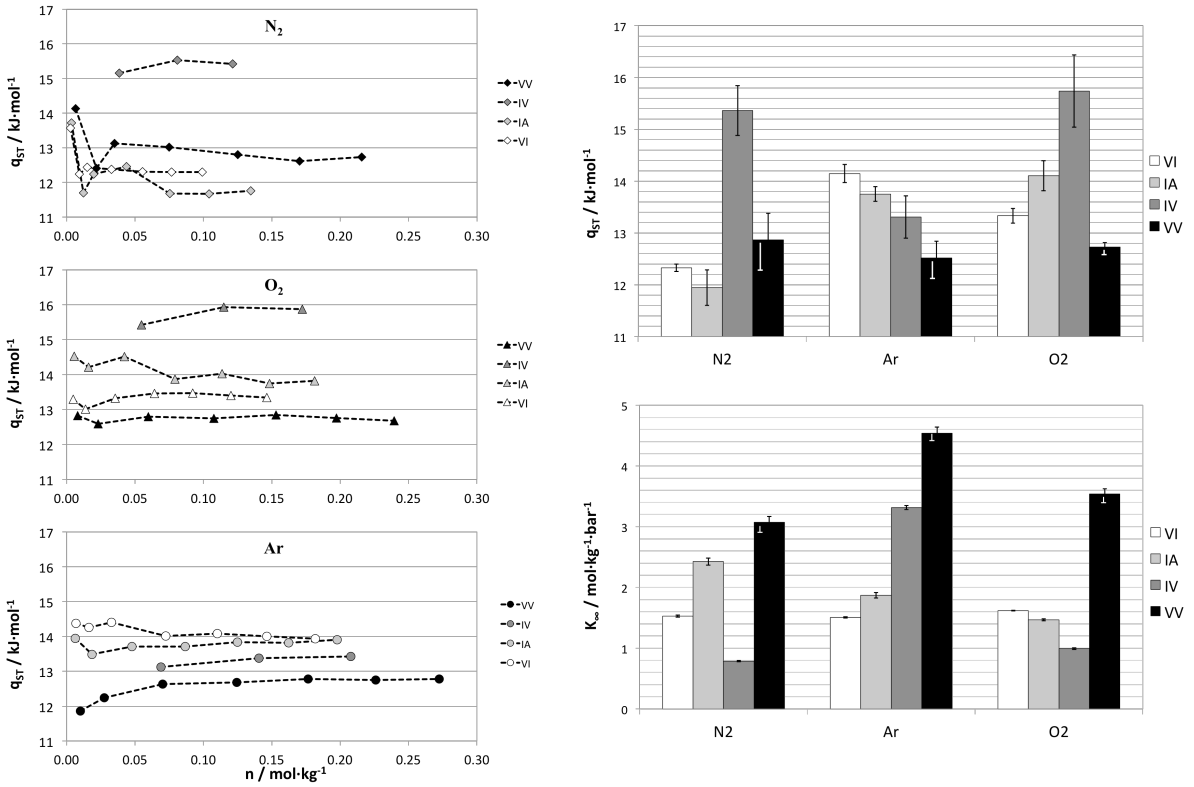

Figure 3.7. On the left, heat of adsorption as a function of the adsorbed concentration, for Ar, O_2 and N_2, in VI, IA, IV and VV, grouped per gas. On the right, average heat of adsorption and pre-exponential constant (as per Eq. (3-2)), for Ar, O_2 and N_2, in VI, IA, IV and VV, grouped per gas.

Apparently, even the smallest pore (0.37 nm) is not too tight in order to hinder adsorption of the 0.36 nm-wide Ar atom. Increasing pore size probably causes a decrease in the intensity of the adsorption potential well inside the pore, lowering the heat of adsorption. In the case of O_2, however, there is an increase in the heat of adsorption from VI to IA and from IA to IV. Given that an O_2 molecule is only slightly smaller than an Ar atom, it is unlikely the pore size increase does not contribute to decrease the adsorption potential intensity, as with Ar. It is

likely that the increased rotational freedom the O_2 molecules experience allows for a better matching of the pore morphology, overcoming the decreased adsorption potential effect. Between IV and the much bigger VV pore, the decreasing trend observed for Ar is established. For the bigger N_2 molecule, there are no sensible differences between VI and IA, and only for the IV framework is the increase in the heat of adsorption clear. Besides the rotational freedom factor mentioned for O_2, there may exist a small contribution from the pore size increase beyond the optimal intermolecular distance of N_2, 0.38 nm. Finally, for N_2 also, the big increase in pore size associated with VV significantly decreases the heat of adsorption. In fact, from IV to VV, the heat of adsorption of all species decreases. Because the Lennard-Jones diameter/widths of Ar, N_2 and O_2 are smaller than the nominal size of the smallest pore (VI), the influence of framework flexibility is not especially significant, with the possible exception of N_2.

If compared for the same material and different species, only VI displays a clear trend in heat of adsorption variation, $Ar>O_2>N_2$. For IA, the Ar and O_2 values are within the error range, although both are still clearly higher than that of N_2, $Ar \approx O_2 > N_2$. For IV, the heats of adsorption of O_2 and N_2 are much larger than that of Ar, $O_2 \approx N_2 > Ar$ and, for VV, no sensible differences exist between the three, $O_2 \approx Ar \approx N_2$.

For exclusively dispersive interactions, the heat of adsorption should only depend on the polarisabilities of the different species, so it would be expectable that Ar be more strongly adsorbed than O_2. The N_2 molecule has a nominal polarisability greater than the Ar atom, but since its confinement limitations are greater than those of Ar, both higher and lower values are reasonable. It is possible that due to their quadrupole moments, the O_2 and N_2 molecules bond, even if weakly, with the slightly polarised H atoms from the aliphatic side-chains forming the pore walls. Since the polarisability of Ar is only marginally higher than that of O_2, that effect could be enough to switch the order of the heats of adsorption of the two species. An heat of adsorption of N_2 similar to that of O_2, in IV, may be only the reflection of the still important confinement effects having a greater impact on the bigger N_2 molecule than on that of O_2. This would also explain why N_2 heats of adsorption are inferior to those of O_2 and Ar for VI and IA, despite having greater polarisability and quadrupole moment. These confinement effects are certainly much less important in VV, if at all significant. Therefore, it would be expectable that a $N_2>O_2>Ar$ order was well established by then, which seems to not be the case.

Only for N_2 does the isosteric heat of adsorption show some kind of trend. For three of the four dipeptides, the isosteric heat of adsorption of N_2 forms a "V-shaped" curve for low adsorbed concentrations, only then stabilizing.

The variation patterns observed for the K_H^∞ are even harder to explain. In the four dipeptides considered, the capacities should be similar, therefore differences in K_H^∞ must be explained by variations in entropic contributions. The entropy of the mobile adsorbate depends on translational, rotational and vibrational components [64]. For Ar, one could tentatively try to interpret the increases in K_H^∞ by considering that rotational entropy is absent in Ar atoms, thus the great increases may reflect increased vibrational and translational freedom as the frameworks become more open. In the case of O_2 and N_2, it is possible the highly hindered non-axial rotation in VI potentiates faster translation inside the pores, while the slightly larger IA and IV allow greater rotational freedom, thus limiting translation inside the pore. This factor is the basis for some separations using microporous membranes [65, 66]. The much bigger VV pores allow such rotational freedom that the increasing trend in K_H^∞ observed for Ar is finally established.

Overall, it is astonishing how such regular patterns in amount adsorbed (adsorption isotherms), indicating equally regular free energy variation patterns, stem from such wide and irregular swings in entropy and enthalpy as those shown in Figure 3.7.

3.4.2.3. Significance for PSA Separation of Air

In spite of the extraordinary Ar/O_2 selectivities reported, use of hydrophobic dipeptides as PSA adsorbents is highly unlikely. Besides good selectivities, good working adsorption capacities are needed to implement any PSA separation [24]. The nearly linear isotherms presented allow a working adsorption capacity essentially proportional to the pressure range used in the PSA, an excellent property. However, the overall capacities are low, when compared to other materials. At ambient temperatures and for 1 bar, values of oxygen/argon adsorption between 0.1 mol/kg and 0.2 mol/kg are the most typical in materials that have been tested as PSA adsorbents [28-30, 33-35, 38]. These results are all significantly above the ~0.05 mol/kg obtained for Ar adsorption in VI. It thus seems these materials show very little potential as a PSA adsorbent, as long as Ag-based adsorbents remain commercially viable.

Nonetheless, that the pores of crystalline hydrophobic VA-class dipeptides can generate good Ar/O_2 selectivities was totally unexpected. This knowledge may be used to search for new (or

otherwise) materials that combine good selectivities with good capacities. The organic materials having the $Ar>O_2>N_2$ adsorption sequence, also observed in this work, also have very hydrophobic pores [52, 53], which leads us to think this is a fundamental property, together with pore size, determining the sequence. This probably results from the limited influence the quadrupolar moment of O_2 has in hydrophobic pores.

The main causes of the low capacities of the materials are their low porosities and micropore concentrations. The four dipeptide frameworks considered have very similar densities, making porosity highly dependent on pore size. The crystallographic porosities of dipeptides VI, IA, IV and VV are 5.7, 6.0, 6.3 and 8.3 % [7] and the micropore concentrations are 0.048, 0.053, 0.053 and 0.067 cm^3/g, respectively. These are very small values, especially the porosities, when compared to materials used in O_2-generation PSA. Ag-mordenite has been reported as having values of 17 % and 0.062 cm^3/g [34], AgLiLSX has 27 % and 0.118 cm^3/g [67] and Ag-ETS-10 has 38 % [37, 68] and 0.13 cm^3/g [69, 70]. The low porosity of the dipeptides is a contingent property, which does not need to exist in other materials with unidimensional pores, even for such small pores; it stems mostly from the low pore concentration existent in the dipeptides, 0.45 pores/nm^2 to 0.48 pores/nm^2. A material possessing cylindrical unidimensional pores has a geometrical limiting porosity of 78.5 %, corresponding, for a material with 0.4 nm-wide pores, to 6.25 pores/nm^2. Therefore, there is plenty of room for improvement of porosities. A material with pores having similar morphologies and chemical properties as those of the four dipeptides studied in this work, but with significantly higher porosity could, perhaps, combine both the good selectivity observed with the desired adsorption capacities. Such a material should have highly hydrophobic and less than 0.5 nm-wide pores, and a porosity of, at least, 20 %. With the large numbers of organic microporous solids discovered in recent years, there are plenty of candidates to be tested [71, 72].

3.5. Conclusions

The first part of this chapter outlines the preliminary results obtained with dipeptide single-crystal permeation experiments, and how they were able to indicate highly positive host-guest interaction potentialities with atmospheric gases. Ar permeation in the millimetre-sized VI crystals seems to have been limited by the presence of pore blockage.

In the second part, crystalline powders of hydrophobic dipeptides VI, IA, IV and VV were tested as adsorbents of N_2, O_2 and Ar. The three gases adsorb in the sequence $Ar>O_2>N_2$, thus displaying Ar/O_2 selectivity, an extremely rare result. The best Ar/O_2 selectivities were obtained for VI; at 5 ºC and near vacuum conditions, the Ar/O_2 selectivity is 1.30, the highest ever measured in Ag-free adsorbents. Despite the good selectivity, the low capacities of the materials strongly hinder their use in PSA for O_2 generation from air. At 20 °C and 1 bar, the adsorption of Ar, O_2 and N_2 on VI is, respectively, 0.048 mol/kg, 0.038 mol/kg and 0.023 mol/kg.

The exceptional adsorption sequence observed, $Ar>O_2>N_2$, stems from the very small pore size of the materials. The combination of geometrical confinement effects, limitation of rotational degrees of freedom and low polarity limit both the enthalpic and the entropic contributions to the adsorption of O_2 and N_2, much more than that of Ar.

The low capacity of the dipeptides tested is strongly related to their low porosity, below 10 % in all cases. A material with chemical and morphologically similar pores, but greater porosities, may be able to combine both the good selectivities observed with greater capacities.

3.6. References

1. C. H. Görbitz, Nanotubes from hydrophobic dipeptides: pore size regulation through side chain substitution, New J. Chem. 27 (2003), 1789-1793.
2. C. H. Görbitz, Microporous Organic Materials from Hydrophobic Dipeptides, Chem. Eur. J. 13 (2007), 1022–1031.
3. R. Anedda, D. V. Soldatov, I. L. Moudrakovski, M. Casu, and J. A. Ripmeester, A New Approach to Characterizing Sorption in Materials with Flexible Micropores, Chem. Mater. 20 (2008), 2908-2920.
4. A. Comotti, A. Fraccarollo, S. Bracco, M. Beretta, G. Distefano, M. Cossi, L. Marchese, C. Riccardi, and P. Sozzani, Porous dipeptide crystals as selective CO2 adsorbents: experimental isotherms vs. grand canonical Monte Carlo simulations and MAS NMR spectroscopy, Cryst. Eng. Commun. 15 (2013), 1503–1507.
5. M. Dvoyashkin, A. Wang, S. Vasenkov, and C. R. Bowers, Xenon in l--alanyl--l--valine nanochannels: A highly ideal molecular single--file system, J. Phys. Chem. Lett. 4 (2013), 3263-3267.
6. M. Dvoyashkin, H. Bhase, N. Mirnazari, S. Vasenkov, and C. R. Bowers, Single-File Nanochannel Persistence Lengths from NMR, Anal. Chem. 86 (2014), 2200-2204.
7. D. V. Soldatov, I. L. Moudrakovski, E. V. Grachev, and J. A. Ripmeester, Micropores in Crystalline Dipeptides as Seen from the Crystal Structure, He Pycnometry, and 129Xe NMR Spectroscopy, J. Am. Chem. Soc. 128 (2006), 6737-6744.
8. D. V. Soldatov, I. L. Moudrakovski, and J. A. Ripmeester, Dipeptides as Microporous Materials, Angew. Chem. Int. Ed. 43 (2004), 6308-6311.
9. A. Comotti, S. Bracco, G. Distefano, and P. Sozzani, Methane, carbon dioxide and hydrogen storage in nanoporous dipeptide-based materials, Chem. Commun. 45 (2009), 284–286.
10. I. Moudrakovski, D. V. Soldatov, J. A. Ripmeester, D. N. Sears, and C. J. Jameson, Xe NMR lineshapes in channels of peptide molecular crystals, Proc. Nat. Acad. Sci. 101 (2004), 17924-17929.
11. C.-Y. Cheng and C. R. Bowers, Observation of Single-File Diffusion in Dipeptide Nanotubes by Continuous-Flow Hyperpolarized Xenon-129 NMR Spectroscopy, Chem. Phys. Chem. 8 (2007), 2077-2081.
12. C. H. Görbitz, M. Nilsen, K. Szeto, and L. W. Tangen, Microporous organic crystals: an unusual case for L-leucyl–L-serine, Chem. Commun. (2005), 4288–4290.
13. C. H. Görbitz, An exceptionally stable peptide nanotube system with flexible pores, Acta Crystallogr. B58 (2002), 849-854.
14. C. H. Görbitz, Monoclinic nanoporous crystal structures for L-valyl–L-alanine acetonitrile solvate hydrate and L-valyl–L-serine trifluoroethanol solvate, Cryst. Eng. Commun. 7 (2005), 670-673.
15. H. Zhang, K. Siegrist, D. F. Plusquellic, and S. K. Gregurick, Terahertz Spectra and Normal Mode Analysis of the Crystalline VA Class Dipeptide Nanotubes, J. Am. Chem. Soc. 130 (2008), 17846–17857.
16. C. H. Görbitz, M. Nilsen, K. Szeto, and L. W. Tangen, Microporous organic crystals: an unusual case for L-leucyl–L-serine, Chem. Commun. 41 (2005), 4288–4290.
17. R. J. Fletterick, C.-c. Tsai, and R. E. Hughes, The Crystal and Molecular Structure of L-Alanyl-L-alanine, J. Phys. Chem. 75 (1971), 918-922.

18. C. F. Macrae, I. J. Bruno, J. A. Chisholm, P. R. Edgington, P. McCabe, E. Pidcock, L. Rodriguez-Monge, R. Taylor, J. v. d. Streek, and P. A. Wood, Mercury CSD 2.0 - new features for the visualization and investigation of crystal structures, J. Appl. Cryst. 41 (2008), 466-470.
19. H. Verweij, M. C. Schillo, and J. Li, Concept: Fast Mass Transport through Carbon Nanotube Membranes, Small 3 (2007), 1996–2004.
20. J. K. Holt, H. G. Park, Y. Wang, M. Stadermann, A. B. Artyukhin, C. P. Grigoropoulos, A. Noy, and O. Bakajin, Fast Mass Transport Through Sub–2-Nanometer Carbon Nanotubes, Science 312 (2006), 1034-1037.
21. J. Durão and L. Gales, Guest diffusion in dipeptide crystals, Cryst. Eng. Comm. 15 (2013), 1532-1535.
22. M. J. Kirschner, in *Ullmann's Encyclopedia of Industrial Chemistry*, (ed. B. Elvers), (Wiley-VCH, 2000).
23. J. G. Hansel and U. b. Staff, in *Kirk-Othmer Encyclopedia of Chemical Technology*, (Wiley-VCH, 2005).
24. D. M. Ruthven, in *Principles of Adsorption and Adsorption Processes*, Ch. Adsorption Separation Processes: I. Cyclic Batch Systems, pp. 336-379 (John Wiley & Sons, 1984).
25. D. Ferreira, R. Magalhães, P. Taveira, and A. Mendes, Effective Adsorption Equilibrium Isotherms and Breakthroughs of Water Vapor and Carbon Dioxide on Different Adsorbents, Ind. Eng. Chem. Res. 50 (2011), 10201–10210.
26. N. D. Hutson, S. U. Rege, and R. T. Yang, Mixed Cation Zeolites: LixAgy-X as a Superior Adsorbent for Air Separation, AIChE J. 95 (1999), 724-734.
27. J.-B. Kim, H. Jo, H. Yoshioka, and H. Kiyama, *Selective Adsorbent for Nitrogen and Method for Separating Air Using the Same*, U.S.P.a.T. Office, Editor. 2006, Air Water, Inc.: U.S.
28. D. P. Dee, R. L. Chiang, E. J. Miller, and R. D. Whitley, *High Purity Oxygen Production by Pressure Swing Adsorption*, U.S.P.a.T. Office, Editor. 2003, Air Products and Chemicals, Inc.: U.S.
29. K. S. Knaebel and A. Kandybin, *Pressure Swing Adsorption System to Purify Oxygen*, U.S.P.a.T. Office, Editor. 1993, Ohio State University: U.S.
30. J. C. Santos, P. Cruz, T. Regala, F. D. Magalhães, and A. Mendes, High-Purity Oxygen Production by Pressure Swing Adsorption, Ind. Eng. Chem. Res. 46 (2007), 591-599.
31. J.-G. Jee, M.-B. Kim, and C.-H. Lee, Pressure Swing Adsorption Processes to Purify Oxygen Using a Carbon Molecular Sieve, Chem. Eng. Sci. 60 (2005), 869-882.
32. S. Hayashi, M. Kawai, and T. Kaneko, Dynamics of High Purity Oxygen PSA, Gas. Sep. Purif. 10 (1996), 19-23.
33. A. I. Kandybin, R. A. Anderson, and D. L. Reichley, *System for Separation of Oxygen from Argon/Oxygen Mixture*, U.S.P.a.T. Office, Editor. 1995, Arbor Research Corporation: U.S.
34. B. E. Wilkerson, *The Adsorption of Argon and on Silver Mordenite*, in *Chemical Engineering Department*. 1990, The Ohio State University.
35. R. T. Yang, Y. D. Chen, J. D. Peck, and N. Chen, Zeolites Containing Mixed Cations for Air Separation by Weak Chemisorption-Assisted Adsorption, Ind. Eng. Chem. Res. 35 (1996), 3093-3099.
36. J. Sebastian and R. V. Jasra, Sorption of Nitrogen, Oxygen, and Argon in Silver-Exchanged Zeolites, Ind. Eng. Chem. Res. 44 (2005), 8014-8024.

37. A. Ansón, S. M. Kuznicki, T. Kuznicki, T. Haastrup, Y. Wang, C. C. H. Lin, J. A. Sawada, E. M. Eyring, and D. Hunter, Adsorption of argon, oxygen, and nitrogen on silver exchanged ETS-10 molecular sieve, Microporous Mesoporous Mater. 109 (2008), 577-580.
38. M. Shi, J. Kim, J. A. Sawada, J. Lam, S. Sarabadan, T. M. Kuznicki, and S. M. Kuznicki, Production of Argon Free Oxygen by Adsorptive Air Separation on Ag-ETS-10, AIChE J. 59 (2013), 982-987.
39. S. A. Peter, A. S. Moharir, and R. V. Jasra, Sr2+ Exchanged Zeolite X as an Adsorbent Material for Chromatographic Separation of Argon-Oxygen Gaseous Mixture, Sep. Sci. Technol. 46 (2011), 500-506.
40. A. Ansón, S. M. Kuznicki, T. Kuznicki, B. C. Dunn, E. M. Eyring, and D. B. Hunter, Separation of Argon and Oxygen by Adsorption on a Titanosilicate Molecular Sieve, Sep. Sci. Technol. 44 (2009), 1604–1620.
41. A. Hazra, S. Bonakala, S. K. Reddy, S. Balasubramanian, and T. K. Maji, Effect of Pillar Modules and Their Stoichiometry in 3D Porous Frameworks of Zn(II) with [Fe(CN)6]3−: High CO2/N2 and CO2/CH4 Selectivity, Inorg. Chem. 52 (2013), 11385–11397.
42. S. M. Humphrey, S. E. Oungoulian, J. W. Yoon, Y. K. Hwang, E. R. Wise, and J.-S. Chang, Hysteretic sorption of light gases by a porous metal–organic framework containing tris(para-carboxylated) triphenylphosphine oxide, Chem. Commun. 44 (2008), 2891–2893.
43. S. W. Rutherford and D. D. Do, Characterization of Carbon Molecular Sieve 3A, Langmuir 16 (2000), 7245-7254.
44. R. S. Pillai, S. A. Peter, and R. V. Jasra, Adsorption of carbon dioxide, methane, nitrogen, oxygen and argon in NaETS-4, Microporous Mesoporous Mater. 113 (2008), 268–276.
45. Y.-S. Bae and C.-H. Lee, Sorption kinetics of eight gases on a carbon molecular sieve at elevated pressure, Carbon 43 (2005), 95-107.
46. M. C. Campo, F. D. Magalhães, and A. Mendes, Comparative study between a CMS membrane and a CMS adsorbent: Part I—Morphology, adsorption equilibrium and kinetics, J. Membr. Sci. 346 (2010), 15-25.
47. S. W. Rutherford and J. E. Coons, Adsorption equilibrium and transport kinetics for a range of probe gases in Takeda 3A carbon molecular sieve, J. Colloid Interface Sci. 284 (2005), 432–439.
48. P. Rallapalli, K. P. Prasanth, D. Patil, R. S. Somani, R. V. Jasra, and H. C. Bajaj, Sorption studies of CO2, CH4, N2, CO, O2 and Ar on nanoporous aluminum terephthalate MIL-53(Al)], J. Porous Mater. 18 (2011), 205–210.
49. S. A. Peter, J. Sebastian, and R. V. Jasra, Adsorption of Nitrogen, Oxygen, and Argon in Mono-, Di-, and Trivalent Cation-Exchanged Zeolite Mordenite, Ind. Eng. Chem. Res. 44 (2005), 6856-6864.
50. C. R. Reid, I. P. O'koye, and K. M. Thomas, Adsorption of Gases on Carbon Molecular Sieves Used for Air Separation. Spherical Adsorptives as Probes for Kinetic Selectivity, Langmuir 14 (1998), 2415-2425.
51. G. Sethia, R. S. Pillai, G. P. Dangi, R. S. Somani, H. C. Bajaj, and R. V. Jasra, Sorption of Methane, Nitrogen, Oxygen, and Argon in ZSM-5 with different SiO2/Al2O3 Ratios: Grand Canonical Monte Carlo Simulation and Volumetric Measurements, Ind. Eng. Chem. Res. 49 (2010), 2353–2362.

52. P. M. Budd, K. J. Msayib, C. E. Tattershall, B. S. Ghanem, K. J. Reynolds, N. B. McKeown, and D. Fritsch, Gas separation membranes from polymers of intrinsic microporosity, J. Membr. Sci. 251 (2005), 263–269.
53. Y. Belmabkhout, G. D. Weireld, and M. Frère, High-Pressure Adsorption Isotherms of N2, CH4, O2, and Ar on Different Carbonaceous Adsorbents, J. Chem. Eng. Data 49 (2004), 1379-1391.
54. A. L. Myers, Thermodynamics of Adsorption in Porous Materials, AIChE J. 48 (2002), 145-160.
55. J.-G. Jee, S.-J. Lee, and C.-H. Lee, Comparison of the Adsorption Dynamics of Air on Zeolite 5A and Carbon Molecular Sieve Beds, Korean J. Chem. Eng. 21 (2004), 1183-1192.
56. T. J. Giesy and M. D. LeVan, Mass transfer rates of oxygen, nitrogen, and argon in carbon molecular sieves determined by pressure-swing frequency response, Chem. Eng. Sci. 90 (2013), 250–257.
57. J. Koresh and A. Soffer, Study of Molecular Sieve Carbons, Part 2.-Estimation of Cross-sectional Diameters of Non-spherical Molecules, J. C. S. Faraday I 76 (1980), 2472-2485.
58. J. A. Dunne, M. Rao, S. Sircar, R. J. Gorte, and A. L. Myers, Calorimetric Heats of Adsorption and Adsorption Isotherms. 2. O2, N2, Ar, CO2, CH4, C2H6, and SF6 on NaX, H-ZSM-5, and Na-ZSM-5 Zeolites, Langmuir 12 (1996), 5896-5904.
59. N. D. Hutson and R. T. Yang, Structural Effects on Adsorption of Atmospheric Gases in Mixed Li,Ag–X-Zeolite, AIChE J. 46 (2000), 2305-2317.
60. S. A. Peter, A. S. Moharir, and R. V. Jasra, Selective Adsorption of Oxygen over Argon in Alkaline-Earth-Metal Cation-Exchanged Zeolite X, Ind. Eng. Chem. Res. 49 (2010), 7524–7529.
61. D. Atkinson and G. Curthoys, The Determination of Entropies of Adsorption by Gas-Solid Chromatography, J. Chem. Educ. 56 (1979), 802-804.
62. F. C. Campanell, R. Battino, and P. G. Seybold, On the Role of Solute Polarizability in Determining the Solubilities of Gases in Liquids, J. Chem. Eng. Data 55 (2010), 37–40.
63. E. G. Derouane, On the physical state of molecules in microporous solids, Micropor. Mesopor. Mater. 104 (2007), 46-51.
64. S. Ross and J. P. Olivier, in *On Physical Adsorption*, Ch. V. Implications of the Concept of Surface Heterogeneity, pp. 150-158 (Interscience Publishers, 1964).
65. K. Solvik, J. A. Weaver, A. M. Brockway, and J. Schrier, Entropy-Driven Molecular Separations in 2D-Nanoporous Materials, with Application to High-Performance Paraffin/Olefin Membrane Separations, J. Phys. Chem. C 117 (2013), 17050−17057.
66. J. V. d. Mynsbrugge, J. D. Ridder, K. Hemelsoet, M. Waroquier, and V. V. Speybroeck, Enthalpy and Entropy Barriers Explain the Effects of Topology on the Kinetics of Zeolite-Catalyzed Reactions, Chem. Eur. J. 19 (2013), 11568–11576.
67. D. Ferreira, R. Magalhães, J. Bessa, P. Taveira, J. Sousa, R. D. Whitley, and A. Mendes, Study of AgLiLSX for single stage high purity oxygen production, Ind. Eng. Chem. Res. (2014),
68. E. L. First, C. E. Gounaris, J. Wei, and C. A. Floudas, Computational characterization of zeolite porous networks: an automated approach, Phys. Chem. Chem. Phys. 13 (2011), 17339–17358.

69. X. Liu, Q. Wang, L. Wang, G. Chu, Q. Wei, and Y. Jin, Synthesis and morphological control of lamellar titano--aluminosilicate ETAS--10 zeolite, Shiyou Huagong 41 (2012), 671--676.
70. G. S. Jung, D. H. Park, D. H. Lee, H. C. Lee, S. B. Hong, and H. C. Woo, Adsorptive removal of tert-butylmercaptan and tetrahydrothiophene using microporous molecular sieve ETS-10, Appl. Catal., B 100 (2010), 264–270.
71. R. Afonso, A. Mendes, and L. Gales, Peptide-based solids: porosity and zeolitic behavior, J. Mater. Chem. 22 (2012), 1709-1723.
72. N. B. McKeown, Nanoporous molecular crystals, J. Mater. Chem. 20 (2010), 10588–10597.

Chapter 4. A Surface Thermodynamics Approach to Modelling Single-File Adsorption in Ultramicroporous Materials*

4.1. Abstract

A new thermodynamic approach is proposed to interpret adsorption equilibrium in ultramicropores with single-file diffusion. By considering the adsorbed phase as a one-dimensional fluid, phase equilibria thermodynamics can be used to derive a one-dimensional analogue of the monocomponent Gibbs adsorption isotherm. Equations such as Langmuir, Volmer, Fowler-Guggenheim or Hill-de Boer can thus be used as representations of phenomenological models of the one-dimensional adsorption system, rather than just as mathematical correlations. The bidirectional relation between the equations of state characterising the adsorbed phase and the adsorption isotherm equations allow great insight to be had simply by adsorption isotherm determination. As an example, the adsorption isotherms of Xe and CO_2 in four crystalline hydrophobic dipeptides of the VA-class are analysed with this approach, showing its potential and limitations.

4.2. Introduction

Most adsorption separation processes involving gases and vapours are based on microporous solids [1, 2]. This is due to the much stronger adsorption potential experienced by adsorbates in micropores relative to mesopores and macropores, allowing operation at lower concentrations. Interestingly, micropore adsorption is still the most poorly understood of the three, due to the complex interactions occurring in the confined environment of a micropore [3].

Micropores (< 2.0 nm) can be divided into supermicropores (> 0.7 nm) and ultramicropores (< 0.7 nm) [4]. Depending on the size of the adsorbate molecule relative to the pore,

* Article currently under submission.

adsorption in ultramicropores is sometimes characterised by single-file diffusion (SFD). In SFD systems, adsorbate molecules cannot bypass each other inside the pores, generating an adsorbed phase that can be described as a one-dimensional gas [5]. Such systems have been intensively studied in recent years, due to their unique molecular transportation patterns [6]. When it is necessary to characterise adsorption equilibrium in these systems, there are no immediately available isotherm equations giving easy and significant insight into the nature of the adsorbed phase. It is frequently the case that single or dual-site Langmuir isotherm equations are used as little more than mathematical correlations. In this respect, single-file systems greatly resemble other microporous systems.

In the last 20 years, molecular simulation studies have greatly increased our understanding of the molecular behaviour and interactions in micropores [7]. However, this has failed to help the development of better phenomenological models of adsorption in micropores, which may be used to extract information from adsorption data. The persistent reliance on the Dubinin and Langmuir equations even when this is incorrect shows clearly this to be the case. From the beginning, the Dubinin equations were, at best, semi-empirical and it was well understood that they did not apply for the smallest micropores [8]. The widely used Langmuir isotherm, originally derived for monolayer surface adsorption, is usually considered (wrongly) to always be no more than a mathematical correlation when applied to micropore adsorption. Only very specialised researchers use other adsorption isotherm equations derived from thermodynamics [9, 10]. This is a terrible state of affairs, given that it has long been known that a lot of information can be extracted out of a single adsorption isotherm. Since the work of Barrer, in the 1950's [11], it is well known that thermodynamics-derived adsorption isotherm equations can be used to model adsorption in zeolites [1, 11, 12]. In this work, the authors wish to show the validity of thermodynamic-derived equations for the modelling of single-file adsorption in ultramicropores, by use of a 1D analogue of the Gibbs adsorption isotherm.

Following the proposal of the Potential Theory of Adsorption (PTA) [13], it was early-on understood that, in molecularly-sized pores, the potential fields of the pore walls overlap [14]. This originates deeper potential wells inside the pore, which increases several times the heat of adsorption relative to that of adsorption on an equivalent surface. Thus, micropore adsorption is typically approached by considering that the entire pore space has a non-negligible adsorption potential, making adsorption capacity dependent on total volume rather than total surface area [4]. In supermicropores (> 0.7 nm), the adsorption potential is radially

uneven, which may lead to the formation of a monolayer at the walls before pore filling becomes predominant [15, 16]. This complex picture emerged after a convoluted history of the understanding of adsorption in micropores, which lies at the root of many prevalent misunderstandings.

4.2.1. Historical Development of Models of Adsorption in Micropores

In 1911, Zsigmondy was the first to propose a specific adsorption mechanism for micropores, speculating that the capillary condensation phenomenon could possibly extend to pores of molecular dimensions [13]. Upon the proposal of the Langmuir equation for monolayer adsorption [17], the consensus view became that pores of molecular dimensions would limit adsorption to monolayer formation, due to the inexistence of space for more than one layer of molecules [4, 18-20]. In fact, data of adsorption in micropores frequently yields an approximately linear Langmuir plot, which was interpreted as proof of applicability of Langmuir's model [4, 18]. This interpretation remained for many years, in spite of the observation of the ubiquitous validity of Gurvitsch's rule in materials with very small pores [19, 20].

Among researchers working with zeolites, gas and vapour sorption were early-on interpreted as the formation of a kind of "solid solution", where the adsorbate would occupy the intracrystalline "capillaries" emptied of water upon heating [21, 22]. Putting together results from adsorption experiments on both zeolites and active carbon, McBain [18] developed the concept of "persorption", *i.e.*, sorption into molecularly sized pores, where the concept of "surface" no longer made sense [18]. In zeolite research, the "zeolitic solid solution" idea gained wide acceptance in the 1930's [18, 23]. In the 1940's, Barrer proposed "occlusion" as a more appropriate term to describe sorption in the channels of zeolites [24, 25] . Barrer also suggested that Gurvitch's rule might hold for zeolites with "large" pores, but not for those only one molecule-wide [25].

It was not until 1947 that Dubinin, in the context of his studies of adsorption in activated carbons, formalised the idea of three-dimensional volume-filling of micropores [26]. Dubinin later systematised his ideas into a "Theory of volume-filling of micropores" (TVFM) [8], supported on the PTA. Dubinin and co-workers observed that adsorption of vapours in activated carbons could be characterised by a temperature-invariant characteristic curve, the condition for applicability of the PTA. The mathematical expression proposed to describe the

characteristic curve became known as the Dubinin-Radushkevich equation (DR). A later generalisation became known as the Dubinin-Astakhov equation (DA). The TVFM and the Dubinin equations enjoyed tremendous success, eventually becoming the standard through which micropore adsorption was considered. Today, however, a consensus seems to be emerging whereby the Dubinin equations should be considered no more than empirical correlations [27-29].

In 1953, Barrer introduced the idea of volume-filling of molecule-sized pores in zeolites [30], apparently independently of the developments in activated carbon. Just like Dubinin, Barrer sought to apply the PTA to adsorption in the enhanced potential field of micropores. However, instead of focusing on the characteristic curve, Barrer decided to mimic the PTA by using an equation of state (EoS) to describe the mobile adsorbed phase. He applied a simplified van der Waals equation, containing only the molar volume correcting term, and, through statistical thermodynamic arguments [24, 31], derived a Volmer-like adsorption isotherm equation [24, 30, 31]. This approach was developed further in the following years, in a series of papers dealing with adsorption in faujasite. In these, Barrer established the uniformity of the potential field of certain non-polar sorbates inside the micropores of zeolites [32], the fluid-like behaviour of the adsorbed phase for large-enough pore systems [33, 34] and the excellent agreement with experimental data upon use of the Hirshfelder modification of the van der Waals equation [35]. In his 1978 book, Barrer systematised the statistical thermodynamic approach to the description of adsorption in zeolitic micropores and the use of EoSs to describe the “intracrystalline fluid” thus formed [11].

The use Barrer made of Statistical Mechanics in micropore adsorption is analogous to that previously done for surface adsorption by Fowler and Guggenheim [36] and Hill [37, 38]. However, its success was very different. Very few studies take the approach originally taken by Barrer. Out of practicality, the Langmuir equation is frequently used to fit Type I adsorption isotherm data, typical of micropores, while taking special attention in remarking it should be viewed only as an empirical relation, given that it may not be possible to assess the phenomenological significance of its use [4, 39]. Other EoS- [9, 10] and virial equation-derived isotherms [40] are also occasionally used, including in the work of Barrer [32, 35].

A Classical Thermodynamics approach yields similar equations to that of statistical mechanics. The Classical Thermodynamics approach involves using the Gibbs Adsorption Isotherm [1, 12]. Originally derived for two dimensions, it can also be used for the three-dimensional adsorption space of micropores by assuming a breadthwise uniform adsorption

potential [1, 12]. The equations stemming from the Gibbs adsorption isotherm, such as Langmuir, Volmer, Fowler-Guggenheim and Hill-de Boer can be applied both in two-dimensional and three-dimensional adsorption. We believe this approach can, and should, be extended to one-dimensional adsorbed phases in ultramicropores.

4.2.2. Gibbs Adsorption Isotherm

4.2.2.1. The Classical 2D Formula

The Gibbs adsorption isotherm was originally proposed as a mathematically convenient way to represent the dependence of surface tension with bulk composition of two phases at equilibrium [41]. The properties of the interface are all represented *as if* the interface was a mathematical plane, even if, in most cases, this is not a good approximation. This imaginary surface can then be treated as another phase at equilibrium, with its characteristic two-dimensional variables. The Gibbs adsorption isotherm results from imposing isothermal conditions on the two-dimensional Gibbs-Duhem equation. In its usual form, the Gibbs adsorption isotherm is written as,

$$\mathrm{d}\gamma = -\sum_i \Gamma_i \,\mathrm{d}\mu_i \qquad (4\text{-}1)$$

where γ represents the surface tension, Γ represents excess concentration at the imaginary interface, i refers to the different components of the system and μ represents the chemical potential. Excess concentration is the amount per unit of area that would have to be located at the imaginary surface for the total amount of i in the system to be the same as it actually is. The location of the imaginary surface can be adjusted so that the excess concentration of one of the components is null. Thus, for two-component systems, it is common that the equation is written as a function of the excess concentration of a single component [41],

$$\mathrm{d}\gamma = -\Gamma \mathrm{d}\mu \qquad (4\text{-}2)$$

The Gibbs adsorption isotherm is used extensively in the study of liquid-liquid and liquid-gas interfaces, mainly due to the fact that the spreading pressure can be measured directly. In this and other systems with monolayer adsorption, the interface greatly resembles the imaginary surface originally conceived by Gibbs. In such cases, the Gibbs adsorption isotherm is the mathematical translation of a physical model of the adsorbed phase, the two-dimensional fluid. In this model, the monolayer molecules are free to move parallel to the surface, in two

dimensions, without any restrictions. This phase is characterised by a spreading pressure and a molar area, akin to the pressure and molar volume of three-dimensional fluids. The excess concentration of the solvent is considered null, so only the concentration of the solutes is considered. For a system with a single solute, Eq. (4-2) applies. Positive adsorption causes a decrease of surface tension, so the spreading pressure is defined as

$$\Pi \equiv \gamma_0 - \gamma \tag{4-3}$$

where Π represents spreading pressure and γ_0 represents the surface tension of the free surface. Molar area, a, is defined as the total surface area divided by the total amount adsorbed, *i.e.*, the inverse of excess concentration. Thus, the Gibbs adsorption isotherm for monocomponent adsorption, by combining Eq. (4-2) and Eq. (4-3), can be written as,

$$\mathrm{d}\Pi = \frac{1}{a}\mathrm{d}\mu \tag{4-4}$$

Considering adsorption of an ideal gas, from Eq. (4-4) is obtained,

$$\left(\frac{\mathrm{d}\ln(P)}{\mathrm{d}\Pi}\right)_T = \frac{a}{RT} \tag{4-5}$$

where P represents three-dimensional pressure, R represents the gas constant and T represents absolute temperature. This equation can be applied equally well to a flat solution surface flat or a solid surface, and so it is the typical form of the Gibbs adsorption isotherm used for monocomponent gas adsorption. For adsorption on a solid surface from liquid solutions, pressure is replaced by concentration.

For systems where the spreading pressure can be measured directly, the applicability of the Gibbs adsorption isotherm can be assessed and the equation of state representing the ΠaT (equivalent to the "PVT" of 3D systems) behaviour of the adsorbed phase determined [41]. In porous solids, it is not possible to measure the spreading pressure, so the appropriateness of an equation of state in describing the ΠaT behaviour of the adsorbed phase must be assessed through indirect methods based on the determination of the adsorption isotherm. The first alternative is to introduce an equation of state into eq. (4-5) and determine the resulting adsorption isotherm equation. There is, thus, a two-directional relation between the equation of state and the adsorption isotherm. The correspondence between some common equations of state and adsorption isotherm equation is shown in Table 4.1.

Table 4.1. Different adsorption isotherm equations obtained from the Gibbs equation, for gases, and respective Equations of State. Adsorption isotherms for solutes in a liquid phase are equivalent to those for gases, but relating concentration, rather than pressure, to the amount adsorbed.

Equation of State	Isotherm Equation	Name of Isotherm
$\Pi a = RT$	$bP = \theta$	Henry
$\Pi(a - a_0) = RT$	$bP = \frac{\theta}{1-\theta}\exp\left(\frac{\theta}{1-\theta}\right)$	Volmer [42]
$\left(\Pi + \frac{\alpha}{a^2}\right)(a - a_0) = RT$	$bP = \frac{\theta}{1-\theta}\exp\left(\frac{\theta}{1-\theta}\right)\exp(-c\,\theta)$	Hill-de Boer [37, 38, 43]
$\Pi a_0 = RT \cdot \ln\left(\frac{a}{a-a_0}\right)$	$bP = \frac{\theta}{1-\theta}$	Langmuir [17]
$\left(\Pi + \frac{\alpha}{a^2}\right) a_0 = RT \cdot \ln\left(\frac{a}{a-a_0}\right)$	$bP = \frac{\theta}{1-\theta}\exp(-c\,\theta)$	Fowler-Guggenheim [36]

The second alternative is to compute the spreading pressure from the adsorption isotherm and directly assess the equation of state best describing the resulting Π-a curve. From the definition of molar area,

$$a = \frac{1}{\Gamma} = \frac{A}{n} \tag{4-6}$$

where A represents specific surface area ($m^2 \cdot kg^{-1}$) and n represents adsorption concentration ($mol \cdot kg^{-1}$) in the solid. Replacing eq. (4-6) into eq. (4-5) and solving for Π,

$$\Pi = \frac{RT}{A}\int_0^P \frac{n}{P}\mathrm{d}P \tag{4-7}$$

This relation, if applicable, allows computation of the spreading pressure from adsorption isotherm data.

4.2.2.2.3D Gibbs Adsorption Isotherm

Adsorption in solids, porous or non-porous, is seldom confined to a monolayer. Multilayer adsorption, capillary condensation and micropore filling make the traditional 2D Gibbs adsorption isotherm inapplicable (with physical significance) to most adsorbents. However, the application of a 3D Gibbs adsorption isotherm allows extension of the thermodynamics-based approach to micropore filling [1, 11, 12, 30, 35] and multilayer adsorption [31]. The 3D analogue of Eq. (4-5) is [1, 11, 12],

$$\left(\frac{\mathrm{d}\ln(P)}{\mathrm{d}\Phi}\right)_T = \frac{v}{RT} \tag{4-8}$$

where Φ is the three-dimensional spreading pressure (*i.e.*, in-pore three-dimensional pressure) and v is the molar pore volume. Application of the 3D Gibbs adsorption isotherm implies the assumption of an adsorption potential field uniform both breadthwise and lengthwise. In systems where the 3D Gibbs adsorption isotherm applies, adsorption isotherm equations can be deduced from Eq. (4-8) by application of an equation of state, just as for 2D. However, because the concept of localised adsorption does not apply to three-dimensional space, only isotherm equations corresponding to distributed adsorption can be used. Thus, for micropores where three-dimensional pore filling is assumed to occur, and there is a uniform adsorption potential, equations such as Volmer and Hill-de Boer can be used as physical models of adsorption, instead of just as mathematical correlations. As previously mentioned, only in zeolite research are the thermodynamic models used and, even in such cases, rarely. As illustrated in Figure 4.1, the assumption there is an adsorption potential approximately uniform breadthwise is typically only correct for small supermicropores [16].

It should be noted that, in the context of adsorption in porous materials, the concept of "excess concentration" has a somewhat different meaning than that originally envisioned by Gibbs for generic phase equilibrium [44]. Excess adsorbate concentration in a pore is usually defined as the amount adsorbed in excess of that occupied by the bulk gas on the free equivalent of total pore volume. Thus, Gibbs' original "excess concentration" is, in the context of 3D adsorption in solids, equivalent to the "absolute adsorbate concentration" of porous materials studies. Absolute adsorbed concentration can be determined from excess concentration, provided total pore volume is known [44]. In fact, for real 2D monolayers, it is also not correct to talk about "excess adsorbate concentration", but simply "adsorbate concentration".

4.2.3. 1D and Single-File Diffusion Systems

The derivation of a 1D Gibbs adsorption isotherm follows the same thermodynamic reasoning as for 2D and 3D. Assuming a one-dimensional gas behaviour for single-file systems, the 1D Gibbs adsorption isotherm can be written as,

$$\left(\frac{\mathrm{d}\ln(P)}{\mathrm{d}\Omega}\right)_T = \frac{l}{RT} \tag{4-9}$$

where,

$$l \equiv \frac{L}{n} \tag{4-10}$$

and L is total micropore length, l is molar length and Ω is 1D spreading pressure (*i.e.*, linear tension). As for 3D, for 1D adsorption, absolute adsorbate concentration should be used, not excess.

Depending on the behaviour of the molecules in the pore, different equations of state and adsorption isotherms may apply. Unlike what happens for 3D systems, purely localised adsorption is a reasonable model of adsorption. Langmuir and Fowler-Guggenheim equations can thus be used in 1D systems as phenomenological relations.

Table 4.2 summarises the characteristic variables for 1D, 2D and 3D adsorbed phases. It is worth noticing that, for single-file systems, the capacity-determining variable is micropore length, not micropore volume as with supermicropores.

A previous instance exists of a proposal of a 1D Gibbs adsorption isotherm, to model the 1D boundary between two 2D monolayers at the surface of a liquid [45]. This has not happened, to the best of our knowledge, for systems with gas adsorption in ultramicroporous solids. There were, however, instances of implicit assumption of the validity of the 1D Gibbs adsorption isotherm, in which the Langmuir [46] and Fowler-Guggenheim [47] isotherm equations were used to model gas adsorption in ultramicroporous solids with clear physical meaning. The concept of "one-dimensional gas" is also frequently used to describe 1D adsorbed phases [5]. Virial equations have also been repeatedly used to model systems where the adsorbed phase is implicitly assumed to be a 1D gas [48].

The main distinction in adsorption systems represented by the equations in Table 4.1 is between mobile and localised adsorption. Any such representation should always be seen as an approximation of an intermediate reality. If none of the two extremes is a good

approximation, then adsorption equilibrium must be modelled by adding the two terms representing the two contributions. Similar reasoning is behind the popular dual-site Langmuir isotherm equation. The fact that this modelling approach generates many fitting parameters limits the physical significance that may be attributed to them. The problem will not go away, and the only real alternative is to use more complex statistical mechanical models [11, 49, 50], which, nonetheless, may exhibit the same problem.

Table 4.2. Characteristic variables of the adsorbent and adsorbed phase, for the models of 1D, 2D and 3D adsorbed phases.

		Variables characterising the adsorbed phase	
Phase	Variable characterising the adsorbent	Inverse of concentration	Pressure equivalent
1D	Specific pore length, L	Molar length, l	Tension, Ω
2D	Specific surface area, A	Molar area, a	Spreading pressure, Π
3D	Specific pore volume, V	Molar volume, v	In-pore pressure, Φ

4.2.3.1. Slab

It is frequently the case that ultramicropores have a slab-like, and not cylindrical, shape. In such cases, if its width is smaller than two times that of the adsorbate molecule, a 2D gas model and isotherm must be used, following Eq. (4-5). If it is bigger (but not too big), the 3D gas model must be used, Eq. (4-8).

4.2.3.2. Heterogeneous Systems

We find it important to emphasise that the thermodynamic approach to adsorption modelling presented above clearly shows that simple phenomenological equations may, sometimes, be used with physical significance to describe 1D, 2D and 3D adsorption systems. The Langmuir isotherm should therefore stop being referred to as having an exclusively empirical character when applied to micropore adsorption, even when localised adsorption with no intermolecular interactions is a gross approximation of the physical reality. In fact, when compared to the

Dubinin equations, its phenomenological significance will always be equal or greater. The same is valid for the Volmer isotherm.

If the adsorbent has a broad pore size distribution, to obtain physically significant parameters it is necessary to integrate the adequate isotherm equation for all pore sizes. The procedure is exactly the same as for the many methods using the Dubinin equations [27]. There is no intrinsic advantage in using them over thermodynamic isotherm equations. For the Dubinin equations, empirical relations have been developed relating "characteristic energy" to pore size, both for slab and for cylindrical pores. If such relations were developed for the parameters of thermodynamic isotherm equations, the integration could be as easily accomplished, while having the advantage of obtaining more meaningful isotherm parameters for each pore size. A mathematical treatment for this approach has, in fact, been proposed [47]. These relations could be developed either experimentally or from molecular simulations of adsorption on pores of different sizes.

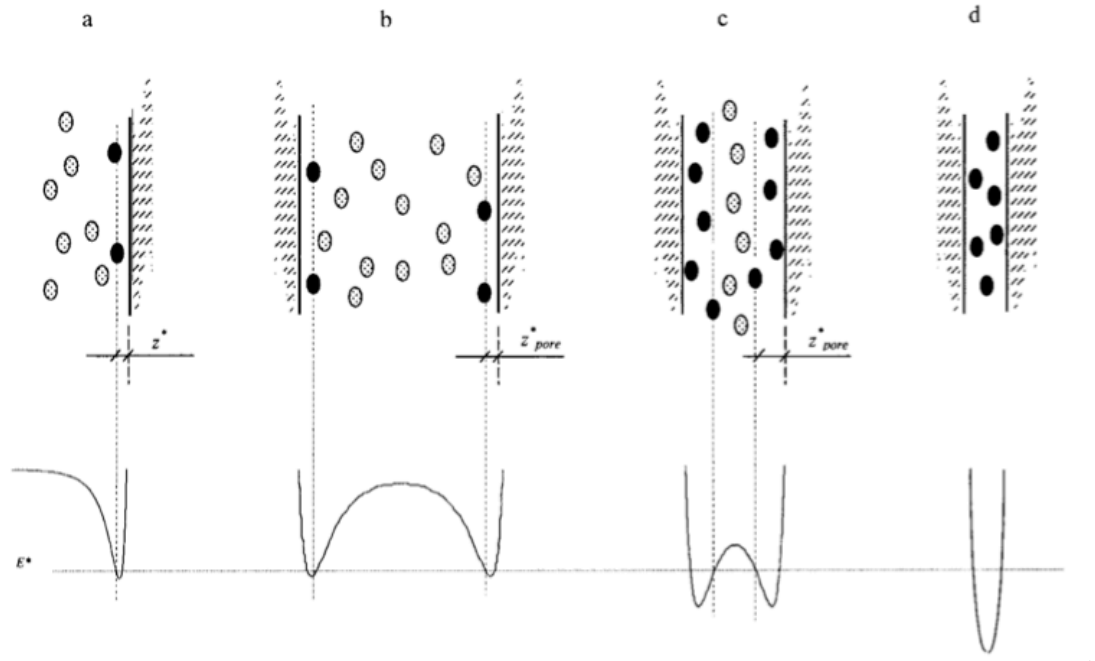

Figure 4.1. Representation of the adsorption potential and molecular distribution on a a.) free surface or macropore, b.) mesopore, c.) supermicropore and d.) ultramicropore. Although all molecules in a supermicropore are under the influence of the adsorption potential, only in an ultramicropore can it be considered that all molecules are under the influence of a similar adsorption potential. Adapted from [16].

Large supermicropores, with breadthwise uneven adsorption potentials such as that shown in Figure 4.1c, cannot be modelled considering a single phase. Instead, the existence of two phases inside the pores must be considered [16], a two-dimensional phase close to the pore walls and a three-dimensional gas phase at the centre of the pore. The latter is still influenced by the adsorption potential, so that its concentration is much higher than that outside the pore.

4.2.3.3. Use in Real 1D Adsorption Systems

Xe and CO_2 adsorption in hydrophobic dipeptides [51, 52] was used to test the insight that could be gained from using phenomenological equations in 1D adsorption systems. These fully organic microporous materials possess unidimensional pores, which, depending on the dipeptide, are 0.4-1.0 nm wide, with varying degrees of helicity. They have recently been suggested as an ideal template for testing SFD models [53, 54]. The four dipetides used in this work were VI, IA, IV and VV, with pore sizes of, respectively, 0.37 nm, 0.37 nm, 0.39 nm and 0.44 nm. IA is usually considered larger than VI [52, 55].

4.3. Experimental

Adsorption isotherms of Xe and CO_2 in VI, IA, IV and VV were determined. Samples of dipeptides VI, IA, IV and VV were purchased from Bachem. Samples were received as a crystalline white powder, which were regenerated overnight, under vacuum (< 1 mbar), at 70 ºC, before being used in the adsorption experiments. The adsorption isotherms were determined using the volumetric method. This method is based on measuring the variation of pressure of the gas after an expansion between two tanks of known volume, one of which contains the adsorbent sample. Using an appropriate equation of state for the gas phase (the Peng-Robinson equation was used in this work) and performing a mass balance, it is possible to determine the total amount adsorbed. The sorbate concentration is determined dividing this value by the sample mass. The sample tank and feed tank volumes were, respectively, 13.32 mL and 54.37 mL. The mass of VI used for the determination of the Xe isotherm was 2.3770 g and for the CO_2 isotherm 2.4927 g. The mass of IA, IV and VV used for the determination of both isotherms was 0.9892, 2.4131 and 1.0064 g. The pressure transducer used was a WIKA P-30, 0-6 bar (accuracy of 0.1 % FS). The temperature of the system was controlled through immersion in a Huber CCE-K12 thermostatic bath. Swagelok tubing and valves were

used to connect the tanks, the gas feed and the exhaust. Pressures below 1 atm were achieved using a Vacuubrand RZ 2.5 vacuum pump. Alphagaz 1 gases, supplied by Air Liquide, were used, with purities of >99.999 %.

4.4. Results and Discussion

The absolute adsorption isotherms of Xe and CO_2 in VI, IA, IV and VV, at 20 ºC, are shown in Figure 4.2. Excess adsorption isotherms are shown in Appendix D. Due to the low porosity of crystalline dipetides, absolute and excess adsorption values are extremely close. CO_2 adsorption isotherms at 25 ºC have been published previously [56], displaying similar values and trends to the ones reported here. Xe adsorption isotherms in VA and AV, at 25 ºC, have been published [57] with similar values and trends as those of the four dipeptides shown here. As for other gases [55], adsorbed concentration and Henry constant of Xe generally increase with pore size, i.e., VV>IV>IA>VI. For CO_2, this trend is not observed. The lines in the two graphs of Figure 4.2 represent the adsorption isotherms obtained from a non-linear fitting procedure, with the Hill-de Boer equation being used for Xe and Fowler-Guggenheim for CO_2. The fitting parameters used are shown in Table 4.3 and Table 4.4. The fitting procedure and choice of the equations to be fitted in each case are discussed below.

The four simple models, Langmuir, Volmer, Fowler-Guggenheim (FG) and Hill-de-Boer (HdB), were used to fit the adsorption isotherms. Instead of fitting the final equations, shown in Table 4.1, directly to the adsorption isotherm data, we chose a two-step procedure based on a graphical evaluation method originally proposed by de Boer [58]. Unlike others [11, 50], this graphical representation does not require *a priori* knowledge of the adsorption capacity parameter. First, the Ω-l diagrams were determined, from the adsorption isotherm data, using Eq. (4-7). One such diagram, for Xe adsorption on VI, is shown in Figure 4.3, in the Ωl vs Ω format, normalised for RT (the other seven diagrams are shown in Appendix D) The shape of the curve in a Ω-l diagram is not dependent on Henry's constant, so curve fitting involves one less parameter than directly using the adsorption isotherms. Henry constants are determined either directly from the n/P ratio at $P \to 0$, or by curve fitting of the n values of the adsorption isotherms, using the previously determined parameters as constants. Thus, the perfect gas (Henry) model always generates the same Ω-l relation ($\Omega\, l = RT$), Langmuir and Volmer have one parameter (adsorption capacity) and Fowler-Guggenheim and Hill-de Boer have two (adsorption capacity and the interactions parameter).

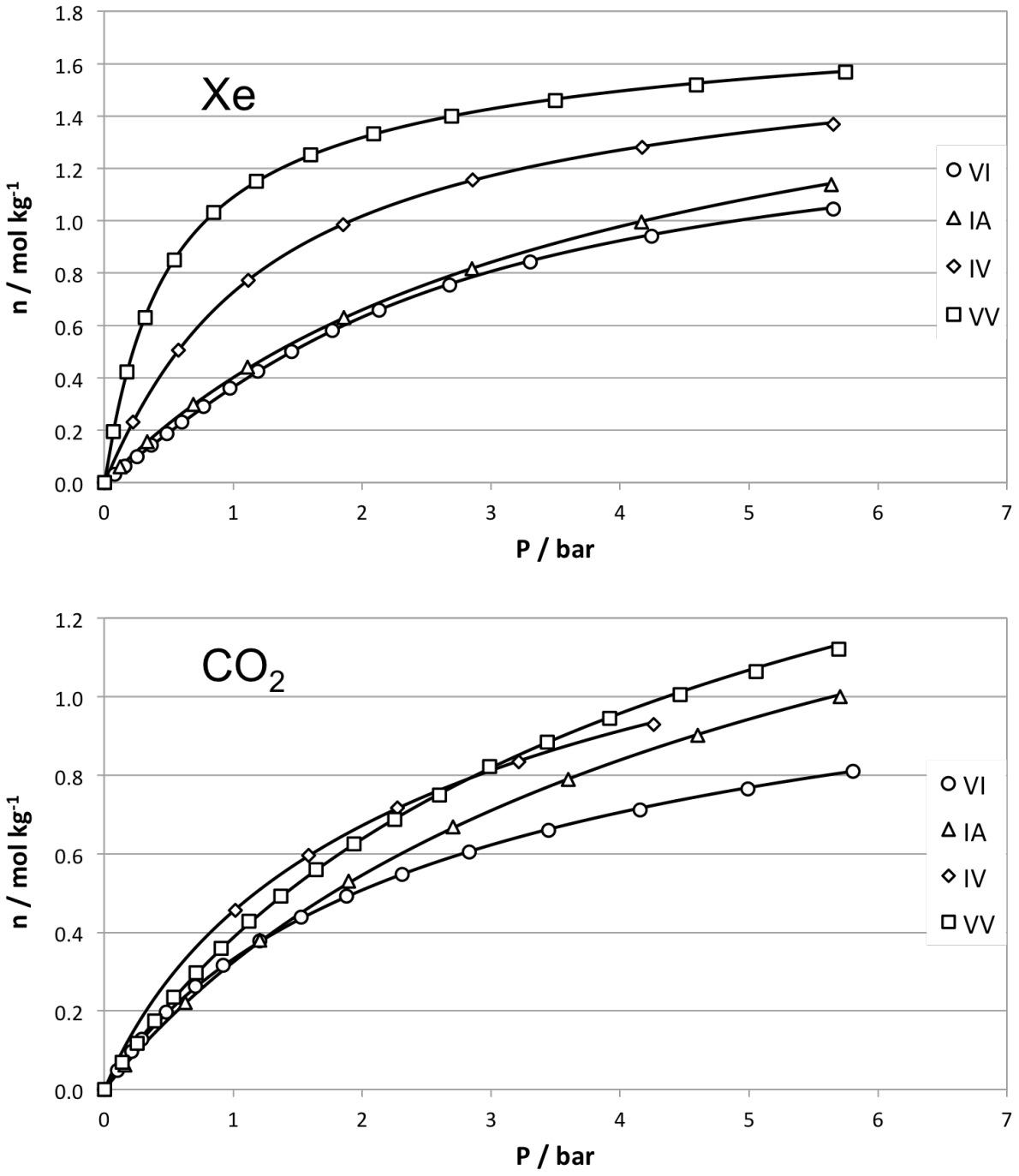

Figure 4.2. Absolute adsorption isotherms of Xe and CO_2 in VI, IA, IV and VV. The solid lines represent the isotherm obtained from the fitting procedure, Hill-de Boer for Xe and Fowler-Guggenheim for CO_2, using the parameters shown in Table 4.3 and Table 4.4, respectively.

Table 4.3. Results of non-linear fitting of Xe adsorption data to the FG and HdB equations. *SS1* is the sum of squares for the n_{max} and c fitting and *SS2* is the sum of squares for the K_H fitting.

		SS1	*c*	n_{max} / mol kg^{-1}	n_{max} / atom u.c.$^{-1}$	l_0 / nm atom^{-1}	*SS2* / mol^2 kg^{-2}	K_H / mol kg^{-1} bar^{-1}
VI	FG	1.58 X 10^{-3}	0.847	1.40	1.9	0.556	2.95 X 10^{-4}	0.394
	HdB	4.61 X 10^{-4}	1.943	2.08	2.8	0.373	1.45 X 10^{-4}	0.389
IA	FG	1.17 X 10^{-4}	-0.101	1.96	2.4	0.487	7.64 X 10^{-5}	0.514
	HdB	6.78 X 10^{-5}	0.347	3.07	3.8	0.311	7.00 X 10^{-5}	0.513
IV	FG	8.91 X 10^{-4}	0.17	1.67	2.2	0.537	6.85 X 10^{-5}	1.18
	HdB	6.25 X 10^{-5}	1.13	2.40	3.2	0.374	1.76 X 10^{-5}	1.15
VV	FG	1.46 X 10^{-2}	-0.238	1.74	2.4	0.454	8.20 X 10^{-4}	3.35
	HdB	1.03 X 10^{-3}	0.941	2.37	3.3	0.333	9.33 X 10^{-5}	3.06

Table 4.4. Results of non-linear fitting of CO_2 adsorption data to the FG and HdB equations. *SS1* is the sum of squares for the n_{max} and c fitting and *SS2* is the sum of squares for the K_H fitting.

		SS1	*c*	n_{max} / mol kg^{-1}	n_{max} / atom u.c.$^{-1}$	l_0 / nm atom^{-1}	*SS2* / mol^2 kg^{-2}	K_H / mol kg^{-1} bar^{-1}
VI	FG	9.00 X 10^{-4}	-0.516	1.30	1.8	0.589	1.03 X 10^{-4}	0.510
	HdB	5.57 X 10^{-4}	-0.253	2.02	2.8	0.380	8.20 X 10^{-5}	0.507
IA	FG	1.40 X 10^{-5}	-0.331	2.05	2.6	0.466	6.60 X 10^{-5}	0.406
	HdB	1.42 X 10^{-5}	-0.089	3.29	4.1	0.291	6.68 X 10^{-5}	0.406
IV	FG	8.13 X 10^{-5}	-0.841	1.70	2.2	0.528	1.55 X 10^{-5}	0.776
	HdB	1.15 X 10^{-4}	-0.831	2.68	3.5	0.335	1.99 X 10^{-5}	0.773
VV	FG	7.28 X 10^{-4}	-0.324	2.14	3.0	0.369	2.81 X 10^{-4}	0.501
	HdB	8.29 X 10^{-4}	-0.076	3.43	4.7	0.231	3.07 X 10^{-4}	0.500

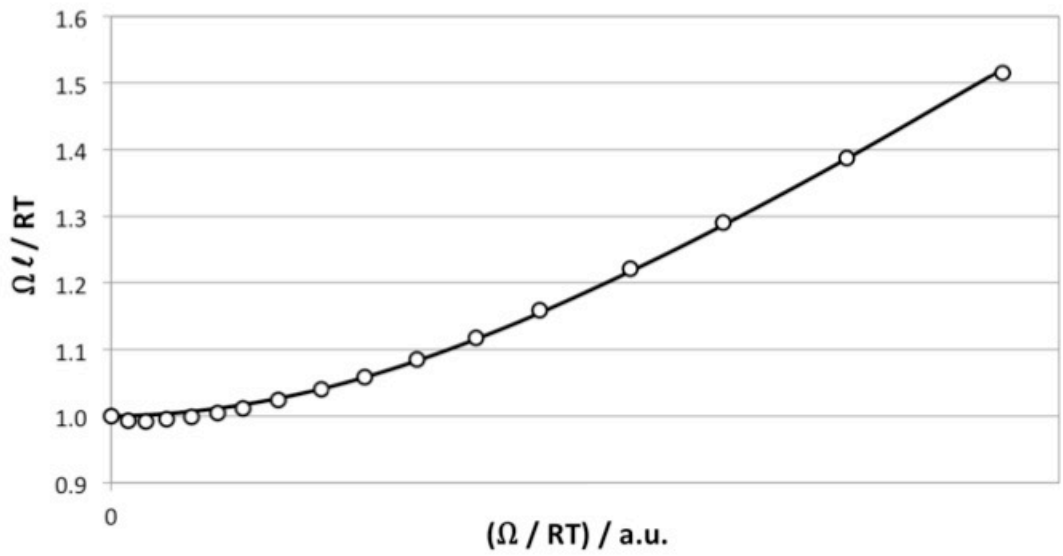

Figure 4.3. Ω-l diagram for Xe adsorption in VI. The points represent experimental results and the line Hill-de Boer fitting.

Involving only one parameter, the adequacy of the fitting of Langmuir and Volmer models can be easily assessed by analysing the residues of the fitting procedure. One example of these is shown in Figure 4.4, the rest in Appendix D. It is quite clear that the errors, although small, are not random, so these models are inadequate to represent the system. This was to be expected, since CO_2 and Xe are highly non-ideal gases, having strong intermolecular interactions. The FG and HdB models were thus fitted to the Ω-l data, with results being shown in Table 4.3 and Table 4.4. The sums of squares of residues of the first and second fittings are represented, respectively, by *SS1* and *SS2*.

For Xe in IV and VV, the HdB fitting *SS1s* are an order of magnitude below those of FG, being a clearly better fit. This may indicate that Xe is predominantly mobile inside IV and VV, the two dipeptides with larger pores. For the other two, the picture is less clear; HdB fitting *SS1s* for VI and IA are, respectively, only 1/3 and 1/2 those of FG. It may be the case that VI and IA pores (0.37 nm) are simply too tight for the 0.394 nm-wide Xe atom to diffuse freely, thus having a more localised character. On the other hand, it may happen that the fact that the isotherms are not as curved as those of IV and VV, and thus closer to the Henry region, makes it harder to identify the best equation. The extensive literature on Xe adsorption in VA-type dipeptides [52-54, 57, 59] does not give, in our view, any hint on which equation would be more appropriate. However, there is still some independent information that can be used to assess this; the size of the Xe atom can be compared to the value of l_0 obtained from

the fitting procedures. The HdB fitting generates l_0 values clearly closer to the Lennard-Jones diameter of the Xe atom, while the FG values are completely unreasonable. Furthermore, the FG fitting for IA generates a negative c, indicating net repulsion between adsorbed atoms, which, for Xe, is not possible. The HdB equation is, thus, the one that best describes Xe adsorption on all four dipeptides, indicating the existence of a predominantly mobile adsorbed phase.

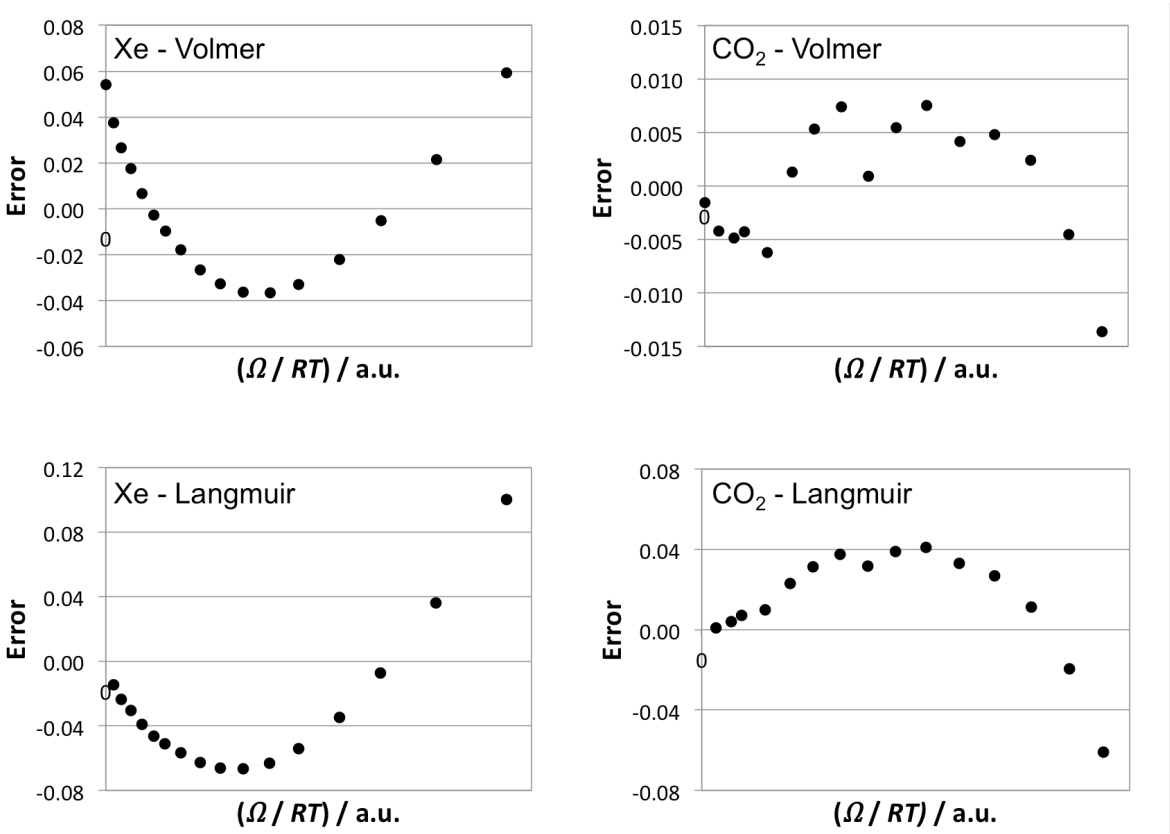

Figure 4.4. Residual errors of non-linear Volmer and Langmuir fittings of Xe and CO_2 adsorption in VI. The errors are dimensionless, as they refer to the fitting of $\Omega l/RT$.

For CO_2, the situation is even less clear. Grand Canonical Monte Carlo (GCMC) simulations performed by Comotti et al. [56] indicate a predominantly localised character of CO_2 adsorption in IA and IV, with two adsorption sites per unit cell. VV and VI seem to have a mixed, localised-distributed adsorption. This is not reflected in the results of Table 4.3 and Table 4.4; values of *SS1* are very similar for both FG and HdB fittings in the four dipeptides. If the GCMC result was not available, it would be tempting to conclude that the adsorbed

phase has a mixed character for all cases. Once again, this may simply be a consequence of the fact that the isotherms cover a too small non-Henry region of the isotherm. These results show quite clearly the limits to the insight that can be gained from the method here proposed, especially when working with relatively low-filling isotherms.

Once again, the l_0 result can give some insight into the more feasible equation for the system. The CO_2 molecule is 0.556 nm-long [60], to which the l_0 value obtained from the FG fitting is systematically closer than that of HdB. In fact, the HdB values are impossibly low in every case. Correspondingly, n_{max} in molecules per unit cell obtained from FG is closer to the GCMC result of 2.0 adsorption sites per unit cell than that obtained from HdB. For VV, the FG fitting yielded a value of 3.0 molecules per unit cell and 0.369 nm of pore per CO_2 molecule, seemingly unreasonable values for the system. The VV width of 0.44 nm, even considering framework flexibility, is unlikely to allow parallel overlap of the 0.31 nm-wide [60] CO_2 molecules. However, the extra pore space, coupled with the helical character of the pores and framework flexibility, may allow a perpendicular arrangement of CO_2 molecules, in a criss-cross configuration, which would create a more compact packing than in the other three dipeptides. It is interesting to notice that the "free" diameter 0.44 nm – 0.31 nm = 0.13 nm is relatively close to the 0.556 nm – 0.369 nm = 0.187 nm of "extra" space occupied by the CO_2 molecule. It is also possible that the flexible framework generates a varying "effective" n_{max}, higher at low fillings, when deformations are unhindered. In such a case, a fitting of low-filling isotherms, as is the case, would overestimate n_{max}.

4.5. Conclusions

A 1D analogue of the Gibbs adsorption isotherm was proposed as a good way to model adsorption in unidimensional ultramicropores with single-file diffusion. For narrow slab-shaped ultramicropores, the 2D Gibbs adsorption isotherm can be used, and for midsize micropores, the 3D version of the Gibbs adsorption isotherm may sometimes be adequate. In this model, the characteristic variable of the 1D system are 1D spreading pressure and molar length. Adsorbent capacity is determined by total specific pore length of the adsorbent, not surface area or total micropore volume. Thus, the phenomenological equations resulting from the implementation of the Gibbs adsorption isotherms, such as Langmuir, Volmer, Fowler-Guggenheim or Hill-de Boer, will frequently be well suited for modelling of adsorption in micropores.

The proposed equations were tested in modelling the single-file diffusion system of Xe and CO_2 adsorbed in hydrophobic dipeptides. It was possible to identify the Xe results as being best modelled by the Hill-de Boer equation, seemingly indicating a mobile adsorbed phase with positive interaction between the Xe atoms. For CO_2, although the situation was less clear, fitting of the Fowler-Guggenheim equation seems to give the most physically reasonable parameters, coherent with previous GCMC results indicating a predominantly localised adsorption, with two adsorption sites per unit cell of the crystalline structure of the dipeptides.

4.6. References

1. D. M. Ruthven, in *Principles of Adsorption and Adsorption Processes*, Ch. 3., pp. 62-85 (John Wiley & Sons, 1984).
2. R. T. Yang, in *Adsorbents: Fundamentals and Applications*, Ch. 1., pp. 1-7 (John Wiley & Sons, 2003).
3. E. G. Derouane, On the physical state of molecules in microporous solids, Micropor. Mesopor. Mater. 104 (2007), 46-51.
4. S. J. Gregg and K. S. W. Sing, in *Adsorption Surface Area and Porosity*, Ch. 4., pp. 195-245 (Academic Press, 1982).
5. T. Takaishi, A. Yusa, and F. Amakasu, Sorption of Nitrogen, Oxygen and Argon in Mordenite, Trans. Faraday Soc. 67 (1971), 3565-3576.
6. J. r. Kärger, Single-File Diffusion in Zeolites, Mol. Sieves 7 (2008), 329–366.
7. S. K. Bhatia, M. R. Bonilla, and D. Nicholson, Molecular transport in nanopores: a theoretical perspective, Phys. Chem. Chem. Phys. 13 (2011), 15350–15383.
8. M. M. Dubinin, The Potential Theory of Adsorption of Gases and Vapors for Adsorbents with Energetically Nonuniform Surfaces, Chem. Rev. 60 (1960), 235–241.
9. A. Khelifa, L. Benchehida, and Z. Derriche, Adsorption of carbon dioxide by X zeolites exchanged with Ni2+ and Cr3+: isotherms and isosteric heat, J. Colloid Interface Sci. 278 (2004), 9–17.
10. C.-J. Guo, O. Talu, and D. T. Hayhurst, Phase transition and structural heterogeneity; benzene adsorption on silicalite, AIChE J. 35 (1989), 573--578.
11. R. M. Barrer, in *Zeolites and Clay Minerals as Sorbents and Molecular Sieves*, Ch. 3, pp. 104-161 (Academic Press Inc., 1978).
12. L. V. C. Rees and D. Shen, in *Introduction to Zeolite Science and Practice*, (eds. H.v. Bekkum, P.A. Jacobs, E.M. Flanigen, and J.C. Jansen), Ch. 13., pp. 579-631 (Elsevier Science B.V., 2001).
13. F. Rouquerol, J. Rouquerol, K. S. W. Sing, G. Maurin, and P. Llewellyn, in *Adsorption by Powders and Porous Solids: Principles, Methodology and Applications*, 2nd ed., Ch. 1.2, pp. 2-6 (Academic Press, 2014).
14. S. Brunauer, in *The Adsorption of Gases and Vapors*, Ch. XI., pp. 365-418 (Oxford University Press, 1943).
15. K. S. W. Sing, F. Rouquerol, P. Llewellyn, and J. Rouquerol, in *Adsorption by Powders and Porous Solids: Principles, Methodology and Applications*, 2nd ed., Ch. 9., pp. 303-320 (Academic Press, 2014).
16. C. Nguyen and D. D. Do, Adsorption of Supercritical Gases in Porous Media: Determination of Micropore Size Distribution, J. Phys. Chem. B 103 (1999), 6900-6908.
17. I. Langmuir, The Adsorption of Gases on Plane Surfaces of Glass, Mica and Platinum, J. Am. Chem. Soc. 40 (1918), 1361-1403.
18. J. W. McBain and G. T.Britton, The Nature of the Sorption by Charcoal of Gases and Vapors Under Great Pressure, J. Am. Chem. Soc. 52 (1930), 2198–2222.
19. G. Foster, The Sorption of Condensible Vapours by Porous Solids. Part I. The Applicability of the Capillary Theory., Trans. Faraday Soc. 28 (1932), 645-657.
20. D. N. Broad and A. G. Foster, The Sorption of Condensable Vapours by Porous Solids. Part II. The Validity of Gurwitsch's Rule., J. Chem. Soc. (1945), 366-371.
21. M. Grandjean, Étude optique des solutions de vapeurs lourdes dans certaines zéolithes, Bull. Soc. Franç. Mineralog. 33 (1910), 5-37.

22. R. Seeliger, The Absorption of Gases by Crystals, Physik. Z. 22 (1921),
23. R. M. Barrer, The sorption of polar and non-polar gases by zeolites, Proc. R. Soc. Lond. A 167 (1938), 392-420.
24. R. M. Barrer, Kinetics of Formation of Zeolitic Solid Solutions, Trans. Faraday Soc. 40 (1944), 206-216.
25. R. M. Barrer and D. W. Riley, Sorptive and Molecular-sieve Properties of a New Zeolitic Mineral, J. Chem. Soc. (1948), 133-143.
26. M. M. Dubinin and L. V. Radushkevich, Three-dimensional filling of micropores, Proc. Acad. Sci. USSR Phys. Chem. Sect. 55 (1947), 331-340.
27. F. Stoeckli, Dubinin´s Theory and its Contribution to Adsorption Science, Russ. Chem. Bulletin Int. Ed. 50 (2001), 2265-2272.
28. A. P. Terzyk, S. Furmaniak, P. A. Gauden, P. J. F. Harris, and J. Włoch, Testing isotherm models and recovering empirical relationships for adsorption in microporous carbons using virtual carbon models and grand canonical Monte Carlo simulations, J. Phys.: Condens. Matter 20 (2008),
29. D. D. Do, D. Nicholson, and H. D. Do, Adsorption in micropores (nanopores): a computer appraisal of the Dubinin equations, Molec. Sim. 35 (2009), 122–137.
30. R. M. Barrer and D. W. Brook, Sorption and Reactivity of Simple Organic Molecules in Chabazite, Trans. Faraday Soc. 49 (1953), 940-948.
31. R. M. Barrer and A. B. Robin, Multilayer Sorption in Terms of an Equation of State, Trans. Faraday Soc. 47 (1951), 773-787.
32. R. M. Barrer, F. W. Bultitude, and J. W. Sutherland, Structure of faujasite and properties of its inclusion complexes with hydrocarbons, Trans. Faraday Soc. 53 (1957), 1111-1123.
33. R. M. Barrer and W. I. Stuart, Ion Exchange and the Thermodynamics of Intracrystalline Sorption. I. Energetics of Occlusion of Argon and Nitrogen by Faujasite -Type Crystals, Proc. R. Soc. Lond. A 249 (1958), 464--483.
34. R. M. Barrer and W. I. Stuart, Ion Exchange and the Thermodynamics of Intracrystalline Sorption. II. Entropy of Occlusion of Argon and Nitrogen by Faujasite-Type Crystals, Proc. R. Soc. Lond. A 249 (1958), 484--497.
35. R. M. Barrer and L. V. C. Rees, Equation of state for fluids sorbed in porous crystals, Trans. Faraday Soc. 55 (1959), 992-998.
36. R. Fowler and E. A. Guggenheim, in *Statistical Thermodynamics*, Ch. X., pp. 421-451 (Cambridge University Press, 1949).
37. T. L. Hill, Statistical Mechanics of Multimolecular Adsorption II. Localized and Mobile Adsorption and Absorption, J. Chem. Phys. 14 (1946), 441-453.
38. T. L. Hill, Statistical Thermodynamics of the Transition Region between Two Phases. II. One Component System with a Plane Interface, J. Chem. Phys. 20 (1952), 141-144.
39. K. S. W. Sing, F. Rouquerol, and J. Rouquerol, in *Adsorption by Powders and Porous Solids: Principles, Methodology and Applications*, 2nd ed., Ch. 5., pp. 159-189 (Academic Press, 2014).
40. G. Sethia, R. S. Somani, and H. C. Bajaj, Sorption of Methane and Nitrogen on Cesium Exchanged Zeolite-X: Structure, Cation Position and Adsorption Relationship, Ind. Eng. Chem. Res. 53 (2014), 6807−6814.
41. P. C. Hiemenz and R. Rajagopalan, in *Principles of Colloid and Surface Chemistry*, 3rd ed., Ch. 7., pp. 297-354 (Marcel Dekker, 1997).
42. M. Volmer, Thermodynamische Folgerungen aus der Zustandsgleichung fur Adsorbierte Stoffe, Z. Phys. Chem. 115 (1925), 253-261.

43. J. H. de Boer, in *The Dynamical Character of Adsorption*, 1st ed., Ch. VIII., pp. 170-199 (Oxford University Press, 1953).
44. A. L. Myers, Thermodynamics of Adsorption in Porous Materials, AIChE J. 48 (2002), 145-160.
45. B. A. Pethica, Two-dimensional colloids. The linear thermodynamics of monolayers, Colloids Surf. A 88 (1994), 147-155.
46. J. Koresh, Study of Molecular Sieve Carbons: The Langmuir Model in Ultramicroporous Adsorbents, J. Colloid Interface Sci. 88 (1982), 398-406.
47. P. Brauer, H.-R. Poosch, M. v. Szombathely, M. Heuchel, and M. Jaroniec, Evaluation of the Micropore-Size Distribution Function from Gas Adsorption Data by Using a Simple Molecular Model, Proc. IVth Int. Conf. Fundament. Adsorpt. 80 (1993), 67-74.
48. T. Takaishi and T. Okada, One-dimensional methane gas in the pores of ferrierite and Kihara's core potential, J. Chem. Soc. Faraday Trans. 94 (1998), 1893-1899.
49. T. L. Hill, Statistical Mechanics of Adsorption. VI. Localized Unimolecular Adsorption on a Heterogeneous Surface, J. Chem. Phys. 17 (1949), 762-771.
50. D. M. Bastidas, P. P. Gómez, and E. Cano, The isotherm slope. A criterion for studying the adsorption mechanism of benzotriazole on copper in sulphuric acid, Rev. Metal Madrid 41 (2005), 98-106.
51. C. H. Görbitz, Microporous Organic Materials from Hydrophobic Dipeptides, Chem. Eur. J. 13 (2007), 1022–1031.
52. D. V. Soldatov, I. L. Moudrakovski, E. V. Grachev, and J. A. Ripmeester, Micropores in Crystalline Dipeptides as Seen from the Crystal Structure, He Pycnometry, and 129Xe NMR Spectroscopy, J. Am. Chem. Soc. 128 (2006), 6737-6744.
53. M. Dvoyashkin, A. Wang, S. Vasenkov, and C. R. Bowers, Xenon in l--alanyl--l--valine nanochannels: A highly ideal molecular single-file system, J. Phys. Chem. Lett. 4 (2013), 3263--3267.
54. M. Dvoyashkin, H. Bhase, N. Mirnazari, S. Vasenkov, and C. R. Bowers, Single-File Nanochannel Persistence Lengths from NMR, Anal. Chem. 86 (2014), 2200-2204.
55. R. Afonso, A. Mendes, and L. Gales, Hydrophobic dipeptide crystals: a promising Ag-free class of ultramicroporous materials showing argon/oxygen adsorption selectivity, Phys. Chem. Chem. Phys. 16 (2014), 19386-19393.
56. A. Comotti, A. Fraccarollo, S. Bracco, M. Beretta, G. Distefano, M. Cossi, L. Marchese, C. Riccardi, and P. Sozzani, Porous dipeptide crystals as selective CO2 adsorbents: experimental isotherms vs. grand canonical Monte Carlo simulations and MAS NMR spectroscopy, Cryst. Eng. Comm. 15 (2013), 1503-1507.
57. D. V. Soldatov, I. L. Moudrakovski, and J. A. Ripmeester, Dipeptides as Microporous Materials, Angew. Chem. Int. Ed. 43 (2004), 6308-6311.
58. J. H. de Boer, in *The Dynamical Character of Adsorption*, 1st ed., Ch. VII. Non-ideal Two-dimensional Gases: Two Dimensional Condensation, pp. 128-131 (Oxford University Press, 1953).
59. C.-Y. Cheng and C. R. Bowers, Observation of Single-File Diffusion in Dipeptide Nanotubes by Continuous-Flow Hyperpolarized Xenon-129 NMR Spectroscopy, Chem. Phys. Chem. 8 (2007), 2077-2081.
60. J. Koresh and A. Soffer, Study of Molecular Sieve Carbons: Part 2.-Estimation of Cross-sectional Diameters of Non-spherical Molecules, J. Chem. Soc. Faraday I 76 (1980), 2472-2485.

Chapter 5. Kinetic Derivation of Common Isotherm Equations for Surface and Micropore Adsorption*

5.1.Abstract

The Langmuir equation is one of the most successful adsorption isotherm equations, being widely used to fit Type I adsorption isotherms. In this article we show that the kinetic approach originally used by Langmuir for 2D monolayer surface adsorption can also be used to derive a 1D analogue of the equation, applicable in single-file diffusion systems. It is hoped that such a demonstration helps dispel the idea that the Langmuir isotherm equation never applies to micropores as more than a mathematical correlation. We seek also to extend the intuitive insight provided by the simple kinetic derivation of the Langmuir equation to other isotherm equations capable of modelling Type I isotherms, namely other thermodynamically derived equations. The kinetic approach is thus also used to derive the Volmer, Fowler-Guggenheim and Hill-de Boer equations, both for surface (2D adsorbed phase) and micropore adsorption (1D and 3D adsorbed phases). In their case, as well, it is hoped that this will make it more intuitively clear that these equations can be used as phenomenological models in some instances of adsorption in micropores.

5.2.Introduction

As with many other phenomena, expressions describing adsorption equilibrium can be derived using both kinetic and thermodynamic arguments. The simplest thermodynamic approach to adsorption is expressed by the Gibbs adsorption isotherm [1]. In the previous Chapter, it was proposed that the Gibbs adsorption isotherm can be accurately applied to some micropores, besides surfaces, by considering uniform one- (1D) and three-dimensional (3D) adsorbed phases. Once this is established, it follows naturally that, if the premises supporting the corresponding equation of state remain valid, an equation obtained from the Gibbs adsorption isotherm for two-dimensional (2D) monolayer adsorption also applies to 1D

* Article currently under submission.

and 3D adsorbed phases. In this article, we propose that some of these isotherm equations can also be derived using a simple kinetic approach.

Table 5.1. Different adsorption isotherm equations obtained from the Gibbs equation, for gases, and Type of Adsorption it models. Type of Adsorption can be localised or distributed and with lateral interactions or without lateral interactions. For adsorption of solutes from liquid solutions, pressure is replaced by concentration. The variables in the equations are defined in the text.

Name of Isotherm	Isotherm Equation	Type of Adsorption
Henry	$bP = \theta$	Any
Langmuir [2]	$bP = \frac{\theta}{1-\theta}$	Localised, without lateral interactions
Fowler-Guggenheim [3]	$bP = \frac{\theta}{1-\theta}\exp(-c\,\theta)$	Localised, with lateral interactions
Volmer [4]	$bP = \frac{\theta}{1-\theta}\exp\left(\frac{\theta}{1-\theta}\right)$	Distributed, without lateral interactions
Hill-de Boer [5-7]	$bP = \frac{\theta}{1-\theta}\exp\left(\frac{\theta}{1-\theta}\right)\exp(-c\,\theta)$	Distributed, with lateral interactions

The simplest equations derived from the Gibbs adsorption isotherm are represented in Table 5.1. These five equations represent the most basic types of adsorption; localised or distributed, with or without lateral interactions. All can generate Type I isotherms, while the Hill-de Boer and Fowler-Guggenheim equations can also generate Type V isotherms. For 3D adsorbed phases, the concept of localised adsorption does not apply, and, thus, the Langmuir and Fowler-Guggenheim equations are only considered for localised 1D and 2D adsorbed phases.

Langmuir pioneered the kinetic approach in 1918 [2], by deriving an expression that considers adsorption of gas-phase molecules on specific sites of the surface, upon hitting on it at a rate given by the Kinetic Gas Theory. To the best of our knowledge, the kinetic approach to adsorption equilibrium used by Langmuir was not followed for the derivation of other adsorption isotherm equations; the more powerful and simple thermodynamic (classic and

statistical) approaches proved much more attractive and productive. In fact, it is only natural that equilibrium is best-studied using thermodynamics, for adsorption as for any other physical phenomenon. In porous solids, even the kinetics of adsorption could not be appropriately described using the kinetic approach of Langmuir, since diffusion through the pores is typically the rate-controlling mechanism.

With the discovery of the distributed nature of London forces and the development of the concept of adsorption potential, it was realised that purely localised adsorption very seldom exists for physical sorption [8]. Nonetheless, the elegance, simplicity and ability to produce fitting parameters with clear physical meaning made the Langmuir isotherm one of the most widely used adsorption isotherms. So much so, that Type I adsorption isotherms are often called "Langmuir-like", or simply "Langmuir" [9-11]. We believe that other adsorption isotherms would greatly benefit from the insight gained from a kinetic derivation. With this purpose in mind, the kinetic derivation of the five isotherm equations of Table 5.1 will be given below, for 1D, 2D and 3D systems. We also hope that by exemplifying a kinetic derivation of the Langmuir equations for 1D systems we may help dispel the idea that it can never represent a physical model of micropore adsorption. To perform these derivations, kinetic arguments as those of Langmuir [2] and de Boer [12, 13] will be used. It will be assumed that adsorbed molecules are hard spheres, behaving according to Newtonian kinematics, and that impacting molecules only interact with the solid upon hitting the surface (2D) or entering the pore (1D and 3D). These crude simplifications, already implicit in the thermodynamic derivations (Chapter 4), will prove to be very powerful in promoting insight into some of the physical realities behind the isotherm equations under consideration, in the same way it occurred with the Langmuir equation.

We should emphasize that we are not proposing that adsorption occurs necessarily or exactly according to the mechanisms proposed in the models. This is especially the case in micropores, where adsorption around the pore mouth plays a decisive role in promoting in-pore adsorption. We seek only to show that simple models such as that originally used by Langmuir can be used to derive other simple isotherm equations, and that they can be used as easily in micropore adsorption as in monolayer surface adsorption.

5.3. Adsorption on a Planar Surface – 2D

5.3.1. Localised Adsorption – The Classic Langmuir Model

The classic Langmuir model describes adsorption on a surface with discrete adsorption sites. It has been described many times before [12, 14], but a small recapitulation will be very helpful in setting the conceptual framework used for the derivations that follow.

The rate of adsorption is equal to the rate of impact of gas-phase molecules on unoccupied adsorption sites. The rate of impact on a surface is given by the Kinetic Gas Theory, having SI units of $mol \cdot m^{-2} \cdot s^{-1}$. If the units desired for the adsorption rate are $mol \cdot kg^{-1} \cdot s^{-1}$, the rate of impact must be multiplied by the specific surface area, with SI units $m^2 \cdot kg^{-1}$. The surface is not entirely covered by adsorption sites and not all impacts on these are successful, so an extra term, α, is included, representing the fraction of successful impacts on the adsorption sites. Finally, not all adsorption sites are free, so the rate of adsorption will be proportional to the fraction of those that are. This fraction is given by $(1-\theta)$, where θ represents the total amount adsorbed relative to the maximum that can be adsorbed (monolayer coverage). Thus, the equation for the rate of adsorption is

$$r_a = \frac{P}{\sqrt{2\pi MRT}} \cdot \alpha \cdot (1-\theta) \cdot A \qquad (5\text{-}1)$$

where r_a represents the rate of adsorption, A represents the specific surface area of the adsorbent, P represents pressure, M represents molar mass, R represents the ideal gas constant and T represents absolute temperature. The first fraction in the equation is the rate of impact on a surface, as given by the Kinetic Gas Theory.

Desorption is an activated phenomenon, the rate of which is proportional to the amount adsorbed. Therefore, the rate of desorption can be expressed as:

$$r_d = k_d \cdot n \qquad (5\text{-}2)$$

where r_d represents the rate of desorption (SI units of $mol \cdot kg^{-1} \cdot s^{-1}$), k_d represents the frequency of desorption (s^{-1}) and n represents the adsorbed concentration ($mol \cdot kg^{-1}$),

The frequency of desorption is given by,

$$k_d = k_0 \cdot \exp\left(-\frac{E_a}{RT}\right) \qquad (5\text{-}3)$$

where E_a is the activation energy of desorption and k_0 is the minimum frequency of adsorption, reached at infinite temperature. The activation energy of desorption is basically the heat of adsorption, that is, $E_a = (-\Delta H)_{ads}$.

Equilibrium is reached when both rates are the same. Equating the rate of adsorption with the rate of desorption results in the Langmuir equation,

$$r_a = r_d \Leftrightarrow bP = \frac{\theta}{1-\theta} \tag{5-4}$$

where b is the so-called affinity constant. This can be reformulated as

$$b = \frac{K_H}{n_{max}} \tag{5-5}$$

where n_{max} represents the maximum specific amount that can be adsorbed and K_H is Henry's constant, which can be expressed as

$$K_H = \frac{\alpha \cdot A}{k_d\sqrt{2\pi MRT}} \tag{5-6}$$

Unlike for the thermodynamic approach [4, 13, 14], where b stems from an integration constant, the kinetic approach yields a relation between Henry's constant and physical variables characteristic of the adsorption system. This is frequently quite helpful in interpreting experimentally determined values of b and K_H especially when comparing different materials.

5.3.2. Distributed Adsorption – Volmer Equation for Surfaces

The derivation of an equation for distributed monolayer adsorption will now be described, using the same kinetic approach as for localised adsorption. From the thermodynamic derivation [7, 14], we know the Volmer equation is the correct final result. As a starting point, it must be considered, as for the thermodynamic derivation, that adsorption occurs on a uniform adsorption potential on the surface of the adsorbent. This means that, when in the adsorbed-phase, the molecules are free to slide through the surface and bump into each other, as a two-dimensional gas [13]. One of the key variables used for the characterisation of the adsorbed phase is the molar area of the system, defined as:

$$a \equiv \frac{A}{n} \tag{5-7}$$

When a monolayer has been formed, the specific amount adsorbed is at its maximum, n_{max}, and the molar area at its minimum, a_0. The minimum molar area is approximately the molar area of a single adsorbed molecule, $a_0 = a_{molecule}$.

The desorption rate is modelled in the same manner as for localised (Langmuir) adsorption,

$$r_d = k_d \cdot n \tag{5-8}$$

where

$$k_d = k_0 \cdot \exp\left(-\frac{E_a}{RT}\right), \quad E_a = (-\Delta H)_{ads} \tag{5-9}$$

However, the adsorption rate cannot be described by Eq. (5-1). The fraction of unoccupied surface, $(1-\theta)$, does not correspond to the surface available for impact of incoming gas molecules, as it occurs for localised adsorption. The freedom of movement leads to the existence of a random distribution of intermolecular distances, unlike the uniform distribution of localised adsorption. Unoccupied area located between two or more molecules with intermolecular distances smaller than necessary for a successful impact is not free for adsorption. Therefore, an extra term must be multiplied, corresponding to the probability that the intermolecular distance, d_{inter}, between the adsorbed molecules at the point of impact is large enough for the incoming molecule to hit the surface. It thus follows that

$$r_a = \frac{P}{\sqrt{2\pi MRT}} \cdot \alpha \cdot (1-\theta) \cdot A \cdot \mathrm{p}(d_{inter} > d^*) \tag{5-10}$$

where d^* represents the critical distance that allows adsorption of incoming molecules to take place and $\mathrm{p}(d_{inter} > d^*)$ represents the probability that $d_{inter} > d^*$. Figure 5.1 shows a representation of an unsuccessful impact on unoccupied area, due to the existence of insufficient space between two adsorbed molecules adjacent to that area. Eq. (5-10) has the implicit assumption that the speed of molecules on the surface is much smaller than that of incoming gas molecules.

The problem with the probability introduced in Eq. (5-10) is that it is very hard to model in a 2D surface. Thus, instead of working with distances, it is far more convenient to work with areas. Under this approach, an impact is successful, or not, depending on the presence of molecules within the area of impact, as represented in Figure 5.2. This area is exactly the

same as the area of an adsorbed molecule, A_0, or, in molar terms, a_0. Therefore, the probability that the impact will be successful is the same as that of the existence of one or more molecules on the impact area, a_0.

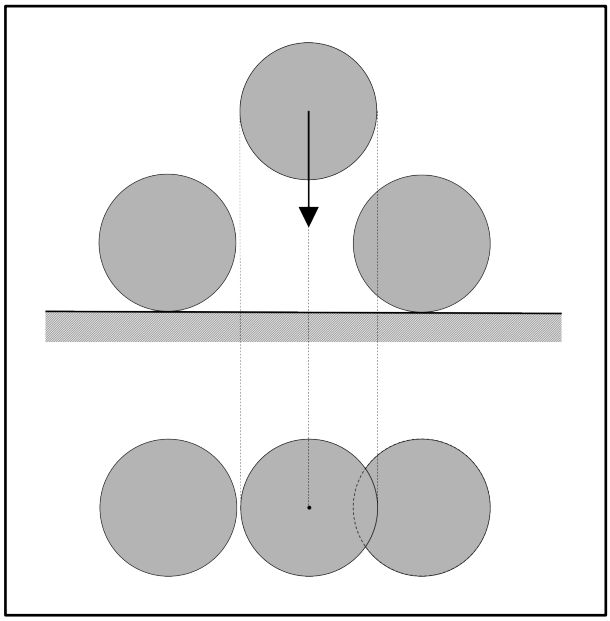

Figure 5.1. Representation of the lateral and top views of an unsuccessful impact on the surface. The impacting molecule is repulsed by molecules already adsorbed on the surface, although the projection of its mass centre is outside the projected area of the surface molecule.

Let us define a variable a_s, the area of the circle centred on the centre of the impact site, and touching the nearest adsorbed molecule, where the *s* stands for "site". Figure 5.2 shows a_s for a successful impact and an unsuccessful impact. It is thus possible to rewrite the probability in Eq. (5-10) as:

$$\mathrm{p}(d_{inter} > d^*) = \mathrm{p}(a_s > a_0) \qquad (5\text{-}11)$$

To determine the new probability, it is now only necessary to know the probability distribution function of a_0. This non-negative continuous random variable, $a_s \geq 0$, has a density distribution function, $\mathrm{f}(a_s)$, such that,

$$\mathrm{p}(a_s > a_0) = 1 - \mathrm{F}(a_0) \qquad (5\text{-}12)$$

where $\mathrm{F}(a_0)$ is the cumulative distribution function of a_s for the molecular area, a_0.

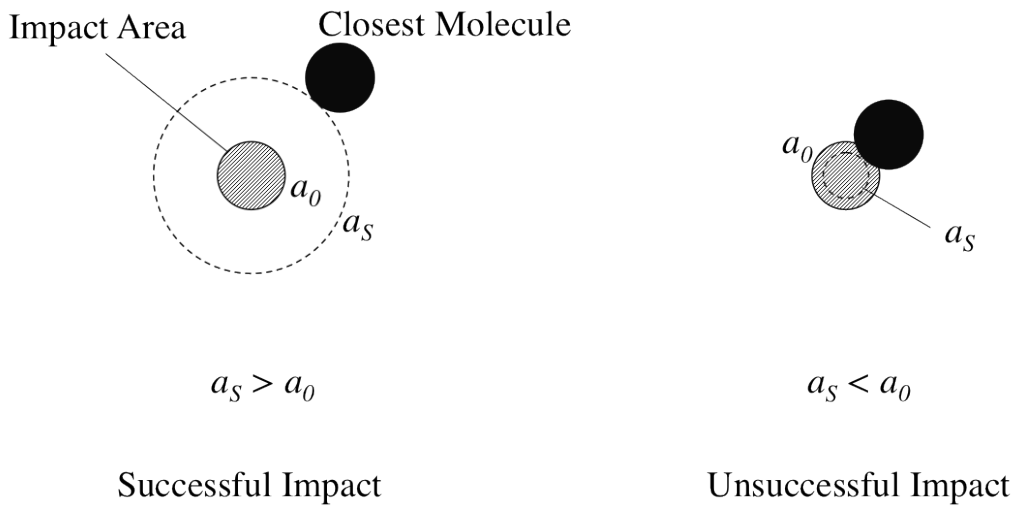

Figure 5.2. Representation of successful and unsuccessful impacts on the surface, depending on the absence, $a_s > a_0$, or presence, $a_s < a_0$, of an adsorbed molecule on the impact area of the incoming molecule.

To determine the distribution function, it must be considered that, under the model of the two-dimensional gas [13], the adsorbed molecules are randomly distributed on the surface. Therefore, the probability that there is a molecule at a given site is always the same, equal to the fraction of surface area occupied, θ, and independent from the presence of other molecules nearby. The presence of a molecule anywhere on the surface can therefore be seen as a Bernoulli trial, where a given site on the surface either has, or has not, molecules on it, with probability θ. The site area a_s needed to encounter the closest molecule to the impact site (Figure 5.2) can be seen as a first "success" in successive Bernoulli trials. For continuous random variables, the variable counting the number of Bernoulli trials until the first success has an exponential distribution [15-17]. The corresponding cumulative function of a_s is given by:

$$\mathrm{F}(a_0) = 1 - \exp(-\lambda \cdot a_0) \tag{5-13}$$

where the distribution parameter λ is given by the relationship

$$\lambda = \frac{1}{\langle a_s \rangle} \tag{5-14}$$

where $\langle a_s \rangle$ is the average of a_s. It is possible to see a_s as the free area at the site of impact, which means its average will be $a - a_0$, the total free molar area at the surface. Hence, Eq. (5-14) can be rewritten as,

$$\lambda = \frac{1}{a - a_0} \tag{5-15}$$

and, from Eq. (5-13),

$$\mathrm{F}(a_0) = 1 - \exp\left(-\frac{a_0}{a - a_0}\right) \tag{5-16}$$

given that,

$$\theta = \frac{a_0}{a} \Rightarrow \frac{a_0}{a - a_0} = \frac{\theta}{1 - \theta} \tag{5-17}$$

substitution of Eq. (5-17) into Eq. (5-16) yields,

$$\mathrm{F}(a_0) = 1 - \exp\left(-\frac{\theta}{1 - \theta}\right) \tag{5-18}$$

Substituting back into the probability equation, Eq. (5-12), and into the equation for the adsorption rate, Eq. (5-10), and equating to the desorption rate, Eq. (5-8), the equation describing the Volmer Isotherm is obtained,

$$bP = \frac{\theta}{1 - \theta} \exp\left(\frac{\theta}{1 - \theta}\right) \tag{5-19}$$

where *b* is the same as for the Langmuir isotherm, Eqs. (5-5) and (5-6).

The kinetic approach used to describe the distributed monolayer adsorption on 2D surfaces, which was just shown to allow the derivation of the Volmer isotherm equation, offers some interesting insight into the physical features behind the different shapes of the Volmer and Langmuir isotherms. The Volmer isotherm is significantly more concave than the Langmuir isotherm. Mathematically, this is expressed by the additional exponential factor existent in the Volmer equation. Physically, this reflects the need for the existence of space between the molecules already adsorbed for new adsorption of gas-phase molecules to take place. For high coverages, there is so little free area, that the frequency with which a large enough space is formed, so that adsorption can occur, is extremely small, thus dramatically reducing the adsorption rate compared to that of localised adsorption at the same coverage. In fact, from Eqs. (5-11), (5-12) and (5-18), one obtains:

$$\mathrm{p}(d_{inter} > d^*) = \exp\left(-\frac{\theta}{1-\theta}\right) \qquad (5\text{-}20)$$

Thus, for high surface coverage, the probability there will be enough free space concentrated for adsorption to occur tends to zero.

As for localised adsorption, for low coverages, the adsorption rate equation, Eq. (5-10), can be considered coverage-independent, with $(1-\theta) \approx 1$ and $\mathrm{p}(d_{inter} > d^*) \approx 1$, resulting in the Henry isotherm equation. Naturally, applying this condition directly to the Volmer isotherm leads to the same outcome.

Finally, it is worth pointing out that this approach does not assume the existence or inexistence of 2D condensation. All the premises of the model presented hold true regardless.

5.3.3.Henry Equation for Surfaces

The Henry isotherm can be obtained directly from the rate equations, Eqs. (5-1), (3-4), (5-8), and (5-10) by considering that, for low coverage, $(1-\theta) \approx 1$. That is, the adsorption rate is independent of coverage. The Henry isotherm easily follows from equating the two rates,

$$K_H P = n \qquad (5\text{-}21)$$

Applying the $(1-\theta) \approx 1$ condition to the Langmuir and Volmer isotherms themselves, the same result is obtained. This result is consistent with the condition of Ideal Gas behaviour of the adsorbed phase, necessary also in the thermodynamic derivation of the Henry isotherm [13, 14]. This condition also implies dimensionless adsorbed molecules, which, thus, would not influence the adsorption rate, independently of superficial density, just as considered. In real systems, the condition of ideality is only met at very low densities.

5.4. 1D and 3D Adsorbed Phases – Adsorption in Micropores

Application of the kinetic approach to the derivation of adsorption isotherm equations for micropores has one significant difference regarding 2D adsorption; the interface between the two phases is available only to a small fraction of the adsorbate, present at the pore mouths. This influences fundamentally the modelling of both adsorption and desorption, as the rates of both are now dependent exclusively on concentration at the pore mouths, not the entire

adsorbed phase. Since we are only interested in dealing with equilibrium, it will be considered that concentration at pore mouth is the same as anywhere else in the pore.

There are two kinds of micropore adsorption that, we proposed in Chapter 4, can sometimes be modelled using the equations in Table 5.1; 1D and 3D adsorbed phases. As for 2D, the models developed for 1D and 3D will be premised on the (likely) supposition that gas molecules move much faster than molecules already adsorbed. As mentioned before, only distributed adsorption will be considered for 3D phases.

5.4.1. 3D Adsorbed Phases - Distributed Adsorption

The key variables relevant for describing a 3D system are the specific pore volume of the adsorbent, V (SI units of $m^3 \cdot kg^{-1}$), the molar volume of the adsorbent/adsorbate system, $v \equiv V/n$ ($m^3 \cdot mol^{-1}$), the average pore mouth area, A_{mouth} ($m^2 \cdot mouth^{-1}$), the total specific number of pores, N_{pore} ($pore \cdot kg^{-1}$) and the average number of mouths per pore, N_{mouth} ($mouth \cdot pore^{-1}$). As with a and a_0, for v, when $n = n_{max}$, $v = v_0$.

The rate of adsorption on a 3D phase is modelled very similarly to that of a distributed 2D phase, but the area available for adsorption is now only that of the pore mouths. That is,

$$r_a = \frac{P}{\sqrt{2\pi MRT}} \cdot A_{mouth} \cdot N_{pore} \cdot N_{mouth} \cdot \mathrm{p}(entry) \tag{5-22}$$

where $\mathrm{p}(entry)$ is the probability of entry of each gas molecule upon hitting the pore mouth. $\mathrm{p}(entry)$ is determined by conditions at the interface, the "surface" of the adsorbed phase inside the pore. In order to model this probability, a new variable is introduced for the 3D system: the interfacial molar area, a_{pore}. It can be defined as the pore mouth area, A_{mouth}, divided by the amount of adsorbed molecules *located at the interface,* $n_{interface}$.

$$a_{pore} \equiv \frac{A_{mouth}}{n_{interface}} \tag{5-23}$$

A visual representation of the concept of 3D adsorbed phase "surface" can be seen in Figure 5.3.

At equilibrium, the interfacial molar area and pore molar volume are related by

$$\frac{a_0}{a_{pore}} = \frac{v_0}{v} = \theta \tag{5-24}$$

As for 2D, the fraction of molecules not being deflected at the interface is given by

$$\mathrm{p}(entry) = (1-\theta)\cdot \mathrm{p}(a_S > a_0) \Leftrightarrow \mathrm{p}(entry) = (1-\theta)\exp\left(-\frac{\theta}{1-\theta}\right) \tag{5-25}$$

where a_S is the area of the circle centred on the centre of the impact site, and touching the nearest molecule inside the volume considered as interface.

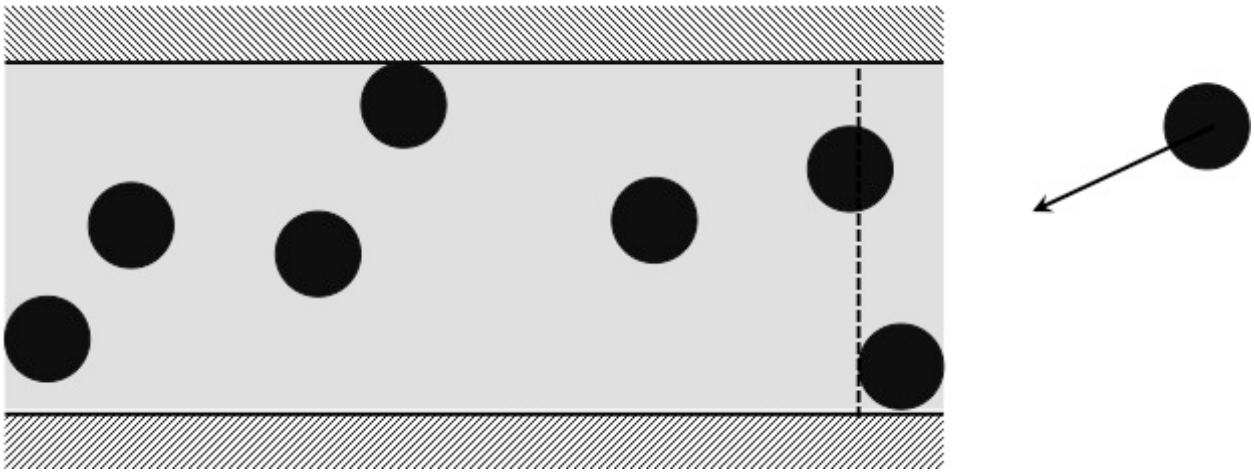

Figure 5.3. Representation of a 3D adsorbed phase and an incoming gas phase molecule. The dotted line represents the limit of the "surface" of the adsorbed phase, being distanced from the limit of the pore by one molecular diameter.

Substituting into Eq. (5-22),

$$r_a = \frac{P}{\sqrt{2\pi MRT}}\cdot A_{mouth}\cdot N_{pore}\cdot N_{mouth}\cdot(1-\theta)\exp\left(-\frac{\theta}{1-\theta}\right) \tag{5-26}$$

The desorption rate can also be modelled equivalently to what has been done for 2D. However, in this case, the desorption frequency is not multiplied by the total amount adsorbed, but by the total amount at the interface,

$$r_d = k_d\cdot\frac{1}{a_{pore}}\cdot A_{mouth}\cdot N_{pore}\cdot N_{mouth} \tag{5-27}$$

Equating r_a and r_d, solving for P and multiplying by a_0 on both sides, the Volmer isotherm equation is obtained,

$$bP = \frac{\theta}{1-\theta}\exp\left(\frac{\theta}{1-\theta}\right) \tag{5-28}$$

with,

$$b = \frac{K_H}{n_{max}} \tag{5-29}$$

and,

$$K_H = \frac{a_0\, n_{max}}{k_d\sqrt{2\pi MRT}} \tag{5-30}$$

It should be noticed that, despite their importance during derivation of the equation, both pore mouth area and the total number of pores do not influence K_H.

The limiting molar area can also be expressed as:

$$a_0 = A_{molecule} \cdot N_A \tag{5-31}$$

where $A_{molecule}$ is the average area occupied by a molecule at the interface. $A_{molecule}$ is determined by the size of the molecule, so bigger molecular sizes should contribute to increase K_H. However, they also decrease n_{max}, since fewer molecules will be able to fill the same volume. Hence, a more convenient way to represent K_H is,

$$K_H = \frac{\frac{a_0}{v_0} \cdot V}{k_d \cdot \sqrt{2\pi MRT}} \tag{5-32}$$

where direct, kinetic dependence on the molecular size and shape (v_0 and a_0) and total pore volume (V) is much clearer. Naturally, k_d will also be affected by molecular size, constituting an indirect influence on K_H.

As for 2D, although the expression is not exactly the same, the probability that an incoming molecule is adsorbed in a 3D adsorbed phase (i.e., enters the pore) decreases for increasing θ, Eq. (5-25). At high fillings, it is very difficult for molecules to enter the pore, even if it is not completely filled.

5.4.2. Henry Equation for 3D Adsorbed Phases

For 3D adsorbed phases, as for 2D, at low θ, the Volmer isotherm reduces to the Henry equation, Eq. (5-21). This corresponds to having an adsorption rate that is effectively independent of θ, with so few molecules inside the pores that entry of incoming gas molecules is, effectively, unimpeded. At higher fillings, the limitations to adsorption arising

from the presence of other molecules in the pore become apparent, and Volmer behaviour is established.

5.5. 1D Adsorbed Phases

In single-file diffusion systems, when pores are so small that it becomes impossible for molecules to bypass each other (so-called "single-file diffusion" systems), the concept of interfacial "surface" introduced in the previous section no longer applies. This means occupancy limitations to the adsorption rate will depend on the presence of a single adsorbed molecule close to the pore mouth. Such a system is represented in Figure 5.4. If there is an adsorbed molecule within a certain distance of the pore mouth, adsorption will not be possible. Similarly, for desorption, there will not be a molecule always available to desorb close to the pore mouth. The molecule closest to it will, instead, move towards and away from it successively, having a given probability of exiting the pore every time it comes close to the pore mouth.

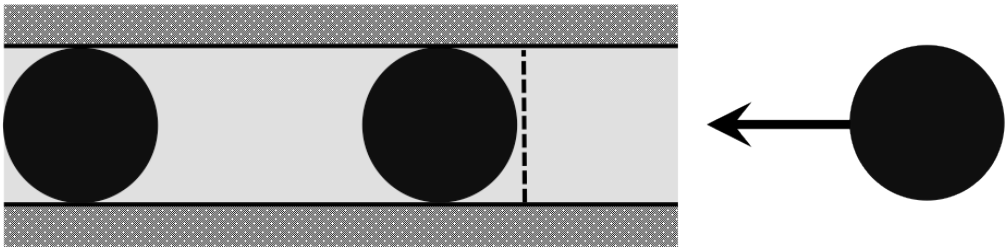

Figure 5.4. Representation of a single-file diffusion 1D adsorbed phase and an incoming gas molecule. The dotted line represents the minimum distance from the pore mouth to the adsorbed molecule closest to it, $\boldsymbol{d_{ads}}$, that allows adsorption to take place.

The key new variables used to characterise the system are the total specific pore length, L, with SI units of m·kg^{-1}, and the molar length, l, with SI units of m·mol^{-1}. Similarly to molar area and molar volume, the molar length is defined as:

$$l \equiv \frac{L}{n} \tag{5-33}$$

5.5.1.Localised Adsorption in 1D Adsorbed Phases

In 1D systems, the concept of localised adsorption is perfectly reasonable. Despite this, the adsorption rate is calculated similarly to that of distributed adsorption in 3D pores,

$$r_a = \frac{P}{\sqrt{2\pi MRT}} \cdot \alpha \cdot A_{mouth} \cdot N_{pore} \cdot N_{mouth} \cdot \mathrm{p}(entry) \tag{5-34}$$

where α represents the fraction of impacts with an angle that allows the molecule to enter the pore.

Since adsorption is now localised, $\mathrm{p}(entry)$ is the probability that a molecule that has entered the pore adsorbs in a free adsorption site. That is, it is equal to the probability of the adsorption site closest to the pore mouth being free, $\mathrm{p}(site\ is\ free)$,

$$\mathrm{p}(entry) = \mathrm{p}(site\ is\ free) \tag{5-35}$$

This probability is equal to the fraction of overall free adsorption sites.

$$\mathrm{p}(entry) = 1 - \theta \tag{5-36}$$

Therefore,

$$r_a = A_{mouth} \cdot N_{pore} \cdot N_{mouth} \cdot \frac{\alpha \cdot P}{\sqrt{2\pi MRT}} \cdot (1 - \theta) \tag{5-37}$$

The desorption rate also depends on the occupancy of the site closest to pore mouth, but on the probability that the site is occupied. When this happens, a characteristic desorption frequency determines the rate at which molecules leave the mouth of the pore. Therefore, the desorption rate is given by,

$$r_d = k_d \cdot N_{pore} \cdot N_{mouth} \cdot \mathrm{p}(site\ is\ occupied) \tag{5-38}$$

At equilibrium, the probability that the site closest to the pore mouth is occupied is equal to the fraction of adsorption sites, θ, so,

$$r_d = k_d \cdot N_{pore} \cdot N_{mouth} \cdot \theta \tag{5-39}$$

Equating r_a and r_d,

$$bP = \frac{\theta}{1-\theta} \tag{5-40}$$

with,

$$b = \frac{K_H}{n_{max}} \tag{5-41}$$

and,

$$K_H = \frac{\alpha \cdot A_{mouth} \cdot 1/l_0 \cdot L}{k_d \cdot \sqrt{2\pi MRT}} \tag{5-42}$$

The kinetic approach thus confirms the result already obtained with the thermodynamic approach, showing that the Langmuir equation adequately describes localised adsorption in 1D adsorbed phases. In fact, the derivation is relatively straightforward, when compared to those of distributed adsorption, thus being especially awkward it was never attempted before.

5.5.2.Distributed Adsorption

For 1D distributed adsorption, the adsorption rate initial formula is exactly the same as for localised adsorption,

$$r_a = \frac{P}{\sqrt{2\pi MRT}} \cdot \alpha \cdot A_{mouth} \cdot N_{pore} \cdot N_{mouth} \cdot \mathrm{p}(entry) \tag{5-43}$$

where α represents the fraction of impacts with an angle that allows the molecule to enter the pore.

In this case, $\mathrm{p}(entry)$ is the probability of a molecule existing close enough to the pore mouth so that it prevents an incoming molecule from entering. If the critical distance allowing adsorption is d_{ads}, then,

$$\mathrm{p}(entry) = \mathrm{P}(d > d_{ads}) \tag{5-44}$$

where d represents the distance between the pore mouth and the adsorbed molecule closest to it.

Using a similar reasoning as that used with areas for 2D surfaces, it can easily be concluded that the distance between adsorbed molecules is well expressed by an exponential distribution. Assuming that, at equilibrium, the distance to the pore mouth is equivalent to the distance between two adsorbed molecules, it is possible to write,

$$\mathrm{f}(d) = \lambda \exp(-\lambda\, d) \tag{5-45}$$

$$\mathrm{F}(d) = 1 - \exp(-\lambda\, d) \tag{5-46}$$

and

$$\lambda = \frac{1}{\langle d \rangle} = \frac{1}{l - l_0} \tag{5-47}$$

giving

$$\mathrm{f}(d) = \frac{1}{l - l_0} \exp\left(-\frac{d}{l - l_0}\right) \tag{5-48}$$

$$\mathrm{F}(d) = 1 - \exp\left(-\frac{d}{l - l_0}\right) \tag{5-49}$$

where frequency $\mathrm{f}(d)$ is given in mol·m^{-1} and $\mathrm{F}(d)$ is dimensionless. $\mathrm{p}(entry)$ can now be expressed in terms of d_{ads},

$$\mathrm{p}(entry) = \mathrm{p}(d > d_{ads}) = 1 - \mathrm{F}(d_{ads}) = \exp\left(-\frac{d_{ads}}{l - l_0}\right) \tag{5-50}$$

where d_{ads} will be considered to correspond to the length of a single molecule, that is, l_0. Therefore,

$$\mathrm{p}(entry) = \exp\left(-\frac{l_0}{l - l_0}\right) \tag{5-51}$$

From Eq. (5-33), it is easy to show that,

$$\frac{l_0}{l - l_0} = \frac{\theta}{1 - \theta} \tag{5-52}$$

The adsorption rate equation can now be rewritten as,

$$r_a = A_{mouth} \cdot N_{pore} \cdot N_{mouth} \cdot \frac{\alpha \cdot P}{\sqrt{2\pi MRT}} \cdot \exp\left(-\frac{\theta}{1 - \theta}\right) \tag{5-53}$$

The desorption rate depends on the frequency with which the molecule closest to the exit "hits" the pore mouth (i.e., is available for adsorption), k_{hit}, and the probability of desorption upon each "hit", $\mathrm{p}(desorb)$. Hence,

$$r_d = N_{pore} \cdot N_{mouth} \cdot k_{hit} \cdot \mathrm{p}(desorb) \tag{5-54}$$

Considering the pore has a smooth and homogeneous internal surface, the "hitting" frequency of adsorbed molecules with the pore mouth is given by

$$k_{hit} = \bar{v} \cdot \mathrm{f}(d = 0) \tag{5-55}$$

where $\bar{v}$ is the mean speed of adsorbed molecules ($\mathrm{m \cdot s^{-1}}$) and $\mathrm{f}(d = 0)$ is the "frequency" ($\mathrm{mol \cdot m^{-1}}$) with which molecules hit each other inside the pores.

From Eq. (5-48),

$$\mathrm{f}(d = 0) = \frac{1}{l - l_0} \tag{5-56}$$

Therefore,

$$k_{hit} = \bar{v} \cdot \frac{1}{l - l_0} \tag{5-57}$$

and,

$$r_d = N_{pore} \cdot N_{mouth} \cdot \bar{v} \cdot \frac{1}{l - l_0} \cdot \mathrm{p}(desorb) \tag{5-58}$$

Using Eq. (5-52), this can be rewritten as

$$r_d = N_{pore} \cdot N_{mouth} \cdot \frac{\bar{v} \cdot \mathrm{p}(desorb)}{l_0} \cdot \frac{\theta}{1 - \theta} \tag{5-59}$$

Thus, the initially hidden frequency of desorption can now be represented explicitly,

$$k_d = \frac{\bar{v} \cdot \mathrm{p}(desorb)}{l_0} \Leftrightarrow k_d = k_0 \cdot \exp\left(-\frac{E_a}{RT}\right) \tag{5-60}$$

given in $\mathrm{mol \cdot s^{-1} \cdot mouth^{-1}}$.

Equating r_a and r_d, multiplying by l_0 on both sides, and solving for bP, it results that,

$$bP = \frac{\theta}{1 - \theta} \exp\left(\frac{\theta}{1 - \theta}\right) \tag{5-61}$$

with,

$$b = \frac{K_H}{n_{max}} \tag{5-62}$$

and,

$$K_H = \frac{\alpha \cdot A_{mouth} \cdot n_{max}}{k_d \cdot \sqrt{2\pi MRT}} = \frac{\alpha \cdot A_{mouth} \cdot 1/l_0 \cdot L}{k_d \cdot \sqrt{2\pi MRT}} \tag{5-63}$$

The expression for K_H is, as expected, exactly the same as the one determined for the Langmuir equation.

The geometric factor present in K_H for 3D phases, a_0/v_0, is now $1/l_0$, given that only pore length occupied by the adsorbed molecule influences equilibrium. It is interesting to notice that, unlike what happens for 1D and 3D, in systems with 2D adsorbed phases, K_H does not depend directly on the size and shape of the adsorbate, reflecting the fact that, for low coverages, molecular size does not influence the extent of adsorption on the surface.

It is worth noticing that l_0 is widely used in the derivation of the Volmer equation for distributed adsorption, while it does not feature in the localised adsorption derivation. This happens because, for localised adsorption, l_0 is variable and does not influence the probabilities of neither adsorption or desorption. l_0 corresponds to the distance between adsorption sites, with molecular length being merely the minimum for this distance. It does, however, influence adsorption, since it represents adsorption site density of the material, and that is why it appears in the expression for K_H.

$\mathrm{p}(entry)$ for 1D localised and distributed adsorption is as different between the two as $\mathrm{p}(d_{inter} > d^*)$ is for 2D adsorption. As with the latter, while for localised adsorption the adsorption rate depends linearly on θ, for distributed adsorption it depends exponentially. With localised adsorption sites, for equivalent filling, the frequency with which the pore mouth is available for adsorption of a new molecule depends only on the fraction of time the site closest to the pore mouth is free, not a confluence of probabilities, as for distributed adsorption. In this case, for high fillings, there is so little free length inside the pore that the probability there will be enough of it concentrated at the pore mouth, allowing adsorption to take place, is extremely small.

5.5.3. Henry Equation for 1D Adsorbed Phases

For 1D adsorbed phases, as in 2D and 3D, the Henry isotherm is obtained, both for localised and distributed adsorption, by considering the effect of low values of θ on the rate of adsorption. In this case, the rate of adsorption is essentially independent of the amount adsorbed, since the probability of a molecule being close to the pore mouth is very small.

5.6. Interactions Between Adsorbed Molecules – The Hill-de Boer and Fowler-Guggenheim Equations

Adsorbate-adsorbate interactions (so-called "lateral interactions") may cause changes in the heat of adsorption, which influences the rate of desorption. We will assume the rate of adsorption is unaffected. For 2D, this is not strictly true, since variations in the strength of adsorption influence parameter α, which was previously assumed to be independent of P and n. The activation energy needed to pull an adsorbed molecule away from the surface (or pore) is now the energy associated with interactions between the adsorbed molecule and the surface (or pore) plus the energy associated with the interactions between adsorbed molecules

$$E_a = (-\Delta H)_{ads} = Q_{ads} + (-\Delta H_{inter}) \tag{5-64}$$

where Q_{ads} represents the energy associated with adsorbate-adsorbent interactions and $(-\Delta H_{inter})$ represents the energy associated with lateral interactions. $(-\Delta H_{inter})$ depends on the number of molecules next to each adsorbed molecule, and can therefore be approximated as,

$$(-\Delta H_{inter}) = z \cdot w \cdot \theta \tag{5-65}$$

where z is the number of positions, adjacent to the molecule, that other molecules can occupy and w is the energy associated with interactions between two adsorbed molecules. θ is equal to the fraction of positions z that are occupied. From Eq. (5-3), it is possible to write that,

$$k_d = k_0 \cdot \exp\left(-\frac{Q_{ads}}{RT}\right) \cdot \exp\left(-\frac{zw\theta}{RT}\right) \Leftrightarrow k_d = k_d' \cdot \exp\left(-\frac{zw\theta}{RT}\right) \tag{5-66}$$

Replacing this expression in Eqs. (3-4), (5-8), (5-27), (5-39) and (5-60), the desorption rate considering interactions between adsorbed molecules is obtained. The Fowler-Guggenheim and Hill-de Boer equations follow naturally from there,

$$bP = \frac{\theta}{1-\theta} \exp(-c\,\theta) \tag{5-67}$$

$$bP = \frac{\theta}{1-\theta}\, exp\left(\frac{\theta}{1-\theta}\right) exp(-c\,\theta) \tag{5-68}$$

with,

$$c = \frac{zw}{RT} \tag{5-69}$$

where c is a system-specific constant.

The Henry constants obtained remain unchanged; only k_d is replaced by k'_d, which are actually the same, since both are exclusively dependent on Q_{ads}.

This approach to incorporation of lateral interactions assumes that the distribution of the molar area, molar volume and molar length are unaffected by the existence of intermolecular forces. An equivalent assumption was central to the derivation of the van der Waals equation [18], and, thus, is already implicit when applying its two-dimensional form to the Gibbs adsorption isotherm [7, 14]. Naturally, if the same isotherm expression is to be obtained using the kinetic approach, this assumption must be built into this derivation.

It should be pointed out that Eq. (5-64) does not imply that Q_{ads} must be constant regarding θ. In fact, Q_{ads} typically decreases with θ [14, 19], and may actually hide the influence of lateral interactions on the heat of adsorption. If the variation is linear, or can be approximated as such, this dependence can be incorporated into an experimentally determined linearity constant, which would also incorporate, but not be equal to, c. If the variation is not linear, the Fowler-Guggenheim and Hill-de Boer equations (as well as the associated equations of state) do not apply to the system in question.

5.7. Conclusions

The Henry, Langmuir, Volmer, Fowler-Guggenheim and Hill-de Boer equations were derived using a kinetic approach. The Kinetic Gas Theory was used as a starting point to determine the rate of adsorption, while the rate of desorption was modelled by considering desorption to be an activated process with an activated energy equal to the heat of adsorption. The exponential term that distinguishes equations for localised and distributed adsorption emerges considering a random distribution of intermolecular distances. This distance influences (in different ways for 1D, 2D and 3D phases) the probability of adsorption occurring upon impact of a gas-phase molecule. Considering localised adsorption in 1D and 2D systems leads to the Langmuir equation. When interactions between adsorbed molecules are considered, through their influence on the heat of adsorption, the Fowler-Guggenheim equation is obtained. Localised adsorption in 3D adsorption systems was considered to be unrealistic and was not

modelled. For distributed adsorption in 1D, 2D and 3D systems, the Volmer isotherm equation was obtained. Incorporating interactions between adsorbed molecules leads to the Hill-de Boer equation. The Henry isotherm can be obtained for 1D, 2D and 3D adsorption phases, from both the Langmuir and the Volmer isotherms, by considering the adsorption rate to be independent from the amount adsorbed. These results are in agreement with those obtained with a thermodynamic approach.

5.8. References

1. R. Ghosal and D. M. Smith, Micropore Characterization using the Dubinin-Astakhov Equation to Analyze High Pressure CO2 (273 K) Adsorption Data, J. Porous Mater. 3 (1996), 247-255.
2. I. Langmuir, The Adsorption of Gases on Plane Surfaces of Glass, Mica and Platinum, J. Am. Chem. Soc. 40 (1918), 1361-1403.
3. R. Fowler and E. A. Guggenheim, in *Statistical Thermodynamics*, Ch. X., pp. 421-451 (Cambridge University Press, 1949).
4. M. Volmer, Thermodynamische Folgerungen aus der Zustandsgleichung fur Adsorbierte Stoffe, Z. Phys. Chem. 115 (1925), 253-261.
5. T. L. Hill, Statistical Mechanics of Multimolecular Adsorption II. Localized and Mobile Adsorption and Absorption, J. Chem. Phys. 14 (1946), 441-453.
6. T. L. Hill, Statistical Thermodynamics of the Transition Region between Two Phases. II. One Component System with a Plane Interface, J. Chem. Phys. 20 (1952), 141-144.
7. J. H. de Boer, in *The Dynamical Character of Adsorption*, 1st ed., Ch. VIII., pp. 170-199 (Oxford University Press, 1953).
8. F. London and M. Polányi, Über die atomtheoretische Deutung der Adsorptionskräfte, Naturwissenschaften 18 (1930),
9. B. H. Lapizco-Encinas and N. G. Pinto, Effectiveness of the H-root method for determining adsorption isotherms of protein–salt systems in open micro-channels, J. Chromatogr. A 1036 (2004), 61-72.
10. T. M. Albayati and A. M. Doyle, Shape-selective adsorption of substituted aniline pollutants from wastewater, Adsorption Science and Technology 31 (2013), 459--468.
11. V. Mishra, C. Balomajumder, and V. K. Agarwal, Design and optimization of simultaneous biosorption and bioaccumulation (SBB) system: A potential method for removal of Zn(II) ion from liquid phase, Desalin. Water Treat. 51 (2013), 3179--3188.
12. J. H. de Boer, in *The Dynamical Character of Adsorption*, 1st ed., pp. 1-53 (Oxford University Press, 1953).
13. J. H. de Boer, in *The Dynamical Character of Adsorption*, 1st ed., Ch. VI., pp. 90-122 (Oxford University Press, 1953).
14. D. D. Do, in *Adsorption Analysis: Equilibria and Kinetics*, Ch. 2, pp. 11-48 (Imperial College Press, 1998).
15. D. P. Bertsekas and J. N. Tsitsiklis, in *Introduction to Probability*, 2nd ed., Ch. 6, pp. 295-338 (Athena Scientific, 2008).
16. M. Dwass, in *Probability: Theory and Applications*, Ch. 11.12, (W. A. Benjamin, 1970).
17. S. M. Ross, in *Introduction to Probability and Statistics for Engineers and Scientists*, 3rd ed., Ch. 5.6, pp. 175-181 (Elsevier Academic Press, 2004).
18. J. D. v. d. Waals, in *On the Continuity of the Gaseous and Liquid States*, (ed. J.S. Rowlinson), Ch. 7. , pp. 173-174 (Dover Phoenix Editions, 1988).
19. J. H. de Boer, in *The Dynamical Character of Adsorption*, 1st ed., Ch. V. The Quantity σ: Unimolecular and Multimolecular Adsorption, pp. 58-60 (Oxford University Press, 1953).

Chapter 6. General Conclusions and Future Work

Crystalline hydrophobic dipetides are microporous materials that have been considered a very promising kind of peptide-based supramolecular microporous material. Like metal-peptide frameworks, they can only be used in the crystalline solid state as membrane material and as adsorbents. Macrocyclic peptides and dendritic peptides, on the other hand, are used mainly in solution, especially the former. These two have thus been those that have better replicated the properties of natural protein and peptide pores, in aqueous environments, while metal-peptide frameworks and hydrophobic dipeptides have shown how typical protein properties such as framework flexibility and guest-specificity can generate unexpected and unusual properties in the crystalline solid state.

The VA-class of crystalline hydrophobic dipeptides (seven dipeptides) displays hydrophobic ultramicropores in the 0.37-0.50 nm range, and is therefore extremely interesting in the adsorption of gases and vapours. AA and LS, technically not included of the VA-class, also form hydrophobic cavities and pores. AA displays isolated cages, while LS displays 0.49 nm-wide pores. Single-crystal permeation experiments with AA, VI and LS were performed with atmospheric gases. The four dipetides with the smallest pores in the VA-class, VI (0.37 nm), IA (0.37 nm), IV (0.39 nm) and VV (0.44 nm), were tested as adsorbents of N_2, O_2, Ar, Xe and CO_2.

The permeation experiments showed that these materials have very high permeabilities. It was also observed that small pore size, framework flexibility and pore blockage can have a dramatic effect on the properties of framework-guest interactions. Millimetre-sized VI single-crystals were capable of permeating O_2, N_2 and He, but not Ar. Initially, it was thought this could be due to the open pore sieving the slightly larger Ar atom and not the other species. As VI crystalline powder (crystal length of 1-50 μm) easily adsorbs Ar and crystalline defects increase with pore length, it is likely that Ar impermeability is due to pore blockage. Framework flexibility probably plays an important role in the permeation of the slightly smaller species of O_2, N_2 and He. AA, being non-porous and forming isolated cavities, was, nonetheless, able to permeate O_2, in a remarkable display of framework flexibility of these "soft" materials. If a hydrophobic dipeptide were to be used in an actual membrane separation process, the retained species would have to be sieved outside the pore, having thus to be clearly bigger than the permeating species.

Adsorption isotherms of atmospheric gases unveiled an unusual property; Ar is preferentially adsorbed against O_2. N_2 adsorption was inferior to both Ar and O_2. This preferential adsorption sequence, $Ar>O_2>N_2$, is highly unusual. All dipeptides tested, VI, IA, IV and VV, showed the same sequence of preferential adsorption. Similarly, all gases used had the same sequence of preferential adsorption for different dipeptides, VI<IA<IV<VV. Adsorption preference thus follows pore size variation sequence, for these four dipeptides.

Given pore morphology and chemistry, a scenario of distributed adsorption with no lateral interactions was assumed for atmospheric gases in the pores of hydrophobic dipeptide crystals. This picture is close to that underlying the derivation of the Volmer equation for two-dimensional surfaces. Although it was, at the time, uncertain whether it would also apply to one-dimensional systems, such as those under consideration, it was decided to use it. It was later possible to show this attribution to be correct.

Interpretation of the simple adsorption preference sequences proved more complicated than initially expected. The heats of adsorption of N_2 and O_2 do not follow such a simple relation, and vary in a non-monotonic fashion with pore size. The heat of adsorption of Ar does vary monotonically, but showing precisely the trend opposite to that of adsorption affinity. Equally, the $Ar>O_2>N_2$ sequence of preferential adsorption for each dipeptide is also not observed in the heats of adsorption. These results were interpreted as stemming from a complex interaction of entropic degrees of freedom (influencing the pre-exponential factor of the van't Hoff equation) and matching between pore and guest molecule morphologies (influencing the heat of adsorption).

The heats of adsorption do not vary significantly with the adsorbed concentration, for any host-guest pair, with the possible exception of N_2. This indicates, on one hand, the existence of a relatively uniform adsorption potential field inside the pores and, on the other, that interactions between guest molecules never becomes significant within the experimental conditions tested, as expected given all isotherms are, for all practical purposes, linear. The values determined are small when compared to those obtained for other materials. In the case of N_2, three of the four values determined are below 15 $kJ \cdot mol^{-1}$, the minimum reported in the literature.

The Ar/O_2 selectivity values determined are very high. Those determined for VI, at any of the three temperatures, are better than any previously reported for Ag-free adsorbents. The best result obtained was 1.30, for VI, at 5 ºC, under vacuum. Selectivity decreases slightly with pressure, for all four dipeptides, as expected given it is the ratio of two Type I adsorption

isotherms barely out of the Henry region. Temperature dependence of selectivity variation is very pressure dependent. At vacuum conditions, it either decreases or increases with increasing temperature depending on whether the heat of adsorption of Ar is bigger or smaller, respectively, than that of O_2. Similar behaviours are observed for O_2/N_2 selectivities. Both Ar/O_2 and O_2/N_2 selectivities decrease with increasing pore size.

Despite the exceptional results obtained, it is unlikely crystalline hydrophobic dipeptides could be used as an adsorbent in PSA-based separation processes, mainly due to poor adsorption capacities; these are caused by the low pore densities of this class of materials. However, the selectivity results obtained could point to extreme confinement in hydrophobic ultramicropores of organic materials as a possible path for systematically obtaining similar selectivities. This can only be confirmed by determination of the adsorption isotherms of other materials with similar structures to those of crystalline VA-class dipeptides. If such structure-property relation does exist, then organic adsorbents with hydrophobic micropores could be a viable alternative to Ag-based adsorbents. Given the large number and wide variety of OSMSs discovered in the last 20 years, materials with such features should be in no short supply. It would also be interesting to assess what are the limits of framework flexibility, in these and other supramolecular adsorbents, and to what extent is the sieving threshold influenced by the intensity of the interactions with the framework. This could possibly have great influence in adsorption and diffusion in the porous framework, with obvious practical implications.

In order to better interpret some of the results obtained, and be able to gain insight into the physical phenomena occurring at the atomic level, adsorption models were developed for unidimensional pores such as those of hydrophobic dipeptide crystals. By using a well-established thermodynamic approach, embodied by the Gibbs Adsorption Isotherm, it was possible to demonstrate that, under certain assumptions, some simple equations used to describe surface adsorption (2D adsorption systems) and micropore-filling (3D adsorption systems) can also be used with equal validity in single-file adsorption (1D adsorption systems). The approach used was exactly the same as that of 2D and 3D adsorption, and its implementation in 1D systems was quite straightforward once appropriate system variables analogue to the spreading pressure and molar area of 2D systems were developed.

The Gibbs Adsorption Isotherm is obtained by equalising the Gibbs energy differentials in the adsorbed phase and the bulk gas/liquid phase. It is, thus, universally applicable, although its phenomenological validity is dependent on the physical significance of the characteristic

variables used for the system under consideration. In the case of 2D systems, it has long been known that the monolayer assumption is very seldom fulfilled, so spreading pressure and molar area are typically used only as mathematical handles. 3D systems are much more common, and are implicitly assumed whenever a Dubinin equation is used to determine a pore size distribution, even if that is not always correct. True 1D systems only occur when there is a degree of in-pore homogeneity that, while not always present, is a reasonable approximation for many porous frameworks. Unlike with 3D systems, for 1D, localised adsorption is a feasible scenario, making equations such as Langmuir and Fowler-Guggenheim applicable to such systems with potential physical significance. It is thus necessary to stop referring to such equations as mere correlations when applied to any case of adsorption in micropores, as the micropore-filling model does not apply to ultramicropores with single-file diffusion. For 1D systems, the capacity-determining variable is total pore length, not surface area (2D) or total pore volume (3D).

Once physically significant equations were available, it was possible, by gauging which one describes the data best, to assess some of the characteristics of the adsorption system. For example, if the equation that best describes a set of data presupposes localised adsorption, it may be reasonable to infer that adsorption in the system in question is localised. 1D adsorption models derived from the Gibbs Adsorption Isotherm were used to analyse adsorption isotherms of Xe and CO_2 in VI, IA, IV and VV. The tested equations were Langmuir, Volmer, Fowler-Guggenheim and Hill-de Boer. As a first step, a graphical method was employed to determine the appropriateness of different equations to describe the data. This allowed the Langmuir and Volmer equations to be excluded. The remaining two equations were fitted to the adsorption data. Both have two fitting parameters, so comparison of the sum of squares for the same isotherm may reasonably indicate which equation is more suited at describing the data. Based on this criterion, it was possible to clearly identify the Hill-de Boer equation as the one that best fits Xe adsorption isotherms in all four dipeptides. Furthermore, the Hill-de Boer fitting gives, in general, more feasible fitting parameters, thus confirming this assessment. It was thus concluded that Xe adsorption has mainly a distributed character (even in such small pores), with positive lateral interactions. For CO_2, the picture is less clear, probably due to a more mixed localised/distributed character of the adsorption. In general, the Fowler-Guggenheim equation provides a better description of the data, together with more feasible values for the fitting parameters, thus hinting that adsorption has a somewhat more localised character. This is confirmed by previous GCMC simulations of CO_2

adsorption in hydrophobic dipeptides. It is possible that CO_2's polarised molecule is able to induce localised transient polarisation of specific points in the aliphatic side-chains, unlike the intrinsically distributed dispersive (London) interactions of Xe atoms. The O_2, N_2 and Ar species are non-polarised, so they probably behave similarly to Xe, adsorbing distributively, just as initially assumed. Once again, the adsorption concentration achieved in crystalline dipeptides is only limited by the low pore density, as in-pore concentration is quite high, both for Xe and CO_2.

Although the thermodynamic derivations conclusively show that equations such as Langmuir's do apply to (certain) ultramicroporous adsorption systems, many suspicions remain on their applicability among researchers. This is probably simply due to inertia, stemming from pervasive misunderstandings on the nature of some equations. It is a well-established fact that the Dubinin equations have been shown to be no more than empirical correlations, and is even admitted by Stoeckli. This fact is independent of the accurate and effective use of the Dubinin equations-based methods to determine pore size distribution in activated carbons. Yet, it is as likely that one of the Dubinin equations will be used in interpreting isotherms of adsorption on microporous solids than an equation such as Langmuir, simpler and clearer. Even when the latter is used, it is frequently remarked that it is so solely as an empirical correlation. Also, the classic derivation of the Langmuir equation, still used today as a means of introducing the phenomenon of adsorption, is based on the traditional 2D monolayer view of surface adsorption. It is thus not always obvious how one fits Langmuir-like equations within a paradigm of "micropore filling". In order to overcome this resistance, simple kinetic derivations, very similar to that originally used by Langmuir, were performed for the Langmuir, Volmer, Fowler-Guggenheim and Hill-de Boer equations, on 1D and 3D adsorption systems.

The thermodynamic derivations prove that the equations can, given certain premises, be derived for such systems. The kinetic derivations, therefore, given the same premises, only show a different path for the derivation of those equations, and serve mainly an illustrative purpose. All the derivations are done assuming the adsorption of a gas, and use the Kinetic Gas Theory to calculate the rate of impact of gas molecules on the area of adsorption. Before moving to 1D and 3D systems, it was necessary to derive the Volmer equations for 2D systems, that is, the isotherm equation of distributed monolayer adsorption. The derivation procedure is almost the same as for the Langmuir equation, but the adsorption rate is further limited by the unavailability of the area between adsorbed molecules in close proximity, a

phenomenon unparalleled in localised adsorption. Area availability was modelled using an exponential distribution, which introduces into the equation of the rate of adsorption the exponential factor of the Volmer equation.

In 1D and 3D systems, unlike for 2D systems, not all molecules are available to desorb; only those at the pore mouth can do so. Similarly, not all adsorption space/length is available to receive adsorbing molecules, only that adjacent to the pore mouth. So, for 1D and 3D, adsorption and desorption rates are not directly dependent on the capacity-determining variables, pore length (1D) and pore volume (3D). Indirectly, capacity influences adsorption and desorption rates through the concentration of adsorbed molecules at the pore mouth. For 3D systems, by equating overall adsorbed concentration with the concentration at the interface, it is possible to model adsorption and desorption rates in a manner identical to what was done for 2D systems. Areal occupation at the interface was also modelled by an exponential distribution, resulting in a 3D version of the Volmer equation. In 1D systems, only one molecule can enter or leave at each moment, so modelling adsorption and desorption required a slightly different strategy. In this case, both adsorption and desorption rates depend on intermolecular distance, and it is through this variable that there is a connection to adsorbed concentration. Unlike for 3D systems, localised adsorption is possible for 1D systems. In this case, the derivation is directly analogue to that of 2D, as the equilibrium results from a balance between an adsorption rate proportional to the fraction of empty adsorption sites and a desorption rate proportional to the fraction of occupied adsorption sites.

The Fowler-Guggenheim and Hill-de Boer equations naturally emerge from the Langmuir and Volmer equations once the affinity constant and the heat of adsorption are related through an Arrhenius-like equation. The contribution of adsorbate-adsorbate interactions to the heat of adsorption can be separated from the adsorbate-adsorbent contribution, thus originating the concentration-dependent exponential factor characteristic of the two equations.

More complex models can be developed, particularly for equilibrium modelling, using more advanced tools, such as Statistical Thermodynamics. For kinetic derivations, very advanced methods are available with Molecular Dynamics computational techniques, but for purely illustrative purposes it is hard to envision something radically different being done.

Appendix A – Permeation Experiments and Results

A.1. Crystallisation

LS, VI and AA peptides were purchased from Bachem. LS crystals were grown through phase inversion of an aqueous solution by acetonitrile, and AA crystals by solvent evaporation of an aqueous solution. VI crystals were grown using both procedures. Phase inversion syntheses were performed on Emerald BioSystems Combiclover, Jr.™ crystallization plates, by sitting drop crystallization, with 200 μL of acetonitrile on each well, and 5 μL of peptide aqueous solution on each drop. The peptide solution concentration was 233 $mg \cdot mL^{-1}$ for LS, and 50 $mg \cdot mL^{-1}$ for VI. The usual crystallization time was two days, for both peptides.

Solvent evaporation was performed on a Memmert UL 30 oven. For AA, 100 μL of a saturated solution / suspension of 500 $mg \cdot mL^{-1}$ were heated at 80 ºC, for 30 - 60 min, until full solvent evaporation was achieved. For VI, 400 μL of a 50 $mg \cdot mL^{-1}$ solution were heated at 60 ºC, for 1 - 2 h, until full solvent evaporation was achieved.

The crystals were dried at 323 K for two days.

A.2. Crystal Data Collection and Refinement

Diffraction data were collected at 293 K with a Gemini PX Ultra equipped with CuKα radiation (λ=1.54184 Å), a 4-circle kappa goniometer and a CCD Detector. Data collection and data processing was carried out using CrysAlisPro software from Oxford diffraction. The structures were solved by direct methods using SHELXS-97 [Sheldrick,G.M. SHELXS-97, Program for the solution of crystal structures; University of Göttingen: Germany 1997] with atomic positions and displacement parameters refined with SHELXL-97 [Sheldrick,G.M. SHELXL-97, Program for the refinement of crystal structures; University of Göttingen: Germany 1997]. The non-hydrogen atoms were refined anisotropically and the hydrogen atoms were refined freely with isotropic displacement parameters.

Precession photographs of the peptide crystals were taken to determine the orientation of the *c*- crystallographic axis (i.e. the orientation of the nanotubes) within the crystals.

X-ray diffraction data was collected from an AA crystal at high O_2 pressure (8.5 bar). The crystal was mounted in a capillary sealed to a valve (Figure A.1). The capillary was evacuated and then pressurised with O_2. The crystal structure of AA is completely retained after gas permeation as can be observed in Figure A.2. Despite the smaller cell dimensions of the crystal of AA in complex with O_2 (Figure A.2), the carbon- carbon distances of opposite methyl groups increased very slightly from 5.467 to 5.473 Å upon pressurization.

Figure A.1. High pressure X-ray data collection: the crystal is mounted in a capillary sealed to a miniature valve.

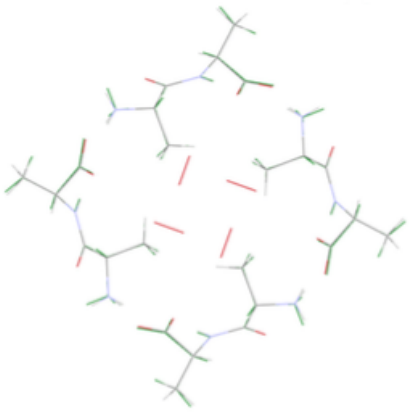

Figure A.2. Superimposed structures of AA crystals before (green) and after O_2 pressurization.

CCDC 749865 (AA), 749866 (AA high pressure O_2), 749867 (LS) and 749868 (VI) contain the supplementary crystallographic data. These data can be obtained free of charge from The Cambridge Crystallographic Data Centre via www.ccdc.cam.ac.uk/data_request/cif. Essential crystal data are given in Table A.1.

Table A.1 – Crystal data for the dipeptides used in the single-crystal permeation experiments.

Dipeptide	AA	VI	LS	AA after permation
Formula	$C_6H_{12}N_2O_3$	$C_{11}H_{22}N_2O_3$	$C_9H_{18}N_2O_4$	$C_6H_{12}N_2O_3$ ·0.018 O_2
M_r	160.2	230.3	218.3	160.8
Crystal system	Tetragonal	Hexagonal	Hexagonal	Tetragonal
Space group	$I4$	$P6_1$	$P6_5$	$I4$
a, Å	17.9540(4)	14.6653(5)	18.1703(3)	17.8674(2)
c, Å	5.1548(2)	10.3321(4)	6.1687(1)	5.1330(7)
V, Å^3	1661.63(7)	1924.4(2)	1763.80(5)	1638.7(3)
Z	8	6	6	8
D_x, g cm^{-3}	1.281	1.192	1.233	1.302
$R[F^2>2s(F^2)]$	0.0349	0.0386	0.0387	0.0467
$wR[F^2>2s(F^2)]$	0.0897	0.0863	0.118	0.1280
peak/hole, e Å^{-3}	0.11,-0.16	0.32, -0.23	0.57, -0.16	0.20, -0.20

A.3. Single-Crystal Permeation Experiments

Single-crystal permeation experiments were performed against the atmosphere using a pressurized feed gas chamber (chamber volume 1.44 mL). Single crystals were mounted in glass capillaries using cyanoacrylate glue (Figure A.3). Leak rate checks were performed to ensure that the glue was not permeable to the gases.

Two different methods were used to measure crystal permeation flow-rates (Figure A.3): 1. Pressure monitoring of the feed gas chamber; 2. Distance and time measurement of a moving liquid (Al's Oil) front on a glass tube glued to the gas chamber exit. Method 1 is the more straightforward of the two, while Method 2 has higher sensitivity. Both methods allow direct determination of flow-rates, with crystal geometry and pressure monitoring allowing permeabilities to be determined. Due to its higher permeation flow-rate, LS crystals were tested using Method 1, while for the slower permeating VI and AA, Method 2 was used.

In both methods, pressure monitoring was done using a Druck PMP 4010 pressure transducer. In Method 2, the liquid front's movement monitoring was done by taking regular pictures of the liquid, using a Nikon SMX800 loupe. Typically, a permeation experiment would take a few days. In Method 1, dP/dt determination, for a narrow pressure range, allows accurate flow-rate calculation using a linear regression. In Method 2, flow-rate calculation is straightforward: flow-rate = travelled distance · tube internal area / experiment time.

Data for the LS experiments using Method 1 are shown in Figures A.4-7.

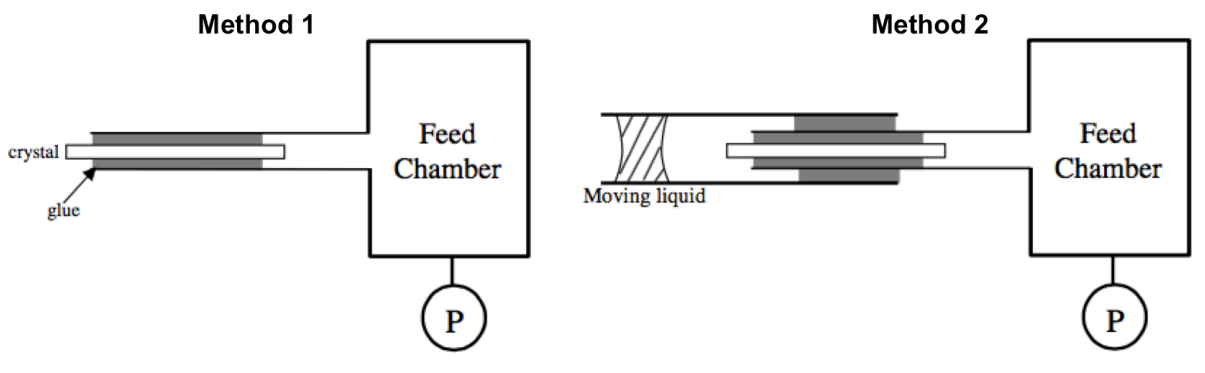

Figure A.3 – Scheme of the setups used for the single-crystal permeation experiments. Method 1, on the left, was used with LS crystals and Method 2, on the right, for the VI and AA experiments.

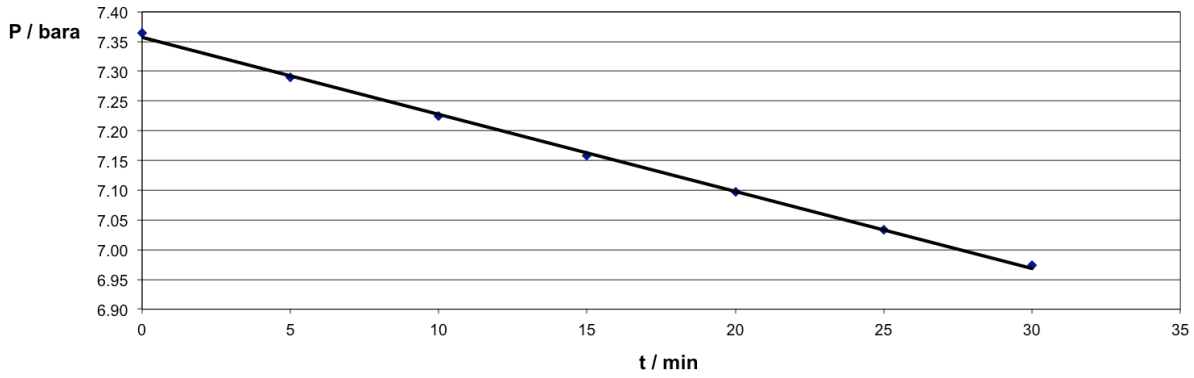

Figure A.4 – Raw data and linear fit of an Ar permeation experiment, done using Method 1. Linearization equation is P (bara) = 7.357 – 1.30 X 10^{-2} · t (min), with R^2 = 0.9991.

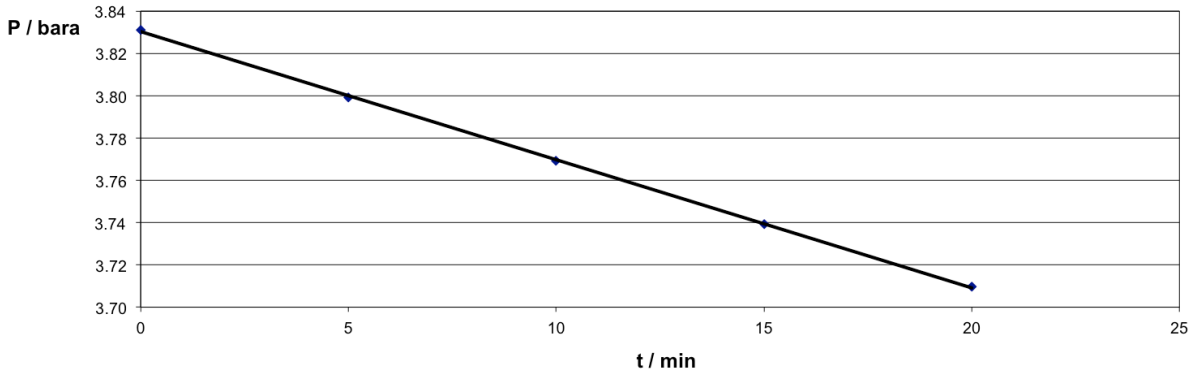

Figure A.5 – Raw data and linear fit of a N_2 permeation experiment, done using Method 1. Linearization equation is P (bara) = 3.830 – 6.06 X 10^{-3} · t (min), with R^2 = 0.9998.

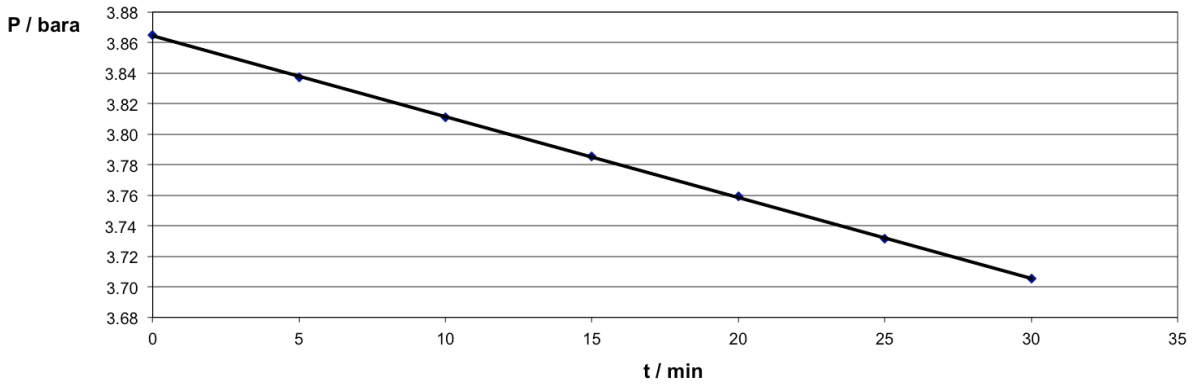

Figure A.6 – Raw data and linear fit of a O_2 permeation experiment, done using Method 1. Linearization equation is P (bara) = 3.864 – 5.30 X 10^{-3} · t (min), with R^2 = 0.99988.

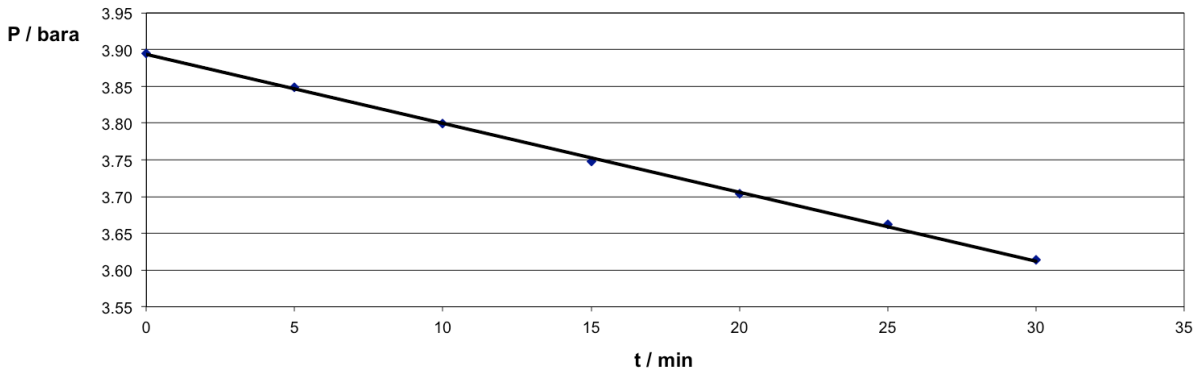

Figure A.7 – Raw data and linear fit of a He permeation experiment, done using Method 1. Linearization equation is P (bara) = 3.894 – 9.38 X 10^{-3} · t (min), with R^2 = 0.9991.

A.4. Knudsen Flow

Knudsen flow permeabilities were calculated using the following form of the Knudsen equation:

$$P_K = \frac{\varepsilon}{\tau} \cdot \frac{D_K}{RT} \tag{A-1}$$

Where

$$D_K = \frac{2}{3} \cdot r_P \cdot \bar{c} \tag{A-2}$$

And

$$\bar{c} = \sqrt{\frac{8RT}{\pi M}} \tag{A-3}$$

ε is the porosity, τ is tortuosity, D_K is the Knudsen diffusion, R is the universal gas constant, T is the temperature, r_P is the pore radius, $\bar{c}$ is the mean molecular speed and M is the gas molecules' molar mass.

Tortuosity and porosity were calculated using crystal structure data from [1]. Tortuosity was calculated by taking the ratio between the effective length per translation and the full translation, 1.019 and 1.008, for VI and LS, respectively. Porosity was calculated by dividing the permeation area per unit cell by the area of the unit cell:

$$\varepsilon = \frac{\pi/4 \cdot d_P^2}{a^2} \tag{A-4}$$

where d_P is the pore diameter and a is a unit cell dimension.

Table A.2 shows the experimental enhancement over what would be expected if the permeating fluid followed a Knudsen regime.

Table A.2 - Enhancement over Knudsen model prediction of mass transport through LS and VI crystals.

Dipeptide	He	O_2	N_2	Ar
LS	1800	2800	3000	4000
VI	8.7	2.4	1.8	-

A.5. References

1. D. V. Soldatov, I. L. Moudrakovski, E. V. Grachev, and J. A. Ripmeester, Micropores in Crystalline Dipeptides as Seen from the Crystal Structure, He Pycnometry, and 129Xe NMR Spectroscopy, J. Am. Chem. Soc. 128 (2006), 6737-6744.

Appendix B – SEM Characterisation

B.1. VI Crystals Grown Through Phase Inversion with Acetonitrile

Millimetre-long VI crystals can be grown either by phase inversion of an aqueous solution (with methanol or acetonitrile, for example), or by rapid water evaporation from an aqueous solution. The crystals used in the single-crystal experiments were obtained by the latter method. The SEM pictures here shown refer to the former, but may be considered loosely representative of crystals produced by both techniques.

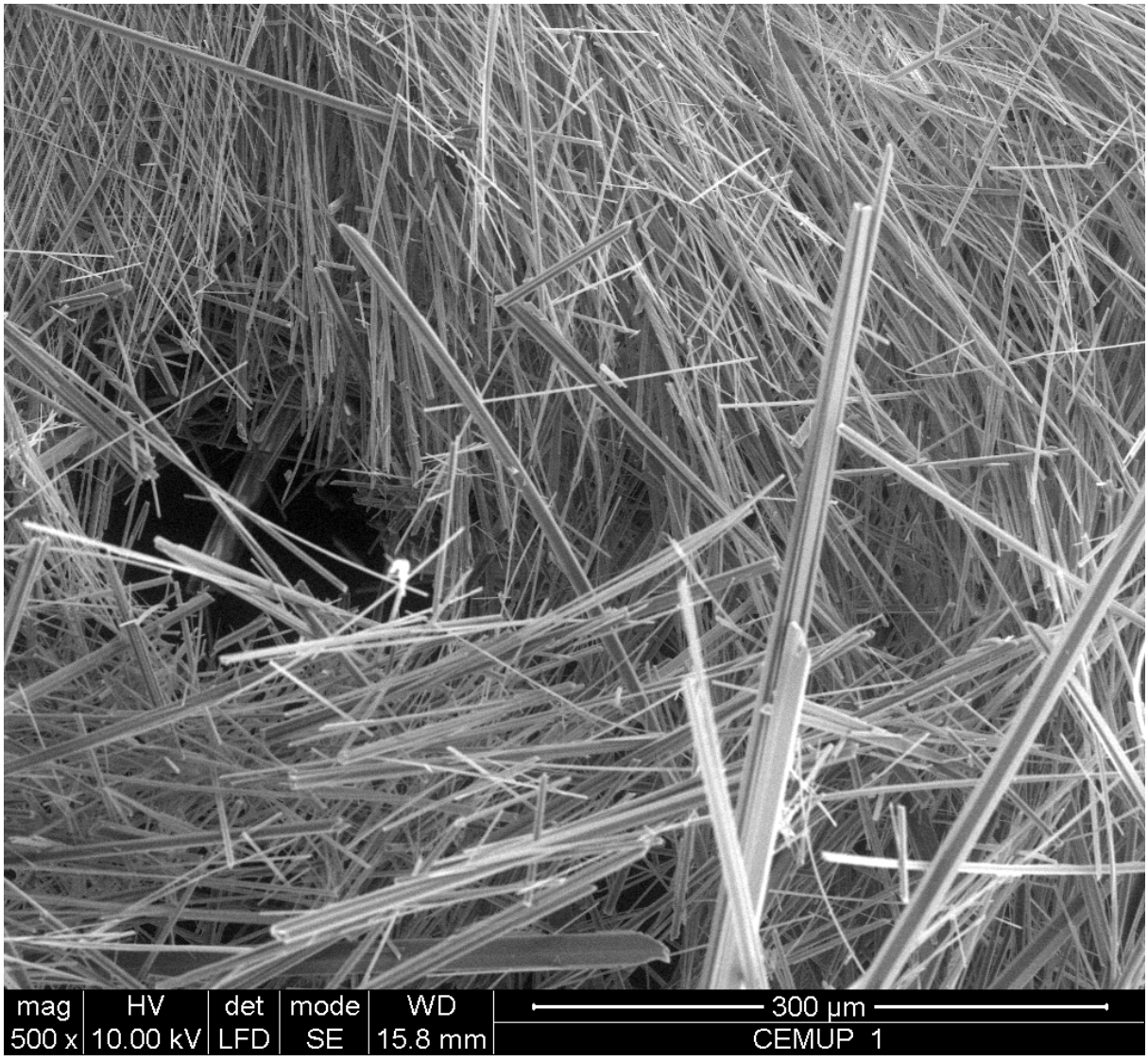

Figure B.1. VI crystals grown through phase-inversion, of an aqueous solution, with acetonitrile.

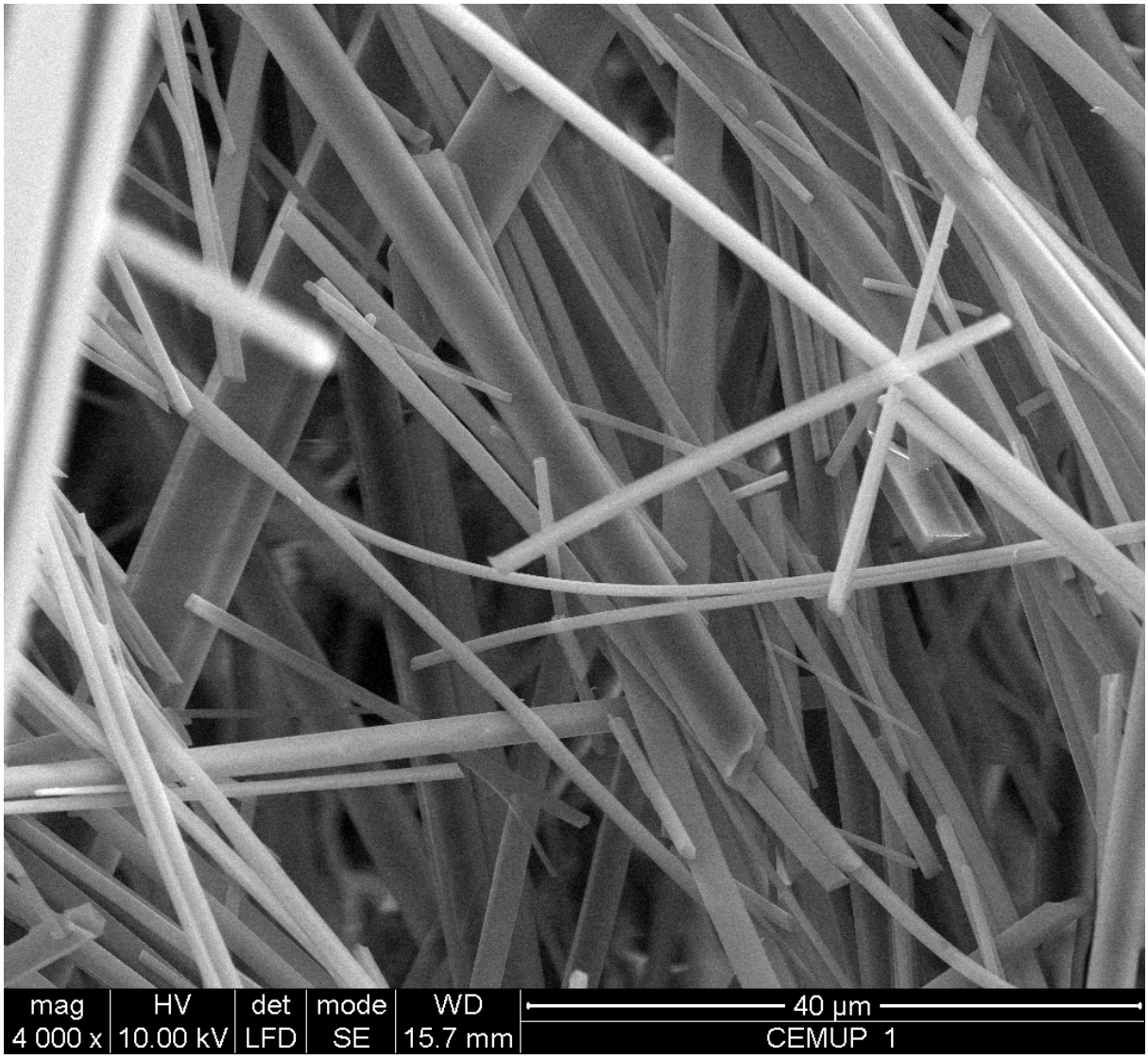

Figure B.2. VI crystals grown through phase-inversion, of an aqueous solution, with acetonitrile.

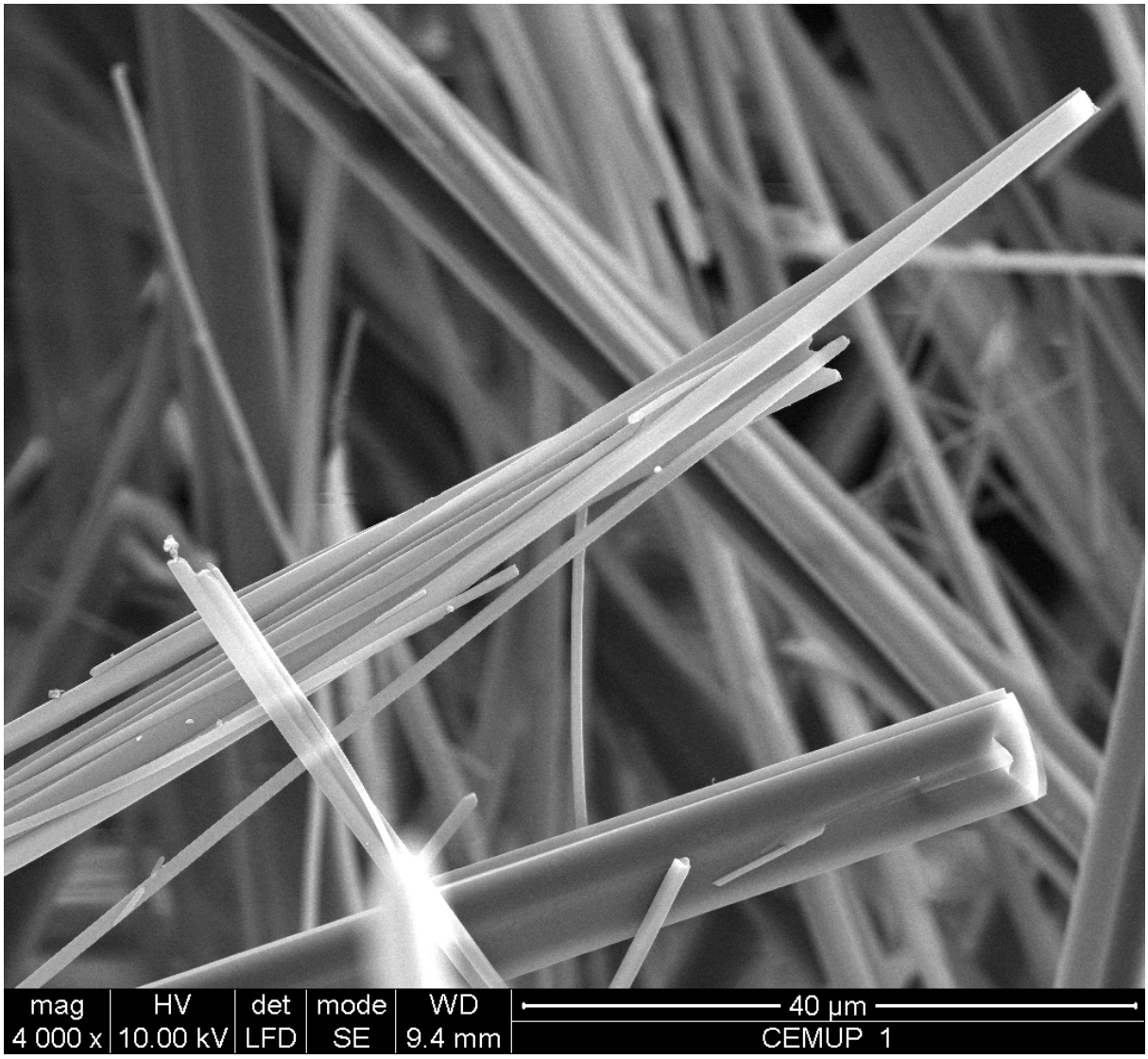

Figure B.3. VI crystals grown through phase-inversion, of an aqueous solution, with acetonitrile.

B.2. VI Crystals as Bought from Bachem

The following SEM pictures are of the crystalline powder bought from Bachem. The powder is produced through fast vacuum precipitation.

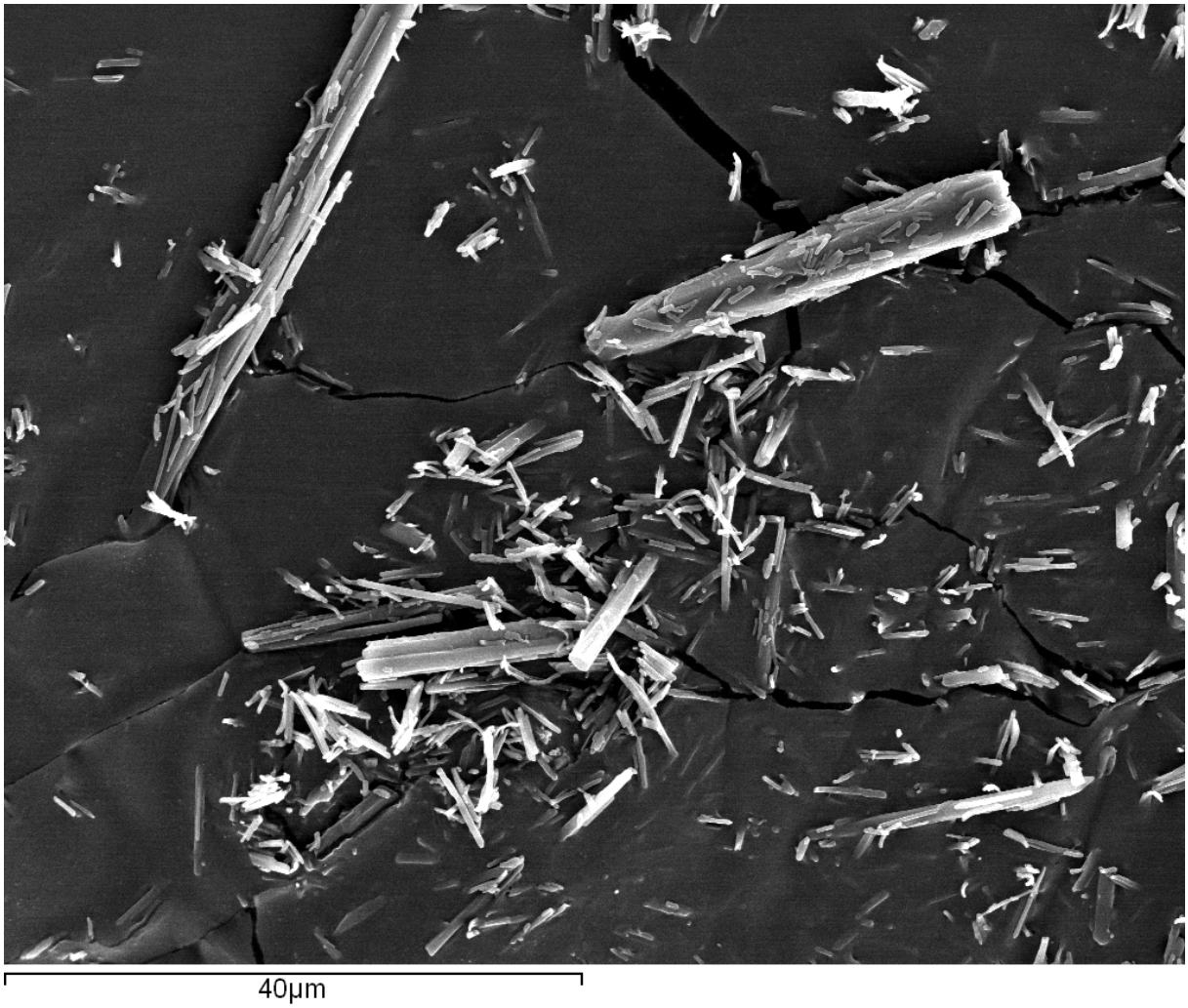

Figure B.4. VI crystals making up the powder bought from Bachem.

Figure B.5. VI crystals making up the powder bought from Bachem.

Appendix C – Adsorption Data and Complementary Results for Chapter 3

C.1. Excess Adsorption Data

Table C.1 – Excess adsorption data of N_2, O_2 and Ar, in VI, at 5 ºC.

N_2		O_2		Ar	
P / bar	n / mol·kg^{-1}	P / bar	n / mol·kg^{-1}	P / bar	n / mol·kg^{-1}
0	0	0	0	0	0
0.16510	0.00476	0.16925	0.00826	0.17750	0.01137
0.50695	0.01466	0.46455	0.02286	0.44705	0.02871
0.81425	0.02355	1.23095	0.05925	0.90025	0.05664
1.81380	0.05113	2.27120	0.10578	2.05805	0.12388
3.09950	0.08570	3.33520	0.14963	3.19380	0.18329
4.34980	0.11540	4.40800	0.19088	4.33810	0.23897
5.71800	0.14616	5.46010	0.23143	5.48840	0.29021

Table C.2 – Excess adsorption data of N_2, O_2 and Ar, in IA, at 5 ºC.

N_2		O_2		Ar	
P / bar	n / mol·kg^{-1}	P / bar	n / mol·kg^{-1}	P / bar	n / mol·kg^{-1}
0	0	0	0	0	0
0.16245	0.00614	0.16600	0.01003	0.16605	0.01128
0.50025	0.01952	0.46610	0.02895	0.46815	0.03203
0.81410	0.03222	1.23460	0.07516	1.23485	0.08207
1.80980	0.06901	2.26705	0.13299	2.22630	0.14426
3.12210	0.11622	3.36080	0.19194	3.34065	0.20948
4.33470	0.15712	4.40370	0.24282	4.40005	0.26696
5.69235	0.19790	5.46590	0.29066	5.46715	0.31900

Table C.3 – Excess adsorption data of N_2, O_2 and Ar, in IV, at 5 ºC.

N_2		O_2		Ar	
P / bar	n / mol·kg^{-1}	P / bar	n / mol·kg^{-1}	P / bar	n / mol·kg^{-1}
0	0	0	0	0	0
1.236575	0.06919	1.197925	0.09949	1.135380	0.10963
2.711740	0.14335	2.643270	0.20472	2.467635	0.22065
4.190250	0.21043	3.252615	0.24481	3.832200	0.31849
		4.174085	0.30144		

Table C.4 – Excess adsorption data of N_2, O_2 and Ar, in VV, at 5 ºC.

N_2		O_2		Ar	
P / bar	n / mol·kg^{-1}	P / bar	n / mol·kg^{-1}	P / bar	n / mol·kg^{-1}
0	0	0	0	0	0
0.16145	0.01148	0.16065	0.01302	0.16310	0.01570
0.49685	0.03586	0.46545	0.03840	0.46485	0.04500
0.81245	0.05777	1.23520	0.09792	1.23340	0.11329
1.80800	0.12083	2.26765	0.17165	2.26650	0.19774
3.09710	0.19549	3.33775	0.24008	3.33670	0.27517
4.33860	0.25859	4.39855	0.30255	4.39670	0.34509
5.69340	0.31898	5.46215	0.36145	5.46570	0.40821

Table C.5 – Excess adsorption data of N_2, O_2 and Ar, in VI, at 20 ºC.

N_2		O_2		Ar	
P / bar	n / mol·kg^{-1}	P / bar	n / mol·kg^{-1}	P / bar	n / mol·kg^{-1}
0	0	0	0	0	0
0.16890	0.00355	0.16390	0.00582	0.17665	0.00827
0.50090	0.01092	0.46660	0.01697	0.44650	0.02099
0.81445	0.01768	1.23150	0.04394	0.89850	0.04148
1.81030	0.03798	2.27065	0.07929	2.05580	0.09225
3.09765	0.06466	3.33550	0.11312	3.19300	0.13822
4.34370	0.08957	4.40360	0.14567	4.33940	0.18197
5.71600	0.11539	5.47050	0.17667	5.48900	0.22311

Table C.6 – Excess adsorption data of N_2, O_2 and Ar, in IA, at 20 ºC.

N_2		O_2		Ar	
P / bar	n / mol·kg^{-1}	P / bar	n / mol·kg^{-1}	P / bar	n / mol·kg^{-1}
0	0	0	0	0	0
0.16165	0.00421	0.16665	0.00746	0.16110	0.00831
0.49715	0.01396	0.46460	0.02108	0.46420	0.02412
0.81305	0.02309	1.23210	0.05426	1.23280	0.06176
1.80660	0.05058	2.26450	0.09757	2.26550	0.11211
3.09200	0.08680	3.33500	0.14099	3.33780	0.15957
4.33740	0.11983	4.40070	0.18234	4.39780	0.20517
5.70440	0.15311	5.46595	0.22109	5.46550	0.24957

Table C.7 – Excess adsorption data of N_2, O_2 and Ar, in IV, at 20 ºC.

N_2		O_2		Ar	
P / bar	n / mol·kg^{-1}	P / bar	n / mol·kg^{-1}	P / bar	n / mol·kg^{-1}
0	0	0	0	0	0
0.424140	0.01725	1.215075	0.07165	1.201995	0.08657
1.718925	0.06768	2.703170	0.15121	2.647605	0.17930
3.187710	0.12031	4.172250	0.22220	4.069070	0.26061
4.853850	0.17511				

Table C.8 – Excess adsorption data of N_2, O_2 and Ar, in VV, at 20 ºC.

N_2		O_2		Ar	
P / bar	n / mol·kg^{-1}	P / bar	n / mol·kg^{-1}	P / bar	n / mol·kg^{-1}
0	0	0	0	0	0
0.16140	0.00856	0.16115	0.01012	0.16885	0.01271
0.49665	0.02680	0.46510	0.02925	0.46480	0.03427
0.81255	0.04335	1.23290	0.07550	1.23100	0.08691
1.80710	0.09341	2.26670	0.13394	2.26620	0.15428
3.09140	0.15459	3.33590	0.18966	3.33575	0.21786
4.33830	0.20794	4.39880	0.24234	4.39710	0.27694
5.69400	0.26029	5.46500	0.29092	5.46545	0.33123

Table C.9 – Excess adsorption data of N_2, O_2 and Ar, in VI, at 35 ºC.

N_2		O_2		Ar	
P / bar	n / mol·kg^{-1}	P / bar	n / mol·kg^{-1}	P / bar	n / mol·kg^{-1}
0	0	0	0	0	0
0.16630	0.00261	0.16805	0.00459	0.18690	0.00642
0.50060	0.00836	0.46650	0.01295	0.44760	0.01547
0.82100	0.01360	1.23370	0.03348	0.91385	0.03128
1.80920	0.02971	2.27040	0.06042	2.05205	0.06914
3.10940	0.05042	3.33590	0.08677	3.19230	0.10481
4.34440	0.06953	4.40630	0.11278	4.33290	0.13917
5.71700	0.08981	5.47010	0.13742	5.50225	0.17281

Table C.10 – Excess adsorption data of N_2, O_2 and Ar, in IA, at 35 ºC.

N_2		O_2		Ar	
P / bar	n / mol·kg^{-1}	P / bar	n / mol·kg^{-1}	P / bar	n / mol·kg^{-1}
0	0	0	0	0	0
0.15825	0.00326	0.16180	0.00520	0.16410	0.00609
0.49605	0.01102	0.46520	0.01539	0.46450	0.01768
0.81370	0.01769	1.23185	0.04032	1.23030	0.04581
1.80755	0.03859	2.26570	0.07537	2.26690	0.08306
3.09395	0.06659	3.36050	0.10815	3.33720	0.11944
4.33670	0.09175	4.40550	0.14118	4.39845	0.15514
5.70400	0.11815	5.47560	0.17227	5.46555	0.18869

Table C.11 – Excess adsorption data of N_2, O_2 and Ar, in IV, at 35 ºC.

N_2		O_2		Ar	
P / bar	n / mol·kg^{-1}	P / bar	n / mol·kg^{-1}	P / bar	n / mol·kg^{-1}
0	0	0	0	0	0
1.255430	0.03623	1.232690	0.05261	1.216250	0.06667
2.721895	0.07620	2.685640	0.11030	2.590125	0.13595
4.191800	0.11404	4.182265	0.16527	3.987230	0.20072

Table C.12 – Excess adsorption data of N_2, O_2 and Ar, in VV, at 35 ºC.

N_2		O_2		Ar	
P / bar	n / mol·kg^{-1}	P / bar	n / mol·kg^{-1}	P / bar	n / mol·kg^{-1}
0	0	0	0	0	0
0.16195	0.00621	0.16320	0.00758	0.16740	0.00966
0.49630	0.02076	0.46430	0.02204	0.46480	0.02646
0.81360	0.03312	1.23310	0.05707	1.23695	0.06733
1.80240	0.07087	2.26660	0.10258	2.26580	0.11930
3.09090	0.11812	3.33460	0.14575	3.33880	0.16919
4.33865	0.16049	4.39810	0.18755	4.39560	0.21625
5.69555	0.20298	5.46360	0.22726	5.46300	0.26023

C.2. Absolute Adsorption Results

Absolute adsorption concentration was calculated as the excess adsorption concentration, except for the substitution of real density for apparent density in the calculation. Apparent density was calculated from the experimentally determined real density and crystallographic porosity [1].

Due to the low porosity of the materials, excess and absolute adsorption concentrations are extremely similar, and can hardly be distinguished in graphic representation.

Table C.13 – Absolute adsorption results of N_2, O_2 and Ar, in VI, at 5 ºC.

N_2		O_2		Ar	
P / bar	n / mol·kg^{-1}	P / bar	n / mol·kg^{-1}	P / bar	n / mol·kg^{-1}
0	0	0	0	0	0
0.16510	0.00506	0.16925	0.00857	0.17750	0.01169
0.50695	0.01558	0.46455	0.023702	0.44705	0.02952
0.81425	0.02503	1.23095	0.06149	0.90025	0.05829
1.81380	0.05444	2.27120	0.10993	2.05805	0.12764
3.09950	0.09136	3.33520	0.15574	3.19380	0.18913
4.34980	0.12335	4.40800	0.19896	4.33810	0.24692
5.71800	0.15663	5.46010	0.24145	5.48840	0.30028

Table C.14 – Absolute adsorption results of N_2, O_2 and Ar, in IA, at 5 ºC.

N_2		O_2		Ar	
P / bar	n / mol·kg^{-1}	P / bar	n / mol·kg^{-1}	P / bar	n / mol·kg^{-1}
0	0	0	0	0	0
0.16245	0.00644	0.16600	0.01033	0.16605	0.01158
0.50025	0.02043	0.46610	0.02980	0.46815	0.03288
0.81410	0.03370	1.23460	0.07741	1.23485	0.08432
1.80980	0.07230	2.26705	0.13712	2.22630	0.14832
3.12210	0.12191	3.36080	0.19808	3.34065	0.21558
4.33470	0.16502	4.40370	0.25086	4.40005	0.27500
5.69235	0.20828	5.46590	0.30066	5.46715	0.32900

Table C.15 – Absolute adsorption results of N_2, O_2 and Ar, in IV, at 5 ºC.

N_2		O_2		Ar	
P / bar	n / mol·kg^{-1}	P / bar	n / mol·kg^{-1}	P / bar	n / mol·kg^{-1}
0	0	0	0	0	0
1.236575	0.07218	1.197925	0.10239	1.135380	0.11223
2.711740	0.14991	2.643270	0.21112	2.467635	0.22631
4.190250	0.22058	3.252615	0.25269	3.832200	0.32731
		4.174085	0.31156		

Table C.16 – Absolute adsorption results of N_2, O_2 and Ar, in VV, at 5 ºC.

N_2		O_2		Ar	
P / bar	n / mol·kg^{-1}	P / bar	n / mol·kg^{-1}	P / bar	n / mol·kg^{-1}
0	0	0	0	0	0
0.16140	0.01196	0.16065	0.01349	0.16310	0.01618
0.49685	0.03733	0.46545	0.03978	0.46485	0.04638
0.81245	0.06017	1.23520	0.10157	1.23340	0.11694
1.80800	0.12618	2.26765	0.17837	2.26650	0.20446
3.09710	0.20467	3.33775	0.24999	3.33670	0.28507
4.33860	0.27146	4.39855	0.31563	4.39670	0.35816
5.69340	0.33588	5.46215	0.37771	5.46570	0.42447

Table C.17 – Absolute adsorption results of N_2, O_2 and Ar, in VI, at 20 ºC.

N_2		O_2		Ar	
P / bar	n / mol·kg^{-1}	P / bar	n / mol·kg^{-1}	P / bar	n / mol·kg^{-1}
0	0	0	0	0	0
0.16890	0.00384	0.16390	0.00610	0.17665	0.00857
0.50090	0.01178	0.46660	0.01778	0.44650	0.02176
0.81445	0.01909	1.23150	0.04607	0.89850	0.04304
1.81030	0.04111	2.27065	0.08322	2.05580	0.09581
3.09765	0.07003	3.33550	0.11890	3.19300	0.14376
4.34370	0.09710	4.40360	0.15332	4.33940	0.18951
5.71600	0.12531	5.47050	0.18618	5.48900	0.23266

Table C.18 – Absolute adsorption results of N_2, O_2 and Ar, in IA, at 20 ºC.

N_2		O_2		Ar	
P / bar	n / mol·kg^{-1}	P / bar	n / mol·kg^{-1}	P / bar	n / mol·kg^{-1}
0	0	0	0	0	0
0.16165	0.00449	0.16665	0.00775	0.16110	0.00859
0.49715	0.01481	0.46460	0.02188	0.46420	0.02492
0.81305	0.02449	1.23210	0.05638	1.23280	0.06389
1.80660	0.05370	2.26450	0.10148	2.26550	0.11602
3.09200	0.09214	3.33500	0.14676	3.33780	0.16535
4.33740	0.12732	4.40070	0.18996	4.39780	0.21279
5.70440	0.16298	5.46595	0.23056	5.46550	0.25905

Table C.19 – Absolute adsorption results of N_2, O_2 and Ar, in IV, at 20 ºC.

N_2		O_2		Ar	
P / bar	n / mol·kg^{-1}	P / bar	n / mol·kg^{-1}	P / bar	n / mol·kg^{-1}
0	0	0	0	0	0
0.424140	0.01823	1.215075	0.07443	1.201995	0.08932
1.718925	0.07162	2.703170	0.15742	2.647605	0.18538
3.187710	0.12761	4.172250	0.23180	4.069070	0.26996
4.853850	0.18625				

Table C.20 – Absolute adsorption results of N_2, O_2 and Ar, in VV, at 20 ºC.

N_2		O_2		Ar	
P / bar	n / mol·kg^{-1}	P / bar	n / mol·kg^{-1}	P / bar	n / mol·kg^{-1}
0	0	0	0	0	0
0.16140	0.00894	0.16115	0.01050	0.16885	0.01310
0.49665	0.02796	0.46510	0.03034	0.46480	0.03536
0.81255	0.04525	1.23290	0.07839	1.23100	0.08980
1.80710	0.09765	2.26670	0.13926	2.26620	0.15960
3.09140	0.16185	3.33590	0.19750	3.33575	0.22570
4.33830	0.21813	4.39880	0.25269	4.39710	0.28729
5.69400	0.27367	5.46500	0.30379	5.46545	0.34411

Table C.21 – Absolute adsorption results of N_2, O_2 and Ar, in VI, at 35 ºC.

N_2		O_2		Ar	
P / bar	n / mol·kg^{-1}	P / bar	n / mol·kg^{-1}	P / bar	n / mol·kg^{-1}
0	0	0	0	0	0
0.16630	0.00288	0.16805	0.00486	0.18690	0.00672
0.50060	0.00918	0.46650	0.01372	0.44760	0.01620
0.82100	0.01495	1.23370	0.03551	0.91385	0.03278
1.80920	0.03268	2.27040	0.06416	2.05205	0.07252
3.10940	0.05554	3.33590	0.09227	3.19230	0.11008
4.34440	0.07669	4.40630	0.12006	4.33290	0.14632
5.71700	0.09924	5.47010	0.14646	5.50225	0.18190

Table C.22 – Absolute adsorption results of N_2, O_2 and Ar, in IA, at 35 ºC.

N_2		O_2		Ar	
P / bar	n / mol·kg^{-1}	P / bar	n / mol·kg^{-1}	P / bar	n / mol·kg^{-1}
0	0	0	0	0	0
0.15825	0.00352	0.16180	0.00546	0.16410	0.00636
0.49605	0.01227	0.46520	0.01615	0.46450	0.01844
0.81370	0.01983	1.23185	0.04234	1.23030	0.04782
1.80755	0.04362	2.26570	0.07909	2.26690	0.08679
3.09395	0.07544	3.36050	0.11368	3.33720	0.12493
4.33670	0.10419	4.40550	0.14843	4.39845	0.16238
5.70400	0.13451	5.47560	0.18129	5.46555	0.19770

Table C.23 – Absolute adsorption results of N_2, O_2 and Ar, in IV, at 35 ºC.

N_2		O_2		Ar	
P / bar	n / mol·kg^{-1}	P / bar	n / mol·kg^{-1}	P / bar	n / mol·kg^{-1}
0	0	0	0	0	0
1.255430	0.03897	1.232690	0.05530	1.216250	0.06946
2.721895	0.08213	2.685640	0.11617	2.590125	0.14189
4.191800	0.12318	4.182265	0.17441	3.987230	0.20988

Table C.24 – Absolute adsorption results of N_2, O_2 and Ar, in VV, at 35 ºC.

N_2		O_2		Ar	
P / bar	n / mol·kg^{-1}	P / bar	n / mol·kg^{-1}	P / bar	n / mol·kg^{-1}
0	0	0	0	0	0
0.16195	0.00665	0.16320	0.00801	0.16740	0.01010
0.49630	0.02209	0.46430	0.02328	0.46480	0.02771
0.81360	0.03529	1.23310	0.06037	1.23695	0.07063
1.80240	0.07569	2.26660	0.10865	2.26580	0.12536
3.09090	0.12638	3.33460	0.15468	3.33880	0.17813
4.33865	0.17209	4.39810	0.19933	4.39560	0.22802
5.69555	0.21821	5.46360	0.24191	5.46300	0.27488

C.3. Fitting Results

The results of absolute adsorption data fitting to the Volmer equation are presented below, in Tables C.25 to C.30.

Table C.25 – Fitting parameters determined for N_2, in VI, IA, IV and VV, at 5 ºC, 20 ºC and 35 ºC.

	n_{max} / mol.kg^{-1}	b / bar^{-1}		
		5 ºC	20 ºC	35 ºC
VI	2.54736	0.012297	0.0094729	0.0073619
IA	3.36315	0.012455	0.0093799	0.0075898
IV	2.99153	0.020315	0.0144090	0.0105010
VV	2.92024	0.026118	0.0203310	0.0153390

Table C.26 – Minimised sum of the squares for N_2, in VI, IA, IV and VV, at 5 ºC, 20 ºC and 35 ºC.

	VI	IA	IV	VV
5 ºC	1.734 X 10^{-6}	2.389 X 10^{-6}	7.575 X 10^{-6}	3.146 X 10^{-6}
20 ºC	2.334 X 10^{-6}	4.079 X 10^{-6}	9.196 X 10^{-6}	4.795 X 10^{-6}
35 ºC	4.129 X 10^{-7}	2.727 X 10^{-6}	5.995 X 10^{-6}	1.421 X 10^{-6}
Total	4.481 X 10^{-6}	9.195 X 10^{-6}	2.277 X 10^{-5}	9.363 X 10^{-6}

Table C.27 – Fitting parameters determined for O_2, in VI, IA, IV and VV, at 5 ºC, 20 ºC and 35 ºC.

	n_{max} / mol.kg^{-1}	b / bar^{-1}		
		5 ºC	20 ºC	35 ºC
VI	3.18554	0.016245	0.012081	0.0092383
IA	3.91143	0.016633	0.012179	0.0092791
IV	3.36954	0.026821	0.018863	0.013610
VV	3.61289	0.024010	0.018580	0.014082

Table C.28 – Minimised sum of the squares for O_2, in VI, IA, IV and VV, at 5 ºC, 20 ºC and 35 ºC.

	VI	IA	IV	VV
5 ºC	1.806 X 10^{-6}	3.162 X 10^{-6}	5.385 X 10^{-6}	1.419 X 10^{-6}
20 ºC	1.708 X 10^{-7}	1.375 X 10^{-6}	6.597 X 10^{-6}	4.908 X 10^{-7}
35 ºC	8.774 X 10^{-8}	4.524 X 10^{-6}	6.073 X 10^{-6}	7.004 X 10^{-7}
Total	2.065 X 10^{-6}	9.060 X 10^{-6}	1.805 X 10^{-5}	2.610 X 10^{-6}

Table C.29 – Fitting parameters determined for Ar, in VI, IA, IV and VV, at 5 ºC, 20 ºC and 35 ºC.

	n_{max} / mol.kg^{-1}	b / bar^{-1}		
		5 ºC	20 ºC	35 ºC
VI	3.17554	0.021140	0.015584	0.011701
IA	4.04617	0.017754	0.013366	0.0098906
IV	3.31336	0.031719	0.023587	0.017922
VV	3.52994	0.028729	0.022153	0.016819

Table C.30 – Minimised sum of the squares for Ar, in VI, IA, IV and VV, at 5 ºC, 20 ºC and 35 ºC.

	VI	IA	IV	VV
5 ºC	4.353 X 10^{-7}	3.145 X 10^{-6}	5.820 X 10^{-6}	1.331 X 10^{-6}
20 ºC	1.451 X 10^{-6}	1.413 X 10^{-6}	6.493 X 10^{-6}	2.427 X 10^{-6}
35 ºC	1.363 X 10^{-6}	3.735 X 10^{-7}	6.373 X 10^{-6}	5.604 X 10^{-7}
Total	3.250 X 10^{-6}	4.931 X 10^{-6}	1.869 X 10^{-5}	4.318 X 10^{-6}

C.4. Heats of Adsorption

Heats of adsorption of N_2, O_2 and Ar, calculated from absolute adsorption data at 5 ºC, 20 ºC and 35 ºC, are presented in Tables C.31 to C34.

Table C.31 – Heats of adsorption of N_2, O_2 and Ar, in VI, for different absolute adsorption concentrations.

N_2		O_2		Ar	
n / mol·kg^{-1}	ΔH / kJ·mol^{-1}	n / mol·kg^{-1}	ΔH / kJ·mol^{-1}	n / mol·kg^{-1}	ΔH / kJ·mol^{-1}
0	—	0	—	0	—
0.00288	13.57	0.00486	13.31	0.00672	14.37
0.00918	12.24	0.01372	13.02	0.01620	14.24
0.01495	12.43	0.03551	13.33	0.03278	14.40
0.03268	12.39	0.06416	13.46	0.07252	14.01
0.05554	12.32	0.0923	13.47	0.11008	14.07
0.07669	12.30	0.12006	13.40	0.14632	14.00
0.09924	12.29	0.14646	13.34	0.18190	13.93

Table C.32 – Heats of adsorption of N_2, O_2 and Ar, in IA, for different absolute adsorption concentrations.

N_2		O_2		Ar	
n / mol·kg^{-1}	ΔH / kJ·mol^{-1}	n / mol·kg^{-1}	ΔH / kJ·mol^{-1}	n / mol·kg^{-1}	ΔH / kJ·mol^{-1}
0	—	0	—	0	—
0.00352	13.76	0.00546	14.50	0.00636	13.92
0.01227	11.74	0.01615	14.20	0.01844	13.46
0.01983	12.27	0.04234	14.51	0.04782	13.69
0.04362	12.48	0.07909	13.89	0.08679	13.69
0.07544	11.70	0.11368	14.03	0.12494	13.81
0.10419	11.69	0.14843	13.75	0.16240	13.80
0.13451	11.78	0.18129	13.83	0.19772	13.89

Table C.33 – Heats of adsorption of N_2, O_2 and Ar, in IV, for different absolute adsorption concentrations.

N_2		O_2		Ar	
n / mol·kg^{-1}	ΔH / kJ·mol^{-1}	n / mol·kg^{-1}	ΔH / kJ·mol^{-1}	n / mol·kg^{-1}	ΔH / kJ·mol^{-1}
0	—	0	—	0	—
0.03841	15.15	0.05471	15.42	0.06885	13.12
0.08096	15.52	0.11488	15.93	0.14060	13.38
0.12139	15.42	0.17241	15.87	0.20789	13.43

Table C.34 – Heats of adsorption of N_2, O_2 and Ar, in VV, for different absolute adsorption concentrations.

N_2		O_2		Ar	
n / mol·kg^{-1}	ΔH / kJ·mol^{-1}	n / mol·kg^{-1}	ΔH / kJ·mol^{-1}	n / mol·kg^{-1}	ΔH / kJ·mol^{-1}
0	—	0	—	0	—
0.00665	14.00	0.00794	12.80	0.01003	11.84
0.02209	12.33	0.02308	12.57	0.02750	12.24
0.03529	13.04	0.05982	12.78	0.07009	12.62
0.07569	12.91	0.10764	12.73	0.12436	12.67
0.12638	12.69	0.15320	12.82	0.17665	12.77
0.17209	12.49	0.19739	12.74	0.22608	12.73
0.21821	12.59	0.23949	12.66	0.27246	12.76

C.5. Excess Adsorption Isotherms

As absolute adsorption isotherms are (for these results) visually indistinguishable from excess adsorption isotherms, only excess adsorption isotherms are shown in graphic form.

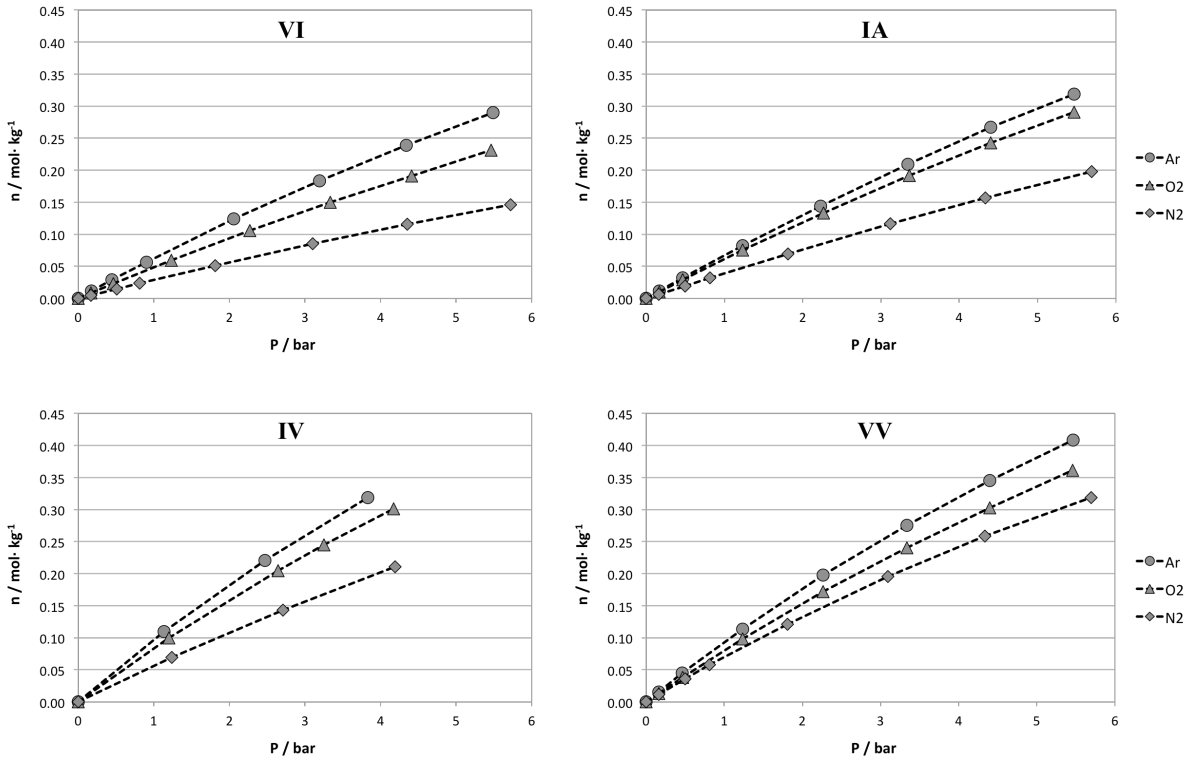

Figure C.1. Excess adsorption isotherms of Ar, O_2 and N_2 on VI, IA, IV and VV, at 5 ºC, grouped per material.

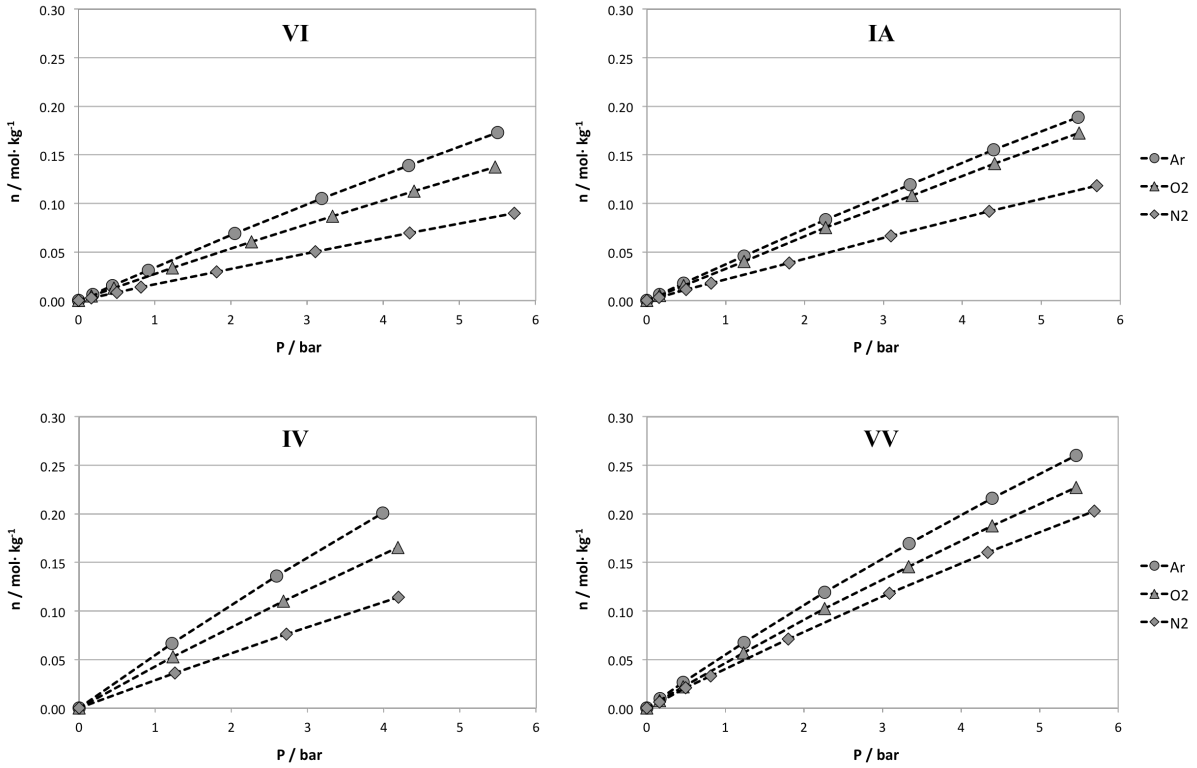

Figure C.2. Excess adsorption isotherms of Ar, O_2 and N_2 on VI, IA, IV and VV, at 35 ºC, grouped per material.

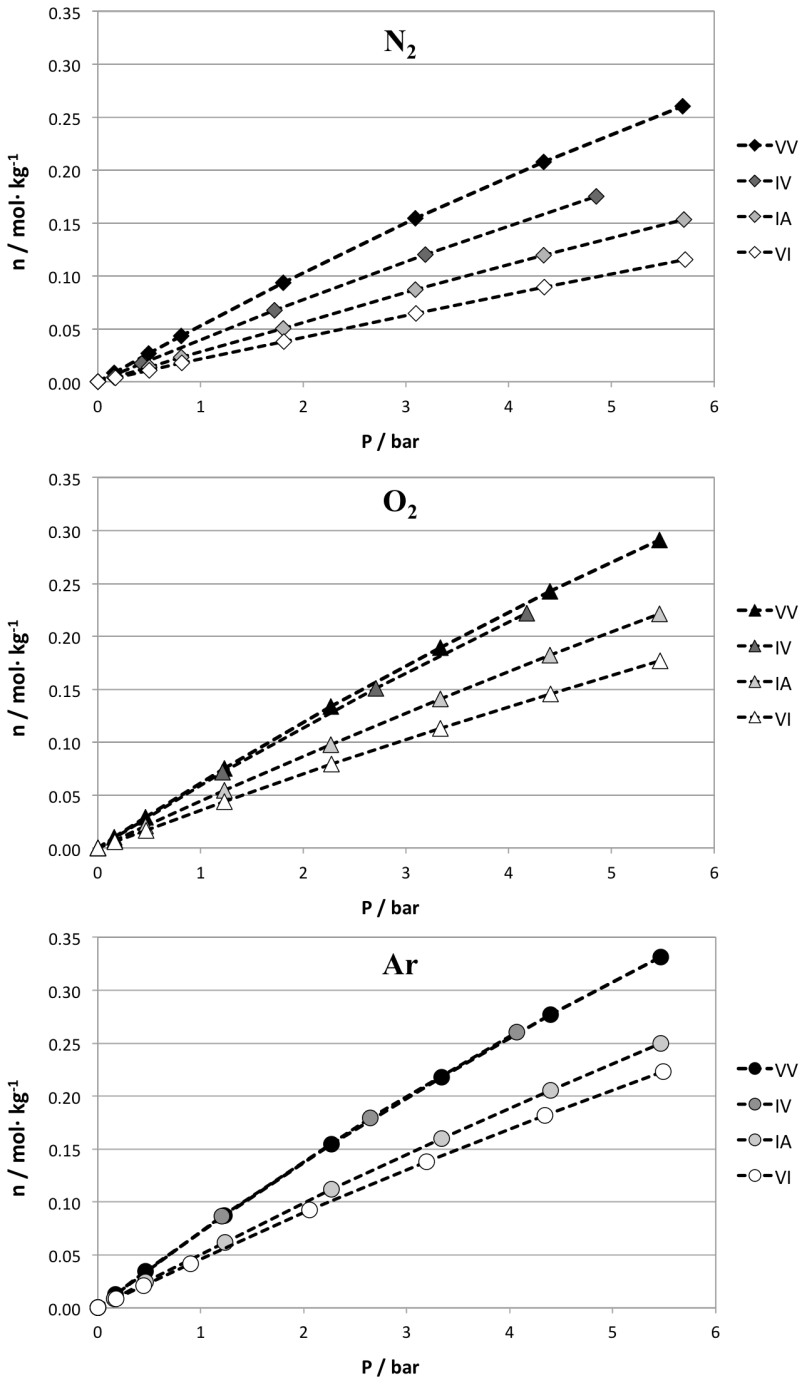

Figure C.3. Excess adsorption isotherms of Ar, O_2 and N_2 on VI, IA, IV and VV, at 20 ºC, grouped per gas.

C.6. Selectivities

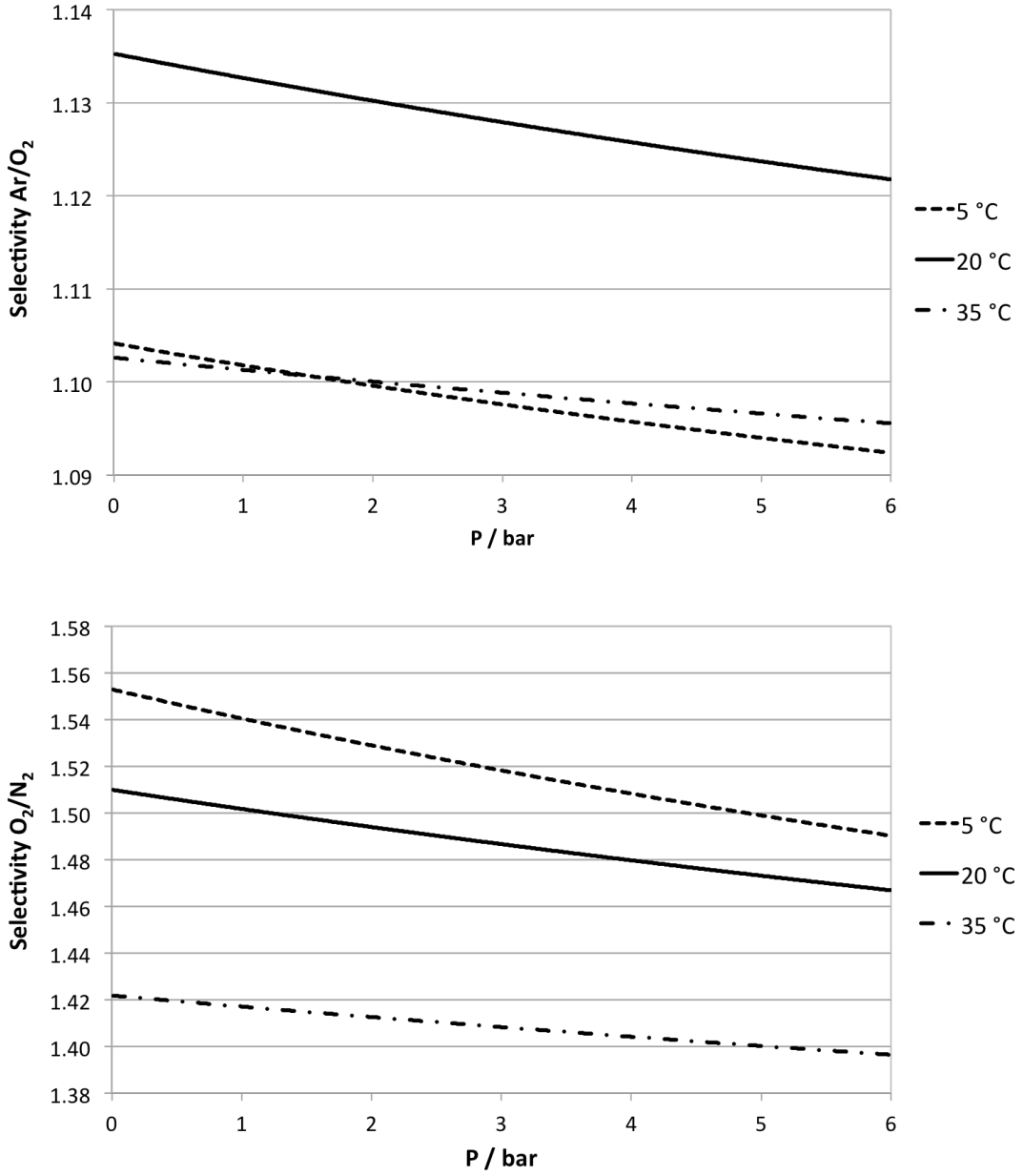

Figure C.4. Variation of Ar/O_2 and O_2/N_2 selectivities with pressure, for IA, at 5 ºC, 20 ºC and 35 ºC.

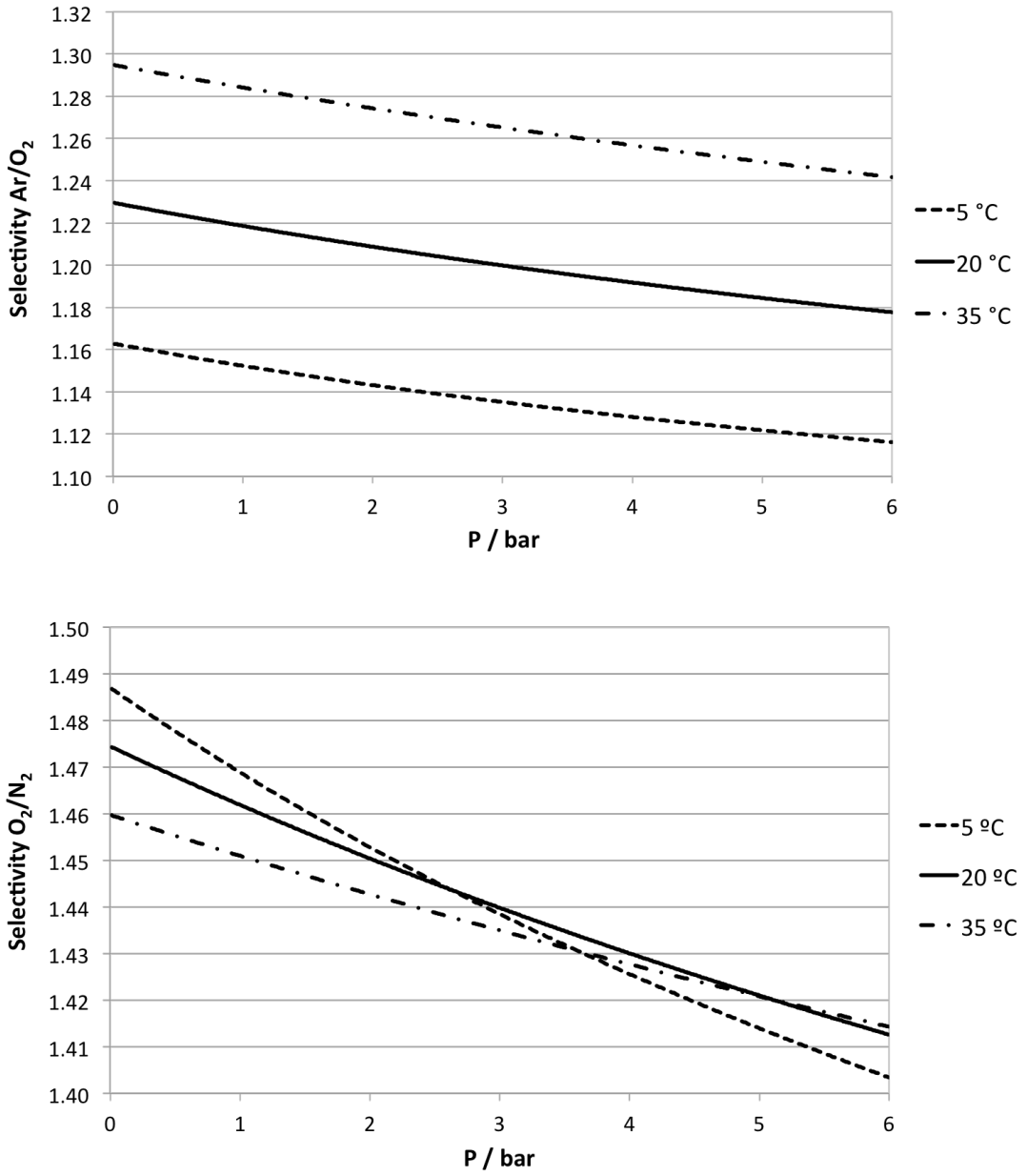

Figure C.5. Variation of Ar/O_2 and O_2/N_2 selectivities with pressure, for IV, at 5 ºC, 20 ºC and 35 ºC.

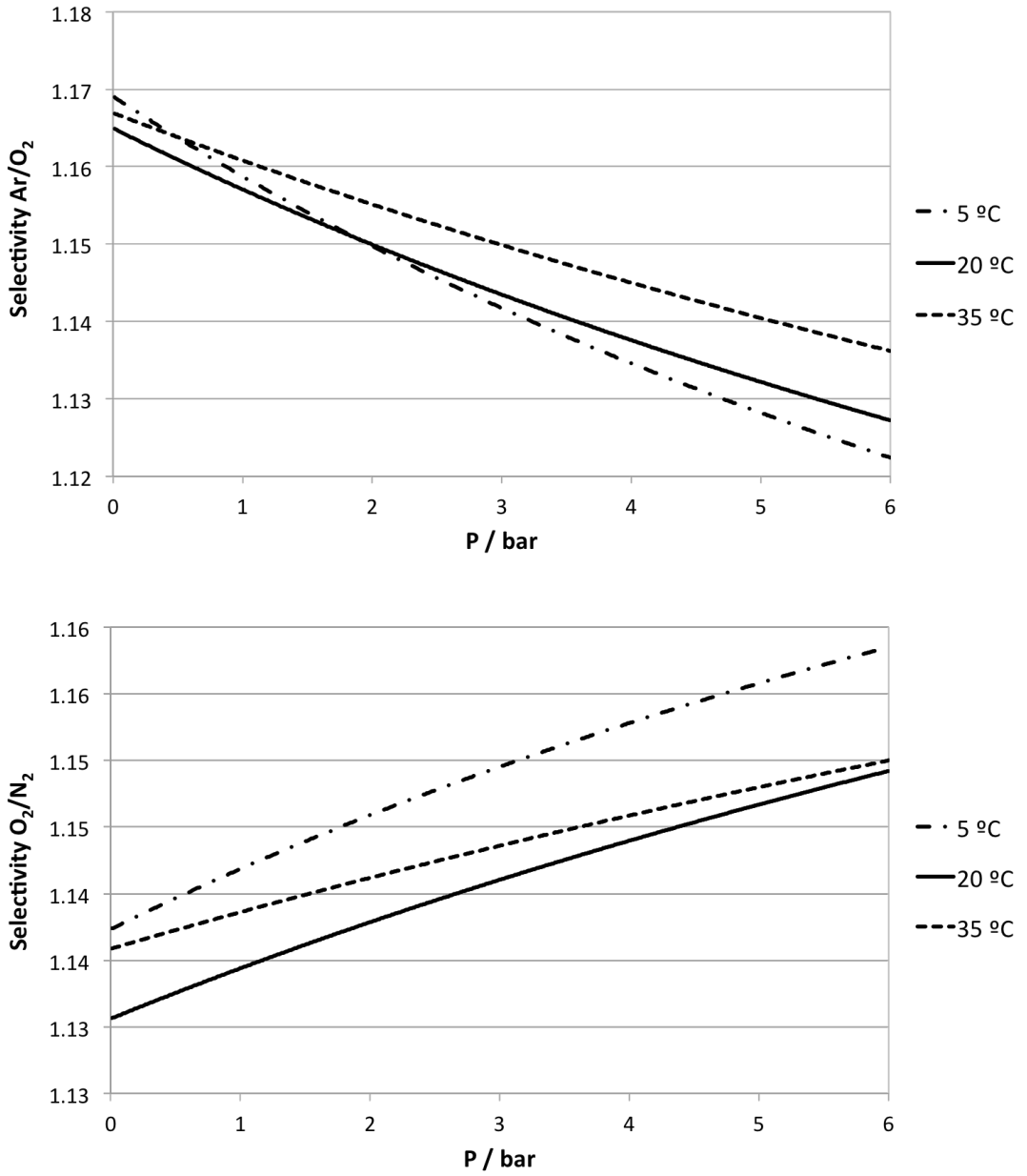

Figure C.6. Variation of Ar/O_2 and O_2/N_2 selectivities with pressure, for VV, at 5 ºC, 20 ºC and 35 ºC.

C.7. References

1. D. V. Soldatov, I. L. Moudrakovski, E. V. Grachev, and J. A. Ripmeester, Micropores in Crystalline Dipeptides as Seen from the Crystal Structure, He Pycnometry, and 129Xe NMR Spectroscopy, J. Am. Chem. Soc. 128 (2006), 6737-6744.

Appendix D – Complementary Data to Chapter 4

D.1. Excess Adsorption Isotherms

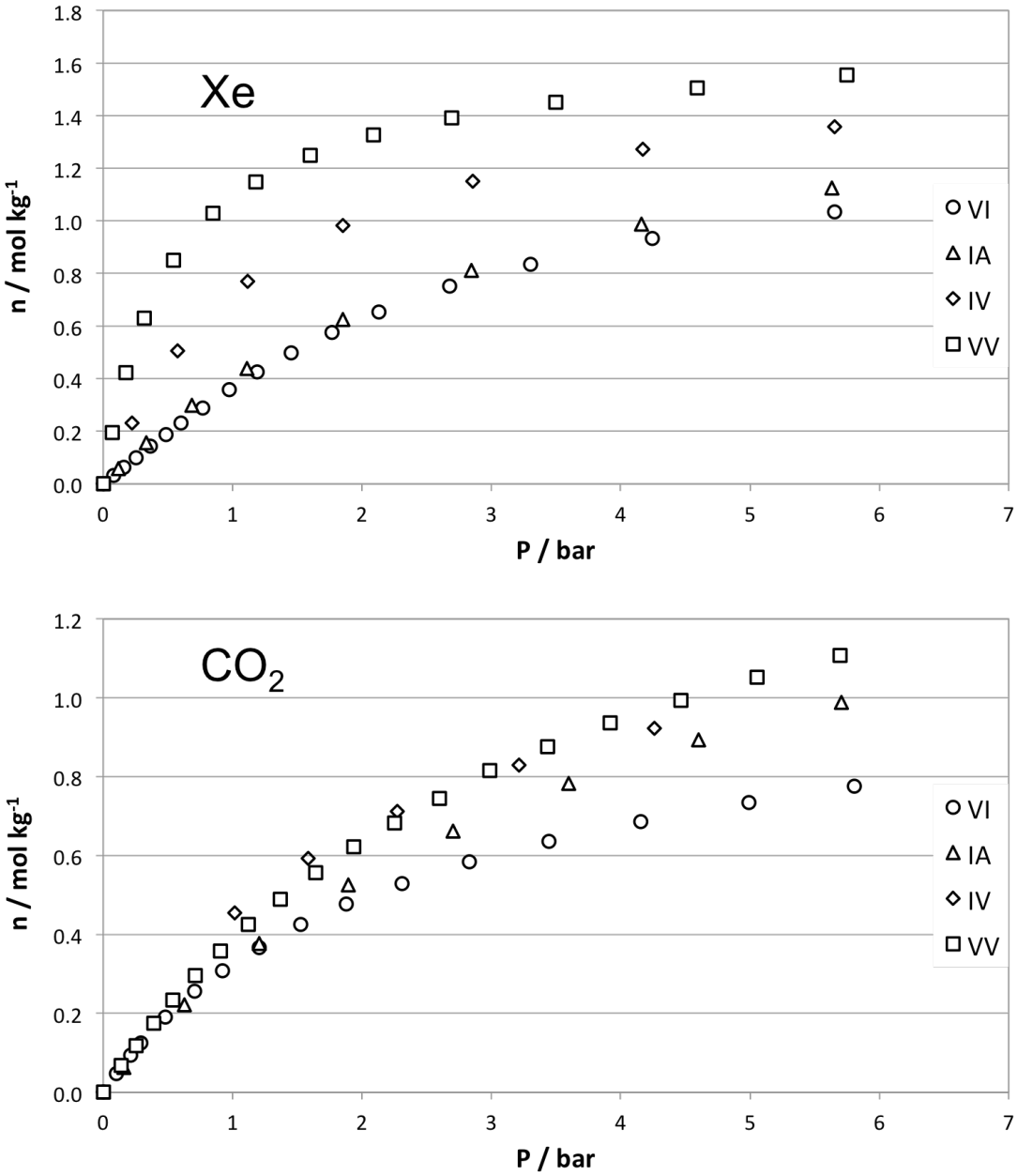

Figure D.1. Excess adsorption isotherms of Xe and CO_2 in VI, IA, IV and VV. Due to the low porosity, values are very close to those of absolute adsorption, shown in Figure 3.3.

D.2. Excess Adsorption Results

Table D.1 – Excess adsorption results of Xe and CO_2 adsorption in VI, at 20 ºC.

Xe		CO_2	
P / bar	n / mol·kg^{-1}	P / bar	n / mol·kg^{-1}
0	0	0	0
0.07997	0.03111	0.09980	0.04679
0.15865	0.06203	0.21220	0.09443
0.25354	0.09905	0.29155	0.12510
0.36682	0.14289	0.48220	0.19127
0.48471	0.18756	0.70640	0.25525
0.60330	0.23112	0.92155	0.30746
0.76788	0.28920	1.20850	0.36702
0.97381	0.35795	1.52810	0.42549
1.18932	0.42470	1.88090	0.47651
1.45334	0.49893	2.31155	0.52927
1.76768	0.57714	2.83070	0.58396
2.12876	0.65430	3.44590	0.63555
2.68014	0.75095	4.15585	0.68532
3.30338	0.83605	4.98990	0.73496
4.24473	0.93309	5.80800	0.77674
5.65356	1.03415		

Table D.2 – Excess adsorption results of Xe and CO_2 adsorption in IA, at 20 ºC.

Xe		CO_2	
P / bar	n / mol·kg^{-1}	P / bar	n / mol·kg^{-1}
0	0	0	0
0.11800	0.05902	0.15990	0.06278
0.33185	0.15664	0.62880	0.22097
0.68670	0.29746	1.20670	0.37761
1.11030	0.43793	1.89670	0.52609
1.85380	0.62540	2.70470	0.66271
2.84820	0.81122	3.59940	0.78233
4.16210	0.98693	4.60380	0.89250
5.63390	1.12491	5.70590	0.98797

Table D.3 – Excess adsorption results of Xe and CO_2 adsorption in IV, at 20 ºC.

Xe		CO_2	
P / bar	n / mol·kg^{-1}	P / bar	n / mol·kg^{-1}
0	0	0	0
0.22220	0.23016	1.01510	0.45512
0.57700	0.50535	1.58286	0.59283
1.11550	0.77051	2.27113	0.71238
1.85405	0.98280	3.21309	0.82921
2.85415	1.15030	4.25902	0.92252
4.17340	1.27361		
5.65610	1.35891		

Table D.4 – Excess adsorption results of Xe and CO_2 adsorption in VV, at 20 ºC.

Xe		CO_2	
P / bar	n / mol·kg^{-1}	P / bar	n / mol·kg^{-1}
0	0	0	0
0.07040	0.19384	0.14110	0.06868
0.17775	0.42211	0.25285	0.11766
0.31660	0.63035	0.38875	0.17443
0.54280	0.84977	0.54065	0.23334
0.84785	1.02940	0.71435	0.29544
1.18030	1.14925	0.90860	0.35819
1.60260	1.24907	1.12305	0.42571
2.09110	1.32808	1.36830	0.49000
2.69445	1.39262	1.64205	0.55643
3.49790	1.45068	1.93875	0.62161
4.59090	1.50703	2.25365	0.68263
5.74950	1.55511	2.59745	0.74454
		2.98765	0.81616
		3.43295	0.87597
		3.92105	0.93580
		4.46515	0.99429
		5.05395	1.05245
		5.69415	1.10685

D.3. Absolute Adsorption Results

Table D.5 – Absolute adsorption results of Xe and CO_2 adsorption in VI, at 20 ºC.

Xe		CO_2	
P / bar	n / mol·kg^{-1}	P / bar	n / mol·kg^{-1}
0	0	0	0
0.07997	0.03124	0.09980	0.04820
0.15865	0.06230	0.21220	0.09731
0.25354	0.09949	0.29155	0.12893
0.36682	0.14353	0.48220	0.19722
0.48471	0.18841	0.70640	0.26333
0.60330	0.23217	0.92155	0.31735
0.76788	0.29054	1.20850	0.37907
0.97381	0.35966	1.52810	0.43976
1.18932	0.42678	1.88090	0.49287
1.45334	0.50148	2.31155	0.54795
1.76768	0.58025	2.83070	0.60522
2.12876	0.65805	3.44590	0.65953
2.68014	0.75569	4.15585	0.71221
3.30338	0.84193	4.98990	0.76508
4.24473	0.94068	5.80800	0.80987
5.65356	1.04437		

Table D.6 – Absolute adsorption results of Xe and CO_2 adsorption in IA, at 20 ºC.

Xe		CO_2	
P / bar	n / mol·kg^{-1}	P / bar	n / mol·kg^{-1}
0	0	0	0
0.12110	0.05927	0.15990	0.06312
0.33495	0.15734	0.62880	0.22230
0.68980	0.29891	1.20670	0.38018
1.11340	0.44029	1.89670	0.53015
1.85690	0.62936	2.70470	0.66853
2.85130	0.81735	3.59940	0.79012
4.16520	0.99596	4.60380	0.90254
5.63700	1.13725	5.70590	1.00048

Table D.7 – Absolute adsorption results of Xe and CO_2 adsorption in IV, at 20 ºC.

Xe		CO_2	
P / bar	n / mol·kg^{-1}	P / bar	n / mol·kg^{-1}
0	0	0	0
0.22220	0.23056	1.01510	0.45694
0.57700	0.50638	1.58286	0.59569
1.11550	0.77252	2.27113	0.71649
1.85405	0.98616	3.21309	0.83506
2.85415	1.15550	4.25902	0.93033
4.17340	1.28128		
5.65610	1.36940		

Table D.8 –Absolute adsorption results of Xe and CO_2 adsorption in VV, at 20 ºC.

Xe		CO_2	
P / bar	n / mol·kg^{-1}	P / bar	n / mol·kg^{-1}
0	0	0	0
0.07040	0.19400	0.14110	0.06901
0.17775	0.42253	0.25285	0.11825
0.31660	0.63109	0.38875	0.17534
0.54280	0.85104	0.54065	0.23461
0.84785	1.03139	0.71435	0.29712
1.18030	1.15204	0.90860	0.36033
1.60260	1.25286	1.12305	0.42836
2.09110	1.33305	1.36830	0.49323
2.69445	1.39904	1.64205	0.56031
3.49790	1.45906	1.93875	0.62620
4.59090	1.51811	2.25365	0.68798
5.74950	1.56910	2.59745	0.75071
		2.98765	0.82328
		3.43295	0.88418
		3.92105	0.94520
		4.46515	1.00503
		5.05395	1.06465
		5.69415	1.12065

D.4. Ω-l Diagrams

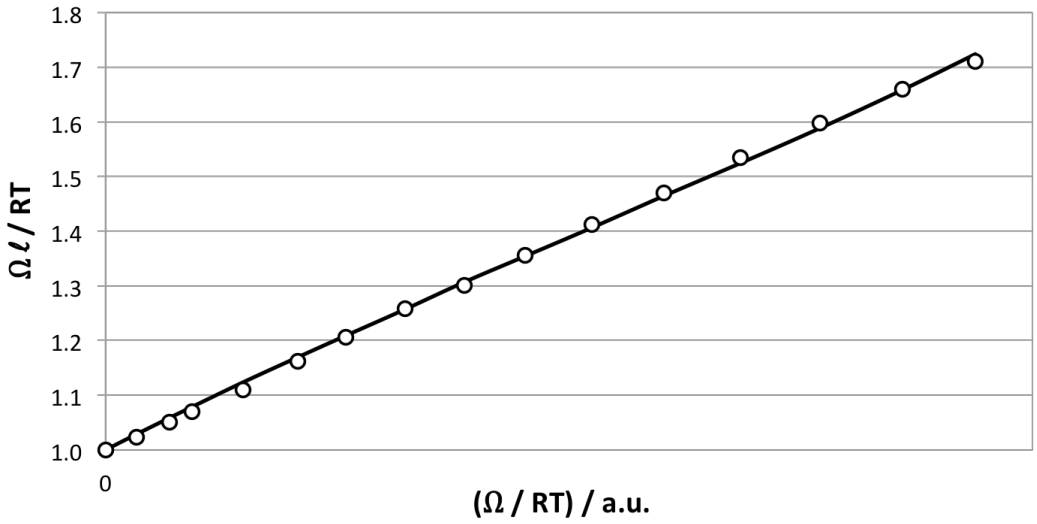

Figure D.2. Ω-l diagram for CO_2 adsorption in VI. The points represent experimental results and the line FG fitting.

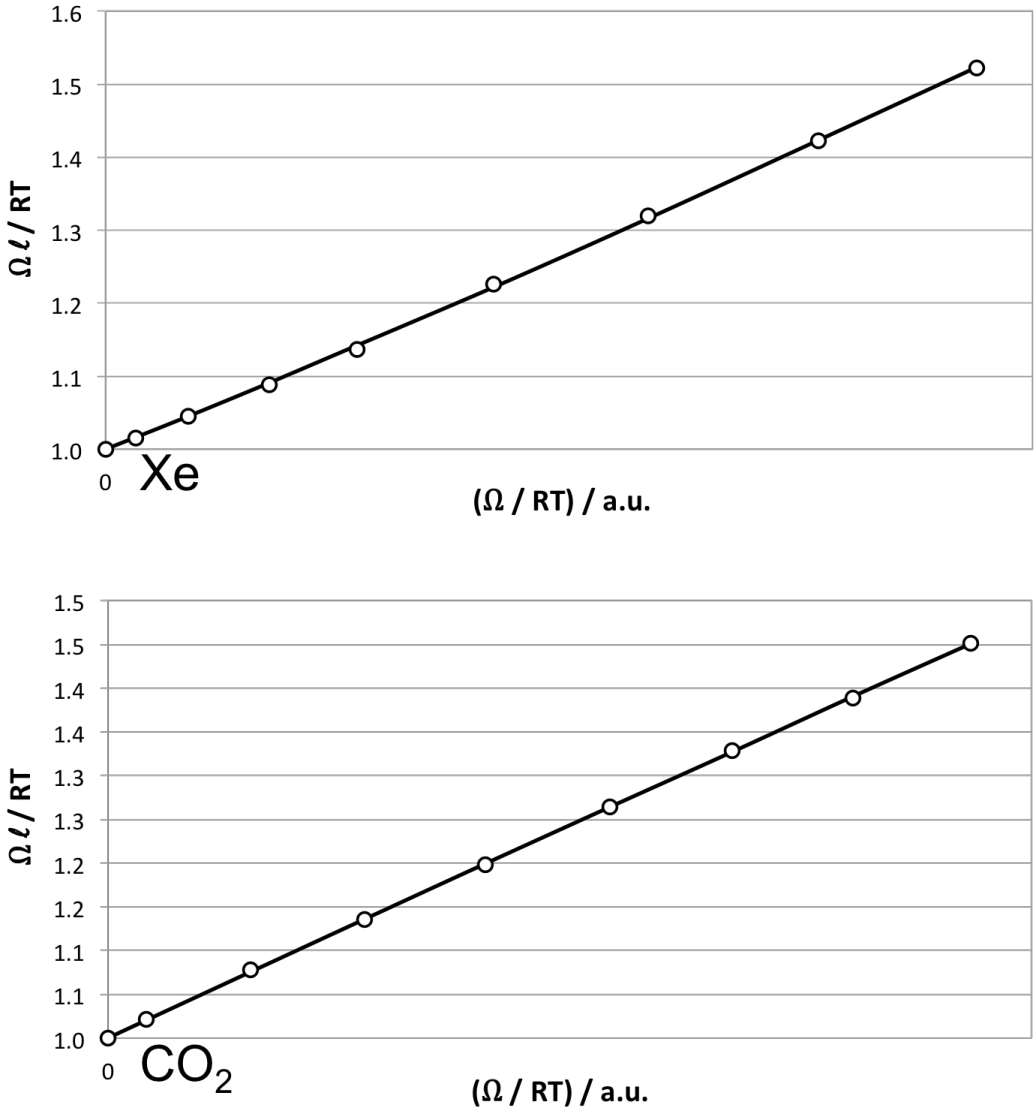

Figure D.3. Ω-l diagram for Xe and CO_2 adsorption in IA. The points represent experimental results and the lines HdB (for Xe) and FG (for CO_2) fitting.

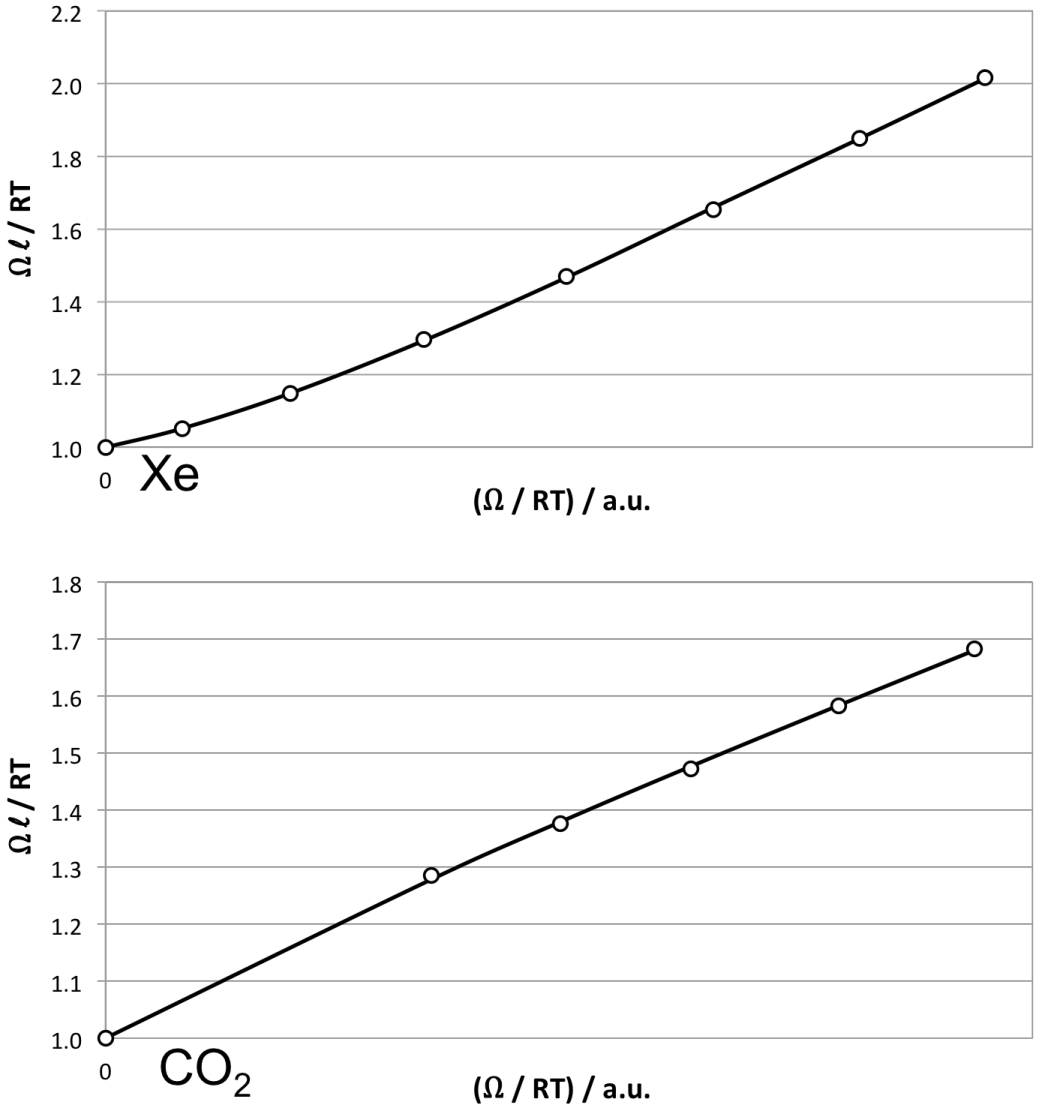

Figure D.4. ***Ω-l*** diagram for Xe and CO_2 adsorption in IV. The points represent experimental results and the lines HdB (for Xe) and FG (for CO_2) fitting.

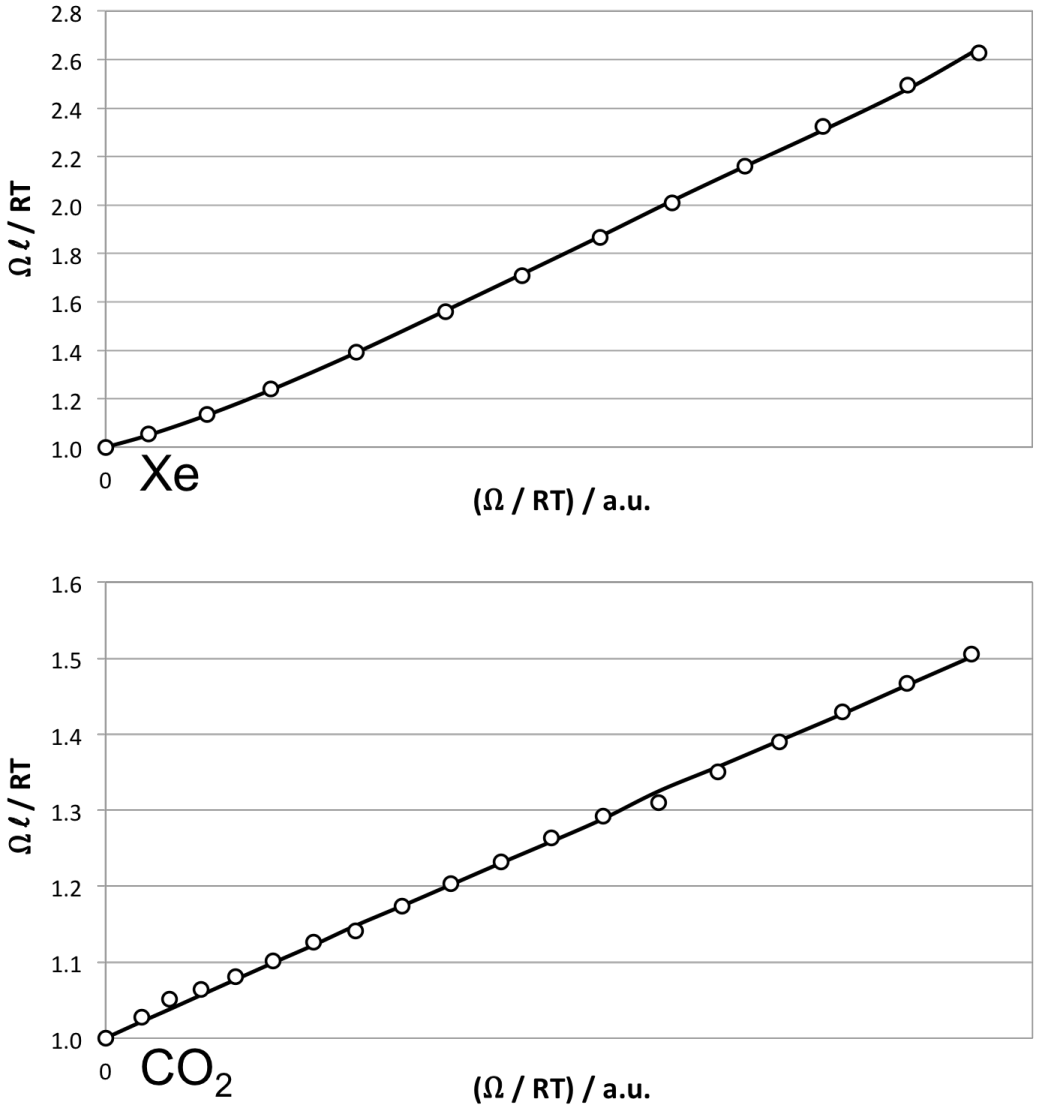

Figure D.5. Ω-l diagram for Xe and CO_2 adsorption in VV. The points represent experimental results and the lines HdB (for Xe) and FG (for CO_2) fitting.

D.5. Residues of Data Fitting

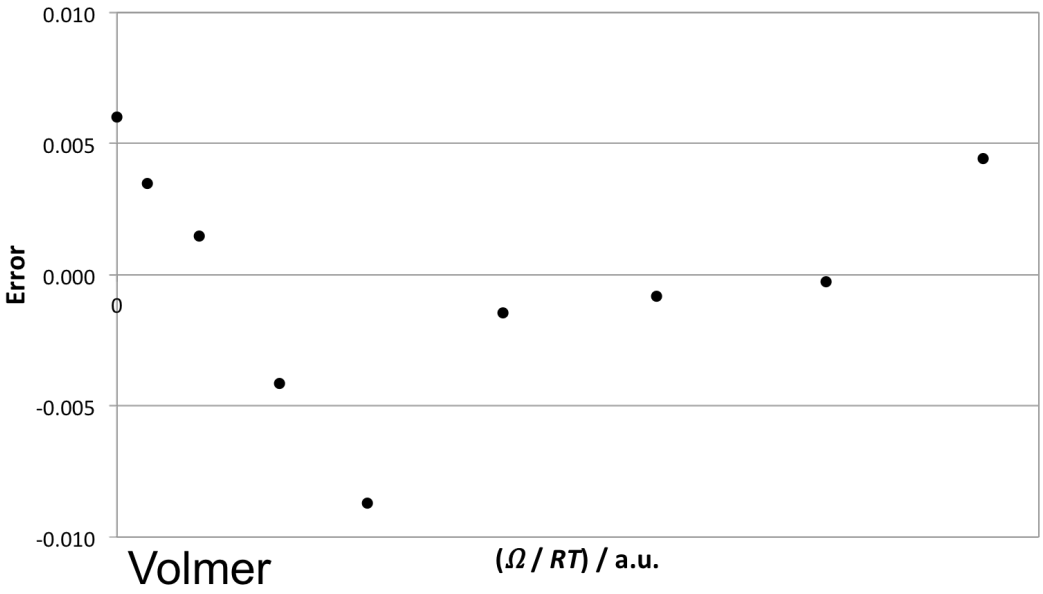

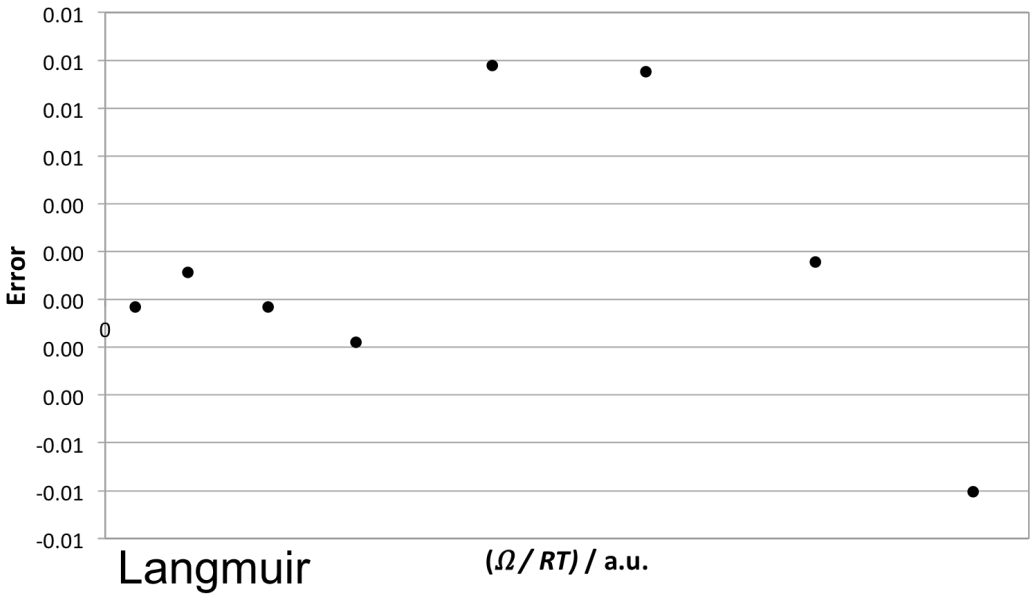

Figure D.6. Residual errors of the Volmer and Langmuir fittings of Xe adsorption in IA.

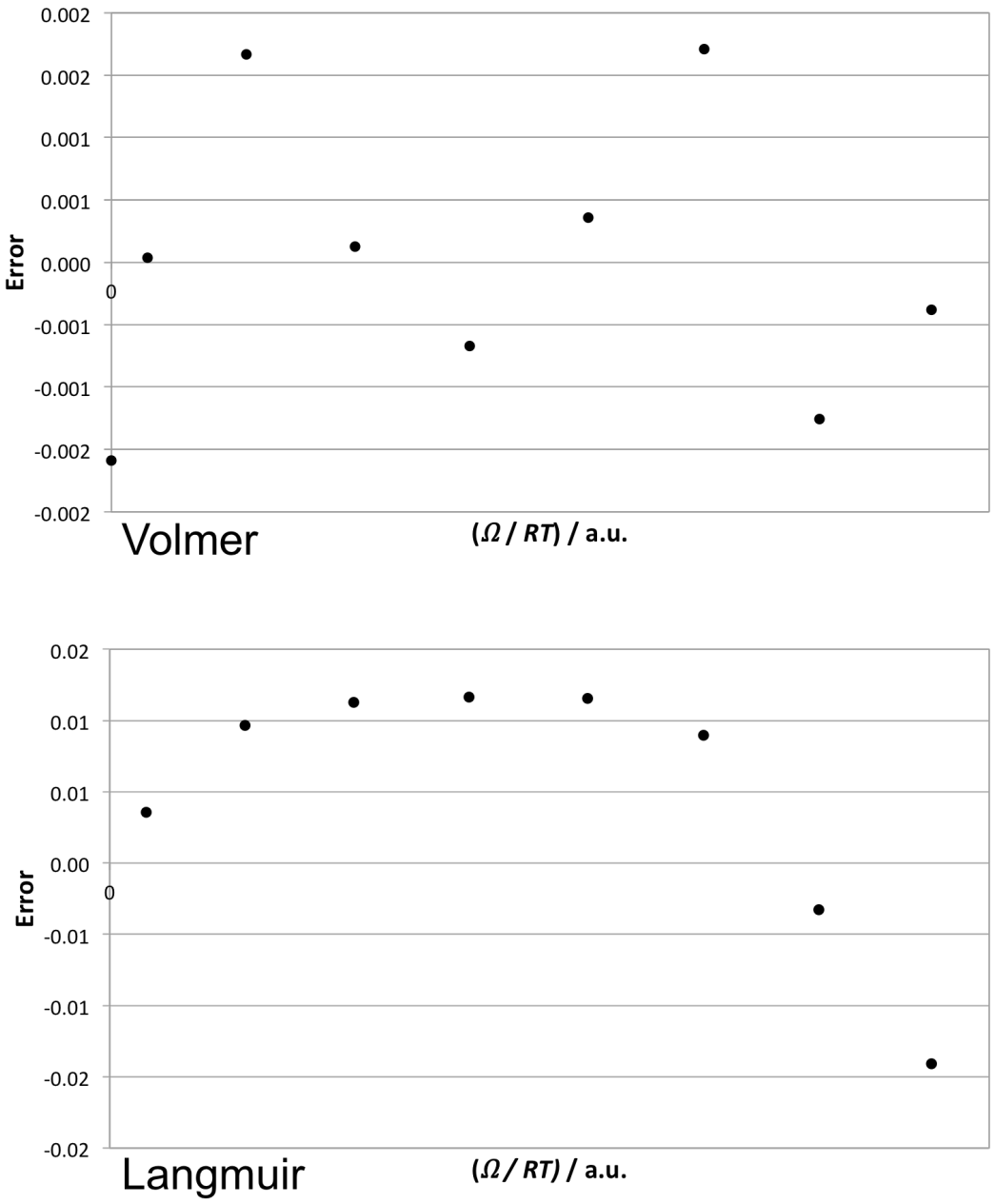

Figure D.7. Residual errors of the Volmer and Langmuir fittings of CO_2 adsorption in IA.

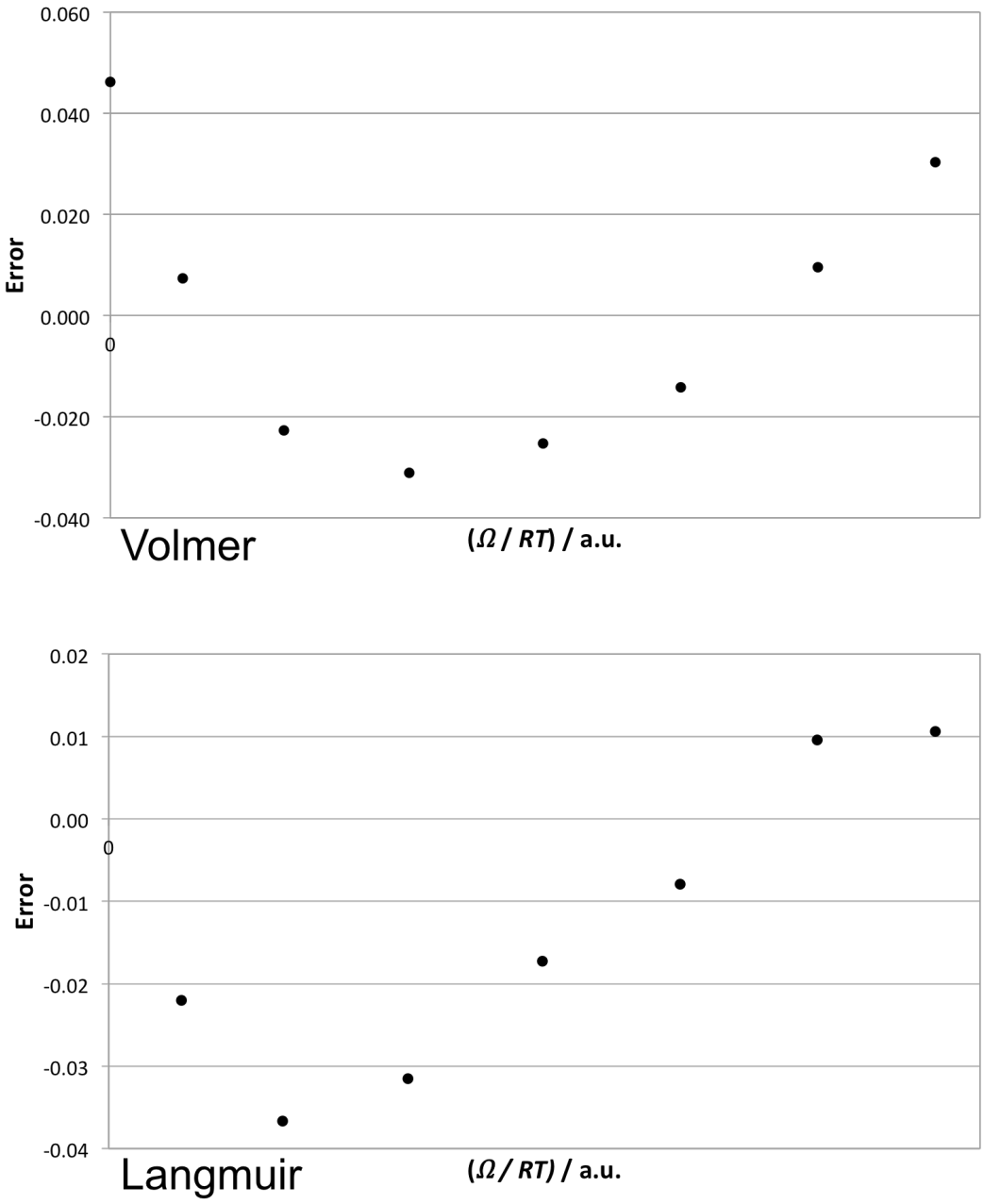

Figure D.8. Residual errors of the Volmer and Langmuir fittings of Xe adsorption in IV.

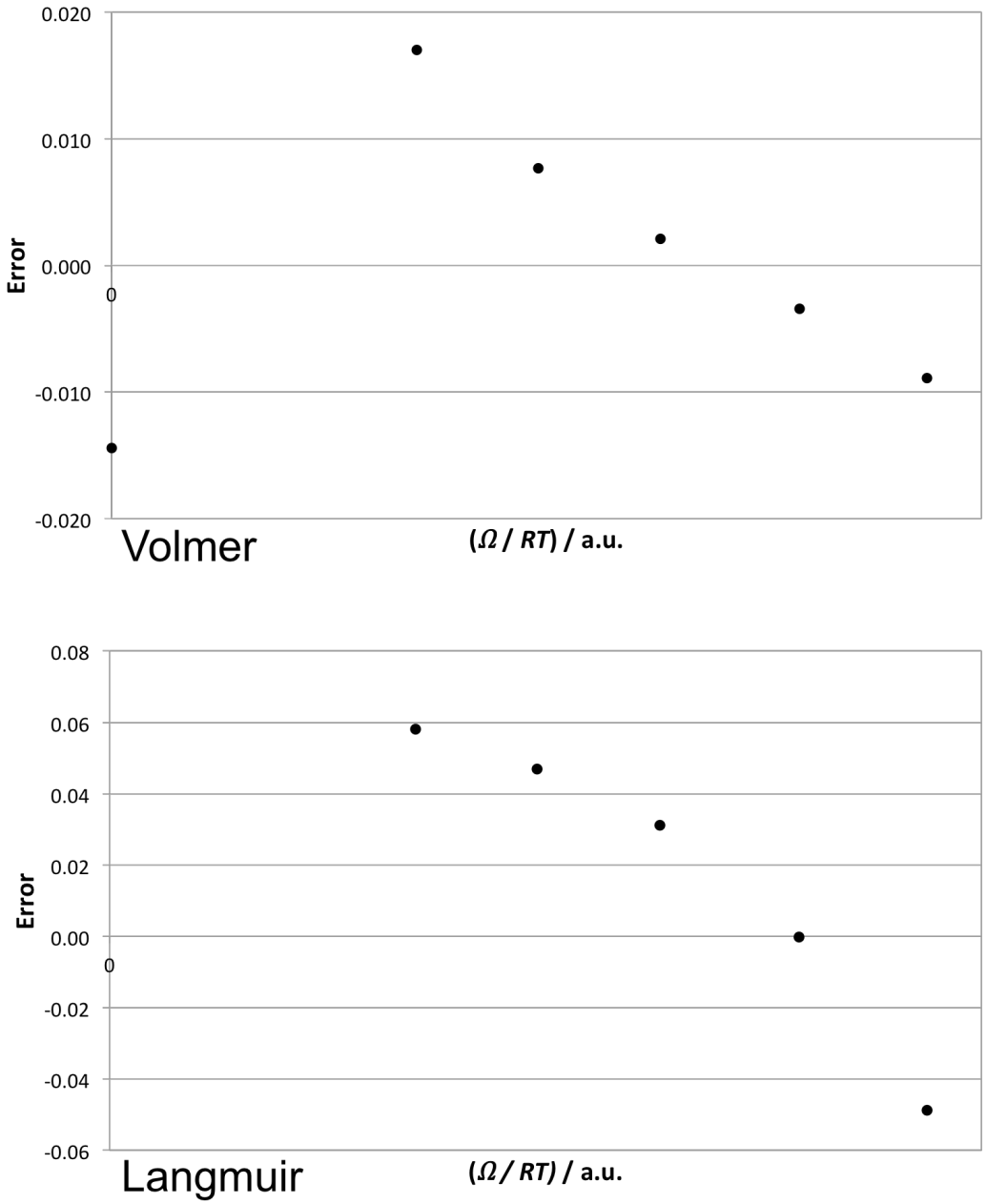

Figure D.9. Residual errors of the Volmer and Langmuir fittings of CO_2 adsorption in IV.

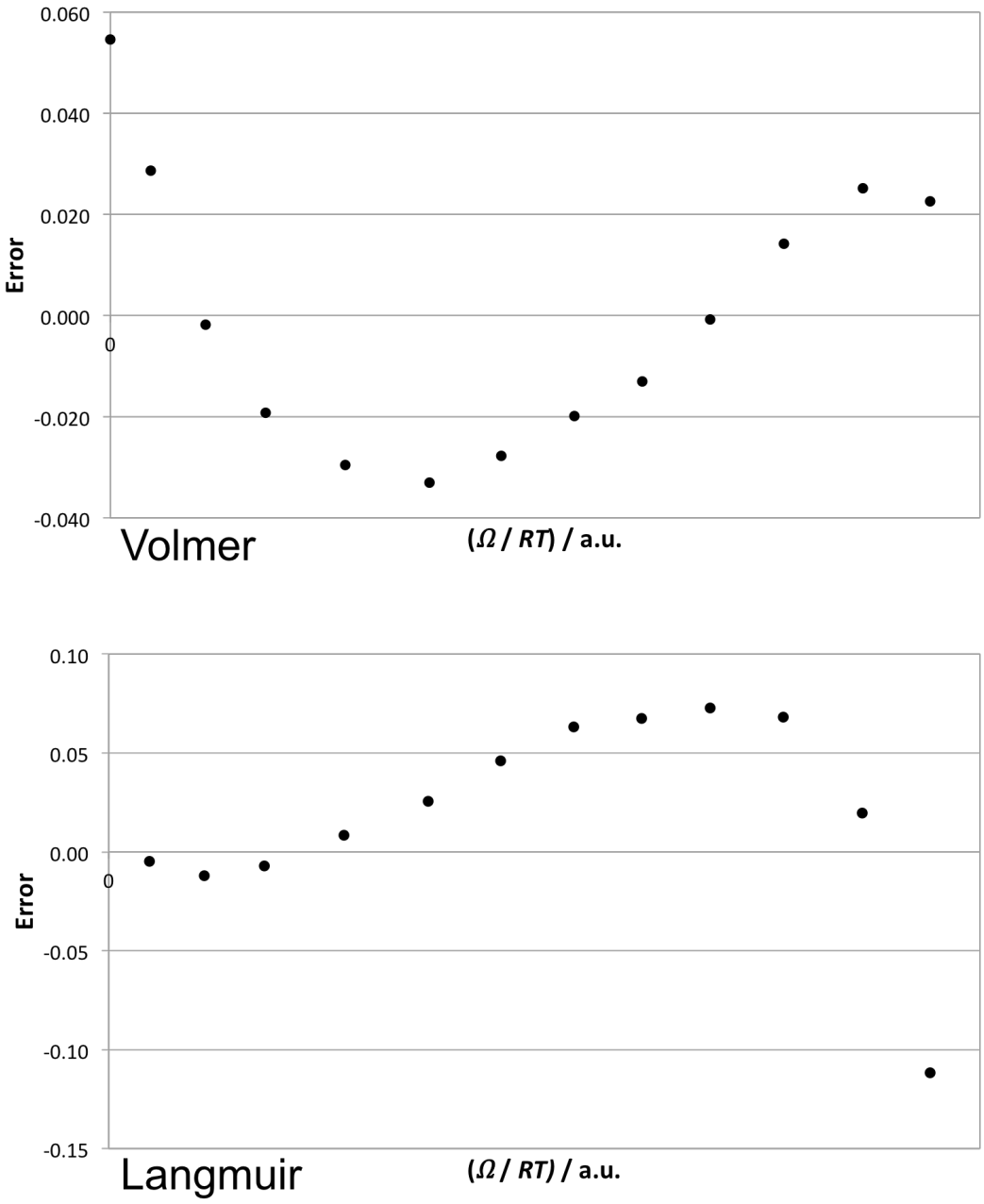

Figure D.10. Residual errors of the Volmer and Langmuir fittings of Xe adsorption in VV.

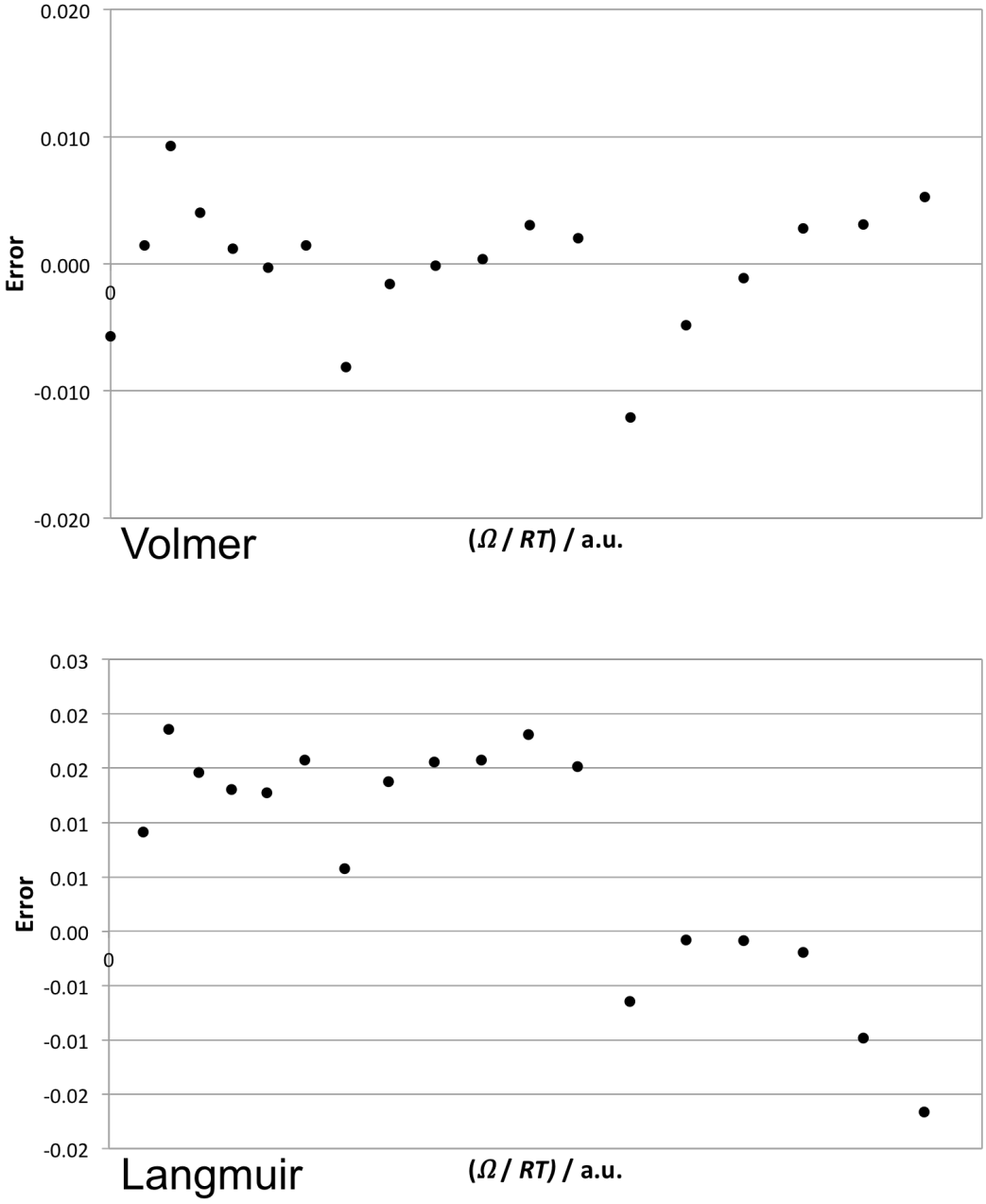

Figure D.11. Residual errors of the Volmer and Langmuir fittings of CO_2 adsorption in VV.